IMPROVED METHOD FOR ASSESSING SOIL RESISTANCE DURING OFFSHORE PILE DRIVING

JOÃO PEDRO SANTOS MONTEIRO SARAIVA

Dissertação submetida para satisfação parcial dos requisitos do grau de

MESTRE EM ENGENHARIA CIVIL — ESPECIALIZAÇÃO EM GEOTECNIA

Orientador: Professor Doutor António Joaquim Pereira Viana da Fonseca

Coorientadores: Doctor David Cathie e Rui Silvano

JULHO DE 2014

MESTRADO INTEGRADO EM ENGENHARIA CIVIL 2013/2014

DEPARTAMENTO DE ENGENHARIA CIVIL

Tel. +351-22-508 1901

Fax +351-22-508 1446

miec@fe.up.pt

Editado por

FACULDADE DE ENGENHARIA DA UNIVERSIDADE DO PORTO

Rua Dr. Roberto Frias

4200-465 PORTO

Portugal

Tel. +351-22-508 1400

Fax +351-22-508 1440

feup@fe.up.pt

http://www.fe.up.pt

Aos meus Pais,

Ao meu Tio

ACKNOWLEDGMENTS

In this important moment of my life I would like to express my sincere gratitude to all who accompanied me during the last five years and to all who have supported and helped during the development of this project. In particular, I would like to acknowledge:

- To my supervisor in Portugal, Professor António Viana da Fonseca, who encouraged me to enrol this project, for the total support, motivation and guidance offered during my academic career;
- To Cathie Associates, for having proposed a so interesting theme. Also, to all the staff of Cathie Associates that received me so well during the time that I was in the company and in Belgium, for their hospitality and for the insights given in the offshore topics;
- To David Cathie, for having shared his experience and knowledge, for all the interest demonstrated in the project and for all the interesting discussions we had during our meetings in the last months;
- To Rui Silvano, who has always supported me during this project and for all the availability shown to discuss particular topics. Also, for his important contributions in some parts of the project and for all the stimulating conversations we had during the time I stayed in Belgium;
- To Christophe Jaeck for all the knowledge regarding subjects such as numerical analysis and CAPWAP signal matching analysis. Also, to Antoine-Mathieu Vernant, for all the information provided regarding wave equation analysis and CAPWAP one-dimensional modelling;
- To Hendrik Versteele, for having received me so well in Leuven and for all the pleasure conversations we had;
- To Professor Pedro Costa, for the suggestions and new ideas and for the guidance throughout the elaboration of this wok;
- To Professor Paulo Pinto, from FCT Univ. Coimbra, for the inputs in the dynamic numerical model developed in the present work;
- To all my friends and family, who although being far away, were always present. For all the good moments, fun and enjoy during these years;
- To my parents, brother, sister and grandparents for all the support and care, for always having encouraged me and for the patience particularly during my staying in Leuven. To my father, for the revision of the thesis.

ABSTRACT

Cathie Associates is an Offshore Geoscience Engineering Consultancy company that is involved in many offshore windfarm projects under development in Europe. Cathie Associates are frequently responsible for the design of the foundations of the wind turbine support structures. This thesis describes some design methods used by Cathie Associates during the design phase of a particular windfarm project located in the North Sea. This project included piled foundations and the Cone Penetration Test (CPT) was used to determine the soil stratigraphy and to estimate the stiffness and strength soil parameters. Afterwards, the axial resistance of the piles was evaluated considering a CPT based approach. This project also included pile driveability analyses namely to select adequate driving equipment and to obtain a bearing graph (blow-count vs depth graph). Finally, a signal matching back-analysis was conducted based on the measured force and velocity signals during pile driving. This analysis was used to assess the measured Soil Resistance during Driving (SRD). This type of back-analyses is often developed using the CAPWAP one-dimensional model.

Using driving data available in the literature and also taken from pile dynamic testing, Cathie Associates noticed that the back-calculated SRD can be significantly smaller than the SRD that is predicted considering existing calculation methods. Differences between predicted and back-calculated SRD were observed in the project that the subject of analysis in this thesis. The reason for this behaviour can eventually be due to some soil mechanisms, as the effect of the soil plug and radiation damping, are not adequately modelled and captured in the CAPWAP one-dimensional model.

This thesis explores these phenomena using dynamic finite element analysis modeling, taking as input in the numerical model the force/velocity signals measured in the field. In this work, a finite numerical model simulation is therefore developed to simulate a dynamic pile testing in offshore conditions. A static model was also developed in order to study the soil mechanisms when a pile is submitted to a static load. The model aims at replicating a real driven pile designed by Cathie Associates for the mentioned project. All the calculations are performed taking advantage of PLAXIS 2D and PLAXIS 2D Dynamics software package.

First of all, the present work concluded that plugging is likely to occur in static conditions. On the other hand, when a pile is dynamically loaded, the pile is unlikely to plug. These considerations are in accordance with other published researches on this topic. Besides that, the developed dynamic numerical model provided SRD values much larger than the calculated in the CAPWAP back-analysis performed by G-Octopus (Cathie Associates operating company dedicated to pile testing) based on pure signal matching. It is therefore concluded that the CAPWAP model does not capture correctly all the soil mechanisms which may lead to an incorrect assessment of the SRD. The main difference between these values is related with the shaft capacity, which is being underestimated by the CAPWAP model. Further conclusions about the soil mechanisms in static and dynamic pile testing are described in this thesis.

KEYWORDS: pile foundation, pile dynamic testing, numerical modelling, soil plugging, wave equation analysis.

RESUMO

A *Cathie Associates* é uma Consultora em Engenharia Geotécnica de *Offshore* e está envolvida em muitos dos projectos de parques eólicos na Europa. Esta empresa é normalmente responsável pelo dimensionamento de fundações das estruturas de suporte das turbinas eólicas. Nesta dissertação são descritos alguns dos métodos utilizados num projecto de um parque eólico situado no Mar do Norte, em que a *Cathie Associates* esteve envolvida. Neste projecto realizaram-se ensaios de penetração (CPT) que foram, em seguida, interpretados para se obter um adequado conhecimento da estratigrafia do solo e para estimar alguns parâmetros de rigidez e resistência. Após esta fase, foi calculada a capacidade axial das estacas utilizando os valores obtidos nos ensaios CPT. Foram também realizadas análises de cravação que permitiram, por exemplo, seleccionar os equipamentos para cravação das estacas e construir gráficos capacidade resistente vs penetração. Por fim, após a instalação das estacas no terreno e com recurso a dados monitorizados durante a cravação (força e velocidade), foi realizada uma '*signal matching back-analysis* que permitiu avaliar a resistência do solo durante a cravação. As análises deste tipo são habitualmente realizadas com recurso ao modelo unidimensional CAPWAP.

Com base em dados publicados na literatura e de diversos ensaios dinâmicos, a *Cathie Associates* verificou que a resistência do solo á cravação apresenta, em geral, valores bastante inferiores aos calculados pelos métodos propostos na literatura. Esta diferença de valores observou-se, em particular, no projecto em estudo. Possíveis razões para este desvio são a incorrecta consideração pelo modelo CAPWAP de fenómenos dinâmicos do solo dentro da estaca e do amortecimento por radiação do solo.

Desta forma, nesta dissertação foram investigados estes mecanismos através da criação de um modelo dinâmico de elementos finitos e utilizando como *input* os dados força/velocidade medidos em campo. Com este propósito, foi desenvolvido um modelo que reproduz um ensaio de carga dinâmico em ambiente *offshore*. Foi igualmente desenvolvido um modelo estático para estudar os mecanismos que ocorrem no solo quando a estaca é submetida a uma carga estática. Os modelos representam uma das estacas dimensionadas pela *Cathie* Associates e instaladas no Mar do Norte. Todos os cálculos foram realizados recorrendo ao pacote de software PLAXIS 2D e PLAXIS 2D Dinâmico.

Em primeiro lugar, esta dissertação permitiu concluir que, em condições estáticas, a estaca apresenta um comportamento '*plugging*' que já não ocorre quando é submetida a uma carga dinâmica. Esta conclusão está de acordo com outras investigações realizadas neste âmbito. Foi também observado que os valores da resistência do solo à cravação calculados pelo modelo de elementos finitos são muito mais elevados do que os obtidos pela análise CAPWAP efectuada pela empresa *G-Octupus* (associada da *Cathie Associates* e dedicada a ensaios de carga em estacas). Pode-se então concluir que o modelo unidimensional utilizado pelo CAPWAP não captura correctamente todos os fenómenos que ocorrem no solo quando uma estaca é submetida a uma carga dinâmica, o que promove avaliações incorrectas da resistência durante a cravação. Esta diferença de valores diz maioritariamente respeito à incorrecta avaliação da capacidade lateral da estaca que é subestimada pelo CAPWAP. Outras conclusões são detalhadas ao longo desta tese, nomeadamente relativas aos mecanismos que ocorrem no solo quando uma estaca é submetida a um ensaio de carga dinâmico e estático.

PALAVRAS-CHAVE: modelos numéricos, *plug*, ensaio de carga, equação da onda, fundações profundas.

TABLE OF CONTENTS

ACKNOWLEDGMENTS I

ABSTRACT III

RESUMO V

1. INTRODUCTION 1

1.1. SCOPE AND MOTIVATION 1

1.2. OBJECTIVES 2

1.3. STRUCTURE OF THE DOCUMENT 2

2. CONE PENETRATION TEST 5

2.1. OVERVIEW 5

2.2. CONE PENETRATION TEST 6

2.2.1. DESCRIPTION 6

2.2.2. DOWNHOLE MODE AND SEABED MODE 7

2.2.3. MEASUREMENT CORRECTION 8

2.2.4. INTERPRETATION OF THE RESULTS 9

2.2.4.1. Relative Density 9

2.2.4.2. Friction Angle 11

2.2.4.1. Young's Modulus 11

2.2.4.3. Constrained Modulus 12

3. PILE FOUNDATIONS 13

3.1. OVERVIEW 13

3.2. OFFSHORE FOUNDATIONS STRUCTURES 13

3.3. PILE TYPES 16

3.3.1. PILES CLASSIFICATION 16

3.3.2. DISPLACEMENT PILES 17

3.3.3. REPLACEMENT PILES 17

3.4. PILE INSTALLATION METHODS 18

3.4.1. CLASSIFICATION OF PILE INSTALLATION METHODS 18

3.4.2. IMPACT DRIVING 19

3.5. PILE DRIVING EQUIPMENT 21

3.5.1. EQUIPMENT CLASSIFICATION 21

3.5.2. HAMMERS 21

3.5.2.1. Drop Hammers 22

3.5.2.2. Air/Steam Hammers 22

3.5.2.3. Diesel Hammers 23

3.5.2.1. Hydraulic Hammers 24

3.5.3. DRIVING SYSTEMS 25

3.5.4. FOLLOWERS 25

4. DESIGN OF PILE FOUNDATIONS 27

4.1. OVERVIEW 27

4.2. AXIAL CAPACITY 28

4.2.1. GENERAL CONCEPTS 28

4.2.2. PLUG AND UNPLUG SOIL BEHAVIOUR 29

4.2.3. CAPACITY OF DRIVEN PILES IN SANDS 32

4.2.3.1. Installation and Friction Fatigue 33

4.2.3.2. Stresses changes when plugging occurs 33

4.2.3.3. Residual stresses 35

4.2.3.4. Loading 36

4.3. DESIGN METHODS 36

4.3.1. ALM AND HAMRE 36

4.3.2. AMERICAN PETROLEUM INSTITUTE (API) DESIGN METHOD 37

4.3.3. IMPERIAL COLLEGE PILE (ICP) DESIGN METHOD 39

4.3.3.1. General Considerations 39

4.3.3.2. Shaft Friction 39

4.3.3.3. Base Resistance 41

4.3.4. DESIGN METHODS COMPARISON 42

4.4. WAVE EQUATION ANALYSIS 45

4.4.1. GENERAL DESCRIPTION 45

4.4.2. WAVE EQUATION FORMULATION 47

4.4.3. FUNDAMENTALS OF WAVE PROPAGATION 51

4.4.3.1. Force-Velocity Proportionality 51

4.4.3.2. Simple Wave Propagation 51

4.4.3.3. Energy Calculation 51

4.4.4. GRLWEAP® 51

4.5. PILE DRIVING MONITORING 52

4.5.1. GENERAL ASPECTS 52

4.5.2. CAPWAP® ANALYSIS 52

4.5.3. CAPWAP RELIABILITY – CATHIE ASSOCIATES INVESTIGATION 54

4.5.3.1 Strain Gauges and Accelerometers 54

4.5.3.2. Cathie Associates Signal Matching Analysis 56

5. STATIC NUMERICAL MODEL FOR SOIL RESISTANCE DURING DRIVING ANALYSIS 59

5.1. OVERVIEW.. 59

5.2. AXISYMMETRIC STATIC MODEL.. 60

5.2.1. MESH 60

5.2.2. PILE MODEL.. 61

5.2.3. SOIL MODEL 62

5.2.3.1 Young's Modulus 64

5.2.3.2 *Poisson*'s ratio 65

5.2.3.3 Effect Cohesion Intercept 65

5.2.3.4 Angle of Shearing Resistance 65

5.2.3.5 Interface Friction Angle.. 66

5.2.3.6 Angle of Dilatancy... 67

5.2.3.7 Lateral Earth Pressure.. 68

5.2.3.8. Triaxial and Direct Simple Shear Tests 69

5.2.4. DISCUSSION OF THE RESULTS 70

5.2.4.1. Plugged Behaviour 70

5.2.4.2. Tension Test.. 73

5.2.4.3. Prescribed Displacement.. 75

5.2.4.4. Surrounding Soil 76

6. DYNAMIC MODEL – GENERAL ANALYSIS 79

6.1. OVERVIEW.. 79

6.2. THEORETICAL BACKGROUND 79

6.2.1. DYNAMIC PROBLEM FORMULATION 79

6.2.2. TIME INTEGRATION 80

6.2.3. VISCOUS BOUNDARIES 80

6.2.4. FREQUENCY SPECTRUM 81

6.2.5. DAMPING 81

6.2.5.1. Radiation damping 82

6.2.5.2. Material damping 82

6.2.5.3. Numerical damping 84

6.2.6. NON-LINEARITY RESPONSE OF THE SOIL 84

6.2.6.1. Soil Stiffness 85

6.2.6.2. Damping 86

6.3. MESH AND DAMPING ANALYSIS 88

6.3.1. MESH REFINEMENT ANALYSIS 88

6.3.2. DAMPING ANALYSIS 91

6.3.2.1. No Damping Considered 91

6.3.2.2. Numerical Damping 93

6.3.2.3. Material Damping 95

6.3.3. FREE OSCILLATION VS FORCED OSCILLATION 97

6.4. WAVE EQUATION MODEL 98

7. DYNAMIC MODEL FOR SOIL RESISTANCE DURING DRIVING ANALYSIS 103

7.1. OVERVIEW 103

7.2. AXISYMMETRIC DYNAMIC MODEL 103

7.2.1. MESH 104

7.2.2. PILE 106

7.2.4. SIGNAL MATCHING ANALYSIS 108

7.2.5. SOIL 111

7.2.5.1. Drained or Undrained Soil Model 112

7.2.5.2. Young's Modulus 112

7.2.5.3. Interface Friction Angle 113

7.2.5.4. Lateral Earth Pressure 113

7.2.5.5. Rayleigh Damping 114

7.2.6 DISCUSSION OF THE RESULTS – CALCULATION PHASE 3 115

7.2.6.1. Plugged vs Unplugged Behaviour 115

7.2.6.2. Analysis at instant t_1 = L/c 116

7.2.6.3. Analysis at instant t_2 = 2L/c 119

7.2.6.4. Analysis at instant t_3 - End of Analysis 121

7.2.6.5. Residual Stresses 123

7.2.6.6. Soil Resistance 125

7.2.7. DISCUSSION OF THE RESULTS – CALCULATION PHASE 4 128

8. CONCLUSIONS AND FUTURE DEVELOPMENTS 133

8.1. CONCLUSIONS 133

8.2. FUTURE DEVELOPMENTS 135

REFERENCES 137

REVIEWED BIBLIOGRAPHY 140

WEBSITE REFERENCES 143

INDEX OF FIGURES

Figure 2.1. – Cone penetrometer, Lunne *et al.* (1997) 7

Figure 2.2. – CPT offshore techniques: seabed mode (left) and downhole mode (right), Lunne (2010) 8

Figure 2.3. – Cone tip and friction sleeve, Robertson and Cabal (2010) 9

Figure 2.4. – Relative density for NC and OC sands, Jamiolkowski *et al.* (2001) 10

Figure 2.5. – Peak drained friction angle and relative density relationship, Kleven *et al.* (1996) 11

Figure 2.6. – Evaluation of Young's Modulus from CPT data for silica sands, Bellotti (1989) 12

Figure 3.1. – Jacket platform (top left) [1]; Jackup (top right) [2]; Gravity foundations (bottom) [1] 14

Figure 3.2. – Tripod (top) [1]; Monopile (bottom left) [3]; Suction bucket (bottom right) [4] 15

Figure 3.3. – Guyed tower (left); Tension leg platform; Articulated tower; Semi-submersible (right), adapted from Lesny (2010) 16

Figure 3.4. – Installation sequence of drilled and grouted piles, adapted from Randolph and Gouvernec (2011) 18

Figure 3.5. – Pile jacking (left) [5]; Vibratory pile driving (right) [6] 19

Figure 3.6. – Impact driving process [7] 20

Figure 3.7. – Bubble curtains [8] 21

Figure 3.8. – Air/Steam hammer [7] 23

Figure 3.9. – Diesel hammer [9] 24

Figure 4.1. – Closed-ended pile failure mechanism 28

Figure 4.2. – Plug behaviour during driving – tubes in depths, adapted from Randolph and Gouvernec (2011) 30

Figure 4.3. – Open-ended pile failure mechanism (a) unplugged behaviour (b) plugged behaviour, adapted from Randolph and Gouvernec (2011) 31

Figure 4.4. – Stress changes during pile installation and loading, adapted from Randolph and Gouvernec (2011) 32

Figure 4.5. – Active plug length, adapted from Henke and Grabe (2008) 34

Figure 4.6. – Plug mechanisms inside an open-ended pile due to pile jacking and vibratory pile driving, adapted from Henke and Grabe (2008) 35

Figure 4.7. – Interface friction angle in sand – illustrative trends from direct shear interface tests, adapted from Jardine *et al.* (2005) 40

Figure 4.8. – Predicted and measured capacities in compression for Tokyo Bay pile load tests, Lacasse *et al.* (2013) 44

Figure 4.9. – Predicted and measured capacities in tension and compression for the Europides pile load tests, Location 1, Lacasse *et al.* (2013) 44

Figure 4.10. – Predicted and measured capacities in tension and compression for the Europides pile load tests, Location 2, Lacasse *et al.* (2013) 45

Figure 4.11. – Smith's model, adapted from Smith's (1960) 46

Figure 4.12. – Physical interpretation of the parameters *z* and *m* 47

Figure 4.13. – External forces applied to a pile section at an instant *t* 49

Figure 4.14. – CAPWAP model: a) Pile model; b) Soil Force-Displacement model; d) Dashpot resistance, adapted from Goble and Rausche (1979) 53

Figure 4.15. – Pile top view – accelerometers and strain gauges location, adapted from G-Octupus . 54

Figure 4.16. – Force and velocity signals measured in the dynamic pile test 55

Figure 4.17. – Wave-up and wave-down measured in the dynamic pile test 55

Figure 4.18. – SRD comparison between Alm and Hamre (2002) calculation and CAPWAP back-analysis 56

Figure 4.19. – Comparison between Alm and Hamre (2002) calculation and CAPWAP back-analysis at different depths: Total skin friction (left); End-bearing capacity (right) 57

Figure 5.1. – Mesh of the 2D Finite Element Model 61

Figure 5.2. – Borehole Log Report, Cathie Associates 63

Figure 5.3. – Soil stress-strain curve, PLAXIS (2014a) 64

Figure 5.4. – Stress-strain curve for dense sands 66

Figure 5.5. – Outside and inside shaft friction profiles for shallow penetration depths 67

Figure 5.6. – Alm and Hamre (2002) and PLAXIS outside shaft friction comparison 69

Figure 5.7. – Triaxial test in drained conditions 70

Figure 5.8. – DSS Test in drained conditions 70

Figure 5.9. – Vertical displacements 71

Figure 5.10. – Principal stresses distribution 72

Figure 5.11. – a) Plastic points: b) Horizontal stresses profiles (right) 73

Figure 5.12. – Shaft friction profiles for both compression and tension tests 74

Figure 5.13. – Load-displacement curve for both compression and tension tests 75

Figure 5.14. – Load-displacement curve for both compression load and prescribed displacement experiment 75

Figure 5.15. – Soil vertical displacements for a depth equal to 14.0 m 76

Figure 5.16. – Volumetric Strains variation with the deviatoric strains 77

Figure 5.17. – s' – t graph 77

Figure 6.1. – Free vibration of critically damped, overdamped and underdamped systems, adapted from Chopra (1995) 82

Figure 6.2. - Rayleigh damping 83

Figure 6.3. – a) Stress strain hysteresis loop, Seed, Idris (1970) b) General stiffness-strain behaviour of soil, Benz (2007) 84

Figure 6.4. – Variation of Shear Modulus with Shear strain for gravely soils, Seed *et al.* (1986) 85

Figure 6.5. – Variation of Shear Modulus with Shear strain for silica sands and calcareous sands, Amoroso (2011) 86

Figure 6.6. – Influence of confining pressure on damping ratio of saturated sand, Seed *et al.* (1986) 86

Figure 6.7. – Damping ratio for sands, Seed *et al.* (1986) 87

Figure 6.8. – Damping ratio and empirical relations for saturated dense Nevada sand, Elgamal *et al.* (2005) 87

Figure 6.9. – Mesh box 89

Figure 6.10. – Acceleration recorded on the five monitored points along time: coarse mesh 90

Figure 6.11. - Acceleration recorded on the five monitored points along time: medium coarse mesh . 90

Figure 6.12. - Acceleration recorded on the five monitored points along time: medium fine mesh 90

Figure 6.13. - Acceleration recorded on the five monitored points along time: fine mesh 91

Figure 6.14. – Displacements recorded on the five monitored points along time: radiation damping... 92

Figure 6.15. – Velocity recorded on the five monitored points along time: radiation damping considered 92

Figure 6.16. – Acceleration recorded on the five monitored points along time: radiation damping considered 92

Figure 6.17. – Power spectrum of the five monitored points: radiation damping considered 93

Figure 6.18. – Displacements recorded on the five monitored points along time: numerical damping. 94

Figure 6.19. – Velocity recorded on the five monitored points along time: numerical damping 94

Figure 6.20. – Accelerations recorded on the five monitored points along time: numerical damping... 94

Figure 6.21. – Power spectrum of the five monitored points: numerical damping 95

Figure 6.22. – Rayleigh damping... 95

Figure 6.23. – Displacements recorded on the five monitored points along time: Rayleigh damping .. 96

Figure 6.24. – Velocity recorded on the five monitored points along time: Rayleigh damping 96

Figure 6.25. – Accelerations recorded on the five monitored points along time: Rayleigh damping 96

Figure 6.26. – Power spectrum of the five monitored points: Rayleigh damping 97

Figure 6.27. – Load case 1 (left); Load case 2 (right) 97

Figure 6.28. – Power spectrum of the five monitored points: Load case 1 98

Figure 6.29. – Power spectrum of the five monitored points: Load case 2 98

Figure 6.30. – Pile model and sections monitored 99

Figure 6.31. – Wave Equation Analysis: force signal calculated in three different sections 100

Figure 6.32. - Wave Equation Analysis: velocity signal calculated in three different sections 101

Figure 7.1. – Velocity times impedance signals: calculated and measured.. 104

Figure 7.2. – Mesh used in the Axisymmetric Dynamic model... 105

Figure 7.3. – Mean range of influence zone for piles in: a) clean sand; b) silty sand, Yang (2006) ... 106

Figure 7.4. – Pile power spectrum.. 108

Figure 7.5. – Rayleigh damping.. 108

Figure 7.6. – Calculated and measured Force signals 109

Figure 7.7. – Calculated and measured Wave-up signals 109

Figure 7.8. – Calculated and measured Force signals: signal matching 110

Figure 7.9. – Calculated and measured Wave-up signals: signal matching 110

Figure 7.10. – Calculated and measured Wave-down signals: signal matching 111

Figure 7.11. - Calculated and measured Energy: signal matching 111

Figure 7.12. – Deviatoric strains of three monitored points 113

Figure 7.13. – Soil Rayleigh damping 114

Figure 7.14. – Velocity x Impedance imposed signal and analysed isntants: t_1, t_2 and t_3........ 115

Figure 7.15. – Principal effective stresses in the studied instants: : t_1 (left), t_2 (middle) and t_3 (right) . 116

Figure 7.16. – Outside and inside Shaft Friction profile: instant t_1 117

Figure 7.17. – Shear stress direction: instant t_1 117

Figure 7.18. – Incremental vertical displacements: instant t_1........ 118

Figure 7.19. – Outside and inside Shaft Friction profile: instant t_2 119

Figure 7.20. – Shear stress direction: instant t_2 120

Figure 7.21. – Incremental vertical displacements: instant t_2........ 120

Figure 7.22. – Outside and inside Shaft Friction profile: instant t_3 121

Figure 7.23. – Shear stress direction: instant t_3 122

Figure 7.24. – Incremental vertical displacements: instant t_3........ 122

Figure 7.25. – Residual stresses........ 124

Figure 7.26. – Residual stresses curve shape: a) adapted from Holloway *et al.* (1978); b) adapted from Wang and Zhang (2008) 124

Figure 7.27. – Pile tip stresses in four points close to the pile tip: no residual stresses considered .. 125

Figure 7.28. – End-bearing capacity: no residual stresses considered 126

Figure 7.29. – Inside and Outside Shaft Capacities: no residual stresses considered........ 126

Figure 7.30. – Shaft Capacity: no residual stresses considered........ 127

Figure 7.31. – Load-Displacement curve: no residual stresses considered.. 128

Figure 7.32 – End-bearing capacity: residual stresses considered... 129

Figure 7.33. – Inside and Outise Shaft Capacities: residual stresses considered 130

Figure 7.34. – Shaft Capacity: residual stresses considered 130

Figure 7.35. – Load-Displacement curve: residual stresses considered... 131

INDEX OF TABLES

Table 4.1. – Coefficients for API design method in sands, adapted from American Petroleum Institute (2010) 38

Table 5.1. – Pile features, static model 62

Table 5.2. – Soil properties, static model 63

Table 6.1. – Soil properties 88

Table 6.2. – Mesh and calculation properties 89

Table 6.3. – Pile features 100

Table 7.1. – Pile features, dynamic model 107

Table 7.2. – Recommended damping values, adapted from Chopra (1995) 107

Table 7.3. – Soil parameters, dynamic model 112

NOMENCLATURE

Capital Latin Characters

A – Pile cross section area

A_s – Surface area of the sleeve of a cone penetrometer

A_c – Projected area of the cone of a cone penetrometer

A_{sb} – Cross section at the base of the sleeve a cone penetrometer

A_{st} – Cross section at the top of the sleeve a cone penetrometer

C – Damping matrix

C_1, C_2 – Relaxation coefficients

D – Outside pile diameter

D_i – Inside pile diameter

D_{CPT} – Diameter of a CPT probe

D_R – Relative density

E' – Young's Modulus

E_0 – Tangent Young's Modulus; Maximum Young's Modulus

E_{50} – Secant Young-s Modulus at 50% strength

$E_{0.1\%}$ – Secant Young's Modulus for an average axial strain of 0.1 %

E_{oed} – Constrained Modulus

F – Force applied to a pile section

F_t – System excitation vector at time *t*

$F\downarrow$ – Wave-down

$F\uparrow$ – Wave-up

G – Shear Modulus

G_0 – Maximum Shear Modulus

I_e – Average element size of a mesh

J – Damping constant

K – Lateral pressure coefficient

K – Stiffness matrix

K_0 – Lateral pressure coefficient at rest

L – Effective height of a pile

M – Mass matrix

M_0 – Tangent modulus for the effective vertical stress before performing CPT

N_q – Dimensionless bearing capacity factor

P – Power of a signal

Q - Quake

Q_{bf} – Ultimate base resistance on a pile

$Q_{bf,p}$ – Ultimate base resistance on soil plug

Q_c – Total force acting on the cone of the cone penetrometer

Q_s – Total force acting on the sleeve of the cone penetrometer

Q_{sf} – Shaft capacity

$Q_{sf,i}$ – Inside shaft capacity on a tubular pile

$Q_{sf,o}$ – Outside shaft capacity on a tubular pile

R_f – Side friction per unit length

V- Point of a pile velocity

V_p – Compression wave velocity

V_s – Shear wave velocity

V_{ult} – Pile axial capacity

W'_p – Submerged weight of a pile

Z – Pile Impedance

Lowercase Latin Characters

a – Net area ratio

a_n, b_n – Fourier coefficients

a (z,t) – acceleration of a point at a time *t* with a depth *z* at *t*=0

c – Wave velocity

c' – Effective cohesion interface

e – *in situ* void ratio

e_{max} – Maximum void ratio of a soil sample

e_{min} – Minimum void ratio of a soil sample

d – Depth to actual layer

f - Frequency

f_1 – Continuous function

f_2 – Continuous function

f_s – Measured side friction in a CPT

f_{sf} – Unit side friction during driving

f_{si} – Initial pile friction

f_t – Corrected side friction in a CPT

h' – Active plug length

h – Soil column within the pile heigh

k – Shape factor for degradation

m(z,t) – depth of a point at a time *t* with a depth *z* at *t*=0

n_c – Parameter which depends on the mesh level of refinement

p – Pile tip penetration

p_a – Reference pressure = 100 kN/m^2

p'_0 – Effective overburden pressure

$p'_{0,TIP}$ – Effective overburden pressure at tip level

q_{bf} – Ultimate unit base resistance

$q_{bf,lim}$ – Limit unit base resistance

$q_{bf,p}$ – Unit base resistance offered by the soil plug

$q_{bf,t}$ – Unit base resistance offered by the pile tip

q_c – Measured cone penetration resistance

q_t – Corrected cone penetration resistance

q_{tip} – Unit base resistance offered by the pile tip during driving

s' – Half of the sum between the maximum and minimum effective stress

t – Half of the difference between the maximum and minimum effective stress

u_1 – Pore pressure filter on the cone in a cone penetrometer

u_2 – Pore pressure filter behind the cone in a cone penetrometer

u_3 – Pore pressure filter behind the sleeve in a cone penetrometer

u_t – Displacement vector at time *t*

$\dot{u}_t$, – Velocity vector at time *t*

$\ddot{u}_t$ – Acceleration vector at time *t*

v (z,t) – Velocity of a point at a time *t* with a depth *z* at *t*=0

x – Horizontal dimension of the mesh box

y – Vertical dimension of the mesh box

z – Depth of a point at *t*=0

Greek Characters

α – Newmark time integration method parameter; Rayleigh parameter

β – Dimensionless shaft friction for sand; Newmark time integration method parameter; Rayleigh parameter

γ' – Unit effective weight

$\Delta\sigma'_r$ – Change in radial effective stress during pile loading

Δt – Time interval

δ_{cv} – Constant volume pile-soil interface friction angle

δ_f – Pile-soil interface friction angle at failure

δh_p – Variation of the plug length during one penetration increment

δL – Variation of the pile length during one penetration increment

$\varepsilon(z,t)$ – axial strains of a point at a time t with a depth z at t=0

ε_v – Volumetric strains

ε_y – Axial strains

ϕ' – Angle of shearing resistance

ν' – *Poisson*'s ratio

ξ – Damping ratio

ρ – Pile density

$\sigma(z,t)$ – axial stress of a point at a time t with a depth z at t=0

σ'_h – Horizontal vertical stress

σ'_{m0} – Mean *in situ* effective stress

σ_N – Normal stress

σ'_f – Effective stress at failure

σ'_{rc} – Radial effective stress acting on the pile shaft after pile installation

σ'_{rf} – Radial effective stress acting on the pile shaft at failure

σ'_v – Vertical vertical stress

τ_f – Shear stress at failure

τ_{sf} – Ultimate unit shaft friction on a pile

$\tau_{s,lim}$ – Limit unit shaft friction on a pile

ψ – Angle of dilatancy

ω – Angular frequency

Abbreviations and Acronyms

1D – One-dimensional

2D – Two-dimensional

API – American Petroleum Institute

CPT – Cone Penetration Test

CPTU – Piezocone Cone Penetration Test

DMT – Flat Dilatometer Test

DSS – Direct Simple Shea

ICP – Imperial College Pile

IFR – Increment Filling Ratio

NGI – Norwegian Geotechnical Institute

PDA – Pile Driving Analyzer

SBP – Self-boring Pressuremeter Test

SCPT – Seismic Cone Penetration Test

SDMT – Seismic Dilatometer Marchetti Test

SRD – Soil Resistance during Driving

UK – United Kingdom

UWA – University of Western Australia

1

INTRODUCTION

1.1. SCOPE AND MOTIVATION

Offshore engineering has been gaining an increasing importance in the energy industry. Therefore, offshore structures have experienced a fast development mainly due to the increase of oil and gas production capacities and volumes. More recently, energy companies have also become interested in offshore windfarms. Along the years the distance from offshore structures to the coast has increased and the environmental conditions became harder. Hence, the offshore industry was required to investigate new pile and structure solutions and new installation method techniques. During the years, many solutions were proposed for offshore structures and piles. The type of foundation depends on the geotechnical conditions of the site. In offshore conditions, piled foundations are frequently preferred instead of shallow foundations. Usually, piled foundations are desired when there are soft soils at the surface and when high horizontal loads are present.

Cathie Associates is an Offshore Geoscience Engineering Consultancy company which is involved in many of the offshore windfarm projects being developed in Europe. Cathie Associates are frequently responsible for the design of the foundations of the wind turbine support structures. This thesis presents some design methods used by Cathie Associates during the design phase of one of their windfarm projects in the North Sea which comprised piled foundations. It will not be mentioned the project name, neither information about the specific project will be provided due to confidentiality reasons. In this project, the Cone Penetration Test (CPT) was used in order to determine the soil stratigraphy and to estimate the stiffness and strength soil parameters. Then, the axial resistance of the piles was calculated according to a CPT based method. Pile driveability analyses were also performed in order to, for example, select adequate driving equipment and to obtain a bearing graph (blow-count vs depth graph). Finally, a signal matching back-analysis was executed based on the measured force and velocity signals during pile driving, which allowed assessing the measured Soil Resistance during Driving (SRD). More detail is now given to the discussed topics along this thesis.

Investigation methods play an essential role in the design of an offshore pile in order to determine the soil stratigraphy and to estimate soil parameters. The CPT is the mostly used site investigation method in offshore environment as it is the basis of the most frequent pile design methods. Still in the design stage, pile driveability analyses are often performed in order to select adequate equipment to install the piles. These studies are usually based in the wave equation formulations proposed by Smith (1960).

During pile installation, strain gauges and accelerometers are usually placed on the pile in order to monitor the pile installation process. The velocity and the force to which the pile is submitted are then calculated from the pile deformation and acceleration measured by the strain gauges and accelerometers. It is then possible to calculate the soil resistance during driving (SRD) of the pile and compare it with the predicted values from the design methods. The same process can be executed in restrike pile dynamic tests in order to calculate the pile axial capacity some days after driving which would consider soil ageing effects. These back-analyses are often performed by CAPWAP signal matching back-analysis.

Based on driving data collected from the literature and on pile dynamic testing, Cathie Associates have noticed that the back-calculated SRD can be significantly smaller than the SRD predicted by existing calculation methods. In particular, discrepancies between predicted and back-calculated SRD were observed for the project studied in this thesis. The possible reason for this may be that some soil mechanisms, such as the effect of the soil plug and radiation damping, are not being correctly captured by the CAPWAP one-dimensional model. In this thesis, these mechanisms will be explored using dynamic finite element analysis modeling using measured force/velocity signals on the pile head as input. All the calculations are performed taking advantage of PLAXIS 2D and PLAXIS 2D Dynamics software package.

1.2. Objectives

Cathie Associates proposed to develop a finite element axisymmetric model in order to analyse the mentioned issues of the one-dimensional CAPWAP analysis. In order to create a robust model and to gain some confidence in numerical modelling subject, it was first proposed to develop a static model. Afterwards, a dynamic model was created. The following objectives were then established for this work:

- Study and comprehension of several subjects regarding offshore pile foundation design such as, site investigation methods, pile installation processes and equipment used in that process, pile design principles;
- Study basic principles regarding soil mechanics and numerical modelling, such as the Mohr-Coulomb model, time integration techniques, damping, frequency spectra, viscous boundaries, non-linear response of the soil;
- Literature review about pile driving numerical modelling and application of this knowledge on the developed models;
- Development of a static axisymmetric model and study of soil mechanisms that arise when a static load is applied to the pile;
- Development of a dynamic axisymmetric model and study of soil mechanisms that occur when a dynamic load is applied to the pile;
- Compare the static and dynamic calculation results, in particular, the soil and pile behaviour;
- Compare PLAXIS and CAPWAP results and identify possible reasons for the observed differences.

1.3. Structure of the Document

Besides this initial introduction chapter, the present work is structured in 7 more chapters. Chapters 2, 3 and 4 cover literature review about site investigation methods and pile foundations. Then, the developed models are described and the results are analysed in Chapters 5, 6 and 7. Literature review about numerical modelling regarding the studied subject is also exposed in these chapters. Finally, conclusions are taken and it is suggested future developments regarding the studied topic.

In a more detailed way, Chapter 2 describes the main principles and techniques of CPT. Then, some correlations based on CPT measured data allow determining the soil stratigraphy, to identify the materials present in the soil and to estimate geotechnical parameters. More relevance is given to the interpretation of the results of sandy soils as the Cathie Associates project that was mentioned was developed in this type of soil.

Chapter 3 covers offshore foundation structures. The pile types and installation methods are addressed and described. Finally, some highlights about pile driving equipment are given.

Chapter 4 presents the basic principles of pile foundations design. Again, more relevance is given to the pile design in sandy soils due to the same reasons mentioned above. This chapter also gives special focus on pile axial capacity as the problem treated in the present work is mainly related with pile axial loading. Hence, in this chapter, pile-soil mechanisms are first detailed. Then, the method proposed by Alm and Hamre (2002) to estimate the SRD is described. Some pile axial capacity design methods are also exposed. This chapter also covers wave equation formulation and pile driveability analysis. Finally, the pile driving monitoring process during installation is detailed. The Cathie Associates project and the CAPWAP back-analysis performed by Cathie Associates in the project studied in the present work are also described in this chapter.

In Chapter 5 it is detailed a static axisymmetric model. It emulates a static pile test at one of the piles designed by Cathie Associates in the project studied in the present work. The procedures that were adopted along this analysis are outlined along this chapter. The dimensional analysis was performed using the software package PLAXIS 2D. Some conclusions are taken regarding soil-pile interaction when a static load is applied to a pile and the pile axial capacity.

Chapter 6 offers a theoretical background about dynamic numerical modelling. Afterwards, several dynamic studies are carried out. The calculations executed in this chapter aim at giving some confidence to develop in a robust way the final dynamic model.

Once having built a robust static model and having studied in detail dynamic numerical modelling, an axisymmetric model was developed taking advantage of the software package PLAXIS 2D Dynamics. Therefore, in Chapter 7 an axisymmetric dynamic model is developed. This model represents a dynamic pile testing. In order to adjust the soil parameters, a signal matching analysis was also performed. At the end of this chapter, conclusions are taken regarding the soil mechanisms when a dynamic load is applied to the pile. Also, a comparison between the pile axial capacity obtained using the numerical model and the CAPWAP back-analysis performed by Cathie Associates is also present.

Finally, Chapter 8 summarizes the conclusions and proposes future developments of the present work.

2
CONE PENETRATION TEST

2.1. OVERVIEW

Investigation methods play an essential role in the design of an offshore pile in order to determine the seabed stratigraphy and to estimate soil parameters. In offshore, these procedures are carried out under particular conditions. One of the problems with offshore investigation is related with the fact that the tests are made from a platform or from a vessel that is always moving. Besides that, due to the high sea water heights, the instrumentation is submitted to high water pressures. Therefore, it is easier to saturate pore water measurement systems thus requiring watertight connections. Comparing with onshore tests, it is also more difficult to handle with the equipment. However, there are other aspects that do not differ from onshore conditions such as the probes that are used, the way the data is processed and how it is interpreted.

The site characterization is divided in three main steps:

- Collection of preliminary met ocean data;
- Geophysical investigation;
- Geotechnical investigation.

The next paragraphs provide details on these three steps. In the first phase, it is made a compilation of all the existing data taking advantage from previous studies developed on the planning area. This information allows the researcher to assess the site conditions and also to identify what necessary data for the design is still missing. In the end of this stage, the design solutions can be discussed taking into account the information obtained so far.

The aim of the geophysical investigation is to obtain information about the seabed topography and soil conditions over a large area. Geophysical studies can reveal seabed features and obstructions. They can also provide information about faulting within the soil and the main stratification boundaries. The measurement systems usually operate sending a seismic signal from a vessel. The reflected waves are recorded in a receiver unit (hydrophones or geophones) in order to be analysed and interpreted afterwards.

Geotechnical studies are normally performed in the design phase. Their main goal is to validate the information assessed in the previous stages and to characterize the soil properties. Geotechnical investigation comprises offshore work and onshore laboratory testing. Offshore work includes sampling and *in situ* testing such as penetration (e.g. CPT) and vane shear testing. The samples recovered offshore are then submitted to onshore laboratory testing. The investigation can be done adopting two different methodologies: seabed mode and downhole mode.

The CPT has been an essential part of offshore soil investigation and its measurements are the basis for a pile axial capacity and SRD estimation. Hence, in Section 2.2 this geotechnical investigation method will be detailed.

2.2. Cone Penetration Test

2.2.1. Description

Lunne *et al.* (1997) and Robertson and Cabal (2010) detailed the specifications, performance, use and interpretation of the CPT. This is one of the most used *in situ* testing. During the last decades, many studies have been carried out in order to develop this investigation method. Initially, CPT was limited to soft soils. However, with the industry development, the CPT can now be performed in stiff soils and, in some cases, even in soft rocks.

CPT tests are usually executed due to their extensive advantages; some of them will now be enumerated. This investigation method provides a fast and continuous profiling and gives reliable data. Besides that, it has a strong theoretical basis for interpretation. However, some disadvantages should be mentioned such as the relatively high capital investment that is required and it does not provide soil samples.

The CPT equipment consists of a cone on the end of a series of rods. The cone is pushed into the ground at a constant rate of 20 mm/s and continuous measurements are made. Thus, CPT provides a continuous profile of the soil response so that different soil layers can be identified. During the test it is measured the resistance to the cone penetration, q_c, and the side friction, f_s. Improved CPT versions can provide measurements of other parameters such as the pore pressure in a piezocone cone penetration test (CPTU).

The standard test equipment consists of a 60° cone having 10 cm^2 base area and a 150 cm^2 sleeve mounted above the tip. However, there are many cone penetrometer sizes available and the cone penetrometer with a base area of 15 cm^2 is increasingly being adopted. The small cones are used for shallow investigation, while the large ones can be used in gravely soils.

The cone resistance is obtained by the division of the total force acting on the cone, Q_c, by the projected area of the cone, A_c. The side friction is given by the division of the total force acting on the sleeve, Q_s, by its surface area, A_s. In a CPTU test the pore pressures can be measured in three different pore pressure filter locations: on the cone (u_1), behind the cone (u_2) and behind the friction sleeve (u_3). Figure 2.1 illustrates the piezocone equipment.

Cone Penetrometer push equipment consists of a push rod, a thrust mechanism and a reaction frame. In offshore tests the used equipment depends on the depth of the water. In shallow waters, for less than 30 m depth, floating platforms and jack-up barges are frequently adopted. In locations with depths of more than 30 m, the pushing equipment is commonly placed on seabed and underwater equipments are used. The CPT tests performed in deeper water can be achieved using the downhole mode or the seabed mode.

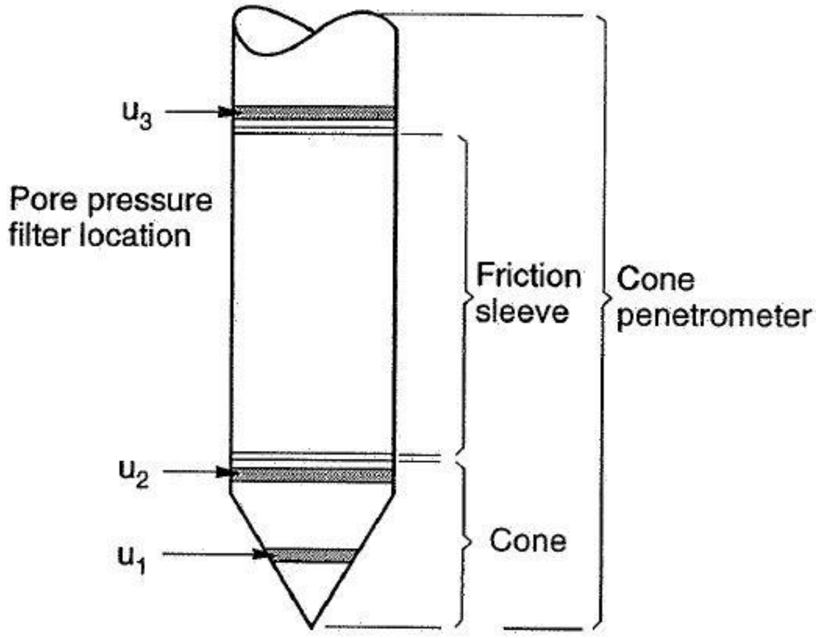

Figure 2.1. – Cone penetrometer, Lunne *et al.* (1997)

2.2.2. Downhole Mode and Seabed Mode

Lunne (2010) described the available techniques for offshore *in situ testing*, including an explanation of the seabed and downhole penetration modes. These penetration techniques correspond to two different ways of execution of the CPT as illustrated in Figure 2.2. While in the seabed mode the cone is pushed into the ground directly from the bottom of the sea, in the downhole mode the penetration is made from the bottom of a drilling hole.

The achievable penetrations by the seabed testing depend on the size of the rings that are used. The size of ‘normal’ rings allows reaching penetrations in the range from 40 to 50 m. This technique allows much faster tests as the tools are always the same during the test period and it is not necessary to repeatedly lower and recover the instrumentation. Thus, in deeper water this can be an important time saver. However, there are some disadvantages of using this system. The test can be forced to stop before the desirable penetration depth has been reached due to the high resistance of hard layers. Besides that, the penetration depths that can be achieved are generally less than the ones reached by the downhole test.

On the other hand, in a downhole test it is drilled a hole and then the CPT test is performed. After the CPT probe is removed, the hole can be extended by drilling again and the process is repeated. Due to the soil disturbance created by the execution of the hole, this technique gives less control of the system. Thus, the quality of the results will be lower and their interpretation should be made carefully. The main advantage of this method is the higher penetration depths that can be achieved, about 150 m at maximum. Besides that, stiff layers can also be drilled through and it is possible to make other type of investigations in the same hole.

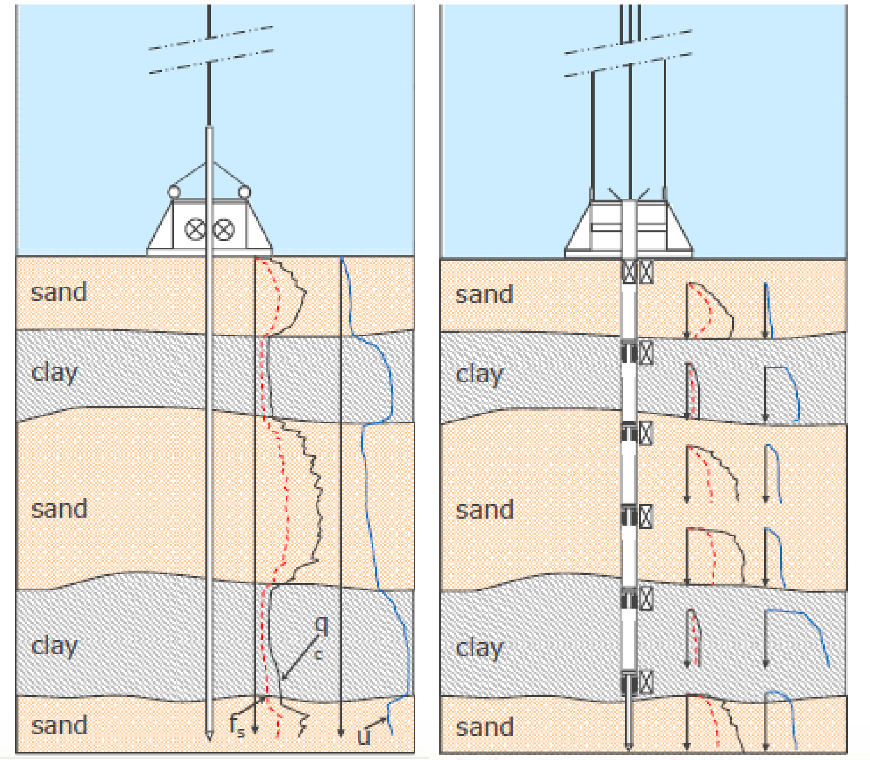

Figure 2.2. – CPT offshore techniques: seabed mode (left) and downhole mode (right), Lunne (2010)

2.2.3. Measurement Correction

There are many factors that can influence the measurements. Some of these factors are the pore water pressures around the cone, the location of the filter, the temperature changes, inclination and calibration of errors.

Regarding the pore water pressure effect, its influence can be very large due to the high hydrostatic water pressures. These effects exist due to the geometry of the cone. The water pressure acts in the section behind the cone and in the bottom of the side shaft, as illustrated in Figure 2.3.

In tests performed underwater, the q_c measured should be corrected using Equation 2.1. In this expression, parameter `$a$` is the net area ratio determined from laboratory calibration. The corrected cone penetration resistance will be named as q_t.

$$q_t = q_c + u_2.(1 - a) \tag{2.1.}$$

The correction to introduce due the sleeve friction is given by Equation 2.2. Here, f_t is the corrected cone penetrometer sleeve friction and A_{sb} and A_{st}, correspond to the cross-section areas of the sleeve at the base and at the top, respectively. However, this correction is not as used as the one detailed before by Equation 2.1.

$$f_t = f_s - \frac{(u_2.A_{sb} - u_3.A_{st})}{A_s} \tag{2.2.}$$

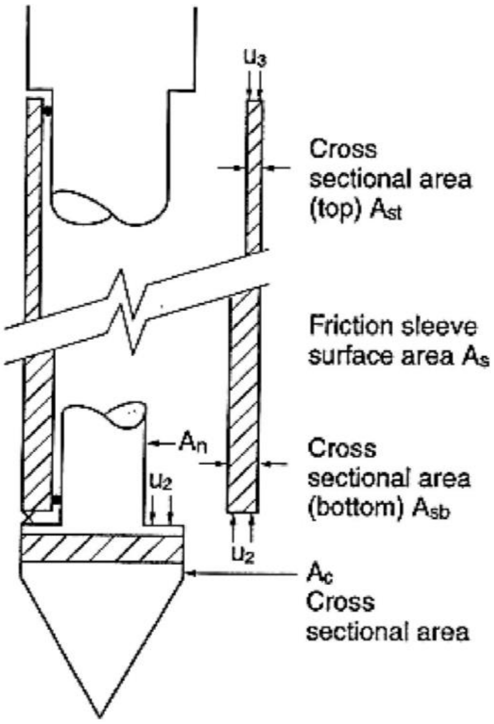

Figure 2.3. – Cone tip and friction sleeve, Robertson and Cabal (2010)

2.2.4. Interpretation of the Results

Some correlations based on CPT and CPTU measured data allow determining the soil stratigraphy, to identify the materials present in the soil and to estimate geotechnical parameters. This section provides some correlations in order to estimate the soil relative density, the friction angle and the constrained modulus from CPT results. These procedures were also used by Cathie Associates during the project that is detailed in the present work in order to estimate soil parameters for a correct design of pile foundations. The procedures exposed are applicable to sandy soils. A fully drained cone penetration is also considered.

2.2.4.1. Relative Density

Relative density is usually used as an intermediate parameter to estimate stress-strain-strength characteristics of sands and gravel soils. The relative density, D_R, can be defined as formulated by Equation 2.3. In this expression e_{max} and e_{min} are the maximum and the minimum void ratios of a soil sample. The parameter *e* is the *in situ* void ratio of the examined sample. The sand is categorized as dense for D_R values between 65% and 85%. Very dense sands present D_R values larger than 85% up to 100%, or occasionally higher.

$$D_R = \frac{e_{max} - e}{e_{max} - e_{min}} \tag{2.3.}$$

Cathie Associates calculates the relative density following the proceedings proposed by Jamiolkowski *et al.* (2001). The correlation between the cone tip resistance and the relative density for normal consolidated (NC) and overconsolidated (OC) dry silica sands is obtained by Equation 2.4, where C_0 = 24.94, C_1 = 0.46 and C_3 = 2.96. Still, σ'_{mo} is the mean *in situ* effective stress in *bar* units. The cone tip resistance, q_c, is also given in *bar*. The relative density can also be estimated from the abacus displayed in Figure 2.4.

$$D_R = \frac{1}{C_2} \ln\left(\frac{q_c}{C_0(\sigma'_{mo})^{C_1}}\right) \tag{2.4.}$$

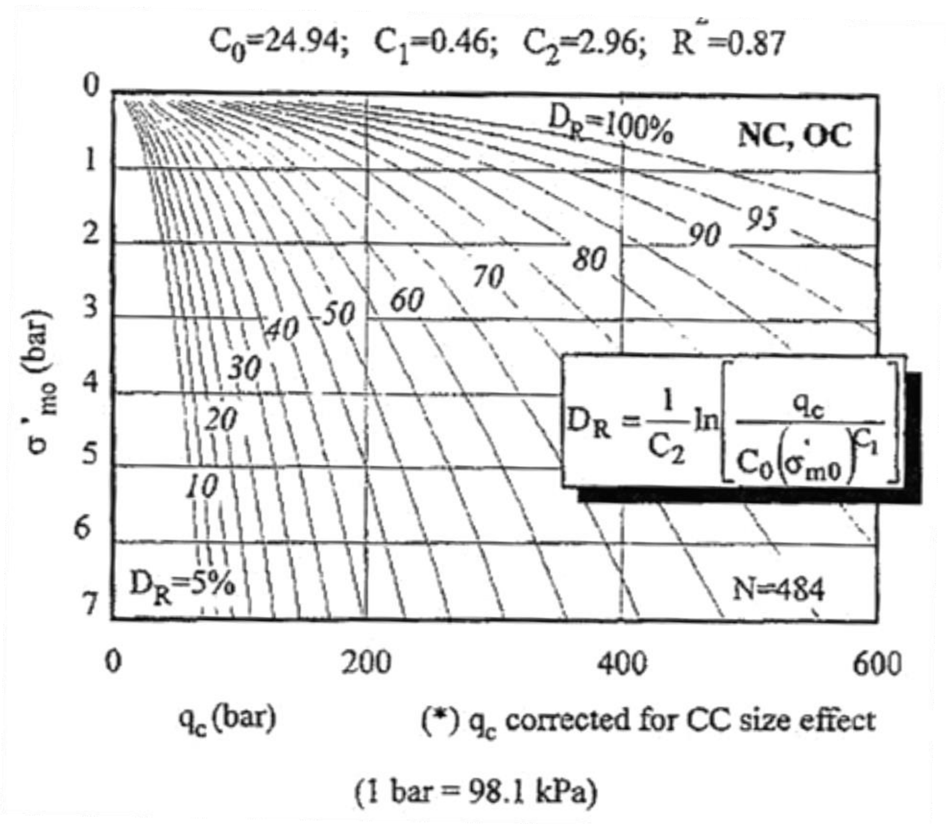

Figure 2.4. – Relative density for NC and OC sands, Jamiolkowski *et al.* (2001)

The previous correlation is derived for dry silica sands. The use of the previous correlation in saturated sands leads to an underestimation of D_R. However, the underestimation of D_R for the studied sands ranges between 7% and 10%. In the studied project, the saturation effect is therefore neglected in the estimation of the relative density.

2.2.4.2. Friction Angle

The shear of cohesionless soils is usually expressed in terms of the peak friction angles, ϕ'. Several methods for assessing ϕ' have been published. Kleven *et al* (1996) proposed estimating the friction angle from the knowledge of the relative density, D_R. Figure 2.5 shows how the friction angle varies with overburden pressure for different soil relative densities.

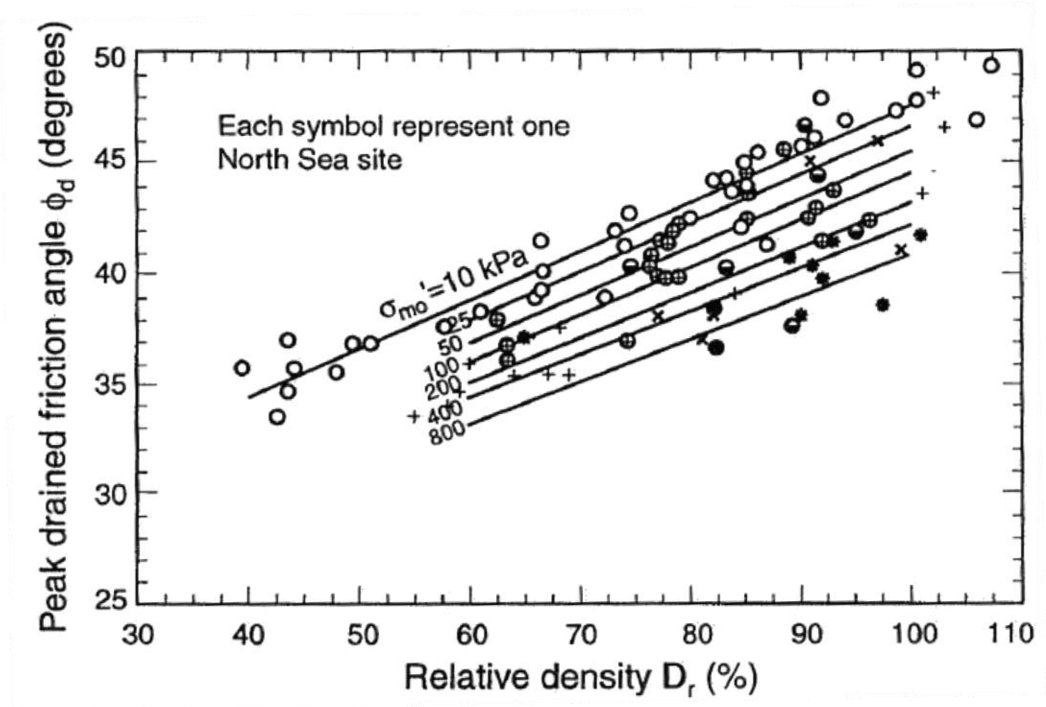

Figure 2.5. – Peak drained friction angle and relative density relationship, Kleven *et al.* (1996)

2.2.4.1. Young's Modulus

The determination of the stiffness from laboratory tests is extremely difficult due to the necessity to obtain undisturbed samples. Thus, it is of major interest to obtain these parameters from *in situ* tests. However, it is still difficult to obtain good Young's Modulus estimations from *in situ* tests because:

- Stiffness depends on effect stresses and ageing effects;
- *In situ* test conditions, drainage and direction of loading cannot be controlled;
- Reference modulus values are rarely documented.

Any correlation needs to be link to a drainage condition of the *in situ* test, stress level and strain level range over which the modulus is applicable.

The Young's Modulus, *E'*, in sands mainly depends on relative density, overconsolidation ratio and the mean effective stress level. Figure 2.6 can be used to estimate the secant Young's Modulus for an average axial strain of 0.1 %. This level of strain is representative for well-designed foundations.

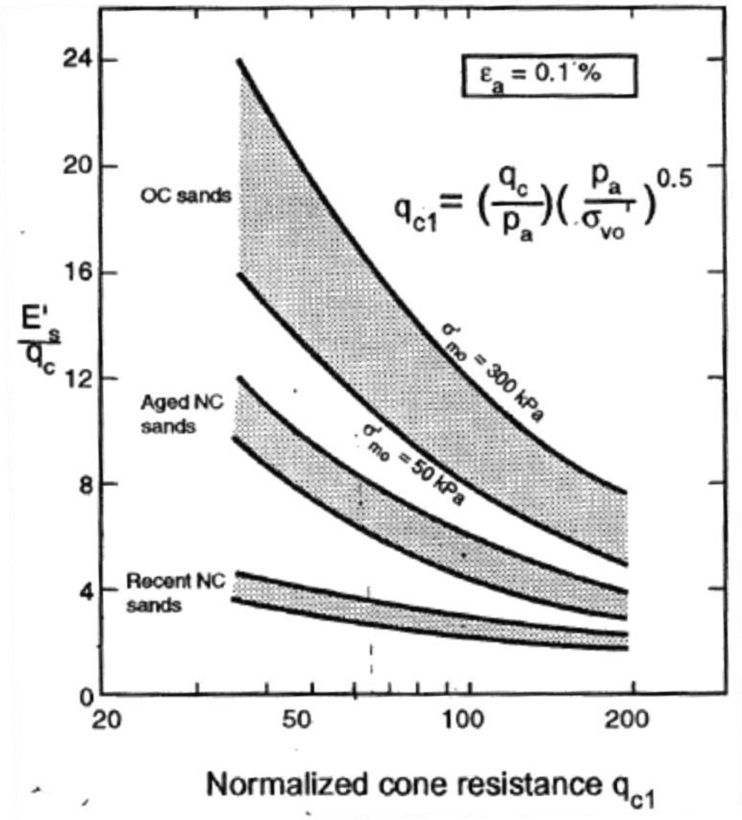

Figure 2.6. – Evaluation of Young's Modulus from CPT data for silica sands, Bellotti (1989)

2.2.4.3. Constrained Modulus

Lunne and Christophersen (1983) proposed a correlation between the drained Constrained Modulus and the cone tip resistance. Depending on the values of q_c, the Constrained Modulus for NC granular soils can be estimated by Equation 2.4, Equation 2.5 and Equation 2.6. In these equations, M_0 is the tangent modulus for the effective vertical stress before performing the *in situ* test.

$$M_0 = 4q_c, \quad q_c < 10\ MPa \tag{2.4.}$$

$$M_0 = 2q_c + 20\ (MPa), \quad 10\ MPa < q_c < 50\ MPa \tag{2.5.}$$

$$M_0 = 120\ MPa, \quad q_c > 50\ MPa \tag{2.6.}$$

For OC sands, it is recommended the use of Equation 2.7 and Equation 2.8 to estimate M_0.

$$M_0 = 5q_c, \quad q_c < 50\ MPa \tag{2.7.}$$

$$M_0 = 250\ MPa, \quad q_c > 50\ MPa \tag{2.8.}$$

3
PILE FOUNDATIONS

3.1. Overview

Civil engineering structures can be divided in onshore, offshore and near-shore structures according to the place where they are located. The present work will only focus on offshore structures. The offshore technology has experienced a fast development mainly due to the increase of oil and gas production capacities and volumes. More recently, energy companies have also became interested in offshore windfarms. Thus, energy companies try to take advantage of the favourable conditions of the sea and also try to avoid onshore environmental impacts.

Offshore structures differ in some aspects from onshore structures. The design life of offshore structures is usually in the range of 25 to 50 years. On the other hand, onshore structures are usually designed for 50 to 100 years. Unlike onshore structures, in offshore conditions the horizontal loads (wind and waves) and cycling loads play a decisive role in the design processes. Due to the large water depths in offshore, many structures need to be taller than what they would have to be in onshore in order not to be destroyed by the rise of the water level caused by storms. Regarding the installation process, most of the offshore structures are constructed in parts in onshore, and are then transported to their location and assembled offshore. Economically, offshore projects are much more expensive than onshore ones. Besides that, in case of failure, there would be high environmental and financial consequences.

Along the years the distance of the offshore structures from the coast have increased and the environmental conditions became harder. Hence, the offshore industry was required to investigate new pile and structure solutions and new installation method techniques. During the years, many solutions were proposed for offshore structures and piles. The type of foundation depends on the geotechnical conditions of the site. In offshore conditions, piled foundations are frequently preferred instead of shallow foundations. Usually, piled foundations are desired when there are soft soils at the surface and when high horizontal loads are present.

This chapter will first focus on the offshore foundation structures. Then, the pile types and installation methods will be addressed and described. Finally, a highlight about pile driving equipment is given.

3.2. Offshore Foundations Structures

Offshore structures were initially constructed to suit the necessities of the oil and gas industries. The most well-known foundation structures for oil and gas projects are jackets, jackup rigs and gravity structures. However, not all of the structures mentioned in the next paragraphs are supported by pile foundations. Figure 3.1 illustrates the three types of structures mentioned above.

Jacket platforms are one of the most common structure types in offshore. These structures comprise a framed steel structure with a deck on the topside modulus. Small jacket structures are commonly supported by one pile at each corner. Intermediate jackets may have skirt piles along the larger side of the platform. On the other hand, the larger jackets are typically sustained by a group of piles at each corner of the platform.

Jackup rigs are mobile platforms and have already been installed in water depths up to 150 m. They consist of a self-elevating platform of a hull and three or more retractable legs. The legs of larger jackups consist of a frame and are supported on independent foundations named ‘spudcans’. On the other hand, smaller jackups can have tubular piles. In this case, the foundations consist of a single and large mat to which the legs are permanently attached. Jackups are typically used to erect other offshore structures and for site investigation.

Gravity foundation structures have been installed in water depths up to 300 m. The stability is given by its selfweight. The deck and topsides are supported by concrete legs that transfer the loads to a caisson base.

Figure 3.1. – Jacket platform (top left) [1]; Jackup (top right) [2]; Gravity foundations (bottom) [1]

The conventional foundation structures for windfarms are based on the ones used firstly by the oil and gas industries. Therefore, in wind energy plants the first adopted solutions were jackets and gravity foundation structures. However, other foundation types were proposed later as tripods, monopiles and suction buckets.

In windfarm projects, the steel frame structures (e.g. jackets and tripods) are prefabricated on land, transported to their location and anchored to the seabed. Tripods consist of a main pile with three legs. The anchoring of these frame structures is carried out with pile foundations.

However, they can also be supported by shallow foundations or suction bucket foundations. Suction bucket foundations comprise a steel cylinder closed on the top. This type of foundation is inserted in the soil by the creation of vacuum inside the cylinder.

Monopiles consist of steel pipe piles that are filled with concrete or soil when greater stiffness is required. As one single pile has to support the total loading, usually monopiles have large diameters and embedded depths. Figure 3.2 illustrates the monopile, the tripod and the suction bucket foundation structure solutions.

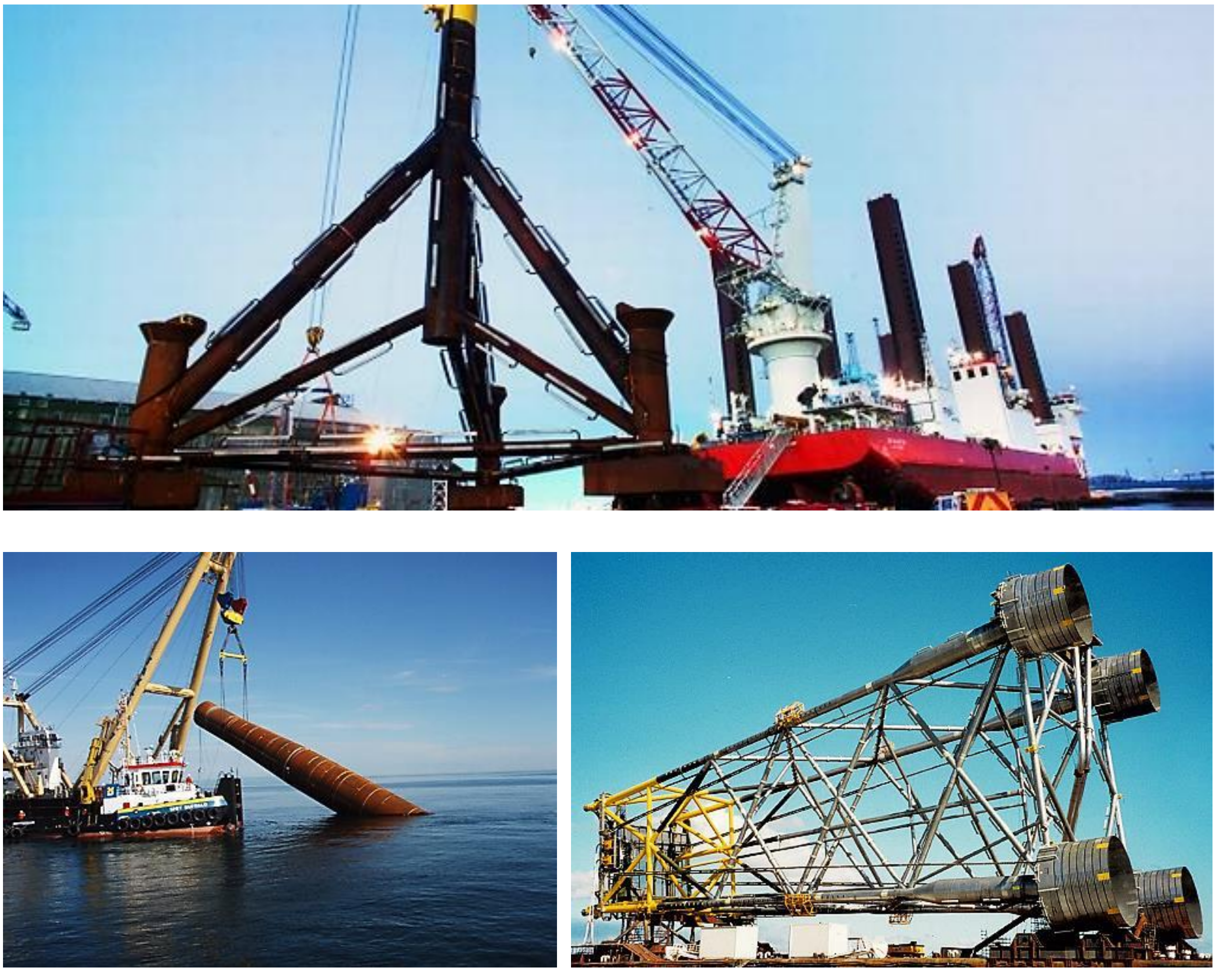

Figure 3.2. – Tripod (top) [1]; Monopile (bottom left) [3]; Suction bucket (bottom right) [4]

Apart from the rigid structures previously detailed, there are also flexible and floating structures. Examples of offshore flexible constructions are the articulated towers or guyed towers, as illustrated in

Figure 3.3. Due to their flexibility, the bending moment is reduced in comparison with rigid structures. Anchoring in the soil is carried out with piles, suction anchors or anchor plates.

In floating structures, such as tension-leg platforms or tethered platforms, the floating body is semi-submersible. Anchoring is offered by pre-stressed anchors or anchor piles or suction anchors. The anchors are designed so that they are always loaded in tension.

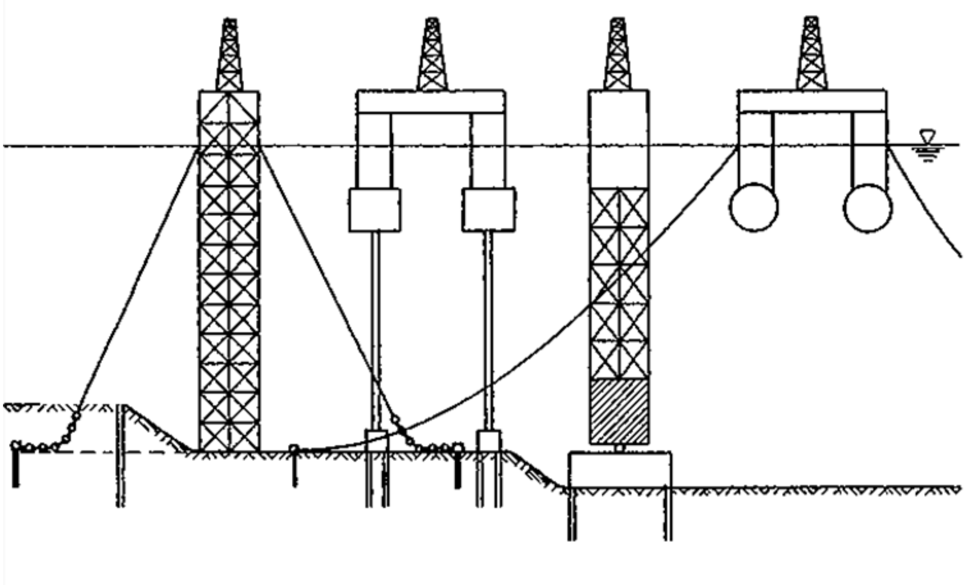

Figure 3.3. – Guyed tower (left); Tension leg platform; Articulated tower; Semi-submersible (right), adapted from Lesny (2010)

3.3. Pile Types

3.3.1. Piles Classification

The selection of a proper pile type depends on the location and the type of structure, the ground conditions and the required durability. Steel tubular piles are the most used piles in offshore conditions. They have the advantages of being robust, light to handle, capable of carrying high compressive loads, capable of being driven hard to a deep penetration to reach a bearing stratum or to develop a high skin friction resistance. They are also not as expensive as concrete piles.

Pile foundations can be divided in three different pile categories, as follows:

- Large displacement piles;
- Small displacement piles;
- Replacement piles.

In the present work, large displacement piles and small displacement piles will be gathered and treated in same pile type. Also, more details will be given about displacement piles as they are the most common pile types used around the world and the numerical model to be detailed in the present work studies a steel driven pile.

3.3.2. Displacement Piles

Displacement piles are installed by displacing the soil. This type of piles can be driven (impact driving or vibratory driving) or jacked. Pile installation methods are addressed in Section 3.4. During the design stage of a displacement pile, some aspects related with driveability and consolidation should be taken into attention.

Driveability concerns are related with the driving stresses, tip damage and refusal. Regarding the pile stresses, the driveability study must ensure that the pile is not overstressed and that the process of driving does not increase significantly the fatigue of the pile.

If the pile tip is damaged during driving, then the pile tip may buckle and collapse. Therefore, usually a thickened wall is built near the pile tip, named a ‘shoe’. This solution reinforces the tip and decreases the pile shaft friction. Sometimes, a stiffer tip is needed. In these cases, a welded steel plate or a conical tip is adopted. The loss of pile shape due to the pile tip damage can result in the reduction of pile capacity or refusal.

Refusal occurs when the desirable penetration cannot be achieved. This phenomenon happens because the soil resistance exceeds the hammer capacity. The first solution when pile refusal occurs is to use a higher performance hammer. Another possibility is to remove the soil inside the pile so that the pile penetration resistance gets reduced. Sometimes, the resistance offered by the soil inside the pile is decisive to the final bearing capacity. In these situations, the pile must be refilled with soil or concrete.

Consolidation issues are related with the period of time that the soil requires to achieve the full capacity. When driving is stopped, the consolidation process starts. Therefore, the soil resistance will increase and pile driveability will be affected. This period of time is also called ‘set-up’ and it will be discussed in more detail in Chapter 4.

Another issue that may come up is the possibility of the pile to sink. This happens if the resistance offered by the soil is less than the pile self-weight.

3.3.3. Replacement Piles

Replacement piles, or drilled piles, are installed by removing the soil and then place the pile in the drilled hole. The installation process of a drilled and grouted pile is illustrated in Figure 3.4 and it can be organized in the next steps:

- An initial steel tubular pile is driven through the shallow soft soils (this phase is not always necessary);
- A rotary drilling rig opens a borehole, beyond the primary pile, until the final penetration depth;
- The final pile is introduced into the drilled hole;
- The annulus between the pile and the hole is filled with grout.

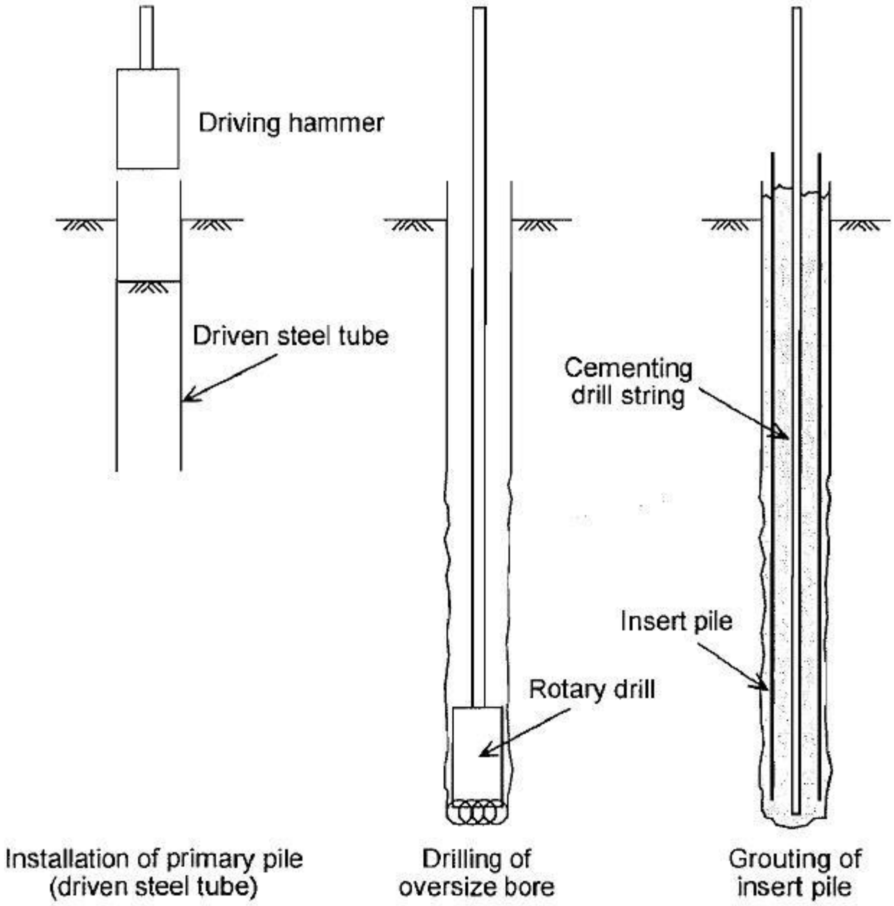

Figure 3.4. – Installation sequence of drilled and grouted piles, adapted from Randolph and Gouvernec (2011)

Drilled piles are mainly used in calcareous sands, where driven piles present low shaft capacities, and in rocks, where driving is not possible. This type of pile is more expensive than driven piles, as the installation process takes more time and because sometimes it is necessary to driven piles through the shallow soft soil that may exist.

During the design stage of drilled and grouted piles some considerations about the hole stability and the grouting operation should be taken into account.

3.4. Pile Installation Methods

3.4.1. Classification Of Pile Installation Methods

Pile installation methods can be classified in static penetration or dynamic penetration methods. The most common installation techniques of displacement piles are:

- Jacking;
- Impact driving;
- Vibratory driving;

In this work, impact driving will be studied further in Section 3.4.2. A general explanation of the other installation methods is provided in this section.

Pile jacking, also called press-in pilling, is a static technique to install piles. The pile is pushed into the ground by hydraulic rams. The pile jacking method offers some advantages in comparison with dynamic pile driving, such as the reduction of the noise and the reduction of the vibrations during driving.

Vibratory driving is performed taking advantage of a vibratory hammer, as illustrated in Figure 3.5. This type of hammer works by eliminating the soil shaft friction acting on the pile. Some advantages in comparison with impact driving can be mentioned. They cause less noise and damage to the pile. Besides that, the shock wave effect from impact driving is eliminated. This technique is very efficient when executed in soft soils. However, it is not so effective in stiff soils.

Figure 3.5. – Pile jacking (left) [5]; Vibratory pile driving (right) [6]

3.4.2. Impact Driving

Impact driving is a dynamic pile installation technique. Figure 3.6 illustrates the installation of a pile by impact driving. Depending on the used hammers, there are different types of impact driving. Hammer categories are addressed in Section 3.5. One important characteristic of impact driving is the formation of a shock wave that propagates along the pile. Its influence in the pile installation is analysed by driveability analyses.

Pile driveability analyses are also performed to select adequate equipment for the installation process. These studies allow the prediction of the energy required to drive the pile, which depends on the pile geometry and on the subsoil conditions. Thus, it compares the driving resistance over a depth with the number of needed blow-counts to install the pile until the desired depth. Driveability analyses are based on the one-dimensional model proposed by Smith (1960). Nowadays, some software packages as GRLWEAP are used to emulate the pile driving process. This topic will be discussed later in the present work.

Figure 3.6. – Impact driving process [7]

Pile driveability analysis is strongly influenced by the pile base resistance, the steel wall thickness of the pile and the steel cross section. As the steel cross section gets larger, more adequate driving energy can be obtained, and so a high driving performance can be achieved. However, if the pile has a high pile base resistance, a reduction of the pile cross section can be advantageous to reduce the pile driving resistance because it will increase the driving performance. A third situation can occur if the soil column within the pile presents plug behaviour. In this case, a large steel cross section implies high pile base resistance. Regarding the wall thickness, a minimum value is required to prevent pile buckling. Pile diameter plays a secondary role in pile driveability. Nevertheless, it is an important aspect in the selection of the installation equipment.

In Section 3.3.2 some issues that can come up during the driveability of a displacement pile were mentioned. Regarding the impact driving installation technique one particular issue should be mentioned. When the pile is stroked by a hammer, a wave with high frequencies is generated. Recently, several investigations have been made in order to assess the environmental impacts (marine fauna risk) of that effect. This aspect gets more relevance in windfarms where a large number of piles need to be installed. The acoustic noise propagates by reflected waves on the seabed and on the surface of the water. This issue can lead to limitations in the number of piles that can be installed at the same time.

Some solutions were proposed to reduce the acoustic noise impact. Drilled piles are one alternative, although they are rarely used in offshore environment. The use of bubble curtains is another solution usually adopted. In some countries as Germany, the usage of bubble curtains is mandatory. However, as the waves propagate mainly by the seabed, bubble curtains are not an efficient solution to dissipate the wave propagation. More research is being made regarding this topic. Figure 3.7 shows a project example where bubble curtains were used.

Figure 3.7. – Bubble curtains [8]

3.5. PILE DRIVING EQUIPMENT

3.5.1. EQUIPMENT CLASSIFICATION

Rausche (2000) presents the state of the art regarding the impact driving equipment. Piled foundations are really expensive and they can correspond to a significant part of the cost of the entire project. Thus, during the years substantial developments have been made in order to optimize the installation process. Therefore, many hammer solutions have been proposed. Some of them will be addressed in Section 3.5.2.

Besides the hammer, a driving system also comprises a hammer cushion, a helmet with inserts (cap) and a pile cushion (only for concrete piles). Some progress was also made to improve the driving systems. Pile driving guides should also be used to make sure that the pile is maintained in the correct vertical alignment during installation. In near-shore and offshore conditions, free riding leads are used almost exclusively to align the hammer and the pile. A template or a jacket structure provides the support for the pile and the hammer.

Some installation aids can be used in special cases. Followers, jetting, predrilling and spudding are the most well-known. In Section 3.5.3 further details will be given about followers.

3.5.2. HAMMERS

Pile driving hammers are usually classified according to their potential energy, which is dependent on the hammer height before the ram starts its downward movement. The kinetic energy available to do work on the driving system, pile and soil, is a portion of the potential energy. Therefore, the ratio between the kinetic energy and the potential energy is called efficiency. For the hammers that record the ram position and velocity at the moment immediately before the impact with the pile, the efficiency is replaced by the available kinetic energy.

Hammers can also be classified by alternatives measures as, for example, the momentum or the product of the ram mass by the impact velocity. This value offers a better indication of the maximum force that the ram can generate in the pile. Hence, it also gives an estimation of the soil resistance that would be available when the pile is stroke.

Hammer mass has an important influence in the system efficiency. As the mass of the hammer increases, the larger is the driving efficiency. Thus, the difference between the maximum impact force and the pile top force gets smaller.

3.5.2.1. Drop Hammers

Drop hammers can be divided in cable suspended drop hammers and free released drop hammers.

Cable suspended drop hammers use a crane mounted winch to raise the ram. When the brake of the winch is released, the hammer drops. Then, the ram pulls the winch and accelerates it. While the ram is falling, some kinetic energy is lost. Besides that, before the impact, the crane is tempted to reapply the brake to prevent the spilling of the winch cable. This action also cushions the impact. Energy losses of 50% of the potential hammer energy are usually observed. Thus, the energy losses may occur due to:

- Inaccurate drop height;
- Friction;
- Winch inertia;
- Early catching of the ram;
- Misalignment.

Free released drop hammers are not often adopted as a solution for pile driving. They are mostly used for dynamic load testing. In this case, the hammer efficiency is larger than the one achieved with a cable suspended drop hammer. Hence, the efficiency can be around the 95%. The energy losses may be caused by:

- Guide friction;
- Misalignment.

3.5.2.2. Air/Steam Hammers

In air and steam hammers the ram is attached to a steam engine that pulls the ram up. Therefore, when the valves are switched, the ram goes up before it starts the downward movement. Shortly before the impact, the valves are switched again generating an upward force on the ram and a new cycle is started. When the valves are switched too early, it will cushion the impact and some energy will be lost (preadmission).

In order to generate hammer blows in quicker succession, the single acting air/steam hammers were developed originating double or differential air/steam hammers. In the second type the strokes are shorter and the downward movement of the ram is accelerated. Thus, hammer blows are generated in a quicker succession. While single acting hammers run at 50 to 60 blows per minute, double or differential hammers run at 100 blows per minute.

Single air/steam hammer efficiencies are in the range of 65% and the energy transfer of 55% on steel piles. On the other hand, double air/steam hammers present a hammer efficiency of around 50% and an energy transfer of about 35% on steel piles. The energy losses in both cases are mainly due to the following factors:

- Guide and piston/cylinder friction;
- Low stroke in easy driving;
- Less than rated stroke when pressure is low;
- Preadmission;
- Misalignment.

Figure 3.8. – Air/Steam hammer [7]

3.5.2.3. Diesel Hammers

Diesel hammers use diesel combustion under the ram to provide the upward movement to the ram. This type of hammers presents some advantages such as its light weight, solid construction and they do not need additional external power supply.

The hammer comprises a cylinder, a ram or a piston, an impact block that closes the bottom of the cylinder and a fuel pump that injects fuel into the cylinder before the impact. Diesel hammers show four stages during and after the hammer impact in the pile. Initially, the ram moves upwards and then falls only subjected to gravity. The second phase is named the compression phase when, on the downward movement, the ram closes the exhaust ports. Thus the air underneath the hammer is compressed and the temperature rises. Then, the impact occurs and fuel is injected. It is the impact and combustion phase. Finally, the expansion phase takes place. The ram moves upwards and this phase ends when the excess pressure dissipates through the exhaust ports and new air is sucked into the cylinder. The final part of this stage corresponds to the first phase. Therefore, the ram goes downward under the action of gravity and a new cycle starts.

In diesel hammers, the hammer efficiency typically averages 80%. The transferred energy is of about 30% on steel piles. Energy losses are usually due to:

- Pre-compression;
- Friction between ram and cylinder;
- Impact and inertia losses of the impact block;
- Low stroke;
- Pre-ignition;
- Misalignment.

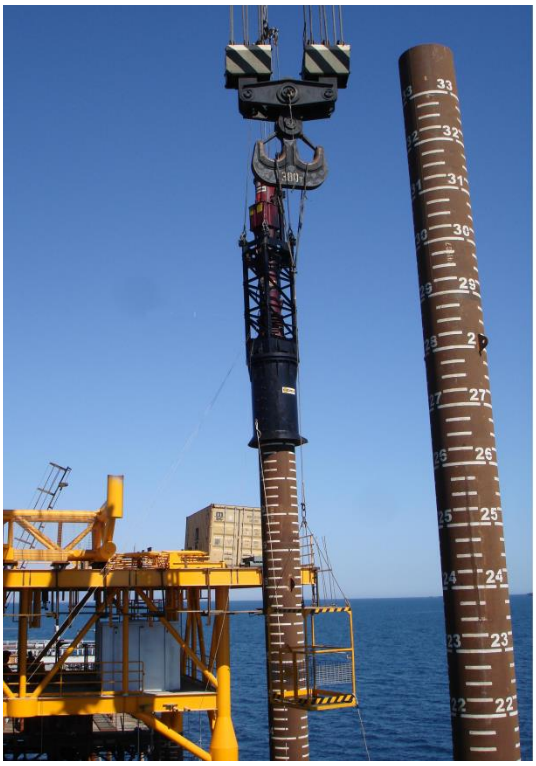

Figure 3.9. – Diesel hammer [9]

3.5.2.1. Hydraulic Hammers

The first hydraulic hammers were simple drop hammers. The hammers were fabricated to low drop heights. Thus, the energy losses were very small. New hydraulic hammers consist of a piston rod and a piston connected to the ram. Hydraulic power pushes the piston downwards. Electronic devices record the hammer speed and the hammer blow-counts.

The energy used to control pile driving is the kinetic energy of the ram prior to the impact. Therefore, in this type of hammers, hammer efficiency only covers losses occurring during the impact. Thus, the hammer efficiency is usually in the range of 95%. The losses observed are due to:

- Measurement errors of impact velocity;
- Misalignment.

3.5.3. Driving Systems

Driving systems comprise the hammer cushions, helmets and pile cushions.

Hammer cushions are usually made of a resilient material. The main objective of using such materials is to protect the ram from excessive fatigue stresses.

Pile cushions are only used in concrete piles. They were designed for two purposes. The first goal is to decrease the stress in the points of steel-concrete contact. On the other hand, they reduce the peak stress in the pile by distributing the impact force over the time.

Helmets serve to align the hammer with the pile and to accommodate the hammer cushion. They are also used to spread the impact force over the pile top.

3.5.4. Followers

In offshore conditions, when the pile installation is executed in larger water depths, if the hammer piles cannot reach the desirable depth it may be necessary to take advantage of the followers. Pile follower is an extension that contacts the top of the pile and is attached to the hammer. Followers present some disadvantages such as:

- Heavy weigh;
- Expensive;
- High energy losses in transmitting a blow to the top of the pile through a follower;
- Attached to the pile with joints, which can have failures and require repairing.

4

DESIGN OF PILE FOUNDATIONS

4.1. OVERVIEW

The design of a pile foundation must consider all aspects of the installation and performance of the system. The design process should take into account some factors as follows:

- Installation – pile driveability, hole stability, grouting;
- Axial capacity and performance under cyclic loading;
- Lateral capacity and performance under cyclic loading;
- Group effects – influence of a pile to an overall foundation stiffness,
- Other aspects – seismic response, scouring.

In the design stage it should be ensured that the piles can be reliably installed or constructed to the target penetration. Also, the resulting foundation needs to have sufficient stiffness and strength to resist the design loads. The foundation should be optimised in order to minimize the number and length of the piles.

Pile foundation differs in some aspects regarding shallow foundations. The analyses that link soil strength and foundation capacity are less rigorous and more empirical for piles. This is because the failure mechanism of a pile cannot be captured by analytical solutions. In addition, the soil properties and stress states that are considered in this analysis are often modified due to the installation process. Still, the analyses of strength and stiffness of piles, accounting for non-linear response and layering of the soil, often require numerical implementation.

In pile foundations the interaction between combined loads is less significant than in a shallow foundation. Thus, the application of a horizontal load to the pile has less influence in the axial pile capacity. Also, application of a vertical load has less influence in the horizontal capacity. This occurs because the upper fewer diameters of the pile resist to the horizontal loads. On the other hand, the vertical load is carried out by the lower part of the pile.

Still in the design phase of a project, it is of extreme importance to select adequately pile driving equipment such as the appropriate type of hammer and the hammer efficiency. These procedures comprise the so-called pile driveability analysis. These analyses are often performed taking advantage of one-dimensional models based on the one proposed by Smith (1960).

During pile installation, strain gauges and accelerometers are usually placed on the pile in order to monitor the pile installation process. The velocity and force to which the pile is submitted are then calculated from the strain gauges and accelerometers measurements. It is therefore possible to calculate the axial capacity of the pile and compare it with the predicted from the design methods.

In this chapter pile-soil mechanisms are first detailed. Then, the method proposed by Alm and Hamre to estimate the SRD is presented. Some pile axial capacity design methods are also exposed. In the present work only the American Petroleum Institute (API) and Imperial College Pile (ICP) design methods are studied. This chapter also covers wave equation formulation and pile driveability analysis. Finally, it is detailed the pile driving monitoring process during installation.

4.2. AXIAL CAPACITY

4.2.1. GENERAL CONCEPTS

The axial capacity of a pile, V_{ult}, is defined as the maximum vertical load that the pile can support. If the load goes on increasing, then failure is achieved. From the equilibrium, as formulated by Equation 4.1, the axial capacity is equal to the sum of the ultimate shaft friction, Q_{sf}, and the ultimate base resistance, Q_{bf}, minus the submerged weight of the pile, W'_p. The failure forces of close-ended piles are illustrated in Figure 4.1.

$$V_{ult} = Q_{sf} + Q_{bf} - W'_p \tag{4.1}$$

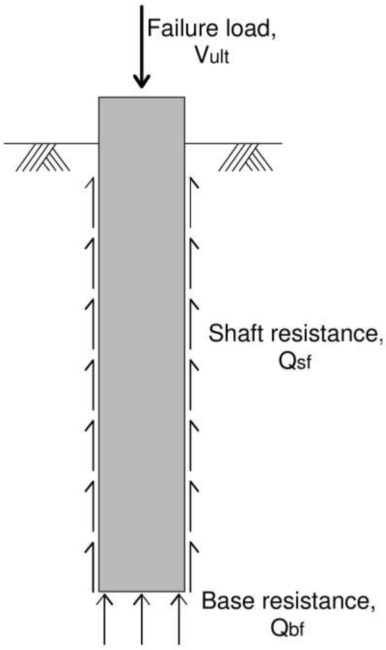

Figure 4.1. – Closed-ended pile failure mechanism

In open-ended piles, shaft friction is observed in both the inner and the outer surfaces. Thus, it is calculated as the sum of two components: the inner shaft capacity, $Q_{sf\text{-}i}$, and the outer shaft capacity, $Q_{sf\text{-}o}$ as indicated by Equation 4.2.

$$Q_{sf} = Q_{sf,i} + Q_{sf,o} \tag{4.2.}$$

The total ultimate shaft friction is obtained by the integration of the ultimate unit shaft friction, $\tau_{sf,}$ over the surface of the pile, as given by Equation 4.3, where D is the outer diameter of the pile.

$$Q_{sf} = \pi.D.\int_0^L \tau_{sf} dz \tag{4.3.}$$

The base resistance is the maximum resistance that can be mobilized on the pile base. In closed-ended piles, the ultimate base resistance is assessed by the ultimate unit base resistance, q_{bf}, multiplied by the base area as it is formulated in Equation 4.4.

In open-ended piles, the base resistance is the sum of two components, one acting on the pile annulus and the other one applied on the soil plug. The failure mechanism of tubular piles and the plug phenomenon will be discussed in Section 4.2.2.

$$Q_{bf} = \frac{\pi.D^2}{4}.q_{bf} \tag{4.4.}$$

An important aspect to notice is that the ultimate base resistance is often mobilized for high pile settlements. In that case, the structure would reach the failure before the pile. Thus, the failure base resistance is often defined as the mobilized base resistance for an allowable displacement so that the structure serviceability is not in risk.

In the presented formulations, the estimation of τ_{sf} and q_{bf} is a challenging task. The complex behaviour of the soil during pile installation and loading promotes changes in the stresses that are difficult to predict. Therefore, the assessment of τ_{sf} and q_{bf} parameters has to be based only on i*n situ* conditions before the pile installation. Thus, site investigation methods (e.g. CPT) are required to provide such information to the designers. It is not always possible to get useful data directly from the results of site investigation methods. In these cases, additional correlations, as the ones mentioned in Section 2.2.4, are necessary to conduct a correct pile design.

4.2.2. Plug and Unplug Soil Behaviour

In tubular piles, the soil within the pile can plug and different failure mechanisms from the ones occurring in closed-ended piles can be observed. Thus, during an open-ended pile installation the following failure mechanisms are possible to arise:

- Unplugged penetration ('coring') – the soil column within the pile remains stationary;
- Plug penetration – the soil column within the pile moves downwards with the pile;
- Partial plug – the soil column moves downwards but slower than the pile.

The degree of plugging is measured by the incremental filling ratio (IFR), formulated by Equation 4.5. The value δh_p defines the variation of the plug length during one penetration increment. The quantity δL indicates the variation of the pile embedded length that occurs during one penetration increment. Figure 4.2 provides a physical understanding of these parameters.

When IFR equals zero, the pile and the active plug length moves downwards the same range during a penetration increment. This situation corresponds to a plugged penetration. On the other hand, when IFR is equal to 1, the soil column within the pile remains stationary and an unplugged penetration occurs. For the remaining cases, when IFR is between zero and the unity, partial plug behaviour occurs.

$$IFR = \frac{\delta h_p}{\delta_L} \tag{4.5.}$$

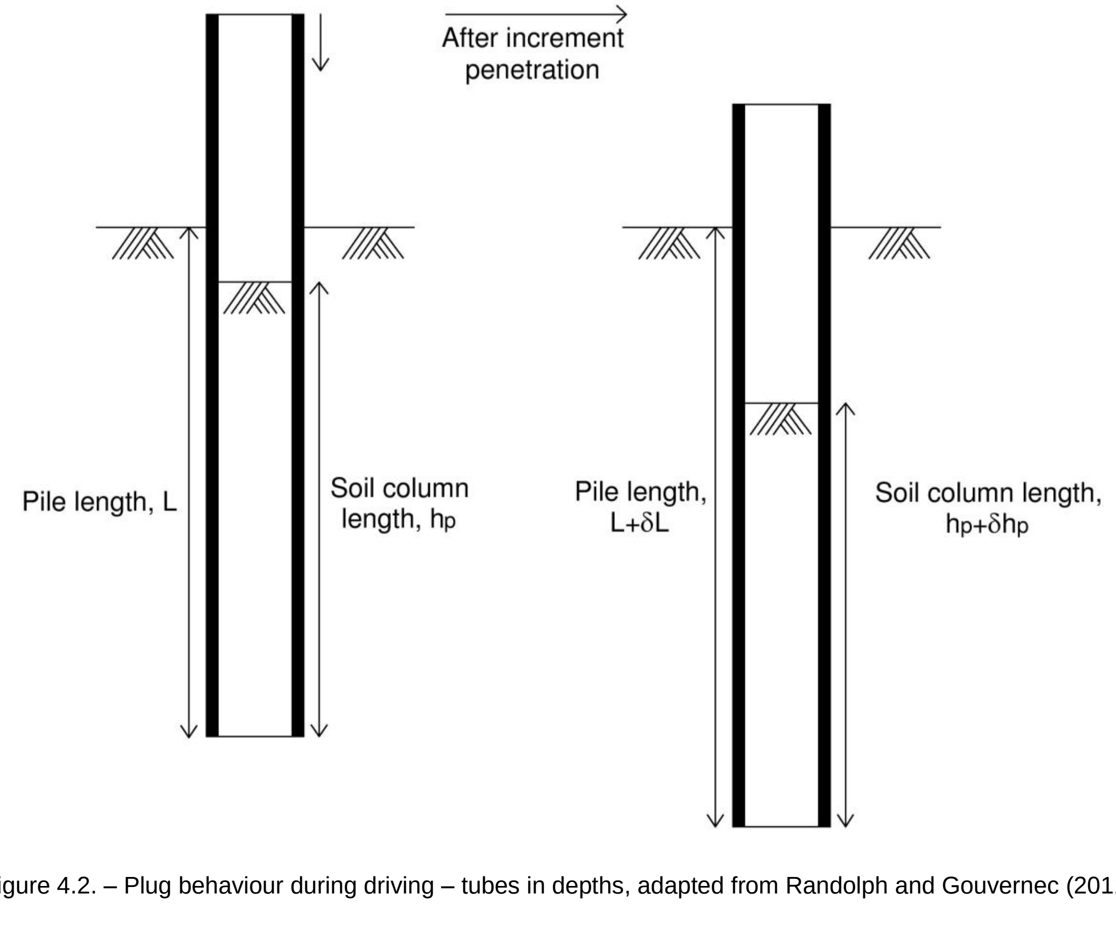

Figure 4.2. – Plug behaviour during driving – tubes in depths, adapted from Randolph and Gouvernec (2011)

Hence, the base resistance in open-ended piles depends on the degree of plug that occurs. In an unplugged penetration, the soil column within the pile does not offer resistance at the pile base. However, in a plug situation, the pile behaves like a closed-ended pile. Therefore, if a pile is fully plugged a reduced base resistance compared to the one calculated to a closed-ended pile can be adopted. Equation 4.6 and Equation 4.7 present the ultimate base resistance for an unplugged and for a plugged penetration, respectively. In these equations, $q_{bf,w}$ and $q_{bf,p}$ correspond to the unit base resistance offered by the pile annulus and by the soil plug respectively. Also, the parameter

D_i is the inside pile diameter. Figure 4.3 illustrates the failure mechanisms of an open-ended pile for an unplugged and a plugged penetration.

$$Q_{bf} = \frac{\pi.(D^2 - D_i^2)}{4} . q_{bf,t} \quad (4.6.)$$

$$Q_{bf} = \frac{\pi.(D^2 - D_i^2)}{4} . q_{bf,t} + \frac{\pi.D_i^2}{4} . q_{bf,p} \quad (4.7.)$$

When designing an open-ended pile, two calculations should be done, one assuming an unplugged failure and another considering a plugged failure. The pile will fail by the mechanism that offers less resistance. From the forces equilibrium, plug occurs when the condition present in Equation 4.8 is valid. Thus, if the shear stress along the length of the soil plug exceeds the mobilized base resistance, the pile penetrates in a plugged manner.

$$Q_{sf,i} > Q_{bf,p} - W_p \quad (4.8.)$$

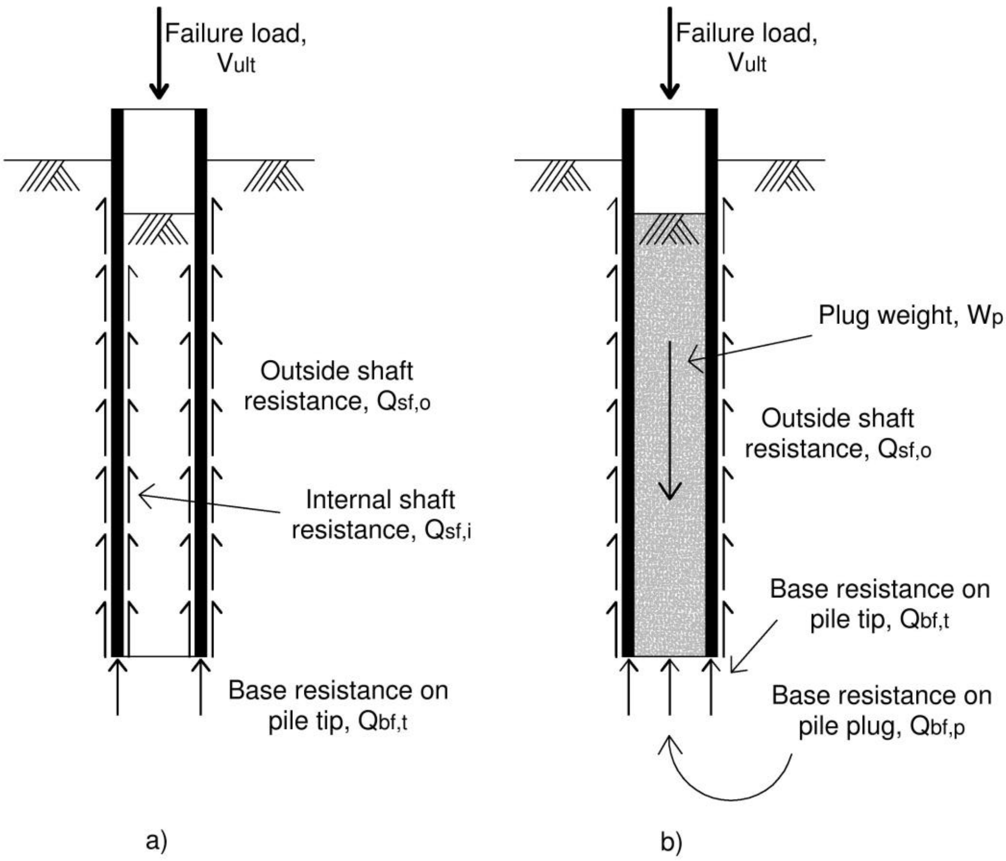

Figure 4.3. – Open-ended pile failure mechanism (a) unplugged behaviour (b) plugged behaviour, adapted from Randolph and Gouvernec (2011)

4.2.3. Capacity of Driven Piles In Sands

During pile installation and loading, many changes in stresses occur. Randolph and Gouvernec (2011) divide the pile installation and loading processes in four stages, as illustrate in Figure 4.4.

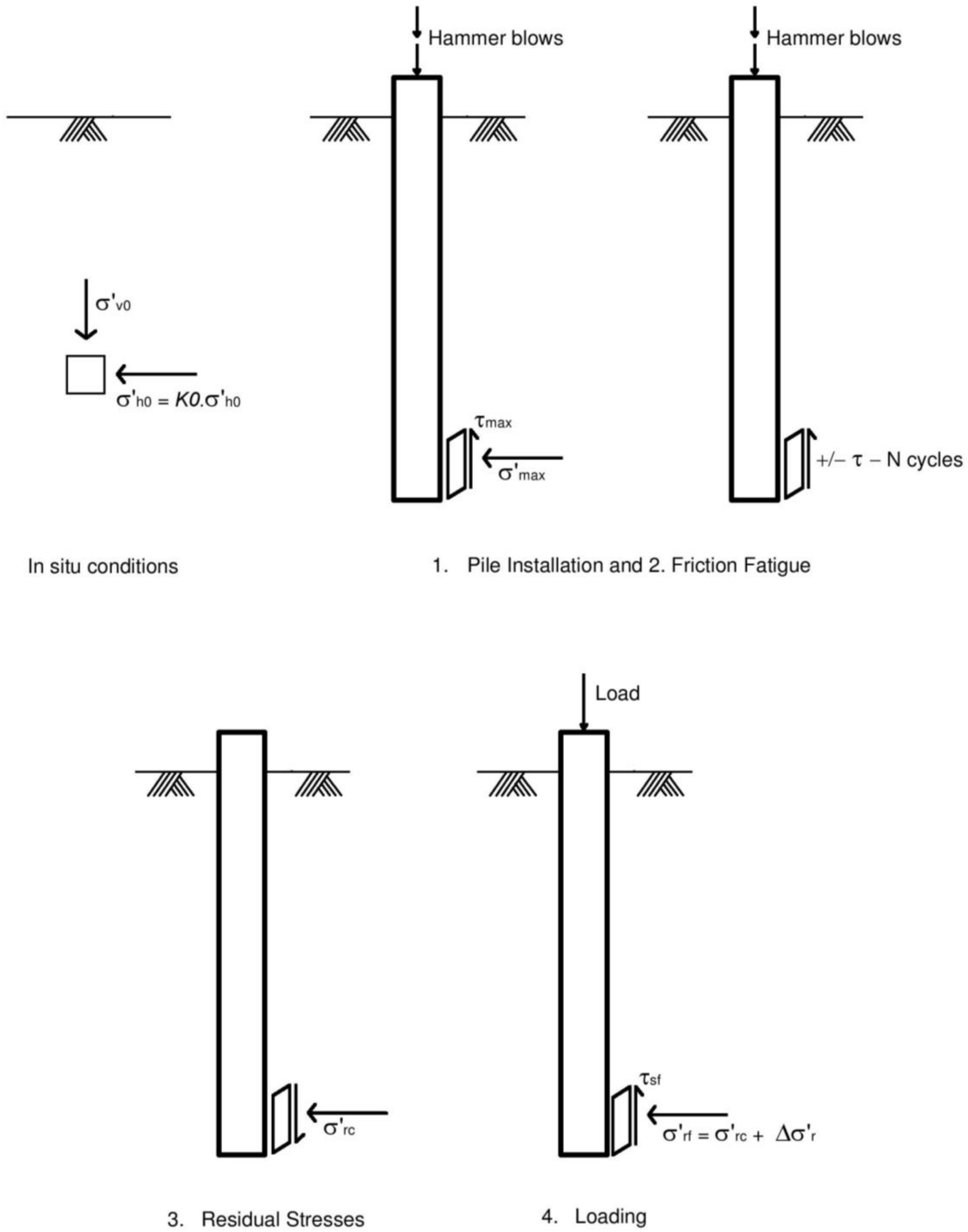

Figure 4.4. – Stress changes during pile installation and loading, adapted from Randolph and Gouvernec (2011)

4.2.3.1. Installation and Friction Fatigue

During pile installation, the stress level in a given element increases significantly due to the radial displacements implemented in the sand. Pile tip stresses are comparable with the measured cone resistance, q_c, from a CPT test.

When the sand passes the tip, it is displaced radially for the pile to penetrate. Thus, sand achieves the pile shaft and stresses decrease considerably since the vertical penetration load is no more acting on that element. At this stage, the stresses behind the pile tip can be comparable with the sleeve friction.

When dynamic installation methods are adopted, the field close to the pile is subjected to continuous cyclic shearing due to the consecutive hammer blows. Since sands permeability is high enough to allow volume changes, cyclic motion leads to contraction inside the pile. Therefore, it causes soil relaxation and a decrease of the normal stresses acting on the pile shaft. Thus, as the pile embedded depth increases, the horizontal stresses at a given element decreases. This process is usually named friction fatigue. Hence, friction fatigue leads to a reduction in the interface shear stress when increasing the distance behind the tip.

In open-ended piles, the degree of plugging affects the amount of soil that is displaced by the pile. Thus, it also influences the magnitude of the set-up effect in the surrounding soil. In one extreme, a closed-ended pile penetrates like a CPT, that is, it opens a cavity from nothing generating high radial soil displacements. Moreover, when a pile penetrates in an unplugged manner, smaller soil displacements are generated. A pile penetrating in a partially plugged manner lies between the two situations mentioned above.

Therefore, besides the IFR parameter, the degree of plugging can also be measured taking into account the volume of displaced soil. So, in the literature it is also suggested using the effective area ratio to quantify the degree of plugging.

4.2.3.2. Stresses changes when plugging occurs

Many researches were developed in order to investigate plug mechanisms. Henke and Grabe (2009) stated that the formation of soil plug depends on a number of factors, such as, the pile diameter, pile length, penetration depth, soil density and installation method.

Randolph *et al.* (1991) proposed the concept of the active length of the soil plug, *h’*. Figure 4.5 provides a better understanding of this concept. It is assumed that the soil inside the pile moves up regarding the pile during installation. Therefore, when plug occurs, it was concluded that not all the soil within the pile moves upwards regarding the pile movement.

The formation of soil plug is explained by the arching effect. The compaction of the soil inside the pile leads to an increase of the horizontal stresses and high internal shaft frictions. Thus, by Equation 4.8, soil plug is formed. As the pile diameter gets smaller, the horizontal stresses are higher and the arching effect plays a major role in the pile axial capacity. Thus, the end-bearing capacity of the soil plug increases with the ratio *h/D,* as concluded by Randolph (1988).

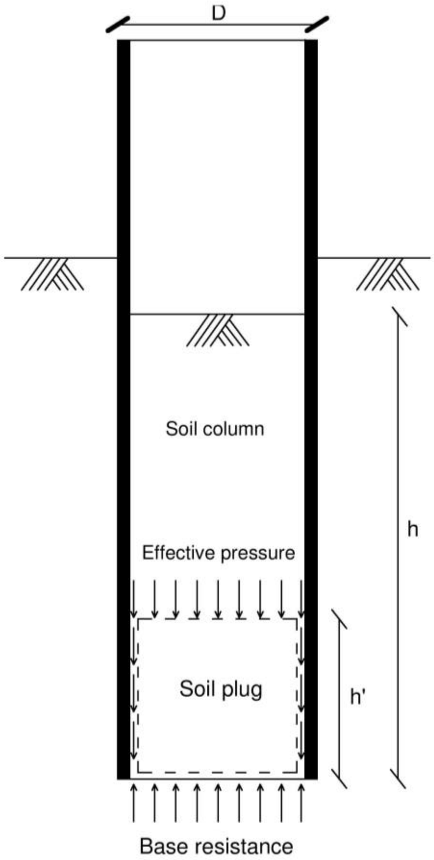

Figure 4.5. – Active plug length, adapted from Henke and Grabe (2008)

Kishida and Isemoto (1977) commented that arching occurs under static loading, which leads to high internal friction. So, the degree of arching effect is clearly influenced by the pile installation method.

Henke and Grabe (2008) and Henke and Grabe (2009) performed an analysis to assess the mechanisms of soil plugging inside open-ended piles in respect to the installation method. They concluded that jacked piles exhibit high horizontal stress peaks inside the pile, which is an indication of soil plug. Furthermore, the monotonic shearing gives rise to dilatancy so that minor compaction is observed inside the pile. As a consequence, soil plug is likely to occur when the pile is installed by static methods.

On the other hand, piles installed by dynamic installation methods of impact driving and vibratory driving, show high soil compaction inside the pile due to the continuous cyclic shearing, This process leads to a reduction in horizontal stresses. Hence, plug is unlikely to occur when the pile is installed by dynamic methods. As piles are usually installed by dynamic methods, plug in open-ended piles rarely occurs. Both plug mechanisms, for pile jacking and vibratory driving, are illustrated in Figure 4.6, where the parameter '*e*' corresponds to the void ratio.

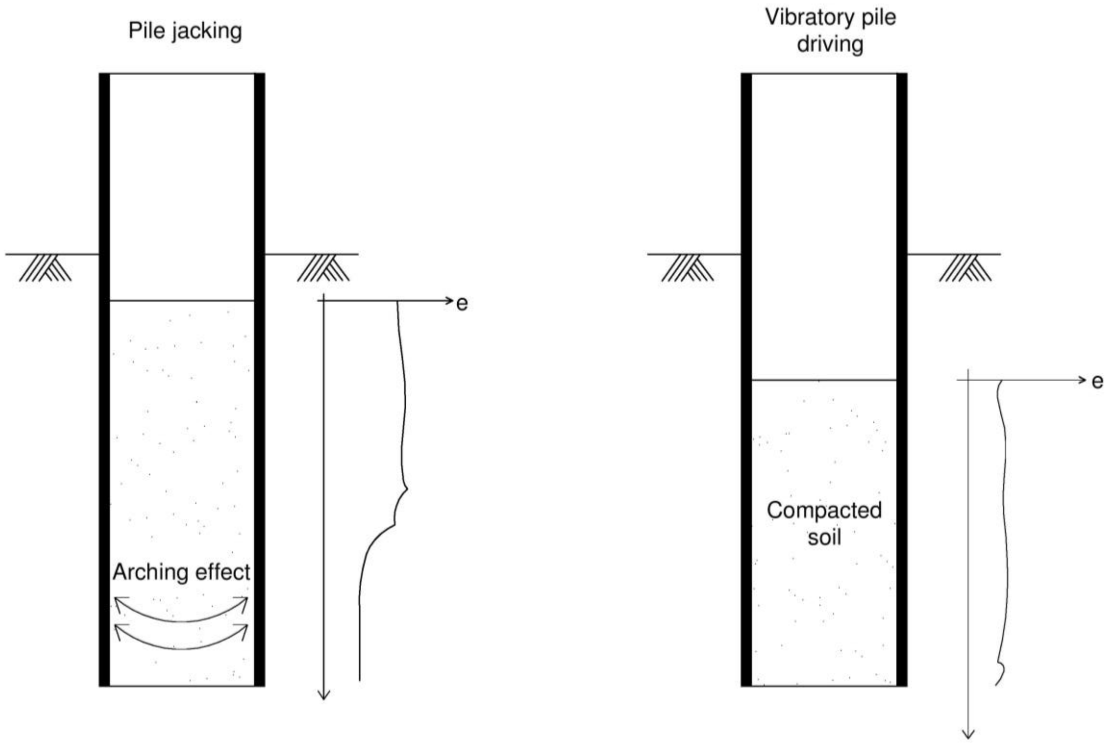

Figure 4.6. – Plug mechanisms inside an open-ended pile due to pile jacking and vibratory pile driving, adapted from Henke and Grabe (2008)

4.2.3.3. Residual stresses

Holloway *et al.* (1978), Mouta da Costa (1994), Wang and Zhang (2008), Briaud (2013) conducted some researches and reported conclusions regarding the residual stresses generated during pile driving.

Also, according to Fellenius *et al*. (2007) and Viana da Fonseca and Santos (2008), residual loads are present in almost all type of piles, being mostly significant in driven piles, but also substantial in cast-in-situ piles. As indicated in Viana da Fonseca and Santos. (2008), small to moderate locked-in load (presence of residual load) in the pile before the start of any load pile test (dynamic or static) have to be taken into account for the correct distribution of load transference along the shaft as to the base.

It is true that the actual amount and distribution of residual load cannot be easily determined, particularly in offshore conditions, because no assumption of locked-in toe resistance will enable the records to be fitted to a fully mobilized shaft resistance immediately above the pile toe. Therefore, the test piles will not be mobilizing full positive shaft resistance above the pile toe. Still a back-analysis by analytical approaches, as in Viana da Fonseca *et al*. (2007) or numerical fitting can be very beneficial in due course. A reasonable trial-and-error study of the data can indicate the presence of residual load made direct evaluation of the data may overestimate the shaft resistance and underestimate the toe resistance by the same amount.

4.2.3.4. Loading

During pile loading, it is observed a small increase in the horizontal stresses. This can be due to:

- *Poisson*'s ratio – compression load causes pile expansion against the surrounding soil;
- Soil dilation close to the pile-soil interface – this effect is more influenced by the particle size than by the pile diameter. So, it is not relevant for the sizes of pile used offshore.

4.3. DESIGN METHODS

4.3.1. ALM AND HAMRE

Alm and Hamre (1998) proposed an improved model to predict the SRD. An update to the previous model was published in 2002, Alm and Hamre (2002).

The total resistance to driving, R_T, is the sum of a static resistance term and a dynamic term (damping). By definition, the SRD corresponds to the static resistance term of the total resistance to driving. The SRD is mobilized as function of a pile displacement. The static resistance is the most important part of the resistance and it is assessed as the sum of the tip resistance and of the shaft friction as explained in Section 4.2.1.

$$R_T = SRD.(1 + v^n) \tag{4.9.}$$

Therefore, Alm and Hamre presented a model to predict the static resistance based on the friction fatigue concept. It is based in large open-ended piles installed in typical North Sea soils. The model suggested is directly correlated with CPT measures. Thus, it is not influenced by wrong interpretation of the measured data. It is also based in dynamic *in situ* pile tests in 16 different locations.

The model proposes a prediction method for clays and another approach for sands. Only the SRD model for sands will be presented in the present work. Hence, the model is supported in dense to very dense sands from the North Sea. The water depth at the different locations lies between 70 and 170 meters and the pile diameters range between 1.8 and 2.5 m. All the piles were driven with hydraulic underwater hammers. Depending on the hammer type, the hammer efficiency considered was of 0.85 or 0.95. All the predictions assume an unplugged pile failure mechanism.

For sands, the proposed formulation of unit side friction, f_{sf} along a pile during driving is presented in Equation 4.10. In this equation:

- f_{si} – initial pile friction (kN/m^2);
- k – shape factor for degradation, calculated by Equation 4.13(-);
- d – depth to actual layer (m);
- p – pile tip penetration (m).

$$f_{sf} = f_{si}.e^{\mathrm{k.(d-p)}} \tag{4.10.}$$

The initial friction is taken as formulated by Equation 4.11, where:

- K – lateral pressure coefficient (-);
- p'_0 – effective overburden pressure (kN/m^2);
- δ_{cv} – constant volume interface friction angle (degrees).

$$f_{si} = K . p'_0 . tan(\delta_{cv}) \tag{4.11.}$$

The lateral pressure coefficient, *K*, is based on the formula proposed by Jardine and Chow (1996), which was also used to the ICP design method. The lateral pressure coefficient equation is presented in Equation 4.12, where:

- q_c – total cone tip resistance from CPT (kN/m^2);
- p_a – reference pressure = 100 kN/m^2;

$$K \times p'_0 = 0.0132 \times q_c \times ({p'_0}/{p_a})^{0.13} \tag{4.12.}$$

$$k = \frac{({q_c}/{p'_0})^{0.5}}{80} \tag{4.13.}$$

With this formulation of the shape factor, a rapid shaft friction degradation will occur for dense sands. It is important to notice that the lateral pressure coefficient formula was established under the assumption that the friction only occurs on the outside of the pile wall. Thus, when calculating the shaft friction, the unit shaft friction is suggested to be assumed 50% of the above formulation and applied on both sides of the pile wall.

The unit pile tip resistance during driving, q_{TIP} is given by Equation 4.14.

$$q_{TIP} = 0.015 \times q_c \times ({q_c}/{p'_0})^{0.2} \tag{4.14.}$$

The ultimate shaft capacity and end-bearing capacity are then calculated by the integration of the unit side friction and the unit base resistance, as formulated by Equation 4.3 and Equation 4.6, respectively. Finally, the SRD is calculated by the sum of the shaft capacity and the end-bearing capacity.

4.3.2. American Petroleum Institute (API) Design Method

The API design method proposes a simplified model to estimate the axial capacity of a pile. It has been developed and applied in the offshore industry for many years. However, it does not provide any information about pile displacements, which are of extreme importance for serviceability assessment.

This model is based on the quasi-static and monotonic application of the axial loads. It does not take into account the mechanisms that occur in the pile-soil interface during pile driving. The API method is known to be a very conservative method.

The API unit shaft friction prediction is a β-approach. For open-ended piles it is given by Equation 4.15, where:

- β – dimensionless shaft friction factor for sand;
- p'_0 – effective overburden pressure (kN/m^2);
- $\tau_{s,lim}$ – limit unit shat friction (kN/m^2).

$$\tau_{sf} = \beta . p'_0(z) \leq \tau_{s,lim} \tag{4.15.}$$

The values of β and of $\tau_{s,lim}$ vary depending on the soil type and density according Table 4.1. For unplugged open-ended piles the values of β may be taken from Table 4.1. For closed-ended piles or tubular piles driven in a plugged manner the values of β can be assumed to be 25% larger than the values present in Table 4.1.

Regarding the bearing capacity, Equation 4.16 is proposed in order to predict the unit base resistance. In this expression:

- N_q– dimensionless bearing capacity factor;
- $p'_{0,TIP}$ – effective overburden pressure at tip level (kN/m^2);
- $q_{bf,lim}$ – limit unit base resistance (kN/m^2).

$$q_{bf} = N_q . p'_{0,TIP} \leq q_{bf,lim} \tag{4.16.}$$

The values of N_q and $q_{bf,lim}$ are given in Table 4.1 depending on the soil type and density.

Table 4.1. – Coefficients for API design method in sands, adapted from American Petroleum Institute (2010)

<table>
<tr><th>Relative density</th><th>Soil description</th><th>Shaft friction factor β (–)</th><th>Limiting shaft friction values (kPa)</th><th>End-bearing factor, N_q</th><th>Limiting unit end-bearing values (MPa)</th></tr>
<tr><td>Very loose</td><td>Sand</td><td rowspan="5">Not applicable</td><td rowspan="5">Not applicable</td><td rowspan="5">Not applicable</td><td rowspan="5">Not applicable</td></tr>
<tr><td>Loose</td><td>Sand</td></tr>
<tr><td>Loose</td><td>Sand-silt</td></tr>
<tr><td>Medium dense</td><td>Silt</td></tr>
<tr><td>Dense</td><td>Silt</td></tr>
<tr><td>Medium dense</td><td>Sand-silt</td><td>0.29</td><td>67</td><td>12</td><td>3</td></tr>
<tr><td>Medium dense</td><td>Sand</td><td>0.37</td><td>81</td><td>20</td><td>5</td></tr>
</table>

Dense	Sand-silt				
Dense	Sand	0.46	96	40	10
Very Dense	Sand-silt				
Very Dense	Sand	0.56	115	50	12

4.3.3. IMPERIAL COLLEGE PILE (ICP) DESIGN METHOD

4.3.3.1. General Considerations

Unlike the API method, the ICP design method is based on CPT data to estimate the axial capacity of a pile. Although the estimation of the end-bearing capacity using the cone resistance parameter (q_c) has a theoretical basis, some care is needed when implementing these procedures due to the different failure mechanisms between a cone penetration and an open-ended pile.

ICP predictions are based on static pile tests, on previously un-failed piles. It also takes into account the set-up effect of the soil. Therefore, all the estimations proposed aim at predicting the capacities that may be mobilized ten days after driving the pile.

4.3.3.2. Shaft Friction

Regarding the shaft friction, the ICP investigations showed that, at failure, the shear stress acting on the pile shaft follows the Mohr-Coulomb failure criterion, as formulated by Equation 4.17.

$$\tau_{sf} = \sigma'_{rf}.\tan\delta_f \qquad (4.17.)$$

In the above equation, σ'_{rf}, represents the radial effective stress acting on the shaft at failure and the parameter δ_f gives the pile-soil interface friction angle at failure. Hence, in sands δ_f is the ultimate value of the interface angle at constant value (δ_{cv}), which is developed when the soil at the interface has stopped to dilate or to contract.

The term σ'_{rf} can be formulated as the sum of two components, as expressed by Equation 4.18. One of them represents the radial effective stresses after installation, σ'_{rc}, which depends on the CPT resistance, the soil overburden pressure and the ratio h_{TIP}/R. The other component is explained based on the conclusions obtained in the ICP field investigations. ICP experiments showed that the radial effective stress experience changes, $\Delta\sigma'_r$, during loading to failure. The main component of these changes is due to the interface dilatation during pile loading. However, other changes as the variation of the ambient stress regime and any radial expansion due to elastic '*Poisson*' effects can also take place during the pile loading process.

$$\sigma'_{rf} = \sigma'_{rc} + \Delta\sigma'_r \qquad (4.18.)$$

The friction fatigue concept is also included in the ICP formulations. Thus, it is considered a decrease of the radial effective stresses, σ'_{rc}, at a given depth, as the pile embedded depth increases. Once, a critical depth of 10D has been exceeded, the shaft friction reaches a constant limit. The friction fatigue effect is considered by the h_{TIP}/R term, where h_{TIP} is the length between a pile element and the pile tip and R is the pile radius. In open-ended piles, the pile radius is calculated as the equivalent solid pile radius that has the same solid cross-sectional area as the tubular pile. It is recommended to assume a lower limit of 8 for the parameter h_{TIP}/R when computing the radial effective stresses. Therefore, σ'_{rc} can be estimated using Equation 4.19 and considering the CPT resistance, the soil overburden pressure and the h_{TIP}/R ratio. In this equation, p_a corresponds to the atmospheric pressure also mentioned in Section 4.3.1 when detailing the Alm and Hamre proposal.

$$\sigma'_{rc} = 0.029 \times q_c \times (\sigma'_{vo}/p_a)^{0.13} \times (h/R)^{-0.38} \tag{4.19.}$$

The interface friction angle, δ_{cv}, depends on the sand's grain size, shape and mineral type, and on the hardness and roughness of the pile's surface. Jardine *et al.* (1992) proposed a relation between the interface friction angle and the mean particle size of the sand under analysis, $d_{50.}$ However, this correlation is more often used when no more feasible information is available about the soil in study. In order to get a better estimation of the interface friction angle, it is recommended to perform ring shear tests. In Figure 4.7 it is shown the interface friction angle in sand trends proposed by Jardine *et al.* (1992).

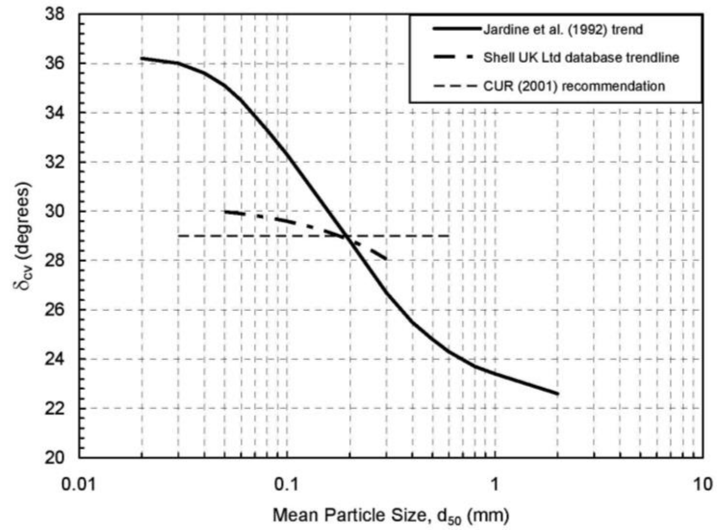

Figure 4.7. – Interface friction angle in sand – illustrative trends from direct shear interface tests, adapted from Jardine *et al.* (2005)

Equation 4.17 is valid when a compression load is applied on the pile. However, when a tension load is applied, the shear stress promotes a reduction on the compressive stress regime and the principal stresses axis rotation leads to a decline in the normal effective stresses. Besides that, some radial contraction of the pile due to the *Poisson* effect should also be taken into consideration. Thus, it promotes soil relaxation and a lower shaft friction comparing with the situation when a pile is compressed. Consequently, Equation 4.20 and Equation 4.21 should be used when treating tension problems in closed-ended piles and tubular piles, respectively.

$$\tau_{sf} = (0.8 \times \sigma'_{rc} + \Delta\sigma'_{r}) \times tan\, \delta_{cv} \qquad (4.20.)$$

$$\tau_{sf} = 0.9 \times (0.8 \times \sigma'_{rc} + \Delta\sigma'_{r}) \times tan\, \delta_{cv} \qquad (4.21.)$$

It is also important to notice that the ICP experiments showed that for a given set of conditions, the shaft resistance increases when other displacement piles are installed close to the tested pile. The tests also revealed an increase of the shaft friction when the piles were allowed to age *in situ*.

As explained in Section 4.2.1, open-ended piles can develop both internal and an external shaft friction components. The ICP method considers that the inner component is concentrated near to the pile end. Therefore, this component is included in the overall base and external shaft components. The base and the outer shaft resistance are calculated in a similar way to those applied in a closed-ended pile.

4.3.3.3. Base Resistance

Regarding the pile base resistance, further details will be provided to the tubular pile investigations. The ICP design method field experimentations confirm that arching is less effective for large pile diameters. Arching effect is directly linked with the soil density. ICP presents two criteria which provide the minimum relative density to achieve a full arch in a pile of a given diameter. These criteria are formalized in Equation 4.22 and Equation 4.21, where:

- D_i – internal diameter of the pile (m);
- D_R – relative density (%);
- D_{CPT} – diameter of a CPT probe (0.036 m)

$$D_i < 0.02 \times (D_R - 30) \qquad (4.22.)$$

$$D_i/D_{CPT} < 0.083 \times q_c/p_a \qquad (4.23.)$$

As mentioned in Section 4.2.2, if a pile is fully plugged, a reduced base resistance regarding the one of a similar closed-ended pile can be adopted. ICP gives two explanations for this approximation:

- Some local settlement is required to establish the arch;
- The soil beneath the soil column has not experienced the same degree of pre-stressing and pre-stiffness during driving.

Therefore, Jardine and Chow proposed that a fully plugged pile develops 50% of the base resistance of a close-ended pile with an equal diameter for a pile settlement of D/10. Then, the unit base resistance, q_{bf}, of a fully plugged pile can be calculated using Equation 4.24. For a closed-ended pile, the unit base resistance would be two times the one given by Equation 4.24.

$$q_{bf} = q_c[0.5 - 0.25 \times log(D/D_{CPT})] \tag{4.24.}$$

ICP also suggests two lower limits for the base resistance due to safety reasons:

- the fully plugged capacity should be no less than the unplugged capacity;
- q_b should be larger than $0.15 \times q_c$.

When a pile is coring (unplugged behaviour), the unit base resistance is assumed to be equal to the unit cone resistance. In this case, only the annulus area contributes to the base resistance as it was formulated in Section 4.2.2.

4.3.4. Design Methods Comparison

Firstly, it is important to mention that the method proposed by Alm and Hamre (2002) offers an estimation of the Static Resistance during Driving (SRD). The other presented methods, API and ICP, provide estimation techniques for the assessment of the static axial capacity considering ageing effects. In this section, other design methods such as, Norwegian Geotechnical Institute (NGI) method, University of Western Australia (UWA) design method and Fugro method are also commented. These last five mentioned methods already include possible set-up and soil relaxation effects. Due to these ageing effects, the pile capacity calculated by static axial capacity approaches will be much larger than the SRD at the end of driving calculated by the method proposed by Alm and Hamre.

Hence, the mentioned methods have different goals during the design stage. On one hand, Alm and Hamre proposal is useful to perform pile driveability analysis. The axial capacity newer methods provide important information regarding the long-term foundation capacity. So, it is clearly that these methods cannot be directly compared.

Regarding the API design method, it is very straightforward to apply. However, it does not capture the governing mechanisms. The API method was also calibrated against an older database. Thus, although it may give reliable estimations if older data is used, it reveals to be unreliable when compared with newer databases. The newer databases include larger diameter piles, usually used in offshore environment.

All the other CPT based methods adopt similar formulations for shaft and base resistance, with some differences in the mechanisms taken into account. Several database studies have been conducted in order to assess the reliability of the axial pile capacity design methods. Database investigations are also of extreme importance for the appropriate calibration of the design methods. The listed methods give similar performance when compared with field test measurements. However, these studies should not be used to assess the reliability of the methods in offshore piles design. Offshore piles are usually larger than the piles comprised in the existing databases and, therefore, they are subjected to higher loads. Therefore, the use of the newer methods may involve extrapolation from the existing databases. This type of analysis may provide inadequate and unreliable results.

Overy (2007*)* documented the use of the ICP design method to obtain axial capacity of driven steel pipe piles for nine platforms in the UK North Sea. The author compares API and ICP capacities. It was concluded that the ICP design method is based on improved soil models that give better predictability of pile load test results in comparison with existing methods. It was also established that in certain situations, the application of the ICP method originates smaller and more cost effective foundations compared to the ones designed based on API.

Overy and Sauyer (2007) also concluded that the ICP pile design method provides a reliable prediction of the capacity of piles installed in both dense and loose sand. The equivalent API methods were in general conservative for the skirt piles in dense sands and were not conservative for the leg piles in loose sand.

Schneider *et al.* (2008) examined the predictive performance of a range of pile design methods (API, ICP, UWA, NGI, Fugro method) against a compiled database of static load tests on driven piles in siliceous sands with adjacent CPT profiles. It was concluded that:

- the API method performs poorly when compared with static load test results;
- the detailed method formulation of UWA, based on recent research into the controlling mechanisms that influence pile capacity in sands, appears to offer better predictive performance than ICP, NGI and Fugro methods;
- none of the studied methods is prepared to deal with the complex time-dependent behaviour of driven piles in sands.

Still about this topic, Lacasse *et al.* (2013) studied the model uncertainty for the API method and the NGI, ICP, Fugro and UWA methods to predict the axial pile capacity in clays and sands. This paper presents comparisons of calculated and measured axial pile capacities in three locations, two from the Europides pile load test (located in the North Sea) and one located in the Tokyo Bay. The piles load test data for the Tokyo Bay test have a pile diameter of 2 m and were driven mainly in dense sand. The Europides tests were performed using 0.76 m diameter piles, driven in dense to very dense sand. The Tokyo Bay test is of particular interest in the present work because it was conducted on a pile in dense sand with a diameter similar to the piles used in offshore environment.

Figure 4.8 presents the measured and calculated axial pile capacity in compression vs depth for the Tokyo Bay pile load test. The cone resistance profile and the value selected for calculation are also shown. Figure 4.9 and Figure 4.10 display similar back calculations for the Europides Location 1 and Europides Location 2. A tension test was also run for these last locations.
According to these studies, it was concluded that the API and the newer design methods (NGI, ICP, Fugro and UWA) need validation against large scale test results. The newer methods are as or even more reliable than the current API method. During the work under analysis, it was clear that all methods offer some degree of uncertainty. The assessment of the uncertainty level can be function of the experience and knowledge of the design engineer. Lacasse *et al.* (2013) proposed to first identify the range of application of each design method and the limitations each one may have for different types of soil, loading conditions and dimensions of the pile.

Finally, it is also important to state that the newer CPT-based methods consider a shaft capacity of a tension test between 0.7 and 0.77 regarding the shaft capacity of a compression test. Cathie Associates checked internally these values for the main design methods. If the formulations of each method were examined, it is easy to obtain the same conclusions. For example, ICP considers a tension shaft capacity (Equation 4.19) equal to 0.8 x 0.9 = 0.72 times the value of the compression test.

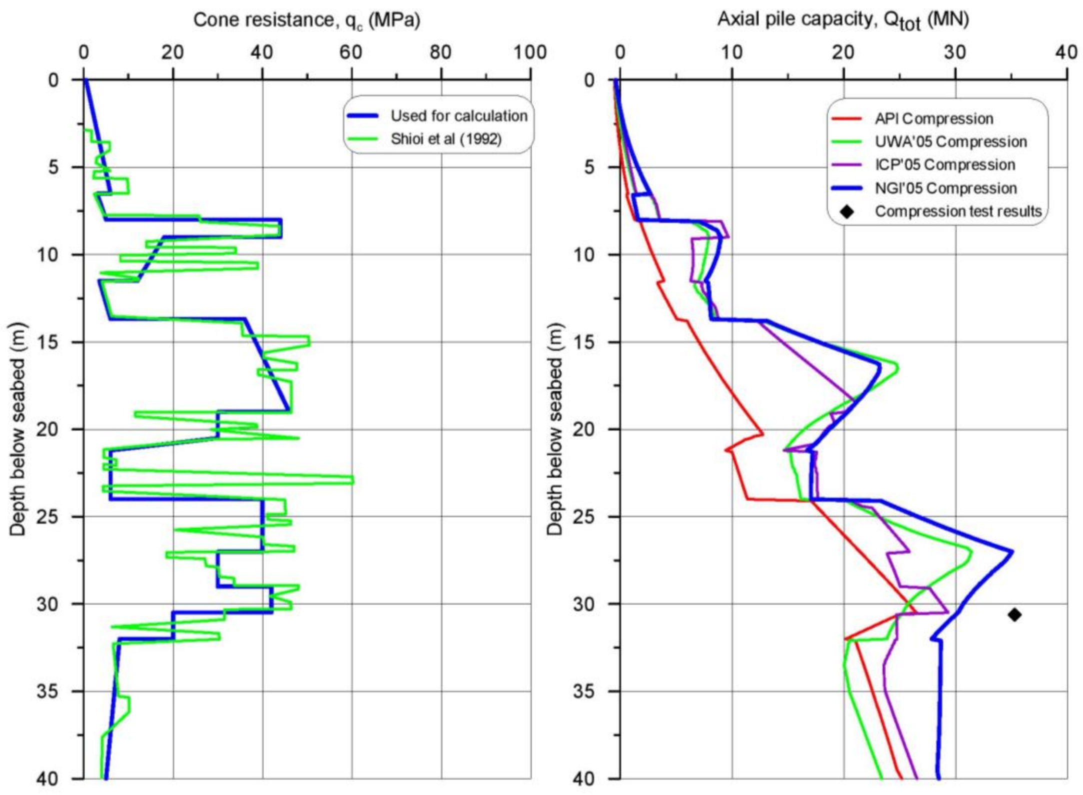

Figure 4.8. – Predicted and measured capacities in compression for Tokyo Bay pile load tests, Lacasse *et al.* (2013)

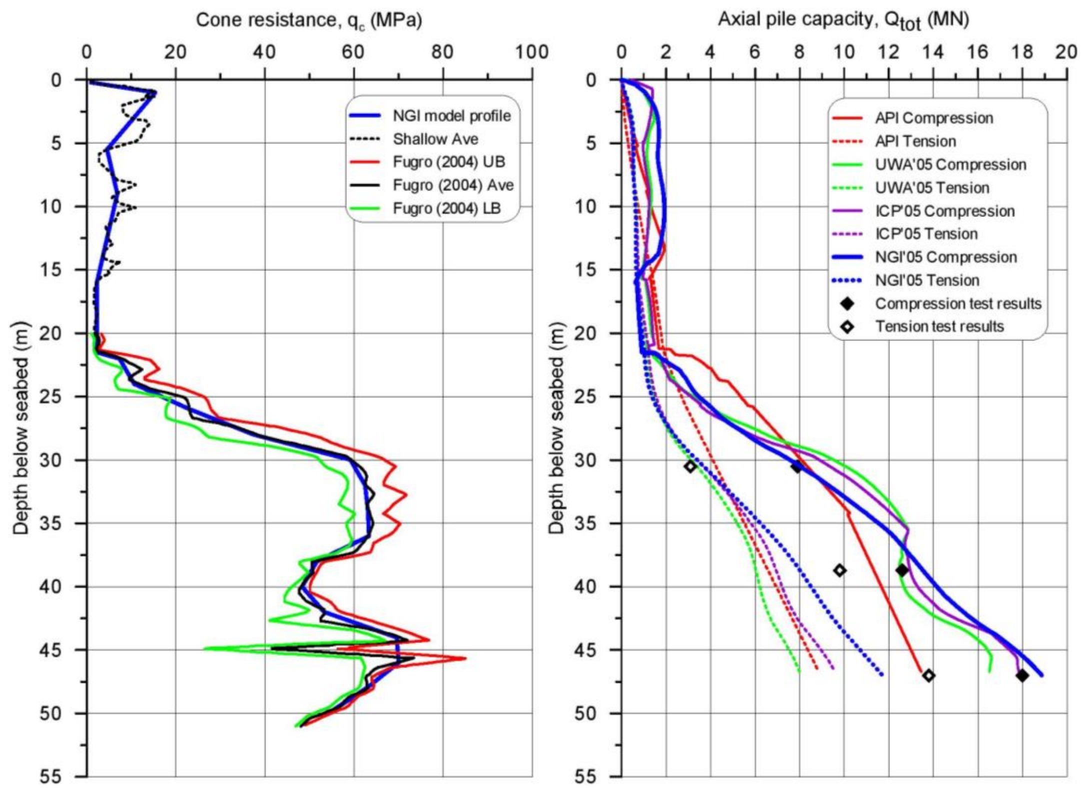

Figure 4.9. – Predicted and measured capacities in tension and compression for the Europides pile load tests, Location 1, Lacasse *et al.* (2013)

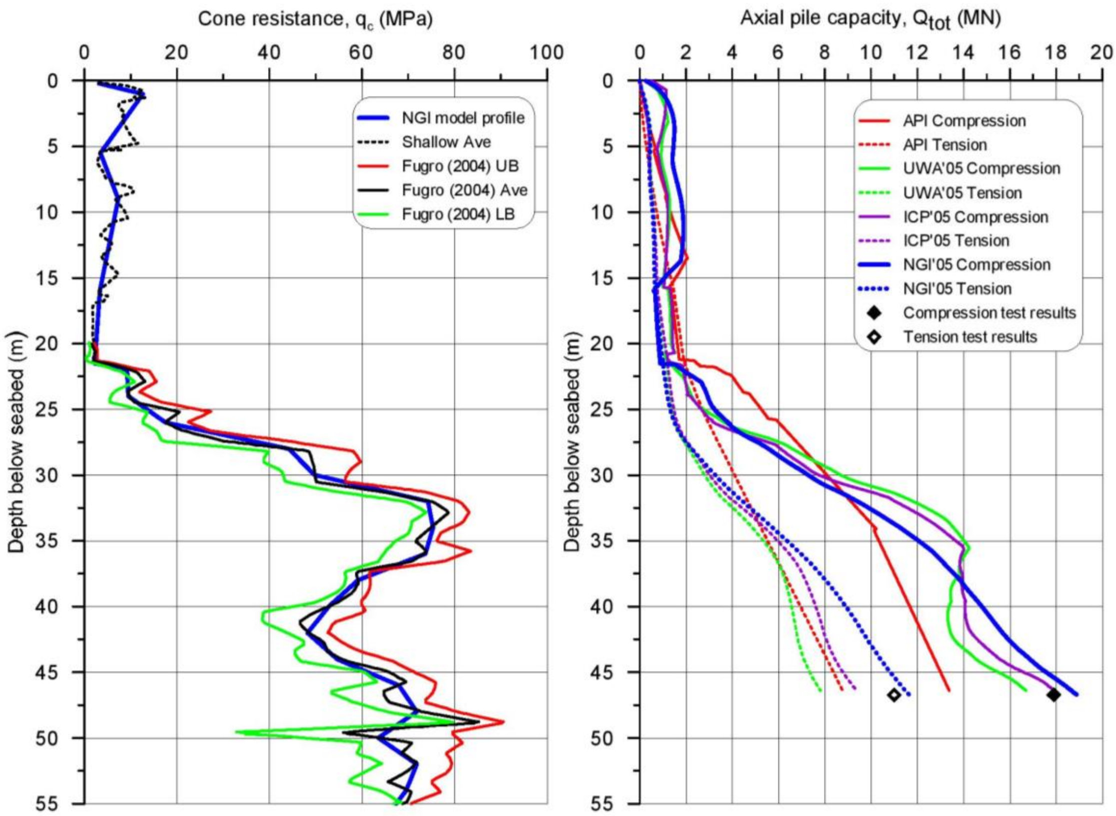

Figure 4.10. – Predicted and measured capacities in tension and compression for the Europides pile load tests, Location 2, Lacasse *et al.* (2013)

4.4. Wave Equation Analysis

4.4.1. General description

Pile driveability is an important topic of study and research since the 1800's. The models used at that time were based on empirical formulations. They were also limited to a short range of pile and soil types. Issacs (1931) was the first researcher to notice the presence of axial compressive waves during pile driving processes. This was confirmed by several experiences conducted by Fox (1932).

The development of computational capacity enabled the development of new ways to study wave propagation. Therefore, along the years several investigations aimed at formulating a simple but reliable model in order to analyse pile response during driving. The first numerical method to analyse pile driveability was proposed by Smith (1960). Nowadays, computer software packages (e.g. GRL WEAP®) are of extreme importance to optimize the selection of driving equipment, to predict driveability and to determine the pile static capacity.

In the one-dimensional model suggested by Smith, the hammer and the pile are replaced by a series of discrete masses and springs. These elements are used to emulate the stiffness of the pile. The resistance of the soil at the pile toe is modelled by a point force at the last pile node. Besides that, the resistance of the soil along the pile shaft is represented by a set of point resistances at each pile node. The magnitude of the resistances is a function of the elastic displacement or quake, Q, and of a damping constant, J. This model is illustrated in Figure 4.11.

The time period during which the wave travels along the pile should also be divided into smaller intervals. In order to capture what occurs in each pile section, as the length of the individual pile sections gets smaller, the shorter should be the mentioned time step.

The velocity of the hammer produces a displacement in the discrete masses. Then, the displacement of two adjacent sections leads to a compression or to an extension in the spring between them. The force generated by the two springs produces a force on the weight which has some effect in the wave velocity. The new force and velocity will be the input for the next time step. This procedure is repeated until the velocity equals zero.

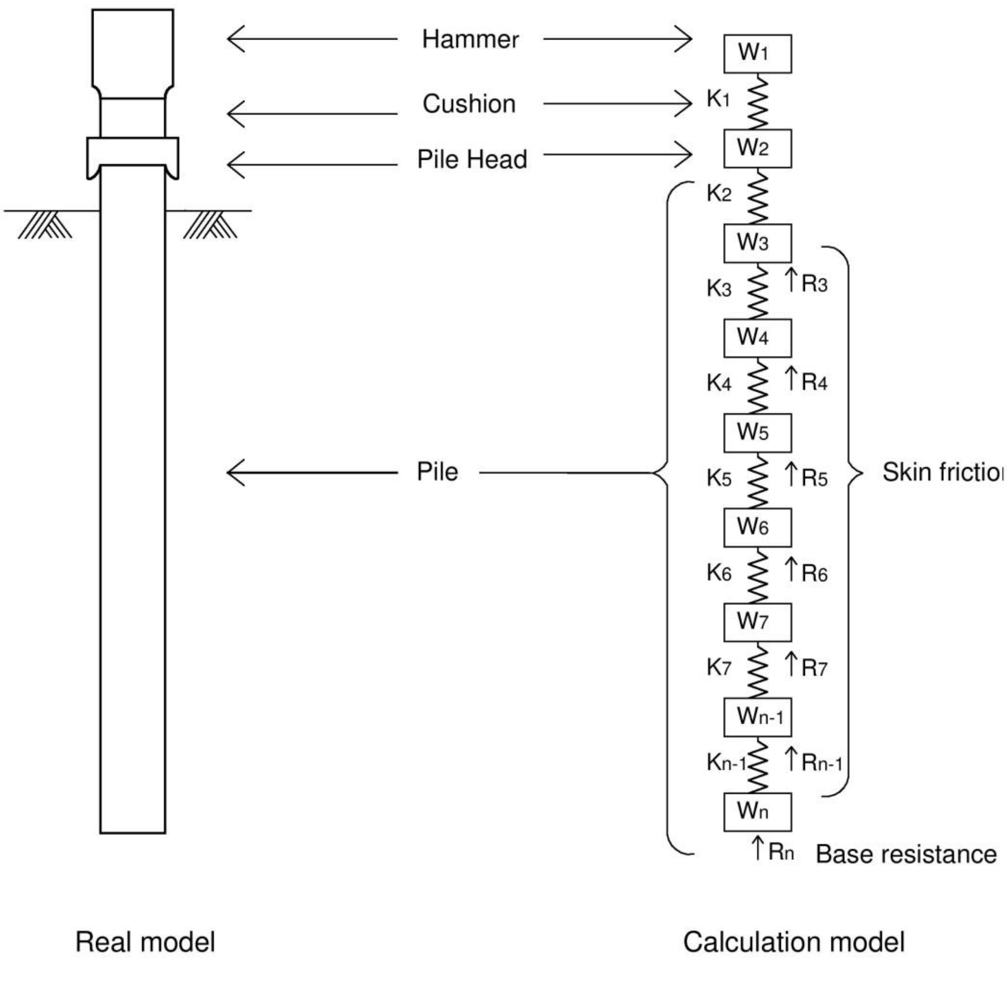

Figure 4.11. – Smith's model, adapted from Smith's (1960)

Although the model proposed by Smith in 1960 has been well accepted for many years, it presents a number of limitations. In pile driveability analysis, the modelling of the soil behaviour is one of the most important issues in order to get accurate SRD predictions. Hence, the reliability of the Smith's model is function of the values used for the soil parameters. The soil parameters used in the Smith's model and in models based on that one cannot be associated with soil properties and they also cannot be measured using common geotechnical investigation methods. Therefore, many researches were carried out in order to get accurate quake and damping values to represent the soil response.

Besides that, in a mass-spring model the boundary conditions are different from the ones that occur in a real system. Also the radiation damping effect cannot be easily considered in a one-dimensional model. Radiation damping is related with the spread of the energy submitted on the pile by the surrounding soil. Investigations were executed by Meynard and Corte (1984) and Simons and Randolph (1985) in order to consider adequate radiation damping in the 1D model proposed by Smith.

Still, one-dimensional modelling ignores dynamic interaction effects between the soil plug base and the soil below the tip level, as shown by Liyanapathirana *et al.* (2001). However, in reality both end-bearing and shaft friction are strongly coupled. In static conditions, inside friction causes plugging and outside friction increases near the tip. These effects are mainly due to end-bearing pressure. In a one-dimensional model the inside friction, the outside friction and the end-bearing pressures remain uncoupled.

4.4.2. Wave Equation Formulation

Let us admit that the parameter $m(z,t)$ is the depth of a point at a time t with a depth z at t=0. Figure 4.12 provides a better understanding of the physical interpretation of the mentioned parameters.

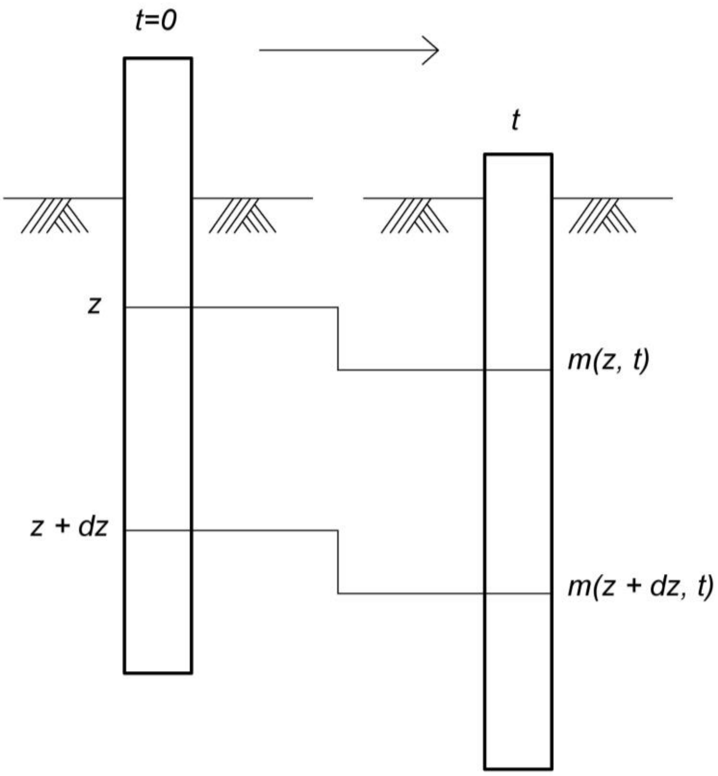

Figure 4.12. – Physical interpretation of the parameters *z* and *m*

It is therefore possible to formulate the axial strains, the velocity and the acceleration that occurs in a given section of the pile by Equation 4.25, Equation 4.26 and Equation 4.27, respectively.

$$\varepsilon(z,t) = \frac{m(z+dz,t)-m(z,t)}{dz} = \frac{dm(z,t)}{dz} \tag{4.25.}$$

$$v(z,t) = \frac{m(z+dz,t)-m(z,t)}{dt} = \frac{dm(z,t)}{dt} \tag{4.26.}$$

$$a(z,t) = \frac{dv(z,t)}{dt} = \frac{d^2v(z,t)}{dt^2} \tag{4.27.}$$

Taking into account the Hooke's Law, the axial stresses, σ(z,t), to which the pile is submitted are obtained by Equation 4.28. In this equation *E* is the Young's Modulus. The force applied on the pile is formulated as the axial stresses multiplied by the pile cross section area, A, as given by Equation 4.29.

$$\sigma(z,t) = E \times \varepsilon(z,t) \tag{4.28.}$$

$$F = A \times \sigma = E \times A \times \varepsilon = E \times A \times \frac{dm(z,t)}{dz} \tag{4.29.}$$

Figure 4.13 provides a representation of the external forces applied to a pile section at instant *t*. In this figure, R_f is the side friction per unit length applied on that section in that instant. The equilibrium of that pile segment at instant *t* is expressed by Equation 4.30.

$$\sum_{m(z+dz,t)}^{m(z,t)} Forces = F[m(z,t)] - F[m(z+dz,t)] - Rf \times dz = \frac{\partial F[m(z,t)]}{\partial z} \times dz - Rf \times dz \tag{4.30.}$$

Considering the 2nd Newton's Law (*F=m.a*) Equation 4.30 can be also be formulated as shown in Equation 4.31. Here, ρ is the pile density.

$$\frac{\partial F[m(z,t)]}{\partial z} \times dz - Rf \times dz = \rho \times A \times dz \times \frac{d^2m(z,t)}{dt^2} \tag{4.31.}$$

Replacing the force, *F*, by Equation 4.29, the equilibrium is given by Equation 4.32.

$$E \times A \times \frac{\partial^2[m(z,t)]}{\partial z^2} \times dz - Rf \times dz = \rho \times A \times dz \times \frac{d^2m(z,t)}{dt^2} \tag{4.32.}$$

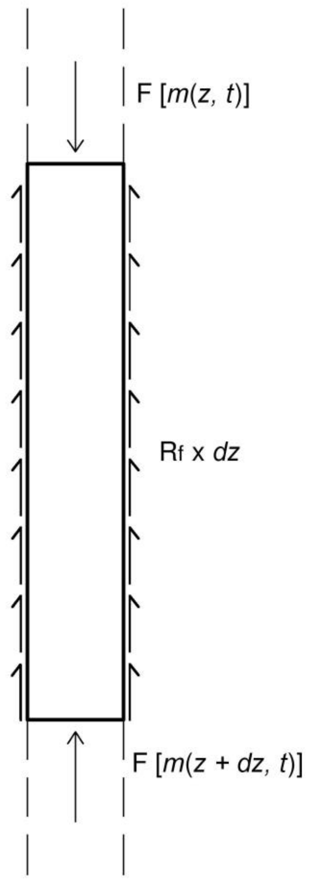

Figure 4.13. – External forces applied to a pile section at an instant *t*

Thus, it is finally obtained a differential equation formulated as Equation 4.33.

$$\frac{E}{\rho} \times \frac{\partial^2[m(z,t)]}{\partial z^2} - \frac{\partial[m(z,t)]}{\partial t} = \frac{R_f}{\rho \times A} \tag{4.33.}$$

The theory of linear differential equations establishes that all the solutions of a linear differential equation can be obtained as the sum of two components, a particular and a complementary solution.

The complementary solution is obtained by the solution of the homogenous equation associated to Equation 4.33. The complementary solution is therefore obtained solving Equation 4.33 without the second member. This corresponds to a situation with no skin friction, as formulated by Equation 4.34.

$$\frac{E}{\rho} \times \frac{\partial^2[m(z,t)]}{\partial z^2} - \frac{\partial[m(z,t)]}{\partial t} = 0 \tag{4.34.}$$

Therefore, the solution of the differential equation is given by the sum of two components as expressed in Equation 4.35, where f_1 and f_2 are continuous functions. A function of the type f(z,t) = f(z-ct) is called a wave equation. Here, the parameter c corresponds to the wave velocity on the pile and it can be calculated by Equation 4.36.

$$m(z,t) = f_1(z - ct) + f_2(z + ct) \tag{4.35.}$$

$$c = \sqrt{\frac{E}{\rho}} \tag{4.36.}$$

Thus, a point velocity and the force can be formulated as shown in Equation 4.37 and Equation 4.38, respectively.

$$V = \left(\frac{\partial m}{\partial t}\right) = -c \times f_1'(z - c \times t) + c \times f_2'(z + c \times t) \tag{4.37.}$$

$$F = E \times A \times \frac{dm(z,t)}{dz} = E \times A \times (f_1'(z - c \times t) + f_2'(z + c \times t) \tag{4.38.}$$

Equation 4.37 and Equation 4.38 can also be expressed as shown by Equation 4.39 and Equation 4.40, respectively.

$$\frac{V}{c} = f_1' + f_2' \tag{4.39.}$$

$$\frac{F}{EA} = f_2' - f_1' \tag{4.40.}$$

It is therefore possible to get a formulation for the wave-down, $F_{\downarrow}$, and for the wave-up, $F_{\uparrow}$. The wave-down represents the signal that the hammer is sending to the pile, thus eliminating the influence of the reflected wave. The wave-up displays the reflected wave which denotes the soil resistance to the impact. The wave-down and the wave-up can be obtained by Equation 4.41 and Equation 4.42, respectively. In these equations, Z represents the pile impedance. The parameter Z can be calculated by Equation 4.43.

$$F_{\downarrow} = EA.f_2' = \frac{1}{2}(F + ZV) \tag{4.41.}$$

$$F_{\uparrow} = EA.f_1' = (F - ZV) \tag{4.42.}$$

$$Z = EA/c \tag{4.43.}$$

4.4.3. Fundamentals of Wave Propagation

4.4.3.1. Force-Velocity Proportionality

For pile driving problems it is usually used the relationship between force and the velocity as formulated by Equation 4.44. The link between these two parameters is provided by the impedance of the pile. This relationship can only be applied when a single wave is considered. Hence, if there are wave reflections due to the soil resistance, the force and the velocity are not proportional and Equation 4.44 is not valid.

$$F = Z \times V \tag{4.44.}$$

4.4.3.2. Simple Wave Propagation

Let us now admit that a force or particle velocity is applied instantaneously at some point of the pile. It is therefore induced a wave on the pile. For simplicity, it is neglected the soil resistance and, therefore the wave propagates unchanged along the rod.

The most critical behaviour of the pile is associated to the wave reflections from the pile end. If a compression wave is induced on the pile, a tension wave will be reflected from the free end with the same velocity. The sum of the compression and tension waves will generate a zero force at the pile end. The velocity at the pile end will be the sum of the downward and the upward velocity. So the velocity doubles at the pile free end.

On the other hand, considering a fixed pile end, a compression wave will reflect up the pile as a compression wave and this wave is reflected with a velocity with the reverse signal. Thus, the force at the fixed end will double during the reflection and the velocity will be zero.

4.4.3.3. Energy Calculation

It is of extreme importance to calculate the energy transmitted to the pile. This is especially useful in order to select adequate driving equipment and to predict driveability analysis. The energy transferred to the pile along time can be determined by Equation 4.45. The maximum energy transferred is called Enthru energy.

$$E'(t) = \int F(t).v(t).dt \tag{4.45.}$$

4.4.4. GRLWEAP®

GRLWEAP® software package (herein termed GRLWEAP) developed by Goble *et al.* (1999) is one of the mostly used programs to optimize driving equipment selection, to predict pile driveability and to determine the pile static capacity. Taking advantage of this software it is possible to simulate pile installation by impact driving. This process has become an important step of the pile design.

The wave equation method generates the so-called bearing graph which is a relation between the pile bearing capacity and pile blow count. These results are an important tool to select adequate pile driving equipment such as the appropriate type of hammer and the hammer efficiency.

GRLWEAP also provides a suitable method to predict the blow count as a function of the pile penetration. These procedures comprise the so-called pile driveability analysis.

In order to calculate the depth vs blow-counts in a realistic way it is necessary to input correct soil parameters based on geotechnical data. From such information it is possible to obtain the total number of blows required to install the pile. In addition, GRLWEAP also allows adjusting the hammer type and efficiency for different pile penetration depths.

Although this is a wide used method, it does not replace the common design methods. GRLWEAP is just an additional effort in the preparation of the driveability analysis.

4.5. PILE DRIVING MONITORING

4.5.1. GENERAL ASPECTS

Pile driving process is usually monitored by recording the force and the velocity to which the pile is submitted during the impact. Pile driving monitoring can be compared as each blow was a dynamic pile test. The aims of pile driving monitoring are the following:

- Establish the pile ultimate bearing capacity and confirm pile design assumptions;
- Assess and manage the risk of pile tip buckling;
- Allow the development of pile driving prediction numerical models;
- Evaluate pile fatigue resulting from the driving process;
- Allow the development of a calibrated model for the back analysis of non-instrumented piles.

The pile is monitored by PDA® (Pile Driving Analyser), herein designated by PDA, system which is a data acquisition system. Two pairs of strain gauges and accelerometers are usually placed 1.5 to 2 pile diameters bellow the pile head in order to record the velocity and force applied in the pile due to the impact. Both pairs of strain gauges are attached to the two opposite side of the pile near the pile head. Dynamic testing in offshore conditions requires special waterproofing sensors and cables. The transducers are connected to the PDA system where the data is recorded for further analysis in the office. The interpretation of the results is based on the wave equation approach detailed in Section 4.4.1.

Because of stress wave effects caused by the rapid loading of the pile, the estimated bearing capacity does not resemble the static load-displacement curve. Hence, in order to obtain the static load-displacement curve it is necessary to remove dynamic effects of both the pile and the soil. This calculation is usually performed by a signal matching analysis. CAPWAP® is the mostly used program for the calculation of the static load-displacement curve from dynamic pile testing.

4.5.2. CAPWAP® ANALYSIS

CAPWAP® (herein termed as CAPWAP) analysis is considered to be a standard procedure for the pile capacity evaluation from dynamic pile testing data. This software is based on a signal matching analysis. In order to perform the CAPWAP analysis, the pile segment bellow the control point is modelled in the form of a series of lump masses and springs. The soil resistance is modelled both along the side and at the toe as an elastic-plastic spring and linear dashpot. This model is similar to the one proposed by Smith (1960). The CAPWAP model is illustrated in Figure 4.14.

Considering the problem to be solved, when a dynamic test is performed two measurements at the pile top are recorded, the deformation and the acceleration. Afterwards, the force and the acceleration present in the pile are deduced from the deformation and acceleration measures. In a CAPWAP analysis, the measured velocity at the pile top is treated as an input quantity. Hence, the measured velocity signal is imposed on the top element in the model. The static and the dynamic soil parameters should then be determined so that when the velocity is applied at the top element, the force calculated at that point will be the same as the measured force. The solution is therefore achieved by a trial and error process until the measured and the calculated force signals match. This procedure is named as inverse analysis, or signal matching analysis. The traditional signal matching technique can be summarized as following:

- Data input – select a record with appropriate energy and data quality;
- Data check and adjustment;
- Check and change resistance distribution;
- Check damping parameters;
- Check quakes and unloading parameters;
- Find the values that produce the best match.

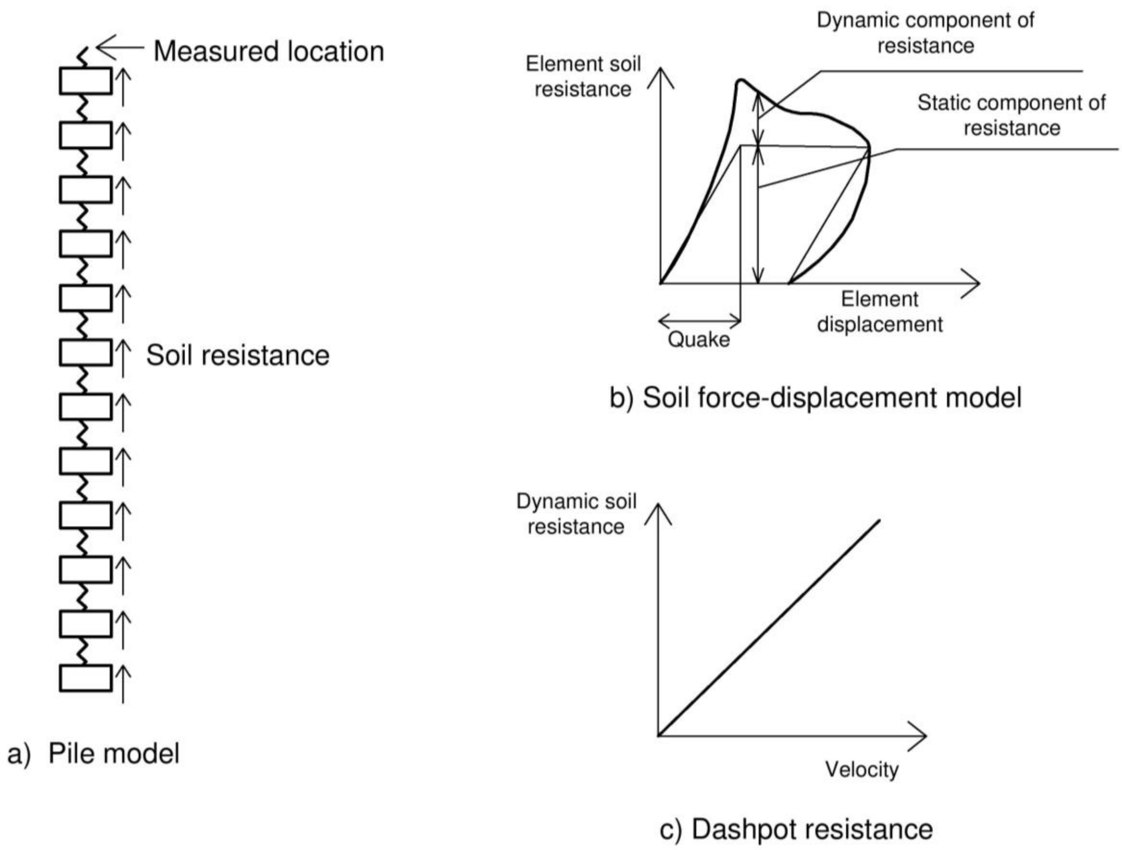

Figure 4.14. – CAPWAP model: a) Pile model; b) Soil Force-Displacement model; d) Dashpot resistance, adapted from Goble and Rausche (1979)

4.5.3. CAPWAP RELIABILITY – CATHIE ASSOCIATES INVESTIGATION

In the majority of Cathie Associates offshore wind projects in the North Sea the wind turbine substructures are founded on pile foundations. According to Eurocode EC 7, the axial bearing capacity of foundation piles shall be verified through pile loading tests. Therefore, dynamic pile loading tests are required to verify the axial resistance of offshore pile foundations. At this specific project, 5 locations were successfully monitored during the pile installation and the pile resistance at the end of drive was then back-calculated using CAPWAP, which was performed by G-Octopus (Cathie Associates operating company dedicated to pile testing).

The analysed tubular piles have an outer diameter of 2.48 m and a wall thickness of 5 cm. The penetration depth equals 28.0 m and the total pile length is of 34.4 m. The water level is 32.2 m above the seabed. The piles are located in medium dense to very dense sand.

4.5.3.1 Strain Gauges and Accelerometers

In one of the dynamic pile test performed in the field, the force and the velocity signal calculated from the measures of two pairs of strain gauges and accelerometers placed 6.25 m bellow the pile head. The pile penetration at the end of the drive was approximately 28.0 m, with a free-length above the seabed of about 6.4 m. Strain gauges, accelerometers and main cables were fully watertight.

The pile instrumentation consists of four strain gauges and two piezo-electric accelerometers. A pile top view with the location of the installed transducers is provided in Figure 4.15.

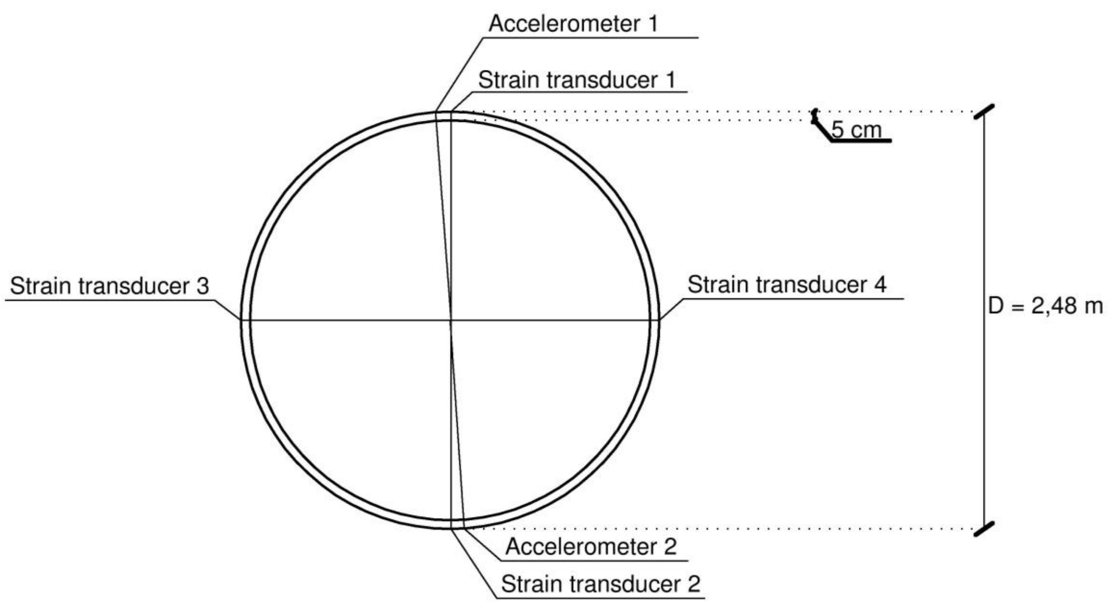

Figure 4.15. – Pile top view – accelerometers and strain gauges location, adapted from G-Octupus

At the end of driving, all sensors and cables were working well and displayed consisting data. Only one of the strain gauges showed some minor electrical instability in some records. Although no restrike test was scheduled for this project location, such a test can still be performed with the PDA equipment left on the pile.

The recorded signals at the end of the drive showed a good consistency and similar trends. One signal was selected for its realistic displacement and wave up curves. Regarding this signal no strain gauge and accelerometer showed instabilities. The collected signals were edited and corrected with the PDA-W software. The recorded signals offer an accuracy of 5%.

The force and the velocity signals measured by the strain gauges and accelerometers in the real pile dynamic test are represented in Figure 4.16. The measured signals are influenced not only by the hammer blow but also by the wave reflections that occur due to the soil resistance. Thus, these signals represent the effects to which the pile is submitted during the dynamic test. The wave-up and wave-down signals are shown in Figure 4.17 and were derived from the measured signals in the pile by Equation 4.41 and Equation 4.42. In the present work the sign convention of soil mechanics is used. Therefore, compression stresses and strains are taken as positive. On the other hand, tensile stresses and strains are taken as negative.

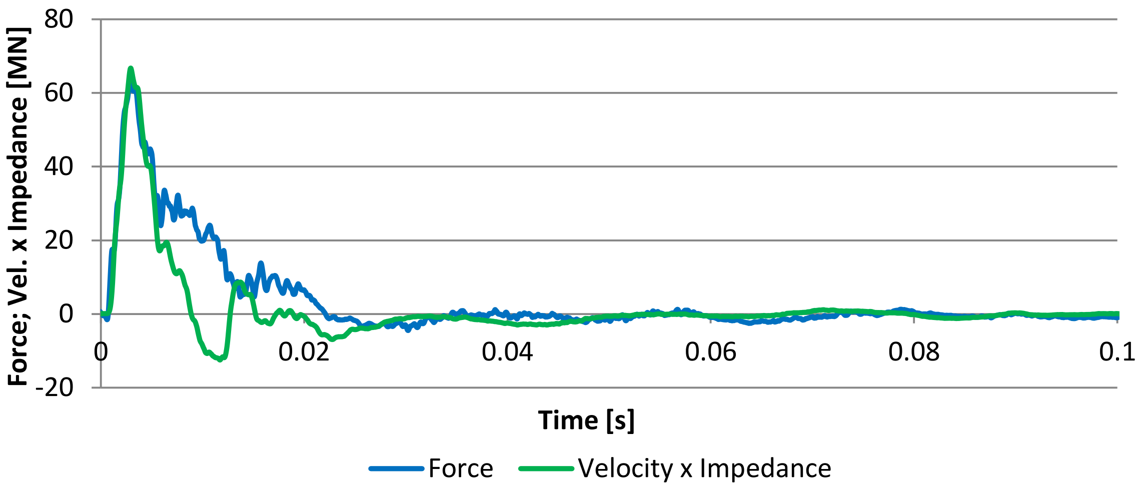

Figure 4.16. – Force and velocity signals measured in the dynamic pile test

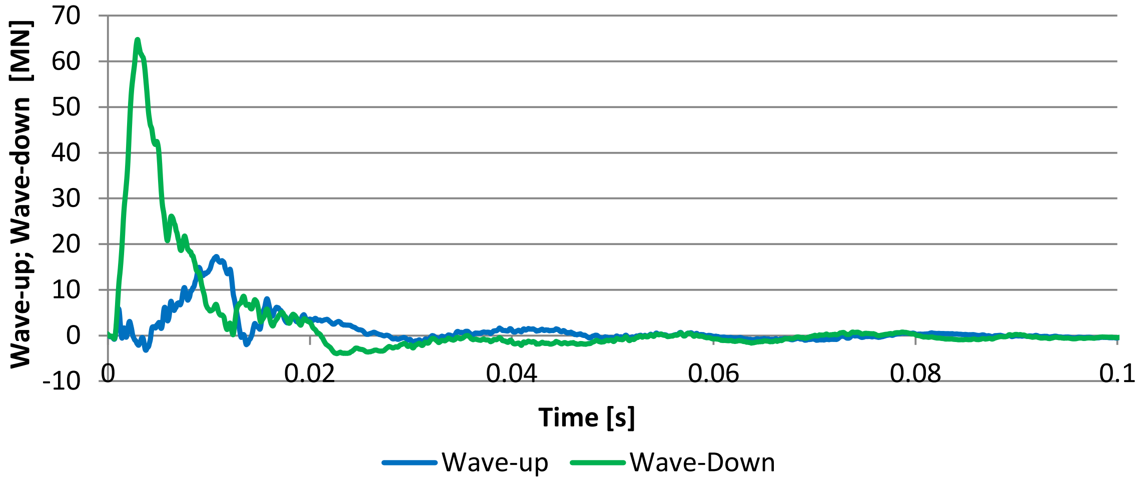

Figure 4.17. – Wave-up and wave-down measured in the dynamic pile test

4.5.3.2. Cathie Associates Signal Matching Analysis

A CAPWAP signal matching analysis was performed in order to back-calculate the axial pile resistance at the end of drive for the purpose of the verification of EC7 design requirements for pile foundations. The signal matching analysis was executed with the limit values of radiation damping as established by the CAPWAP manual. Figure 4.18 displays a comparison of the SRD calculated by CAPWAP and the estimated by Alm and Hamre ('SRD Lower Bound') for various pile penetration depths and for one of the monitored locations. Figure 4.19 a) and Figure 4.19 b) show a comparison of the end-bearing capacity and the shaft capacity between the performed analyses for several pile penetration depths and for the same location mentioned in the previous section.

These results are more interesting to examine since they correspond to the results of the SRD divided in two components: the end-bearing and the shaft capacity. From the internal investigation performed at Cathie Associates it was noticed that:

- The tip resistance is clearly different;
- The friction profile does not match.

Thus, Cathie Associates concluded that the pile-soil interaction behaviour during driving may not be correctly assessed. Hence, Cathie Associates is looking for reliable methods to assess the static axial pile capacity from dynamic measurements of open-ended pipe piles installed by impact driving in very dense sands. An axisymmetric model is proposed in the next chapters in order to evaluate the SRD.

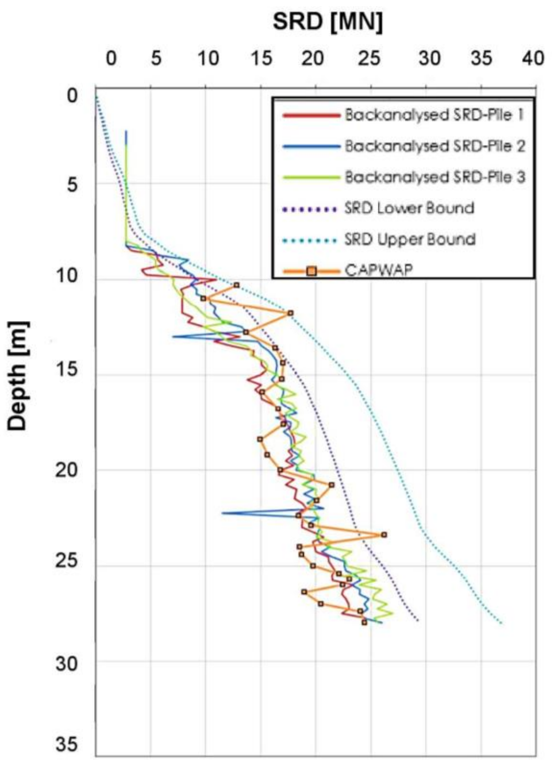

Figure 4.18. – SRD comparison between Alm and Hamre (2002) calculation and CAPWAP back-analysis

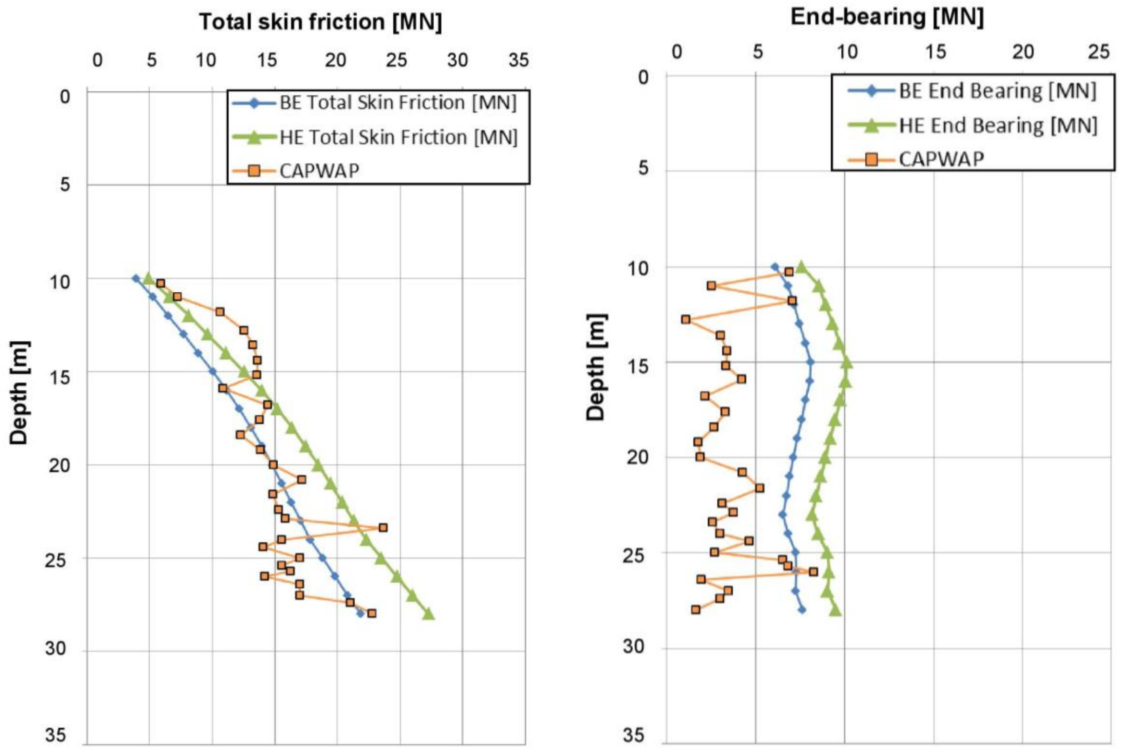

Figure 4.19. – Comparison between Alm and Hamre (2002) calculation and CAPWAP back-analysis at different depths: Total skin friction (left); End-bearing capacity (right)

5

STATIC NUMERICAL MODEL FOR SOIL RESISTANCE DURING DRIVING ANALYSIS

5.1. OVERVIEW

As it was mentioned before, Cathie Associates is looking for reliable methods for assessing the static axial pile capacity from dynamic measurements of tubular piles installed by impact driving in dense to very dense sands. A finite element model is developed in order to have a better understanding about the soil mechanisms during static and dynamic pile tests. The present work proposes a finite element model to assess SRD.

Due the increase of computer speed, calculation times have dropped significantly. Therefore, finite element applications became easier to use and more resources are available to study this subject. The first pile driveability analysis using finite element analysis was carried out by Chow (1981). Many researches were performed more recently using finite element models namely the ones conducted by Liyanapathirana *et al.* (1998), Liyanapathirana *et al.* (2001), Pinto *et al.* (2008). However, the mentioned analyses do not compare their prediction results with the ones available from design method calculations. Masouleh and Fakharian (2008) compared their predictions with real-life pile driving data. They concluded that numerical modelling is a promising tool for pile driveability assessment compared to conventional lumped models.

The finite element modelling offers some advantages compared with the models based on the one proposed by Smith 1960. It leads to a more realistic modelling and it allows a better understanding of the soil response during pile driveability. Besides that, it is based on conventional soil parameters instead of empirically determined ones. However, there are also several limitations and some aspects that should be taken into account when adopting a finite element approach. These shortcomings will be discussed while the static and the dynamic models are detailed.

Therefore, the present work aims at emulating a dynamic pile testing using PLAXIS 2D numerical modelling. Despite that, a 2D static model was modelled in the first place in order to gain some confidence with numerical simulations and with the PLAXIS® software package herein designated by PLAXIS. It is also important to develop a static model in the first place as it is simple to build (less parameters involved) and it can be used as a first approximation to the dynamic model. It also allows getting a better understanding about soil mechanisms that occur when a static load is applied to the pile.

This chapter presents the mentioned static axisymmetric model. It emulates a static pile test at one of the piles designed by Cathie Associates in the project detailed in Section 4.5.3. The procedures that were adopted along this analysis are outlined along this chapter. The dimensional analysis was performed using the software package PLAXIS 2D. Conclusions are taken regarding the soil plug behaviour and the pile axial capacity.

The simulations were done in a workstation equipped with an Intel ® Xeon (R) CPU X5650, 24.0 Gb of RAM memory at 2.67 GH. Each static simulation took about 20 min to be completed.

5.2. AXISYMMETRIC STATIC MODEL

In static conditions there are a small number of parameters to be considered if compared with the number of parameters required in dynamic conditions. Therefore, initially it was developed a static model. The static model intends to replicate the soil and pile behaviour when a load is applied in static conditions to the pile at the end of the drive.

In order to study the soil behavior during pile driveability it was created an axisymmetric finite element model. The model was developed in three stages:

- Generation of the initial stresses;
- Pile installation – stresses equilibrium between the pile and the soil;
- Static load applied on the pile head.

In the first stage, the initial stresses are generated by creating the soil layers. Afterwards, the resulted deformation is set to zero. In the second step, the pile is created and it is allowed to achieve equilibrium with the soil layers. The final deformations of this phase are also set to zero. In the third phase, a static load is input on the pile head.

In this chapter, it will initially be given some considerations about the mesh used in the analysis. The pile and the soil model will also be detailed in Section 5.2.2 and Section 5.2.3. Finally, the results of the analysis are discussed and validated. This is an important step before moving to the dynamic model. The validations are based on several researches about pile driveability made by the geotechnical community. They are mainly related with the soil and pile response when a static load is applied.

In order to get a reliable model, the results are compared with the predictions suggested by Alm and Hamre (2002). The method proposed by these authors assumes unplugged piles during driving. Therefore, as it is expectable that in static conditions the pile will plug, the SRD determined by Alm and Hamre method is not directly comparable with the numerical analysis results. In the present work it is considered that the outside shaft friction profiles in plugged and unplugged conditions are similar.

5.2.1. MESH

The soil layers and the pile are modelled with 15-noded triangular elements. The 15-noded triangle is recommended to axisymmetric problems and offers more accurate results than the 6-noded triangle elements. The mesh box used is illustrated in Figure 5.1. It was defined a mesh box that allowed to capture the plug effects bellow the pile tip and the skin friction load spread. It was also checked that no failed zones invaded the boundaries of the model. A more refined mesh was used close to the pile since it is in that region that larger effects occur during the loading.

Therefore, the pile near field has more influence in the final results and a refined mesh allows a better interpretation of the results in this region.

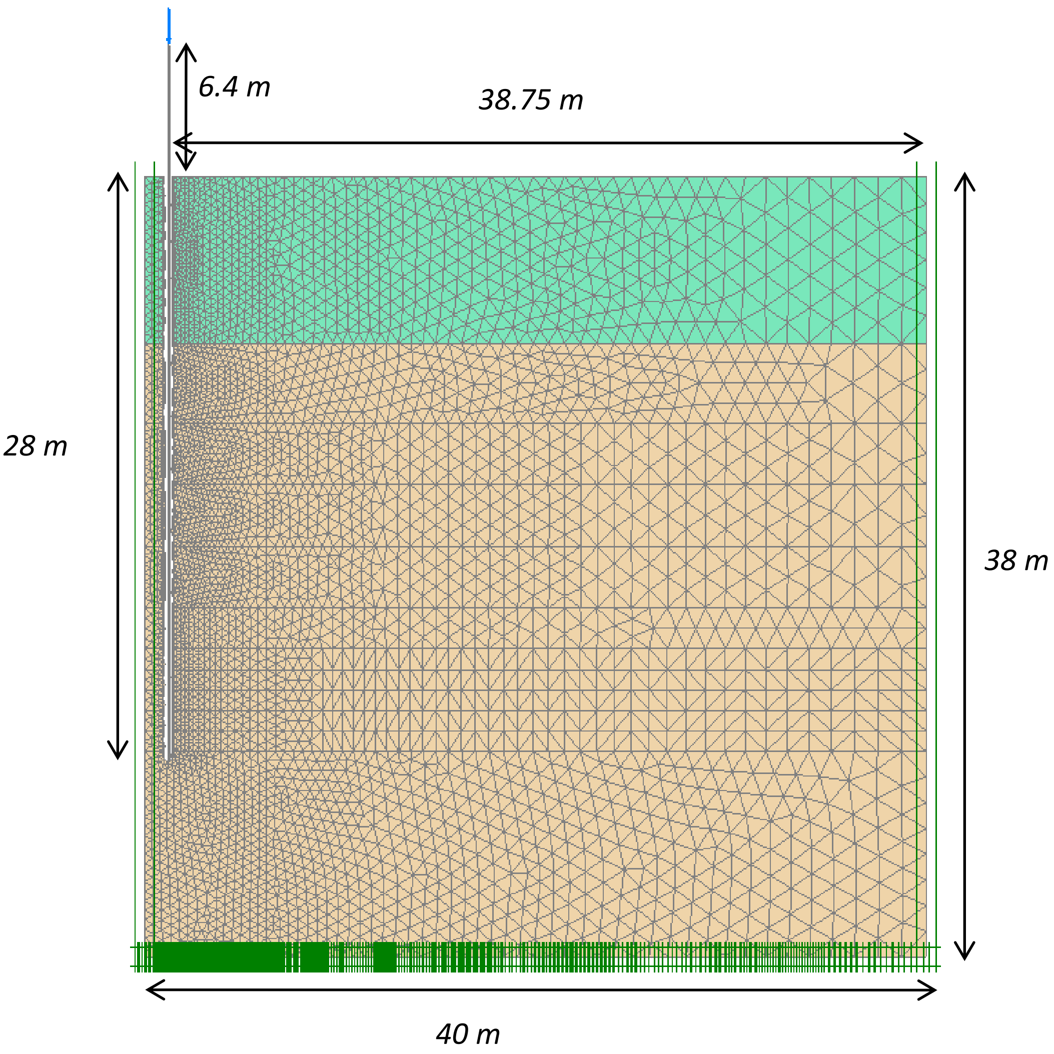

Figure 5.1. – Mesh of the 2D Finite Element Model

5.2.2. PILE MODEL

The pile in study is one of the piles designed by Cathie Associates for the described project in the North Sea. It supports a tripod structure in offshore conditions. Therefore, the steel open-ended pile has a depth penetration of 28.0 m and a stick-up of 6.4 m. The cross-section is defined with an outer-diameter of 2.5 m and a thickness of 5 cm.

The tubular pile was modelled using a single column of continuum elements. These elements allow modelling the axial wave and radial expansions of the pile. As the pile is much stiffer than the soil, it was defined a linear-elastic and non-porous material model to represent its behaviour. The non-porous feature excludes the presence of pore pressures in this element. Other pile characteristics are detailed in Table 5.1.

Table 5.1. – Pile features, static model

Properties	Units	Steel Pile
Unit weight, γ	kN/m^3	78.5
Young's Modulus, *E*	GPa	210
Poisson's ratio, ν	-	0.3

5.2.3. Soil Model

The soil was modelled based on a CPT borehole log report, illustrated in Figure 5.2, taken from the same Cathie Associates project in the North Sea. Lesny (2010) provides a general description about North Sea soils. The stratification of the North Sea soils was shaped by sedimentation processes and transport conditions during the ice ages. North Sea soils are characterized by an upper layer of Holocene sands with a height between 1 to 15 meters. The bottom layers consist in Pleistocene sands. These layers are heavily over-consolidated due to the processes suffered during the ice ages.

In this phase, a simple drained elasto-perfecty plastic model (herein designated "the Mohr-Coulomb model", according to PLAXIS (2014a)) was used to emulate the soil behaviour. In static conditions it is considered that the load is applied to the pile slowly and any excess pore pressures are generated in the soil. Thus, a drained soil model was established in this model. The phreatic level is defined 32.2 m above the seabed. The Mohr-Coulomb yield condition is formulated as shown in Equation 5.1, where:

- τ_f – Shear stress at failure;
- c' – Effective Cohesion Intercept;
- σ'_f – Effective stress at failure;
- ϕ' – Angle of Shearing Resistance.

$$\tau_f = c' + \sigma'_f . \tan \phi' \qquad (5.1.)$$

When using a Mohr-Coulomb model we are dealing with a limited number of parameters, five in this case, corresponding to two stiff parameters and three strength parameters, as follows:

- Young's Modulus (E');
- *Poisson*'s ratio (ν');
- Effective Cohesion Intercept (c');
- Angle of Shearing Resistance (ϕ');
- Angle of dilatancy (ψ).

Table 5.2 details the soil properties defined in the static model.

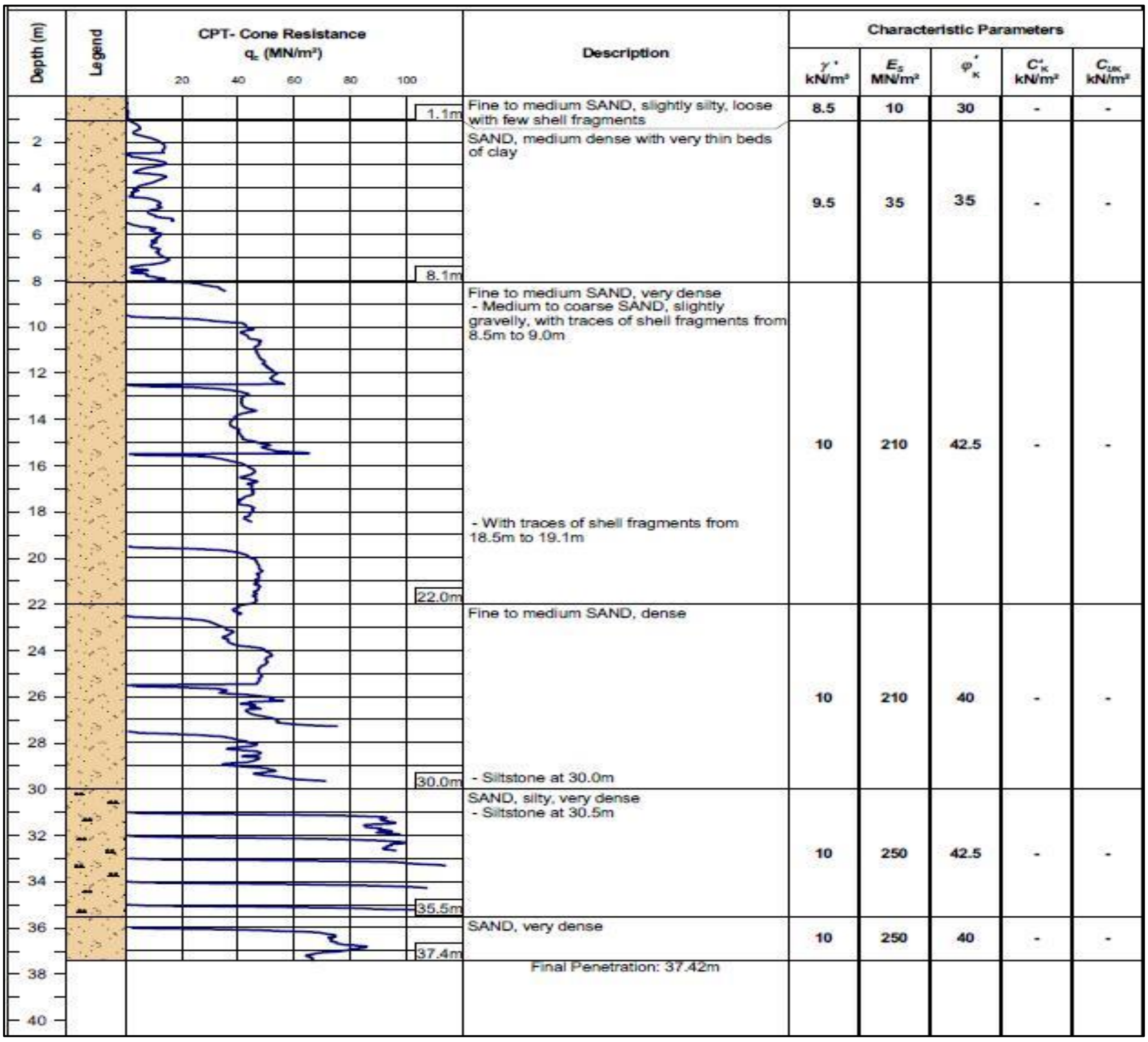

Figure 5.2. – Borehole Log Report, Cathie Associates

Table 5.2. – Soil properties, static model

Properties	Units	Medium Sand	Very Dense Sand
Effective Unit Weight, γ'	kN/m^3	9.5	10
Young's Modulus, *E'*	MPa	Linear increasing 23.3 to 140	140
Poisson's ratio, ν	-	0.3	0.3
Effective cohesion intercept, *c*	kPa	1.0	1.0
Angle of shearing resistance, ϕ'	º	35	42.5
Interface friction angle, δ_f	-	21	26.5
Angle of dilatancy, ψ	º	0	0
Lateral Earth Pressure, *K*	-	0.46	0.5 to 1.5

5.2.3.1 Young's Modulus

The Constrained Modulus given by the borehole log report is estimated based on Lunne and Christophersen (1983) studies. The correlations proposed by the authors between the Constrained Modulus and the CPT results for over-consolidated (aged) sands were presented in Section 2.2.4.3 by Equation 2.7 and Equation 2.8.

The Young's Modulus is the most common stiffness parameter of a perfect plastic model. The initial slope of the stress-strain curve, currently named as tangent modulus, is usually indicated as E_0. The secant modulus at 50% strength is defined as E_{50}. For materials with a large elastic range it is reliable to use the tangent modulus to define the stiffness of the soil. However, for text-book soils (meaning, sedimentary, non-cemented or highly aged, soils) the use of the E_{50} gives a more representative stress-strain behaviour of the soil in a non-advanced soil model (without considering non-linearity soil response, etc.). Figure 5.3 provides a scheme illustrating this issue.

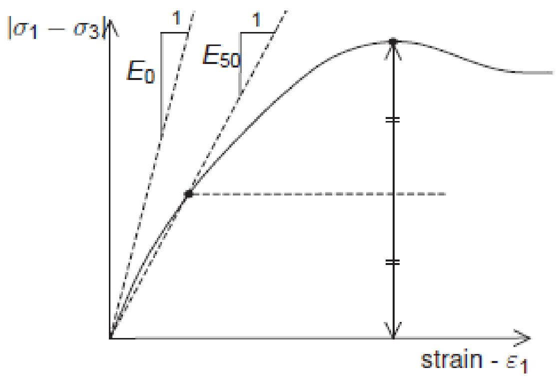

Figure 5.3. – Soil stress-strain curve, PLAXIS (2014a)

The Constrained Modulus, E_{oed}, is derived from the *in situ* test executed in geotechnical characterization of the field. The relationship between the Young's Modulus and the Constrained Modulus is given by Equation 5.4. Using a *Poisson* coefficient of 0.3, then we get the relation E_{oed}=1.34E.

$$E_{oed} = \frac{(1-\nu).E}{(1-2\nu).(1+\nu)} \tag{5.4.}$$

In order to estimate E_{50} it was adopted a first approximation considering E_{50}=2/3E_{oed}, as suggested by PLAXIS (2014a). Therefore, this assumption leads us to a value for E_{50} equal to 23.3 MPa and 140 MPa in the top and in the bottom layers respectively.

Some investigations showed that the Young's Modulus in sand mainly depends on the relative density, 'over-consolidation' ratio (due to ageing and cementation effects) and current mean stress level. Bellotti (1989) suggested an evaluation of an average axial strain of 0.1% for a range of stress histories and ageing (Section 2.2.4.1). Thus, using the empirical correlation suggested by Bellotti for a cone penetration resistance of 40 MPa, $E_{0.1\%}$ assumes values in the range of 160 MPa. This value is close to 140 MPa that was estimated before, which gives some confidence in this estimation.

It is well-known from geotechnical studies that the stiffness depends significantly of the stress level, both increasing with the mean effective stress, by one side, as decreasing with the deviatoric stress level towards strength (no linearity), by the other side. Thus, normally, the stiffness of the soil increases with depth. This effect is more significant for lower depths. Therefore, the constant constrained modulus given by the CPT borehole for each layer is explained by the failure mechanisms of the soil when the CPT test is being performed.

In order to emulate the soil realistically, in the upper layer the Young's Modulus increases gradually from 23.3 MPa to 140 MPa. The bottom layer is defined with a constant Young's Modulus of 140 MPa. Otherwise, the stiffness of the soil bellow the pile tip could be overestimated.

5.2.3.2 *Poisson*'s ratio

When very dense sands submitted to a drained triaxial test, a volume decrease at the beginning of axial loading occurs. The relation between the volume change (ε_v) and the axial strains (ε_y) (as defined by PLAXIS (2014a) is defined by the *Poisson*`s ratio. For sandy soils a *Poisson*`s ratio between 0.25 and 0.35 is commonly used.

5.2.3.3 Effect Cohesion Intercept

The cohesion parameter, in combination with a realistic friction, is used to model the Mohr-Coulomb failure criteria. The low value of the cohesion assumed in both of layers is used to take into account a limited amount of cementation in the soil layers. It can also be established to simple consider moderate to high relative densities, which, due to a mathematical linearization of the Mohr-Coulomb strength envelope, can confer a constant in the deviatoric axis. Therefore, numerical instability near the surface is avoided, as this region offers almost no resistance.

5.2.3.4 Angle of Shearing Resistance

Figure 5.4 shows typical stress-strain curves for dense sands obtained from triaxial drained tests and a constant σ'. During shearing, dense sands achieve a peak shear stress before reaching the critical state. The peak strength is mobilized for the so-called angle of shearing resistance (ϕ'). This incorporates both the friction component and the increment in strength. These two components are due to the energy necessary to separate the particles, increasing the volume (dilatancy) of the sheared zone, and falling then towards a residual strength, due to the friction component, commanded by a constant volume friction angle (ϕ'_{cv}).

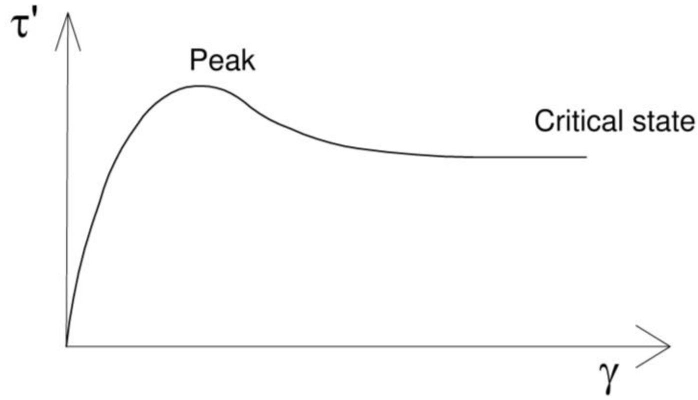

Figure 5.4. – Stress-strain curve for dense sands

The so-called ‘Mohr-Coulomb model’ is in PLAXIS an elastic perfect plastic model. Thus, it does not allow emulating this softening soil behaviour. Therefore, it should be taken into account that for large deformation problems it must be used the critical friction angle value in order to represent realistically the soil behaviour. On the other hand, for small deformations the peak angle of shearing resistance value is more appropriate.

As large displacements only occur in the soil-pile interface and bellow the pile tip, the soil was modelled using the critical friction angle provided by the borehole log report. In order to simulate a better response of the soil-pile interface it was used an interface element provided by the PLAXIS software.

5.2.3.5 Interface Friction Angle

The interface element provided by PLAXIS allows a more adequate modelling of the soil-structure interface. These inner and outer pile zones are highly sheared during both static and dynamic loading. Therefore, interface elements offer a better simulation of the thin zone at the contact between the pile and the surrounding soil. Besides that, they facilitate the pile-soil slip during driving.

The Mohr-Coulomb friction model was also used for the contact law between the pile and the soil. The same properties of the surrounding soil were defined with only a degradation of the friction angle.

Alm and Hamre (2002) approach suggested an outside skin friction that equals the inside skin friction. Also, all the estimations made using the Alm and Hamre method assume unplugged piles. In order to choose reasonable values for the interface friction angle, the same model was tested for a pile with a shallow penetration depth. Thus, an unplug pile behaviour was adopted for a pile penetration depth of 10 m. It was possible to estimate the interface friction angle by equalizing the inner and outer shaft friction profile, as illustrate in Figure 5.6. A good approximation was obtained with values of the interface friction angle equal to 21° and 26.5° for the top and bottom layers respectively.

The inside and the outside skin friction of this model are shown in Figure 5.5. In this representation, when the pile is loaded in compression, the inside shaft friction stresses (resistance) are negative when directed upwards, while the outside reaction is positive, although with the same direction (upwards), consequence of the convention in PLAXIS. This convention is used from this point onwards. In some cases, the plots use real values while in other for better visual comparison of the two sides trends, the absolute values are plotted aside, as it happens for instance in Figure 5.5.

It is observed that the inside and the outside shaft profiles are similar. Thus, from this approach on, it was assumed an equal distribution of the outside and the inside shaft profiles for unplugged piles. This conclusion is in accordance with which was suggested by Alm and Hamre (2002).

In the following studies, all the analyses will only compare the outside skin friction of PLAXIS results with the outside skin friction of the Alm and Hamre proposal. It is assumed that the outside skin friction of a plugged and unplugged piles are similar.

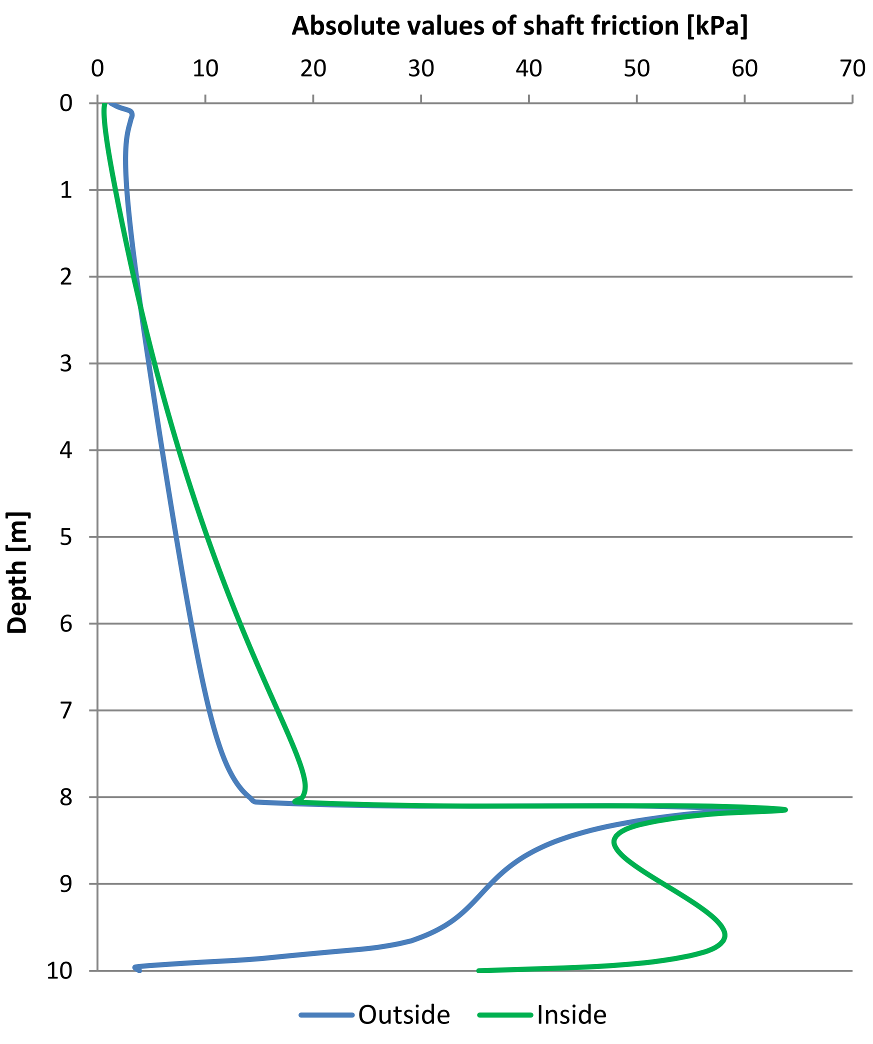

Figure 5.5. – Outside and inside shaft friction profiles for shallow penetration depths

5.2.3.6 Angle of Dilatancy

As explained in Section 5.2.3.4, during shearing, dense sands achieve a peak shear stress before reaching the critical state. The difference between the peak and the residual friction angle is due to soil dilatancy (ψ). The angle of dilatancy also gives an indication of the rate at which the soil volume changes as it is sheared. Bolton (1986) proposed an empirical relation between the soil peak friction angle and the soil dilatancy angle as indicated by Equation 5.5. In this equation 'a' has the value of 0.8 for plane strain conditions and 0.5, for triaxial test conditions.

$$\phi' = \phi'_{cv} + a.\psi \tag{5.5.}$$

As the Mohr-Coulomb is a linear perfect plastic failure criterion, the dilatancy angle does not affect the stresses state. Hence, it has only effect in the deformation state. Therefore, a positive dilatancy means that the soil dilates as long as shearing occurs. This approach is not realistic at all because this way the soil would never reach a critical state and it would suffer volume deformations indefinitely. Thus, a dilatancy angle of zero was defined in the model.

This issue corresponds to one of the limitations of the Mohr Coulomb model. In fact, due to the confining pressure that the soil within the pile is submitted, the dilatancy of the soil can promote significant changes in the stresses of the soil, mainly inside the tubular pile. As a future development, it is suggested to test the implemented model defining an improved soil model which would allow assessing the influence of the dilatancy parameter in the results.

5.2.3.7 Lateral Earth Pressure

The lateral earth pressure at rest coefficient (K_0) gives the relationship between the horizontal and the vertical effective stresses, as shown by Equation 5.6.

$$K_0 = \frac{\sigma'_h}{\sigma'_v} \tag{5.6.}$$

This ratio depends mostly on the geological history of stresses. The value of K_0 for recent (normally consolidated) sandy soils can be estimated by Equation 5.7, proposed by Jaky (1944). In this type of soils the values are usually about 0.5. For over-consolidated soils the values are usually much larger. Although there are some reference values for K_0, there are no reliable methods to determine the lateral earth pressure at rest coefficient from CPT results in fine-grained soils.

$$K_0 = 1 - sin\,\phi \tag{5.7.}$$

Pile installation causes a significant amount of soil radial displacements close to the pile tip and an increase in the values of horizontal stresses. In order to take into account the pile installation effects, the K value was gradually increased along the over-consolidated soil. This approach was adopted taking as reference the calculated shaft friction by Alm and Hamre (2002) predictions. By consecutive iterations, it was achieved a good match between the pile shaft friction and the outside friction proposed by Alm and Hamre. This approximation is presented in Figure 5.6, with the same convention defined above for Figure 5.5.

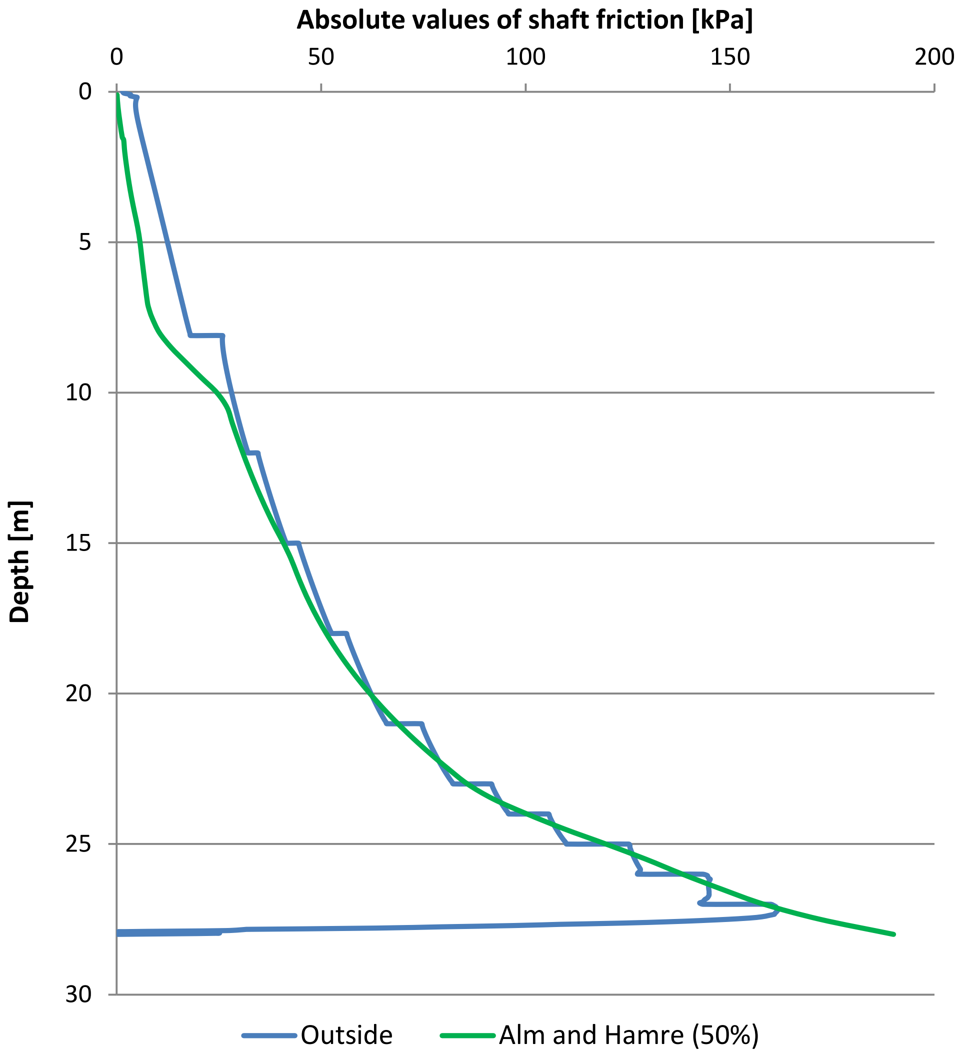

Figure 5.6. – Alm and Hamre (2002) and PLAXIS outside shaft friction comparison

5.2.3.8. Triaxial and Direct Simple Shear Tests

Figure 5.7 and Figure 5.8 show what should be expected regarding the soil response when it is submitted to a triaxial test and to a Direct Simple Shear (DSS) test, respectively. These tests were performed taking advantage of 'PLAXIS Soil Test' tool.

Regarding the triaxial test, the soil is induced to a confining pressure and then it is tested until failure by triaxial compression loads. The confining pressure is kept constant during the test. The analysis of Figure 5.7 offers a better understanding of the soil response when submitted to a drained triaxial test. After the confining pressure is installed, the deviatoric stress remains constant. For a zero dilatancy angle, the soil does not also present any changes of volumetric strains after the target confining pressure is reached.

In the DSS test, the sample is loaded with a normal load, constant during the test. The shear stress is incremented gradually, with a given velocity, which corresponds to the extension rate. Figure 5.8 shows that through this process, the volumetric strains remains zero. That situation is associated with a soil with zero dilatancy.

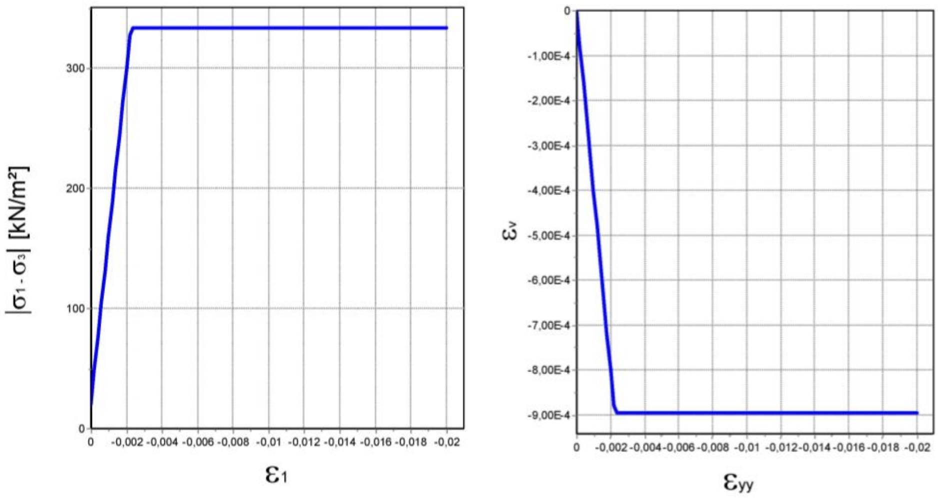

Figure 5.7. – Triaxial test in drained conditions

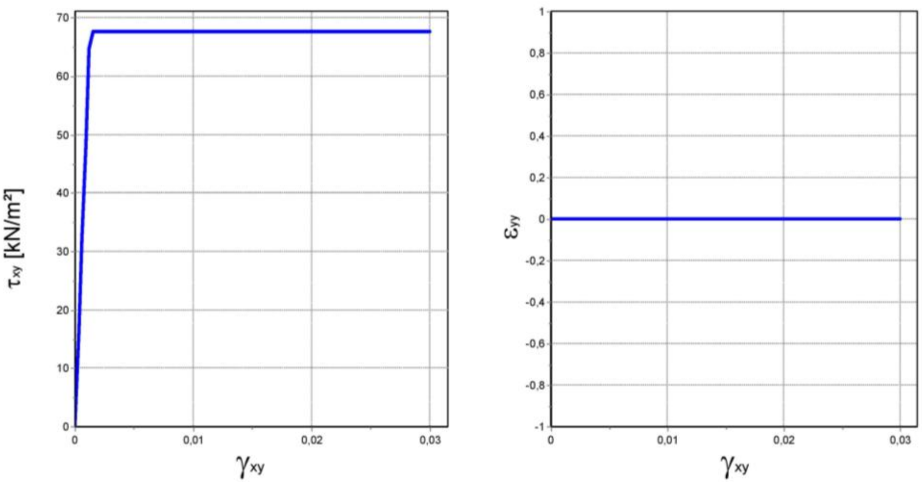

Figure 5.8. – DSS Test in drained conditions

5.2.4. Discussion of the Results

In order to create a reliable model, some validations were executed during the development of the static model. Most of the confirmations were based in information collected from the literature and detailed along Chapter 4. The first and more obvious validation corresponds to check the degree of plugging of the pile. Then, a tension load and a prescribed displacement were applied on the pile and the results are present in Section 5.2.4.2 and in Section 5.2.4.3. Finally the soil surrounding the pile is aim of study.

5.2.4.1. Plugged Behaviour

As mentioned in Section 4.2.3, accordingly with Henke and Grabe (2009), when a pile is induced to a compression static load, it exhibits high horizontal stress peaks inside the pile. Thus, an arching effect is likely to arise inside static loaded piles and plugging is expected to occur as concluded by Kishida and Isemoto (1970). Plugging occurs when the IFR parameter is equal to zero, which corresponds to a situation when the pile settlement is equal to the soil column within the pile vertical displacement. By analysing Figure 5.9 it can be observed that both the vertical displacements of the pile and of the soil column are approximately 0.20m. It is therefore confirmed that plug occurs in static conditions, as concluded by Henke and Grabe.

In the present work, when the soil displaces upwards, the vertical displacements are positive, which is in accordance with PLAXIS sign convention. This convention is used from this point onwards. In some cases, the plots use real values while in others the absolute values are plotted aside.

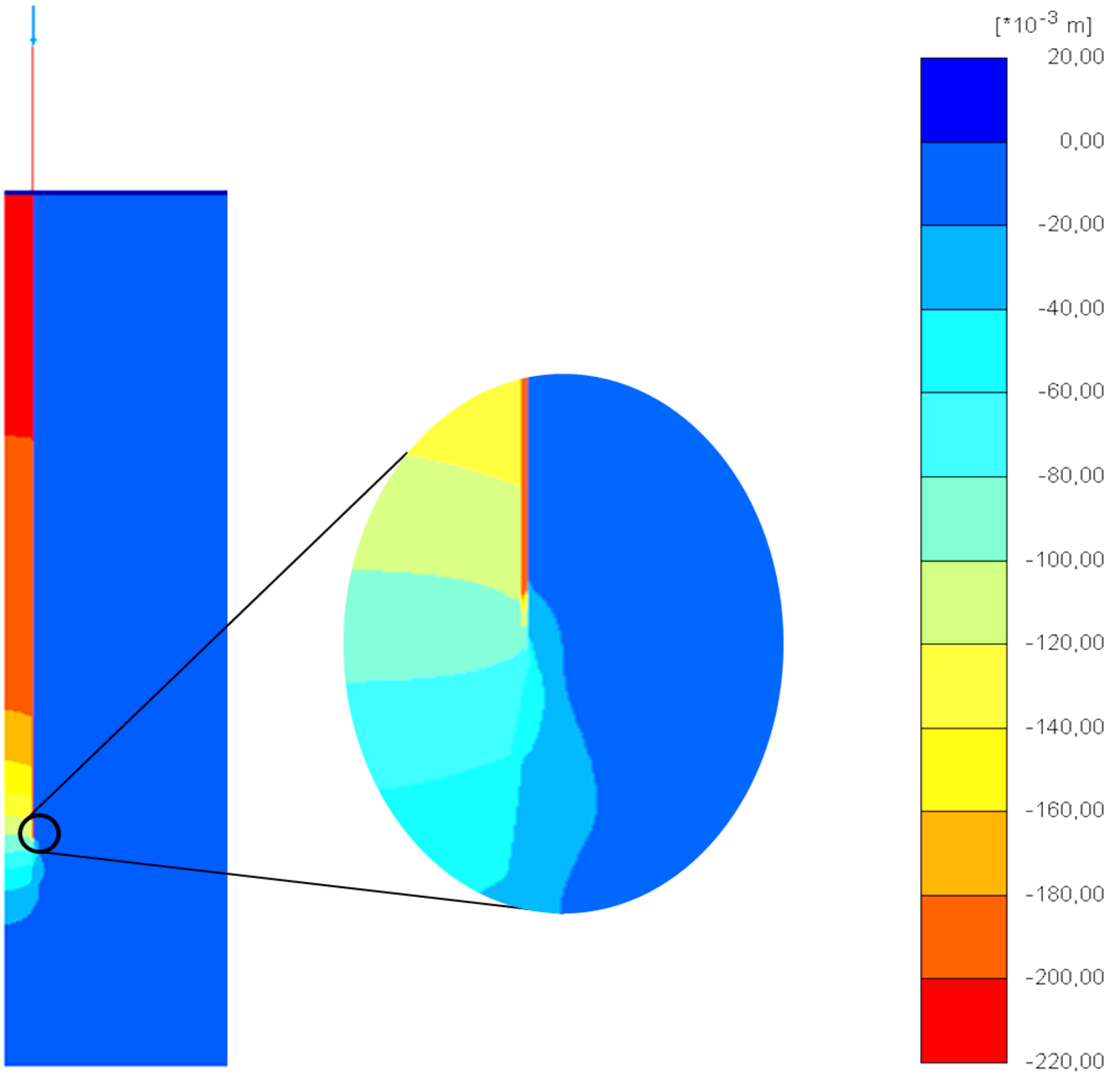

Figure 5.9. – Vertical displacements

A closed-ended pile penetrates in the soil, opening a cavity from nothing. The same behaviour occurs if a pile penetrates by a plugged manner. Hence, it generates high radial displacements close to the pile tip and so high pressures are exhibit in the region bellow the pile. Figure 5.10 shows the distribution of the principal stresses in the region close to the pile. As indicated by this figure, the principal stresses involve the overall pile base. As mentioned in Chapter 4, in this thesis compression stresses and strains are taken as positive and tensile stresses and strains are taken as negative.

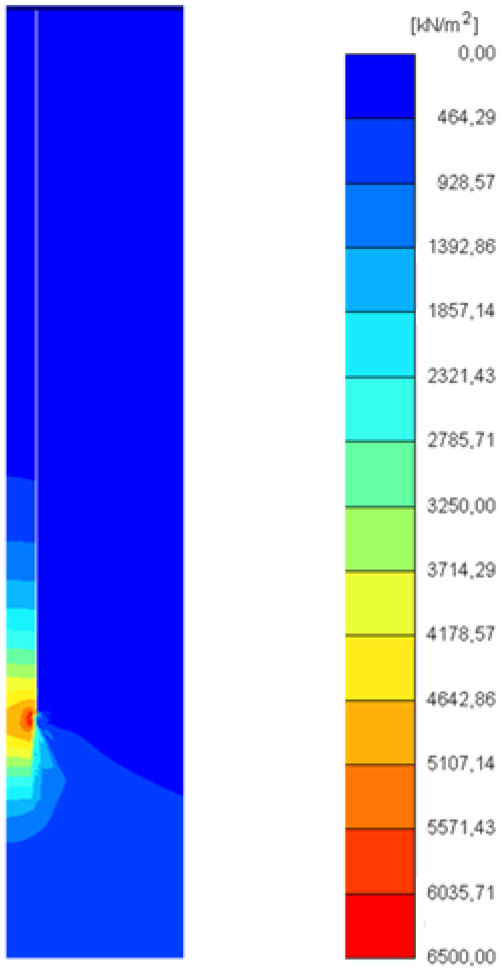

Figure 5.10. – Principal stresses distribution

Still regarding plug and unplug behaviour, Leong and Randolph (1991) concluded, based on a finite element analyses, that under typical loading conditions, adequate end bearing may be mobilized by the soil plug, largely by high effective stresses in the bottom 3-5 diameters (7.5 – 12.5 m) of the soil plug. This measure can be interpreted as the active plug length, *h'*, as it was also proposed by Randolph. Then, as the plastic points are the ones with larger effective stresses, their evaluation is an easy way to assess the previous reference.

Figure 5.11 a) presents the distribution of the plastic points, in red, for the last stage of loading. These points, inside the pile wall, extend from the pile toe until *8.8 m* above it. It is therefore in the same range of the active plug length proposed by Leong and Randolph. The same conclusion can be taken when studying the inside horizontal stresses along the shaft, as represented in Figure 5.11 b). Thus, this is another indication that confirms that plug occurs in static conditions.

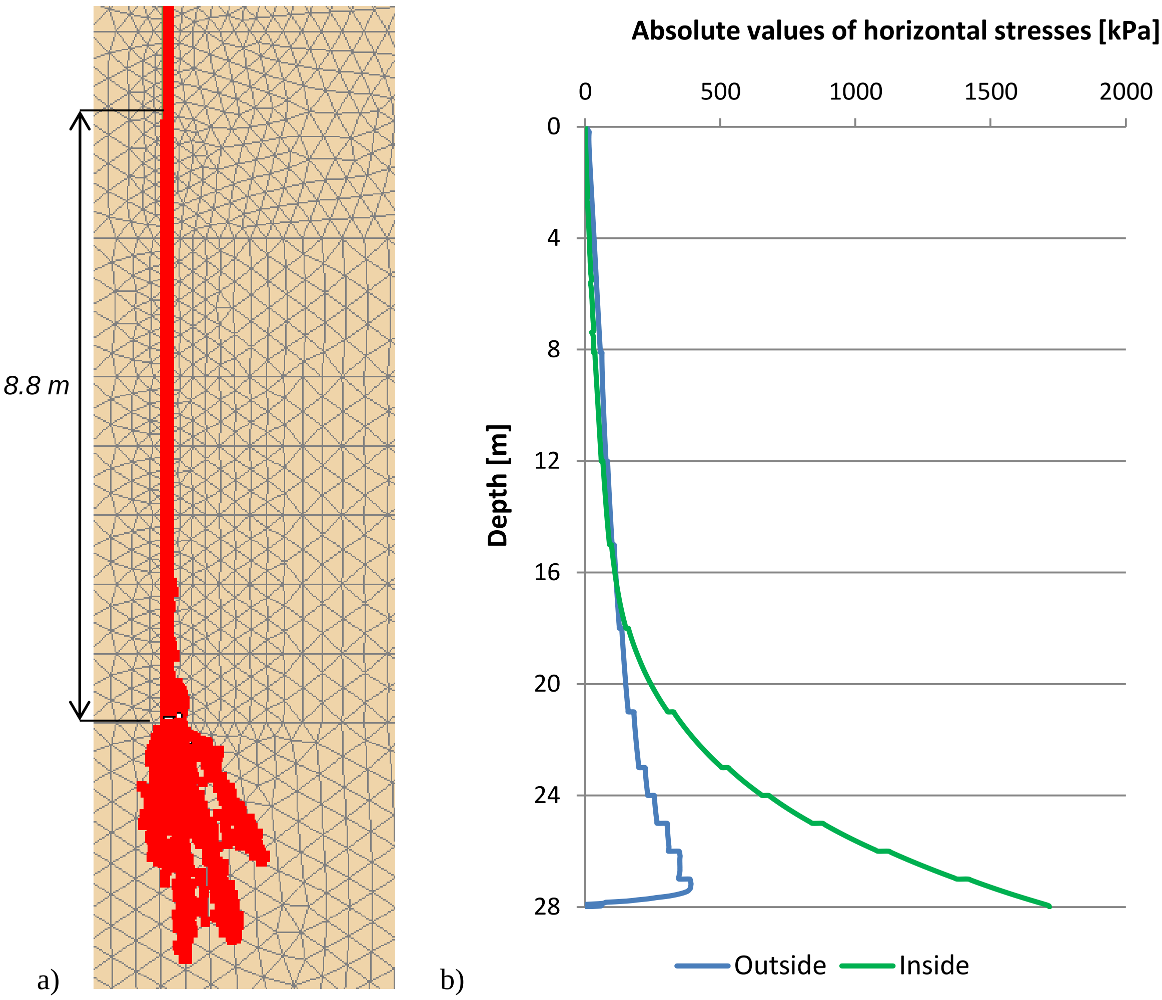

Figure 5.11. – a) Plastic points: b) Horizontal stresses profiles (right)

5.2.4.2. Tension Test

A tension test was also performed. Instead of applying a compression load on the pile, a tension load is applied until all the pile skin friction is mobilized. The total outside shaft friction for both the tests is:

- Compression load – 11.0 MN;
- Tension load – 9.0 MN.

The ratio between the tension and the compression outside shaft capacities equals 0.82. This value can be compared with the formulations of the pile tension capacity adopted by the different design methods. Design methods assume a tension capacity between 0.7 and 0.77 of the compression pile resistance. The ratio between tension and compression shaft capacities is therefore close to the range of values proposed by the design methods. Figure 5.12 shows the inside and the outside shaft friction profiles for the compression and tension models. In this representation, as already mentioned, in compression, the inside shaft friction stresses (resistance) are negative when directed upwards, while the outside reaction is positive, although with the same direction (upwards), consequence of the convention in PLAXIS. The same convention, but in the opposite direction, applies for the tension loading. Values are in this figure considered with the real value.

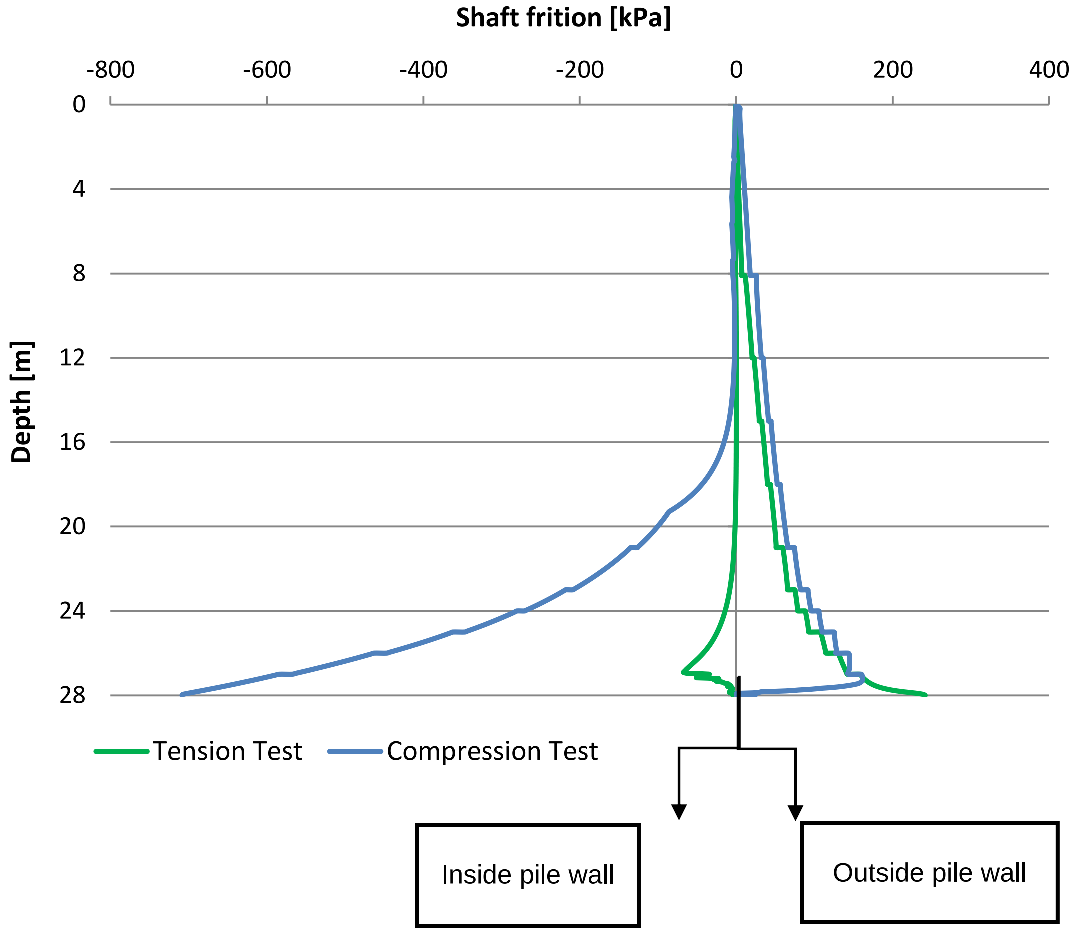

Figure 5.12. – Shaft friction profiles for both compression and tension tests

It is important to notice that, when a pile is submitted to a tension test, the soil bellow the tip is not mobilized. Thus, only the skin friction actuates and this is the unique component that accounts for the pile tension capacity. The comparison of the compression and the tension tests load-displacement curves are of the most interest, as shown in Figure 5.13. Vertical displacements are in this figure considered with the absolute value.

Firstly, regarding the compression load-displacement curve it is observed that it never reaches a limit state. This response may indicate that the pile starts to mobilize the skin friction and the base resistance. However, at the moment that the outside shaft friction is being entirely mobilized, which in Figure 5.13 corresponds to the end of the first stretch of the curve for a load of about 12 MN, the base capacity continues to be mobilized. Consequently, while the pile is loaded, soil bellow tip offers increasingly more resistance.

Taking that point into consideration, it can now be analysed the curve obtained for the tension test. As a tension load only actuates in the shaft friction, it can be concluded that the pile shaft capacity is about 10 MN. Thus, the total shaft friction is lower when a tension load is applied on the pile rather than a compression a load.

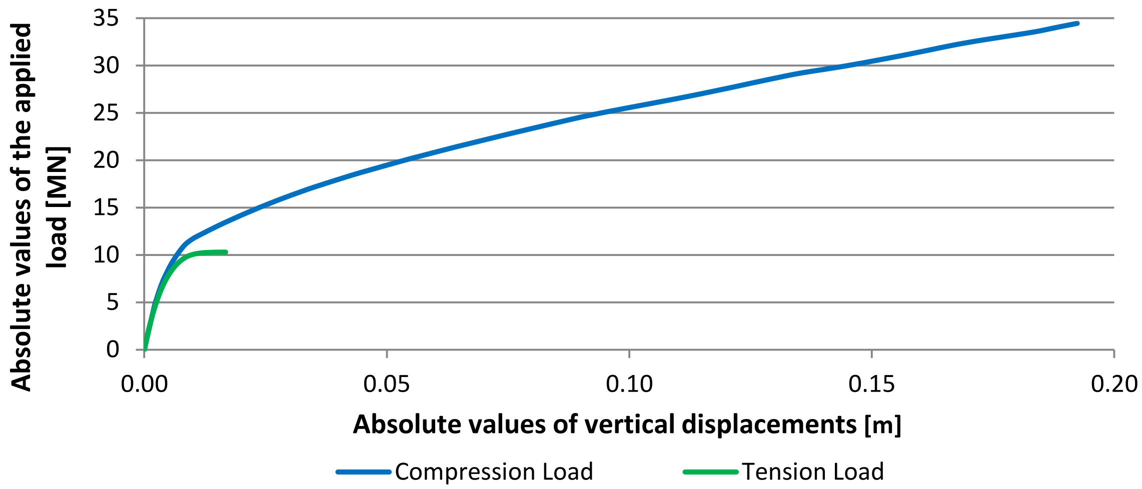

Figure 5.13. – Load-displacement curve for both compression and tension tests

5.2.4.3. Prescribed Displacement

Finally, as it was expected, there is no difference between applying a load or a prescribed displacement. This can be observed by the load-displacement curves of both cases as illustrated in Figure 5.14. Both of the curves match perfectly. When performing this model it should be taken care to apply the load and the prescribed displacement on the pile head in order not to modify the imposed boundary conditions.

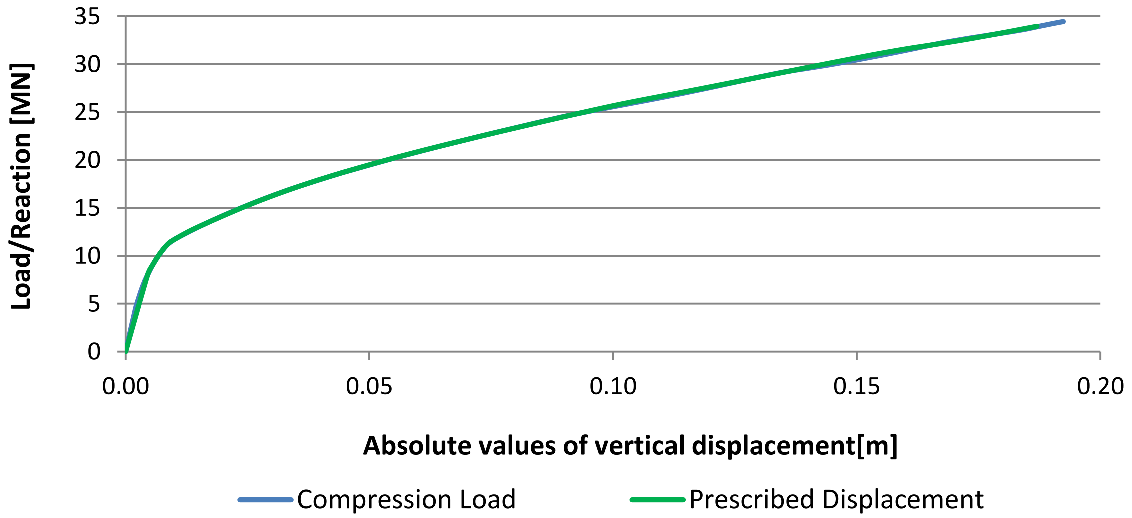

Figure 5.14. – Load-displacement curve for both compression load and prescribed displacement experiment

5.2.4.4. Surrounding Soil

The soil surrounding the pile was also subjected to study. It is easy to physically understand that the vertical displacements of the soil decrease when increasing the distance from the pile. Thus, the soil near the pile supports the higher percentage of the load. These conclusions are obtained analysing the vertical displacement of the soil along a horizontal section. The results regarding this topic are presented in Figure 5.15.

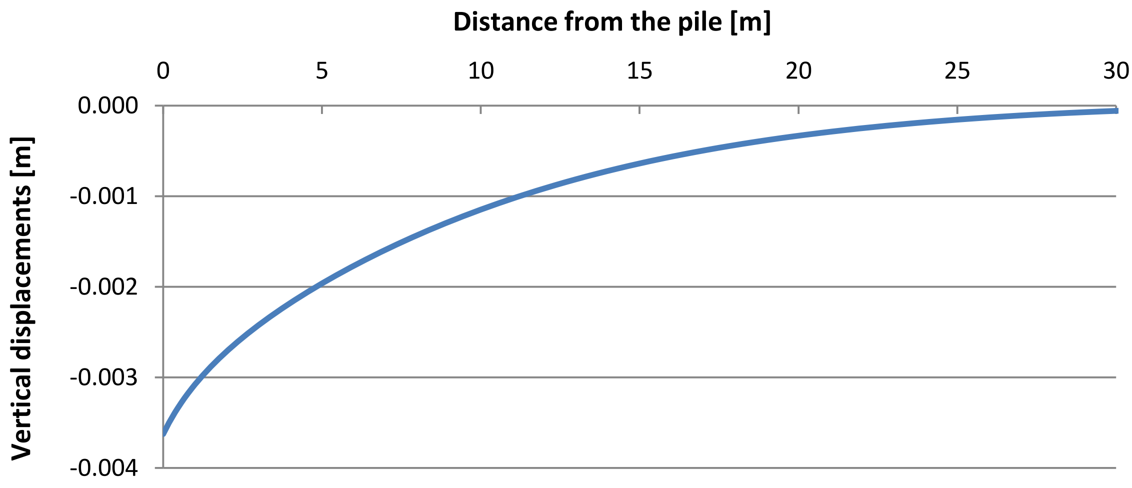

Figure 5.15. – Soil vertical displacements for a depth equal to 14.0 m

Finally, Figure 5.16 plot the volumetric strains against to the shear stress and the s’-t graphs is presented in Figure 5.17. Both these graphs display the behaviour during loading of three points with the 20 m depth and close to the pile shaft. The distance of the points from the pile is as following:

- Point A – 1 cm far from the pile;
- Point B – 25 cm from the pile;
- Point C – 50 cm from the pile.

By the analyses of these figures, it can be concluded that all the three points provide a similar behaviour during loading. When looking at Figure 5.16, some negative volumetric strains and later on some positive volumetric strains are observed in the first place. As the soil dilatancy parameter was set at zero, the variations of the volumetric strains may cause some strangeness. In general, the volumetric strains can be generated due to:

- Changes in mean effective stresses;
- Dilatancy effects caused by shear stress.

Since the dilatancy of the soil model is zero, the volumetric strains are caused by the changes in the mean effective stress. Thus, when looking at Figure 5.17, the observed volumetric strains agree with the changes in mean principal effective stress (s') for the same stress point.

The changes in the mean effective stress can be explained by the analysis of how the load is transferred to the soil. In the first stage the pile is loaded and it transfers this load to the soil. Thus, the mean effective stress increases in the soil around the pile. However, after a certain loading the interface becomes plastic at the level of the observed stress points. Hence, it does not further increase locally. At that moment, another effect becomes relevant which is the soil deformation caused by the load transfer to the pile tip (since the shaft is becoming almost fully plastic). This deformation causes unloading in the soil reducing again the s' value.

Since the volumetric strain changes occur due to the mean effective stress variation, the shape of the curve should be compared with the results given by the triaxial test present in Figure 5.6. However, PLAXIS results do not achieve any critical state as it would be expectable. No explanation was found for the occurrence of volumetric strains variation.

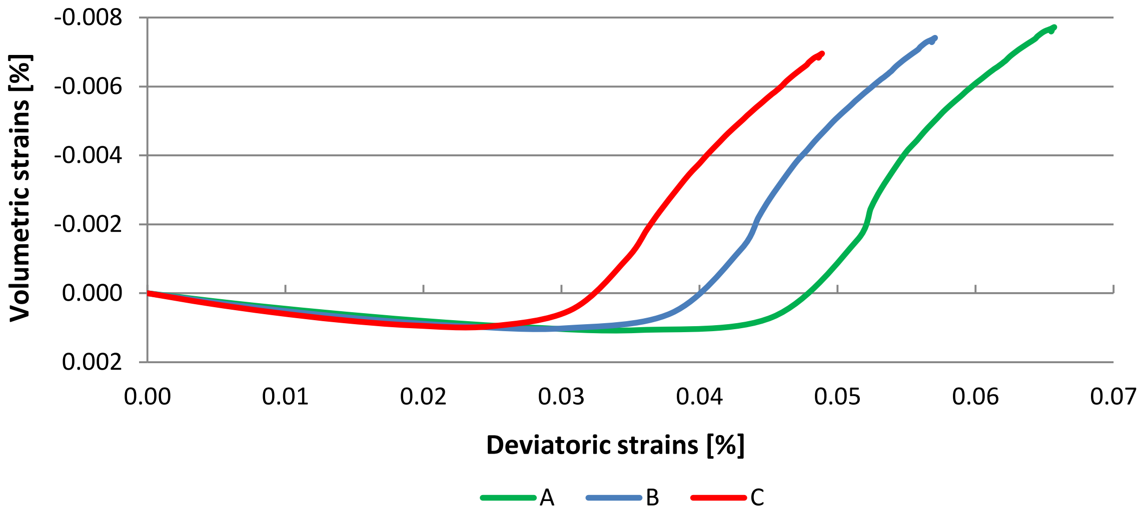

Figure 5.16. – Volumetric Strains variation with the deviatoric strains

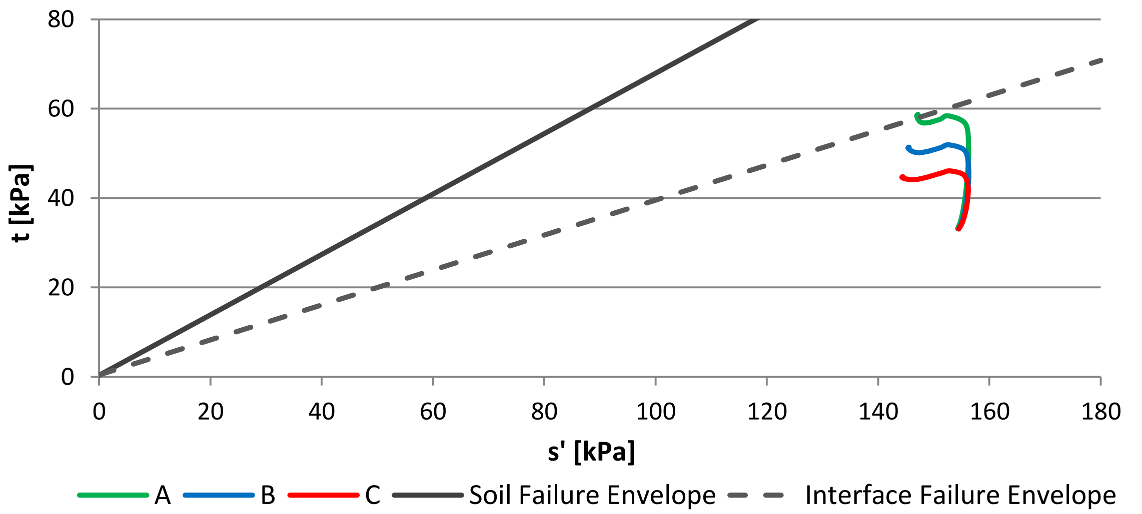

Figure 5.17. – s' – t graph

6
DYNAMIC MODEL – GENERAL ANALYSIS

I

6.1. Overview

Once having built a robust static model, a dynamic analysis was performed. Initially, general analyses about dynamic numerical modelling were performed. This is an important step as it provides important knowledge and confidence for the final dynamic model.

Therefore, first it is presented a theoretical background about dynamic investigations. Afterwards several studies are carried out regarding the following subjects:

- Mesh refinement;
- Viscous boundaries;
- Damping;
- Wave equation analysis.

6.2. Theoretical Background

6.2.1. Dynamic Problem Formulation

The PLAXIS (2014c) provides a general description about PLAXIS dynamic models. Faria (1994), Chopra (1995) and Kramer (1996) offer a more detailed description about dynamic problems. The basic relation for the time-dependent movement of a volume under the influence of a dynamic load is given by Equation 6.1, where M is the mass matrix, C is the damping matrix and K is the stiffness matrix. Still, vectors u_t, $\dot{u}_t$, $\ddot{u}_t$ represent, respectively, the displacement, the velocity and the acceleration in a given instant. The vector F_t corresponds to the system excitation at that time, *t*.

$$[M]\ddot{u}_t + [C]\dot{u}_t + [K]u_t = F_t \tag{6.1.}$$

In a static analysis the acceleration and the velocity vectors of Equation 6.1 are equal to zero. Hence, in comparison with a static model, in a dynamic problem the mass structure assumes a singular relevance. In particular, in geotechnical models special attention should be given to the definition of the phreatic level and to the selection of the soil unit weights.

6.2.2. Time Integration

The solution of Equation 6.1 provides the determination of the vector u_t for a given initial condition: $\dot{u}_0$ and u_0. The analytical solution of the motion equation is usually not possible due to the variation of the excitation along the time. Such a problem is solved by numerical time stepping integration methods. These methods are based on a time discretization procedure. Thus, some moments, t_i, separated by a time interval of Δt are selected. The differential equation is then solved for these moments, t_i, making sure that the equilibrium conditions are satisfied.

Explicit and implicit time integration methods are the two of most commonly used approaches. Although explicit integration schemes are simple to formulate, the calculation process is not as robust as the implicit methods and they impose some limitations regarding the time step. On the other hand, implicit integration is more complex. However, by implicit schemes it is possible to obtain unconditionally stable algorithms, in which Δt is only defined by accurate reasons and not by stable issues. Thus, implicit integration provides a more stable calculation process, more accurate solutions and lower calculation times.

Due to the above considerations, the Newmark implicit method is one of the mostly accepted time integration methods. It is also the time integration scheme that is implemented in the PLAXIS code. In the scope of the Newmark method, the displacement and the velocity of one point at a moment t+Δt are expressed by Equation 6.2 and Equation 6.3, respectively.

$$u_{t+\Delta t} = u_t + \dot{u}.\Delta t + \left(\left(\frac{1}{2} - \alpha\right).\ddot{u}_t + \alpha.\ddot{u}_{t+\Delta t}\right).\Delta t^2 \tag{6.2.}$$

$$\dot{u}_{t+\Delta t} = \dot{u}_t + \left((1-\beta).\ddot{u}_t + \beta.\ddot{u}_{t+\Delta t}\right).\Delta t \tag{6.3.}$$

The parameters α and β determine the stability and the accuracy of the numerical time integration. The Newmark method is unconditionally stable for β ≥ 1/2. For β = 1/2 a second order accuracy solution is obtained. The Newmark parameters that offer the maximum efficiency regarding the stability and the accuracy are: β = 1/2 and α = 1/4.

The selection of the time step, Δt, used in the calculations raises some concerns. This time step is chosen to ensure that a wave during a single step does not travel a distance larger than the minimum dimension of an element. If the time step is too large, the solution will display significant deviations from the exact solution. The value of the time step depends on the maximum frequency and on the mesh size. PLAXIS controls this issue automatically.

6.2.3. Viscous Boundaries

In a dynamic model, the boundaries should be kept away from the point where the load is applied. Otherwise, spurious reflections can appear which leads to distortions in the results. However, it would require more elements and consequently, higher memory usage and calculation time. To avoid these problems, viscous boundaries are usually used to reduce the mesh box without affecting the accuracy of the results.

Viscous boundaries are computed by attaching dampers to the boundaries nodes. These elements ensure that an increase of the stress on the boundary is absorbed without reflections. The normal and shear stress components absorbed by the damper are formulated in Equation 6.4 and Equation 6.5.

$$\sigma_n = -C_1.\rho.V_p.\dot{u}_h \tag{6.4.}$$

$$\tau = -C_2.\rho.V_s.\dot{u}_v \tag{6.5.}$$

In the above equations, ρ is the density of the materials, V_p and V_s are the compression and shear wave velocities respectively and C_1 and C_2 are the relaxation coefficients.

6.2.4. Frequency Spectrum

The dynamic response of the structures is very sensitive to the frequency at which they are loaded. Thus, one of the most important topics to study in a dynamic analysis is the frequency content in which the tested structure is oscillating. The frequency content describes how the amplitude of a ground motion is distributed among different frequencies.

Frequency spectrums are often used to analyse how a structure oscillates. There are many types of spectra, such as, ground motion spectra, Fourier spectra, power spectra and response spectra. PLAXIS provides the power spectrum to describe the frequency content of a ground motion. It illustrates how the strength of a quantity varies with frequency. The power of a signal, *x(t)*, can be expressed as defined by Equation 6.6, where a_n and b_n are Fourier coefficients. The power signal can be applied to any type of signal (e.g. force, velocity, acceleration). In the present work it will generally be determined for the velocity signal of a point.

$$P(\omega_n) = \frac{1}{2}.(a_n^2 + b_n^2) \tag{6.6.}$$

6.2.5. Damping

The damping ratio parameter, ξ, is usually used as a measure of the damping. A critical damping situation is defined for ξ = 1. This condition corresponds to a case in which the system, under some initial conditions, returns to its initial position without oscillating. When ξ > 1, the system is overdamped and, once again, the system does not oscillate and returns to its initial position although in a lower rate. Most of the structures are underdamped, ξ < 1. In these cases, the system oscillates with progressive decreasing amplitude. Figure 6.1 shows how a structure responds in the three mentioned situations.

In a PLAXIS numerical simulation three types of damping can be modelled. Therefore, radiation (or geometrical) damping, material damping and numerical damping need to be taken into account when performing a dynamic analysis. These three types of damping will be explained in the following sections.

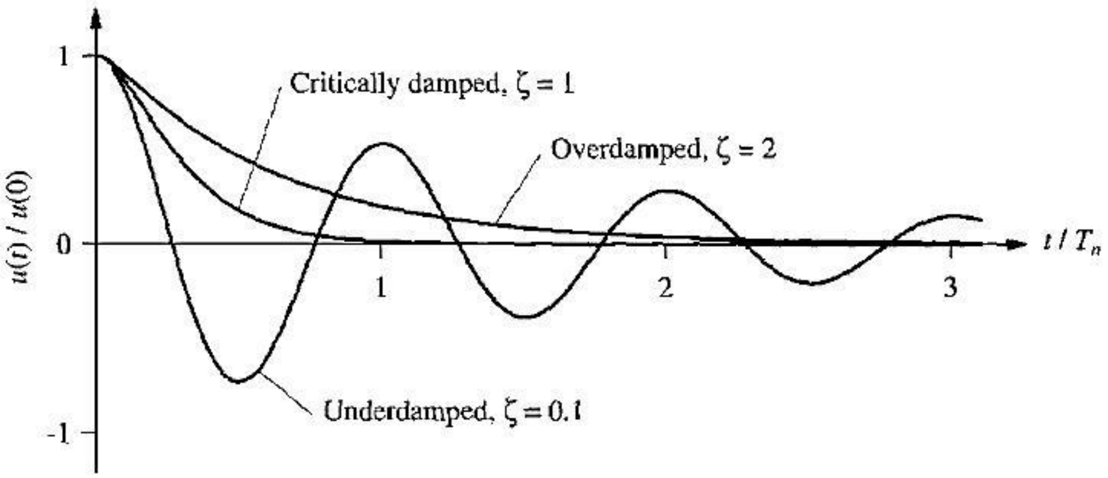

Figure 6.1. – Free vibration of critically damped, overdamped and underdamped systems, adapted from Chopra (1995)

6.2.5.1. Radiation damping

The amplitude of a stress wave decreases as the wave travels through the soil. One explanation for this behaviour can be the radiation damping. It results from the spreading of the wave energy over a larger volume of material as it travels away from the source. This feature is automatically represented by PLAXIS. Hence, in the region that is discretized, radiation damping happens in a natural way. However, when an infinite media is reproduced, artificial boundaries have to be placed to limit the mesh size. Viscous boundaries are therefore used to represent the radiation damping (wave propagations for the far field).

6.2.5.2. Material damping

Material damping also promotes the decrease of the amplitude with distance. It is represented by the matrix C that is included in Equation 6.1. Material damping is usually considered to take into account the energy dissipation that occurs in a structure due to material mechanisms. In reality, material damping is caused by viscous properties of the soil, friction between soil particles and the development of irreversible deformations.

In regions with large deformations (plastic behaviour), material damping is naturally considered by PLAXIS, However, when the soil is in the elastic range, material damping is caused in microscopic regions. Then, they cannot be captured by large scale models and, in particular, by PLAXIS numerical models. Rayleigh damping is therefore used to emulate all the damping phenomena that cannot be captured naturally by the numerical model.

The formulation proposed by Rayleigh is often used to express the material damping matrix, as presented in Equation 6.7. Thus, as established by the Rayleigh damping, matrix C is composed by a linear combination of the mass matrix, M, and of the stiffness matrix, K.

$$[C] = \alpha.[M] + \beta.[K] \tag{6.7.}$$

In the above equation, the parameter α determines the influence of the mass in the damping of the structure. As higher α is, the more the lower frequencies are damped. On the other hand, β defines the influence of the stiffness in the damping. The higher β is, the more the higher frequencies are damped.

Equation 6.8 establishes a relationship between the damping ratio, ξ, and the Rayleigh parameters. In this equation the parameter ω represents the angular frequency and the *f* denotes the frequency.

$$\alpha + \beta . \omega^2 = 2\omega f \tag{6.8.}$$

The Rayleigh parameters are calculated solving Equation 6.8 for two target frequencies and two damping values. Thus, α and β are obtained using Equation 6.9 and Equation 6.10, respectively. It is therefore possible to obtain a graph that shows the relation between the damping ratio and the frequency for two target frequencies and for the damping ratios previous established. Figure 6.2 illustrates one example of the considerations made for the following parameters:

- Target damping values: ω_1=5% and ω_2=5%;
- Target frequencies: f_1 = 10 Hz and f_2 = 80 Hz.

$$\alpha = 2\omega_1\omega_2 \frac{\omega_1\xi_2 - \omega_2\xi_1}{\omega_1^2 - \omega_2^2} \tag{6.9.}$$

$$\beta = 2 \frac{\omega_1\xi_1 - \omega_2\xi_2}{\omega_1^2 - \omega_2^2} \tag{6.10.}$$

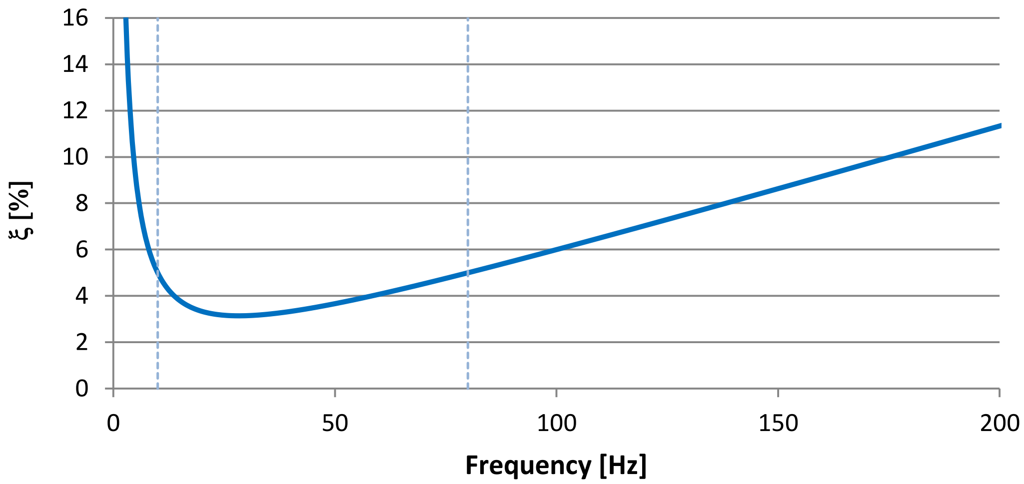

Figure 6.2. - Rayleigh damping

6.2.5.3. Numerical damping

Finally, the numerical damping will be commented. Usually, the response of a structure submitted to a dynamic load is mainly conditioned by the oscillation modes in the range of the lower frequencies. The direct integration of the equilibrium equations originates the appearance of high frequency modes overlapped with the main solution, so called numerical noise.

As implicit integration methods try to provide accurate results of the first vibration modes, the high frequency modes should be interpreted as spurious reflections. Thus, it is advantageous to include some numerical damping in order to dissipate the high frequency oscillations. Despite that, numerical damping should only be added if the accuracy of the results is reduced.

According to the literature, in the Newmark implicit method, numerical damping is imposed in the model when the Newmark parameter, β, is larger than 1/2. The value of α is given by a condition that leads to the maximum dissipation of the high frequencies. Thus, Newmark parameters β and α can be obtained by Equation 6.11 and Equation 6.12, respectively.

$$\beta \geq \frac{1}{2} \tag{6.11.}$$

$$\alpha = \frac{1}{4}.\left(\frac{1}{2} + \beta\right)^2 \tag{6.12.}$$

6.2.6. NON-LINEARITY RESPONSE OF THE SOIL

From dynamic experimentations, it was found that most of the soils display a curvilinear stress-strain relationship, as illustrated in Figure 6.3 a). Seed and Idriss (1970) concluded that the shear modulus is expressed by the secant modulus determined by the extreme points on the hysteresis loop. The damping factor is proportional to the area inside the hysteresis loop. Both the shear modulus and the damping factor will depend on the magnitude of the strain for which the hysteresis loop was determined. Thus, both of these parameters must be determined as functions of the induced strain in a soil specimen or soil deposit. On a logarithmic scale, stiffness reduction curves exhibit a shape like the curve present in Figure 6.3 b). In wave propagation problems the soil often exhibits small strain strains levels, which corresponds to strains lower than 10^{-3}.

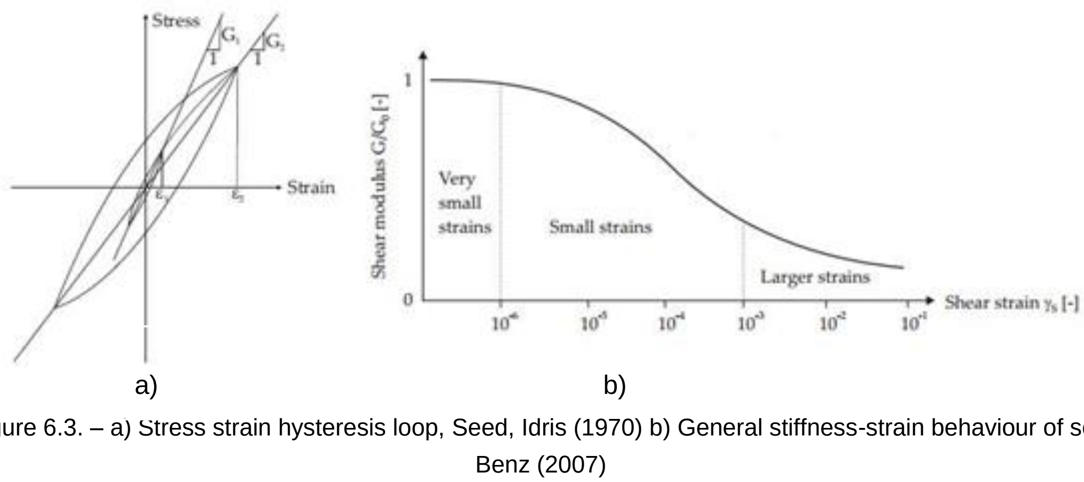

a) b)

Figure 6.3. – a) Stress strain hysteresis loop, Seed, Idris (1970) b) General stiffness-strain behaviour of soil, Benz (2007)

6.2.6.1. Soil Stiffness

Many investigations were carried out to better understand the non-linear behaviour of the soil. Benz (2007) described the small-strain stiffness as the stiffness of soils at small shear strains. The maximum soil stiffness found in stiffness reduction curves is usually mentioned as initial or maximum soil stiffness. The maximum Shear and Young's Modulus is represented as G_0 and E_0 respectively. These parameters are commonly associated to the range of very small strains. The relationship between the normal and the maximum shear modulus is exposed in Equation 6.13, where ρ is the soil density in kN/m^3 and V_s is the soil shear velocity. The normal shear modulus, *G*, can be obtained by Equation 6.14.

$$G_0 = \rho \times V_s^{\,2} \tag{6.13.}$$

$$G = \frac{E}{2.(1+\nu)} \tag{6.14.}$$

Seed *et al.* (1986) suggested some curves to determine the variation of Shear Modulus with shear strain. Figure 6.4 presents the variation of the Shear Modulus with shear strain for gravelly soils proposed in that study.

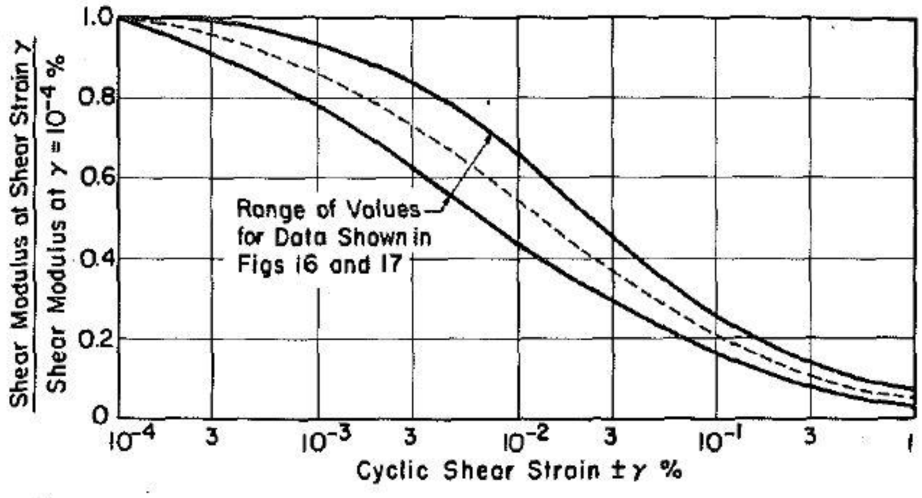

Figure 6.4. – Variation of Shear Modulus with Shear strain for gravely soils, Seed *et al.* (1986)

Amoroso *et al.* (2011) constructed the curves at different test sites in Western Australia based on the results of several *in situ* tests. In the developed study, it was performed a seismic dilatometer test (DMT/SDMT), a seismic cone penetration test (SCPT) and self-boring pressuremeter test (SBP) and laboratory triaxial tests. The G/G_0-γ curves displayed in Figure 6.5 were reconstructed by combining the information resulting from SCPT and SBP. This investigation was developed for silica sand and calcareous sand deposits located in Western Australia.

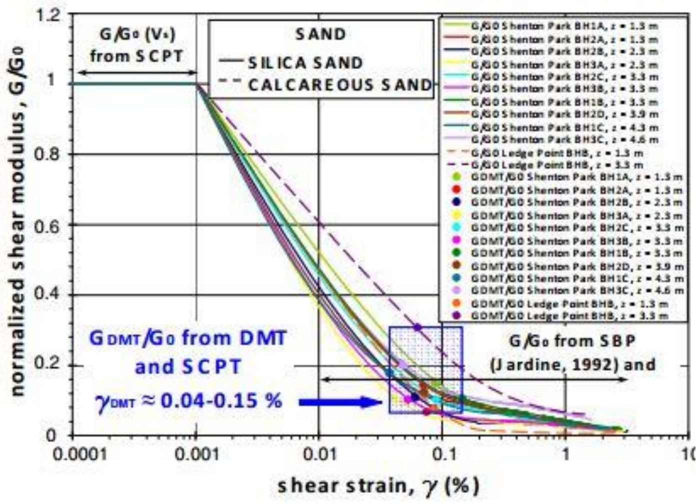

Figure 6.5. – Variation of Shear Modulus with Shear strain for silica sands and calcareous sands, Amoroso (2011)

6.2.6.2. Damping

The damping subject is a critical and controversial topic regarding numerical model simulations. In order to establish adequate values of damping in the numerical model, some literature was reviewed.

Seed *et al.* (1986) provided data concerning the damping ratio of sands and gravelly soils determined by laboratory and field tests. Although, the damping ratio depends of several factors such as, grain size, degree of saturation, void ratio, lateral earth pressure coefficient, friction angle, they concluded that the main factor affecting the damping ratio are the strain level induced in the sand and the confining pressure to which it is subjected. The influence of confining pressure is shown in Figure 6.6. It can be observed that the damping ratio decreases with the increase of the confined pressure. Figure 6.7 provides a relationship between the damping ratio and the shear strain for the studied sands.

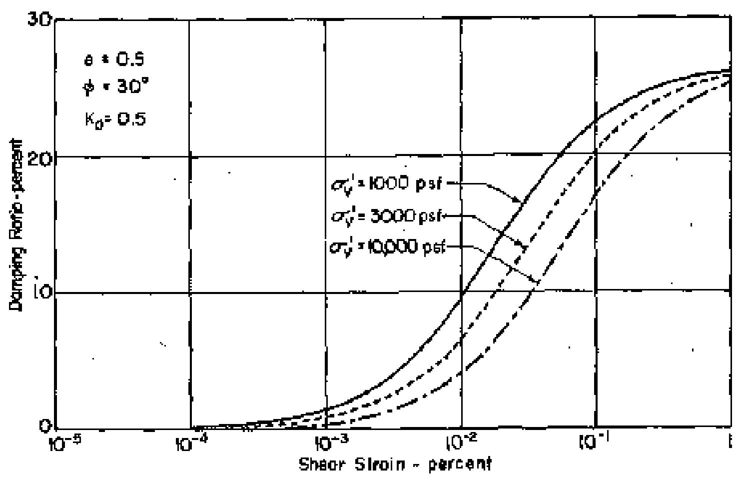

Figure 6.6. – Influence of confining pressure on damping ratio of saturated sand, Seed *et al.* (1986)

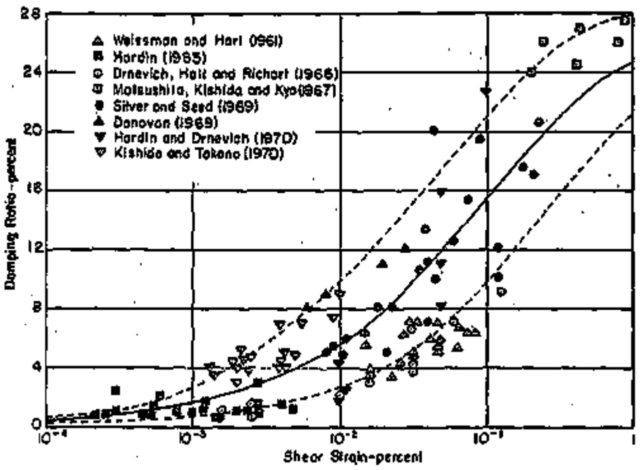

Figure 6.7. – Damping ratio for sands, Seed *et al.* (1986)

Kim and Lee (2000) investigated the propagation and attenuation characteristics of ground vibrations caused by train loading, blasting, friction pile driving and hydraulic hammer compaction. According with Kim and Lee, generally the attenuation of the vibrations is composed of two factors: radiation damping and material damping. The geometrical damping depends on the type and location of the vibration source and the material damping is related with ground properties and vibration amplitudes. Regarding the propagation and attenuation characteristics of friction pile driving, it was measured a damping ratio of the site equal to 5-6 %. The measurements were performed in a site composed by gravel fill, medium silty sand, clay and sand layers.

A highly instrumented centrifuge experiment was conducted by Elgamal *et al.* (2005) in order to investigate the seismic response of a saturated dense sand stratum. They also evaluated the influence of the confining pressure in soil damping. Thus, the studies were performed for different depths in order to evaluate this topic. It was concluded that, in general, the damping ratio decreases with the increase in depth (or confinement). Figure 6.8 exposes the identified damping and empirical relations for saturated dense sand in Nevada.

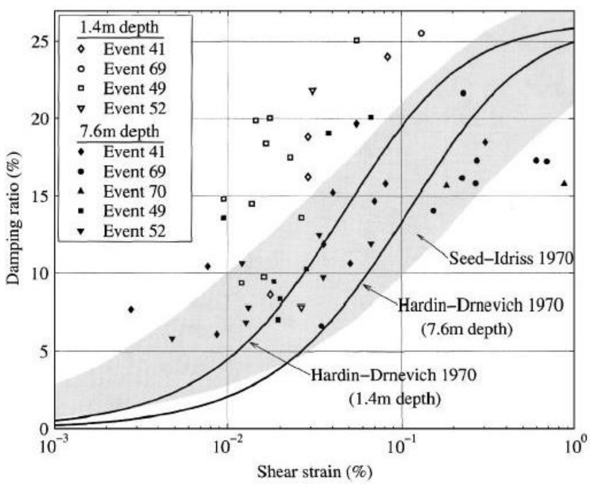

Figure 6.8. – Damping ratio and empirical relations for saturated dense Nevada sand, Elgamal *et al.* (2005)

6.3. Mesh and Damping Analysis

6.3.1. Mesh Refinement Analysis

A mesh analysis was conducted before advancing to the modelling of the complete axisymmetric dynamic model (soil and pile model). This is an important step as it allows understanding the influence of the mesh refinement in the accuracy of the results. The PLAXIS viscous boundaries are also evaluate during the calculations. The following analyses offer some confidence to the next calculations.

A study was carried out following the principles of the one performed by Lopes *et al.* (2013). In the revised study, a full space model is represented by a 2D plane strain model and excited by a Ricker pulse. Then, the vertical displacements of two given points are analysed and compared with the theoretical solution. The results clearly show a wave passing through both of the points and no spurious reflections are observed. Thus, it provides an important validation regarding the accuracy of the results.

Hence, a simple axisymmetric model was created. It was defined a linear-elastic model for the soil with the properties present in Table 6.1 and the water level was placed in the soil surface. At this point, to avoid any possible numerical instability due to a damping ratio equal to zero, it was considered 1% of Rayleigh damping. No numerical damping is included. The soil was then excited by a harmonic load, during 4 ms (half a period), with a frequency of 125 Hz and amplitude of 10 kN.

Table 6.1. – Soil properties

Properties	Units	Pile
Unit weight, γ'	kN/m^3	19.5
Young's Modulus, *E'*	MPa	23.3
Poisson's ratio, ν'	-	0.3

After the soil is loaded, four different mesh refinements were tested. The mesh box used is illustrated in Figure 6.9. The displacements, velocities and accelerations of five points along the soil surface were recorded. The coordinates (*x*,*z*) of the monitored points are:

- A (1.52 ; 0);
- B (3.00 ; 0);
- C (5.97 ; 0);
- D (11.98 ; 0);
- E (20.00 ; 0).

In order to assess the mesh refinement of each calculation, PLAXIS provides the parameter 'Average Element Size', I_e, which characterizes the mesh. This parameter is calculated as present in Equation 6.15. Here, the values x and y represent the outer geometry dimensions. In the studied case, x = 20 m and y = 10 m. The parameter n_c depends on the refinement level of the mesh. As lower is n_c, the more refined is the mesh. The mesh properties and calculations times of the four performed simulations are shown in Table 6.2.

$$I_e = \frac{n_c}{12}\sqrt{x.y} \tag{6.15.}$$

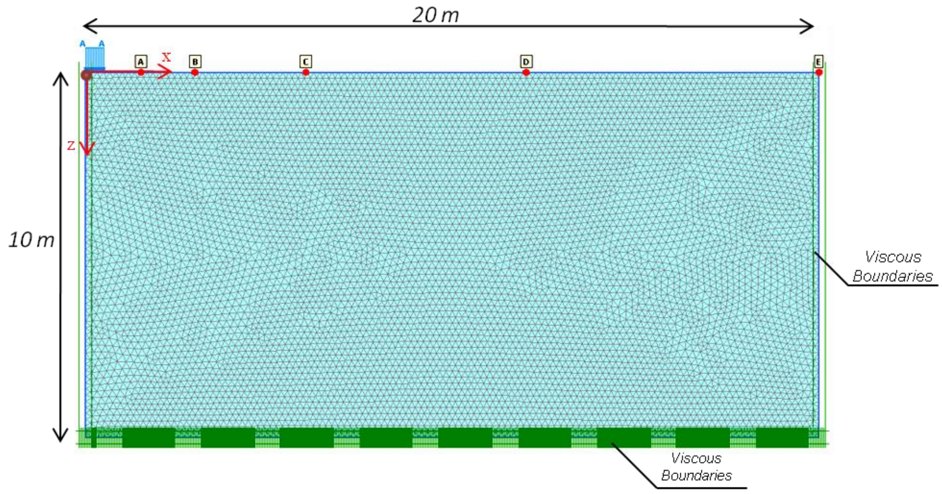

Figure 6.9. – Mesh box

Table 6.2. – Mesh and calculation properties

Mesh level	Average element size, I_e [m]	Number of elements	Approximate calculation time	Approximate memory used [Gb]
Coarse	0.1752	6518	1h	1.0
Medium coarse	0.1206	13746	1h 30min	2.5
Medium fine	0.08773	25983	4h	6.0
Fine	0.05934	56793	7h	16.5

In order to evaluate the accuracy of the results, the monitored points were studied. Special focus was given to the assessment of the accelerations along the time because, as Faria (1994) mentioned, these are more sensible to any numerical instability than the displacements evaluation. It is simple to understand this point. Actually, the accelerations are the displacements second order derivative over the time. Thus, any variation or any instability detected in the displacements, appears in the acceleration results in a much larger scale. Hence, the acceleration results for the four cases studied are presented in Figure 6.10, Figure 6.11, Figure 6.12, Figure 6.13.

From the presented results it is realized that the accuracy of the results is clearly influenced by the elements size. However, it is important to remember that no numerical damping is considered in the executed analyses and low values of Rayleigh damping were established for the soil. It is also interesting to verify that, for the applied load, no response is measured in points D and E.

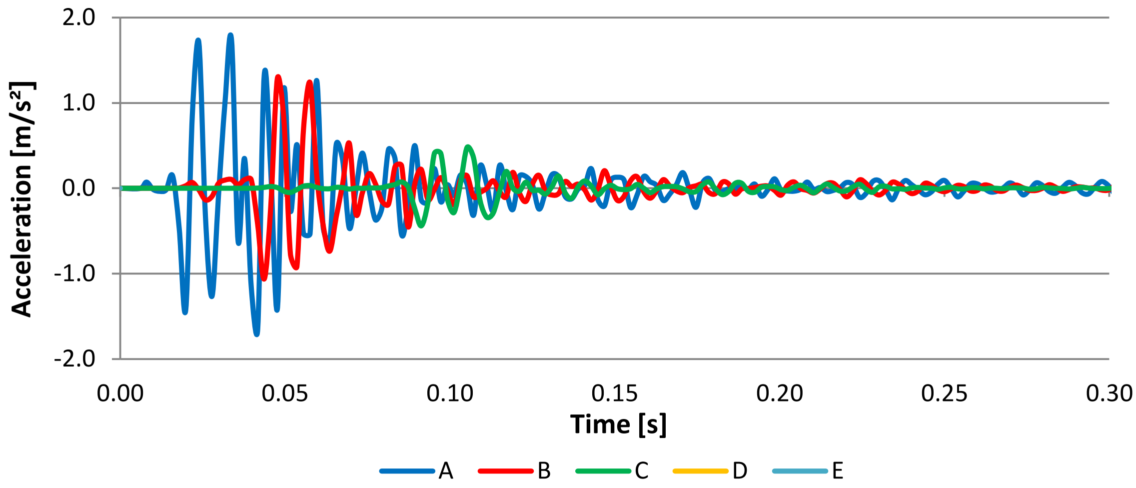

Figure 6.10. – Acceleration recorded on the five monitored points along time: coarse mesh

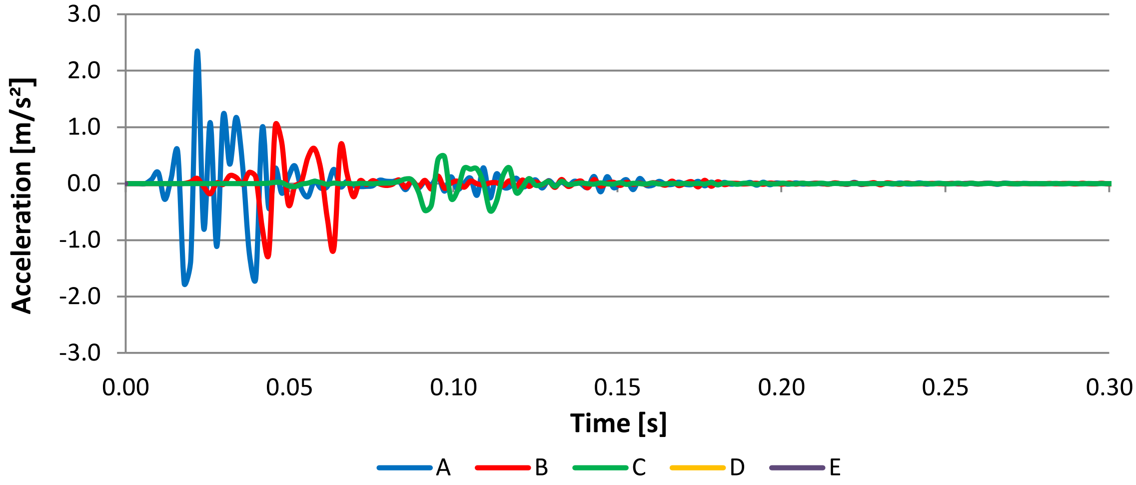

Figure 6.11. - Acceleration recorded on the five monitored points along time: medium coarse mesh

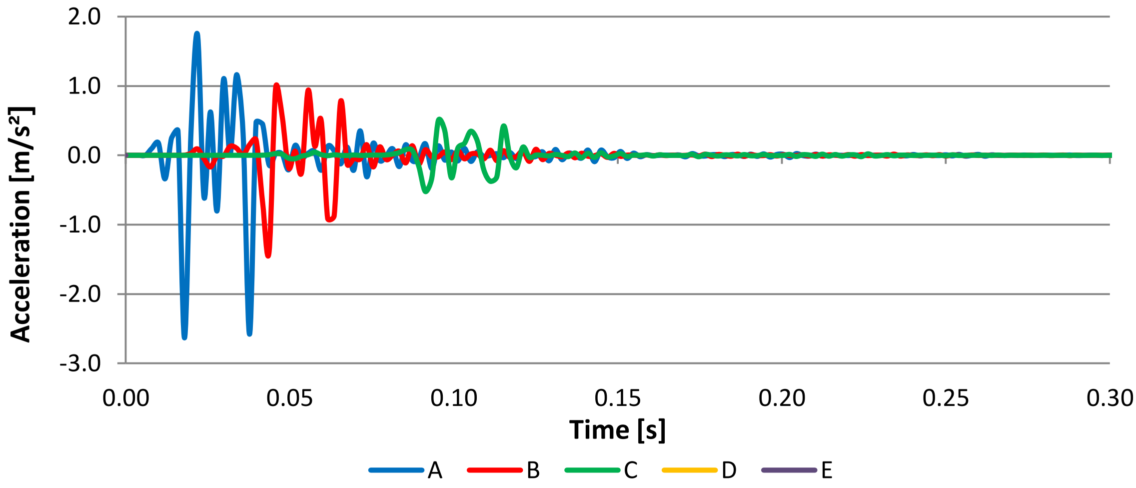

Figure 6.12. - Acceleration recorded on the five monitored points along time: medium fine mesh

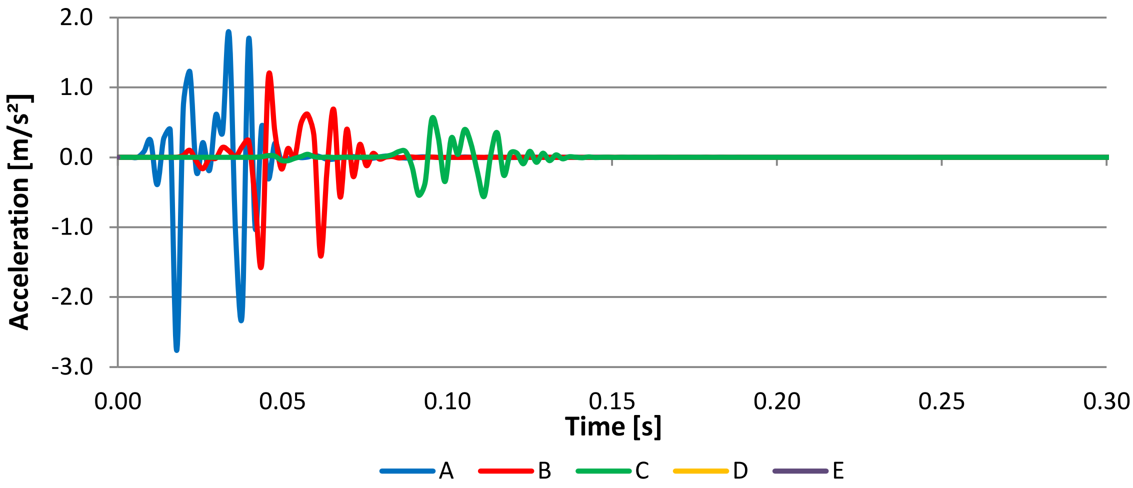

Figure 6.13. - Acceleration recorded on the five monitored points along time: fine mesh

6.3.2. Damping Analysis

6.3.2.1. No Damping Considered

Considering the exposed results in the mesh refinement analysis, and because at this initial phase of modelling the calculation time is an important aspect to take into account, it was started to model the soil with the first proposed mesh level. It was expectable that the introduction of more damping in the soil would then lead to a more stable model.

It was started to model the soil with the same mesh box shown in Figure 6.9 and the mesh mentioned as ‘Coarse Mesh’ at that point. No damping was introduced in the first analyses, nor material, neither numerical (β = 1/2; α = 1/4). Only radiation damping is considered as it is automatically assumed by PLAXIS. Viscous boundaries were placed on the right and bottom mesh boundaries. The same five points are monitored in the following analyses.

The obtained results are shown in Figure 6.14, Figure 6.15, Figure 6.16 and Figure 6.17. For the five studied points, these figures provide the vertical displacements, velocities, accelerations and a frequency spectrum representation. As it was expected, the results are really instable given that no damping was considered. High frequency vibration can be observed due to the absence of numerical filtering. It is also confirmed the presence of more numerical noise in the acceleration plot compared with the displacements graph.

Despite the low accuracy of the results, it was also analysed the power spectrum of the velocity of the defined points. Although the spectrum is not clear, it is possible to conclude that the soil responds with a large range of frequencies. Another aspect to take into attention is that the soil does not oscillate with the load frequency but with its natural frequencies. This occurs due to the short signal time during which the load is applied. It is possible to conclude that the soil is induced to a free oscillation motion. This point is consistent with the considerations mentioned in Section 6.2.5. Further analyses about this topic are provided in Section 6.3.3.

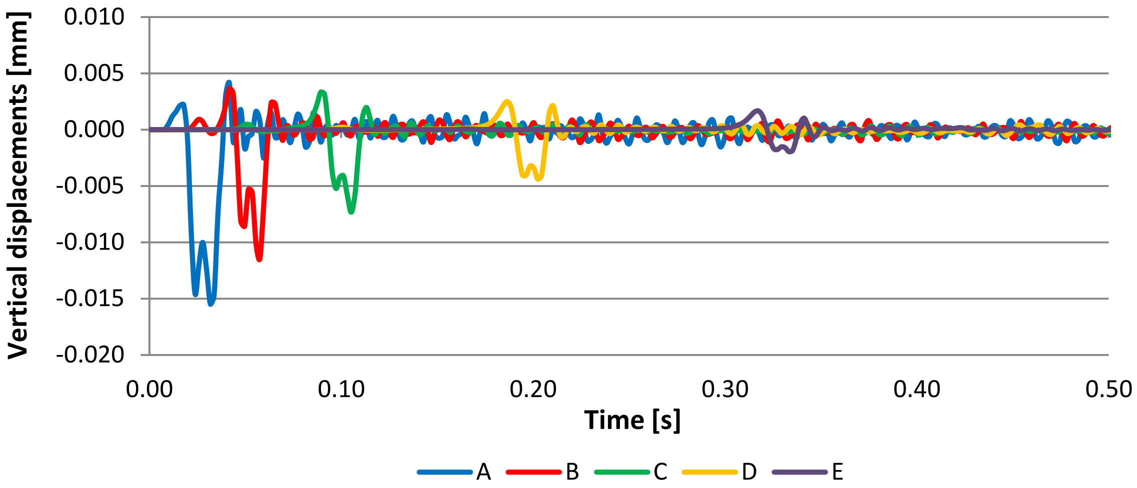

Figure 6.14. – Displacements recorded on the five monitored points along time: radiation damping

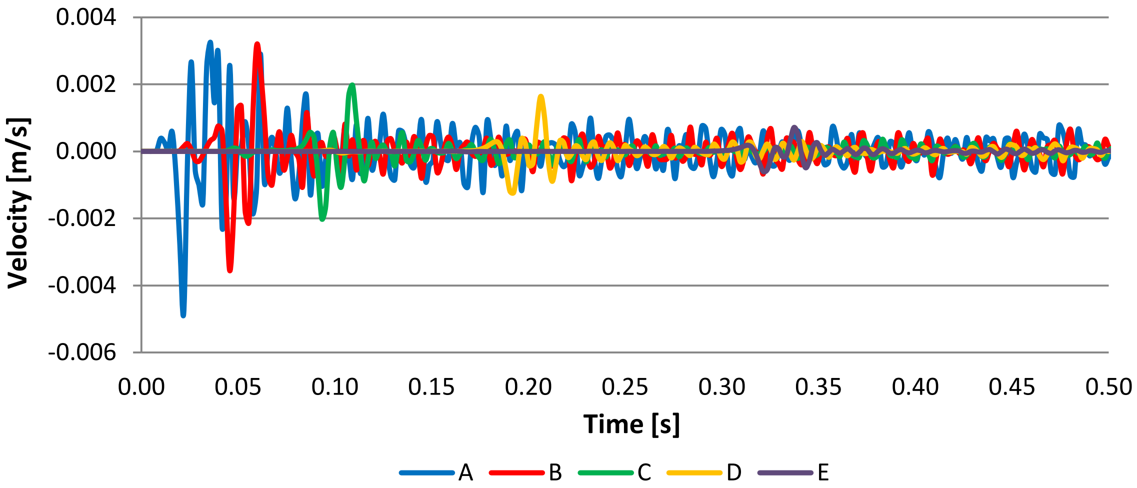

Figure 6.15. – Velocity recorded on the five monitored points along time: radiation damping considered

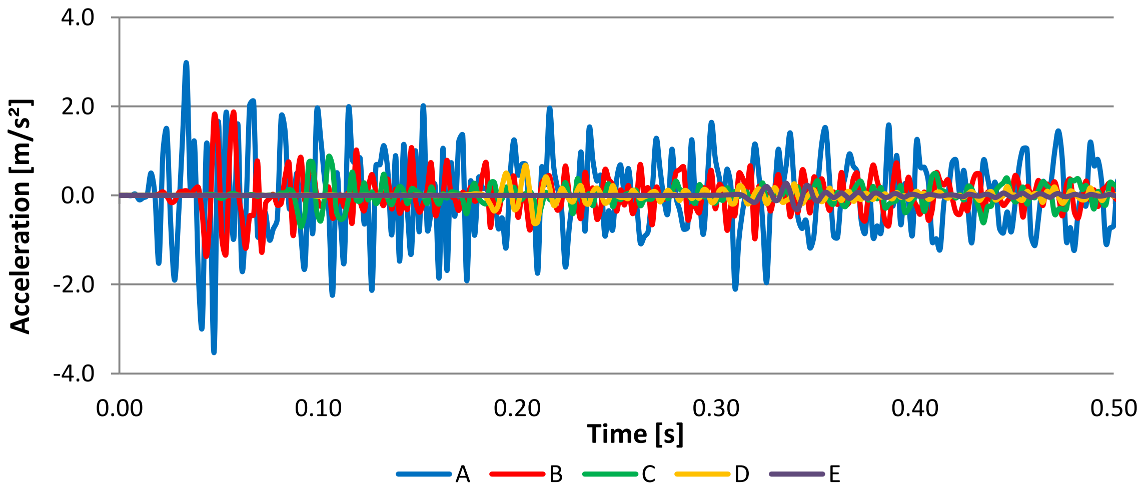

Figure 6.16. – Acceleration recorded on the five monitored points along time: radiation damping considered

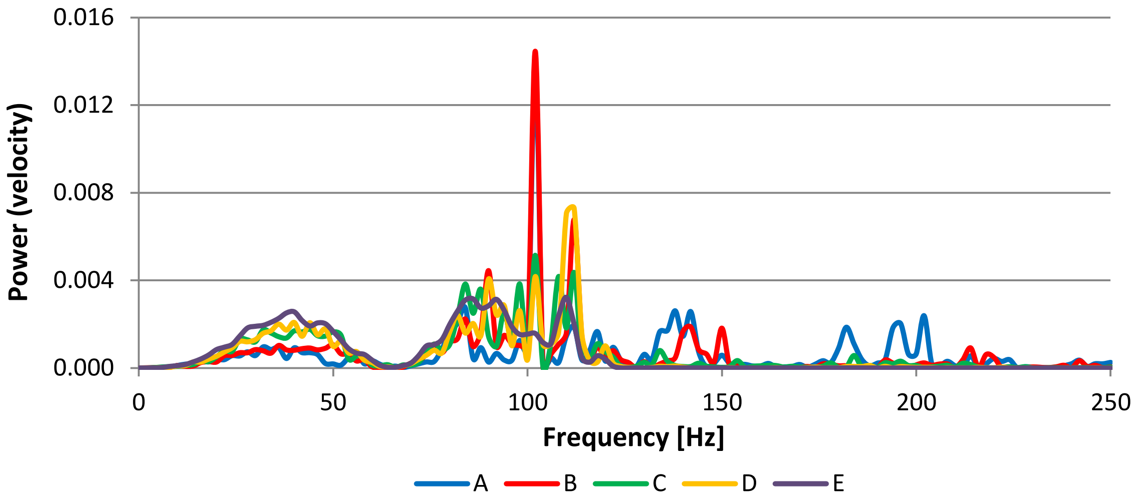

Figure 6.17. – Power spectrum of the five monitored points: radiation damping considered

6.3.2.2. Numerical Damping

In order to reduce the high frequencies observed in the previous results, some numerical damping was introduced in the model. Numerical noise is related with the time and space discretization. Hence, the time integration parameters were modified following the principles exposed in Section 6.2.2. It was used Newmark parameters, β and α, of 0.6 and 0.3025 respectively. The results are presented in Figure 6.18, Figure 6.19, Figure 6.20 and Figure 6.21 and they are now much more stable and the high frequency vibrations were reduced significantly due to the included numerical damping.

Analysing the results, it can also be observed the generated wave passing through all the monitored points. No spurious reflections appear then, which is an indication that viscous boundaries programmed by PLAXIS work well.

Regarding the soil frequency vibrations, by the frequency spectrum it is concluded that the frequency content of ground vibrations reduces as the distance from the pile is increased. Such behaviour is expected due to the soil damping. This point was previously mentioned by Masoumi and Degrande (2008) when investigating the field vibrations due to pile driving.

The power spectrum also provides important information in order to establish adequate target frequencies for Rayleigh damping inclusion. The frequency content is sensible in a range between 10 Hz and 200 Hz. This topic is discussed in detail in Section 6.3.2.3.´

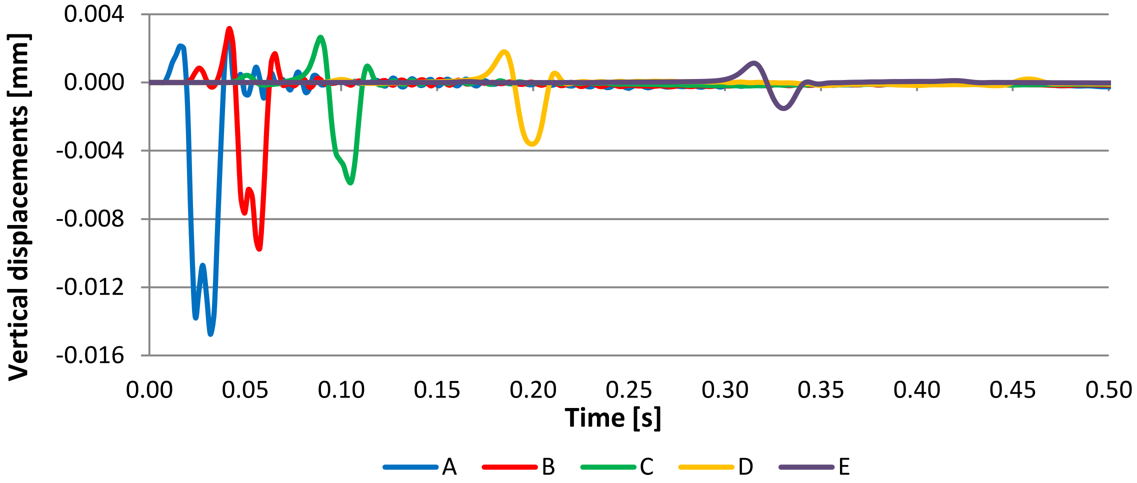

Figure 6.18. – Displacements recorded on the five monitored points along time: numerical damping

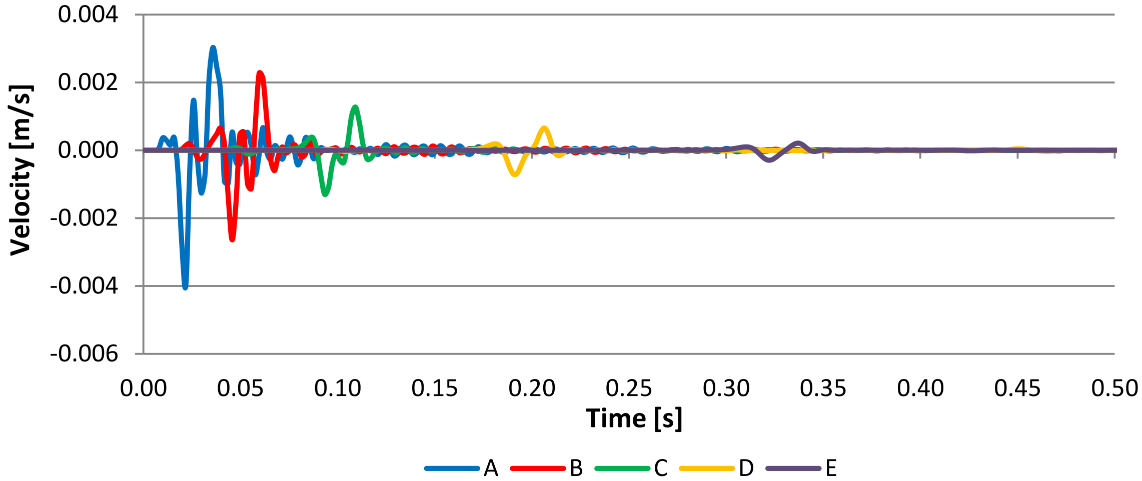

Figure 6.19. – Velocity recorded on the five monitored points along time: numerical damping

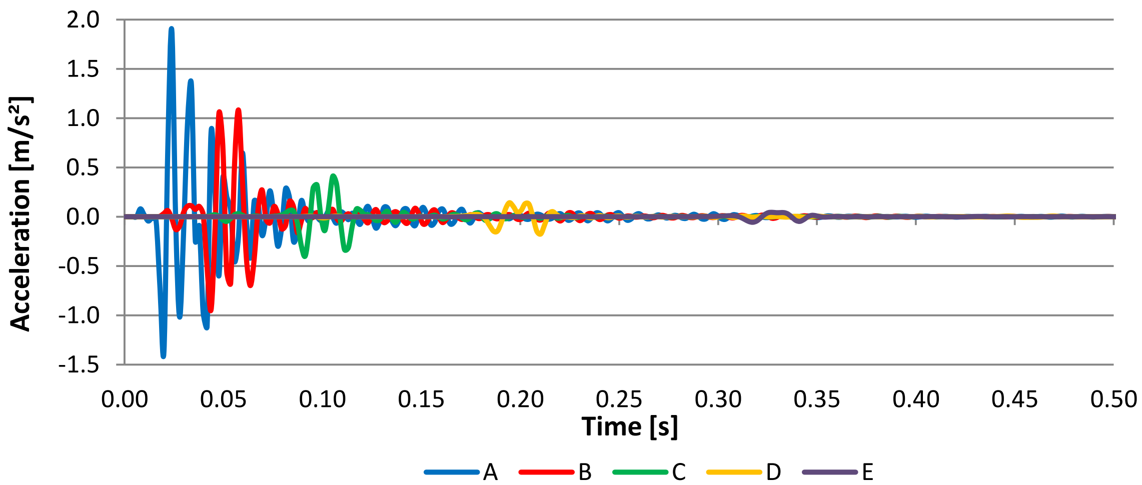

Figure 6.20. – Accelerations recorded on the five monitored points along time: numerical damping

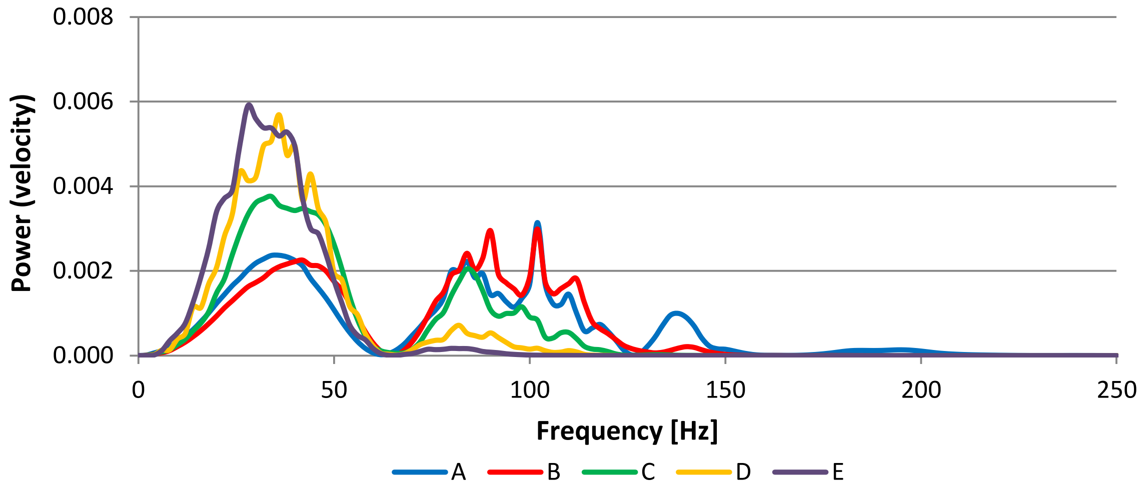

Figure 6.21. – Power spectrum of the five monitored points: numerical damping

6.3.2.3. Material Damping

Material damping tries to replicate all the damping that is not considered naturally by PLAXIS. It is important to notice that all the analyses performed so far considered a simple linear-elastic soil model. Thus, no material damping was considered in the previous calculations, neither Rayleigh damping, nor damping due to irreversible deformations.

The literature reviewed in Section 6.2.6.2 was the basis for an adequate establishment of soil damping values. Due to the non-linearity of the soil response, dynamic problems usually present small level of shear strains, generally lower than 10^{-3} (Figure 6.3 b)). Thus, according with the researches completed, the damping ratios in the soil can be about 3%.

Taking into account the last considerations, at this stage the Rayleigh damping values, ξ_1 and ξ_2, were set at 5% for target frequencies of f_1 = 10 Hz and f_2 = 200 Hz. These values lead to the Rayleigh parameters of α = 5.98 and β = 7.68E-5. Fig, 6.22 shows the relationship between the damping and the frequency for these Rayleigh damping parameters. The results of these calculations are presented in Figure 6.23, Figure 6.24, Figure 6.25 and Figure 6.26.

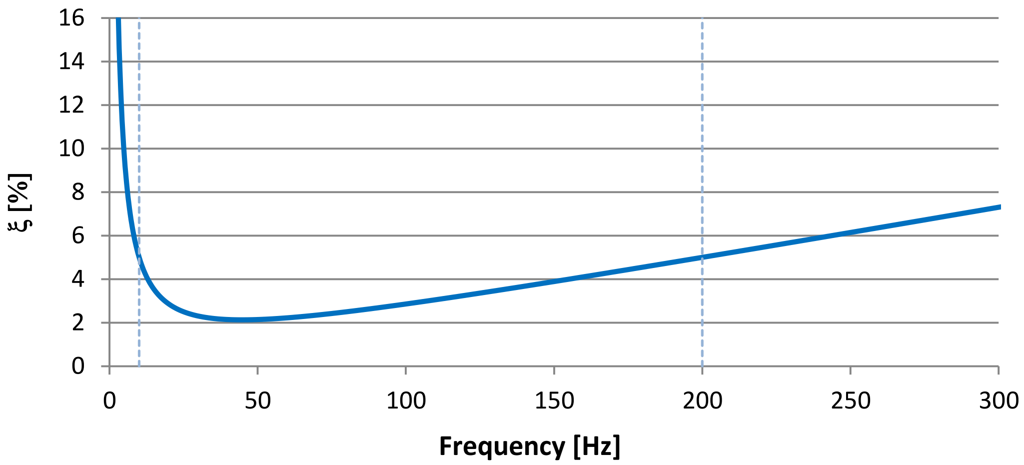

Figure 6.22. – Rayleigh damping

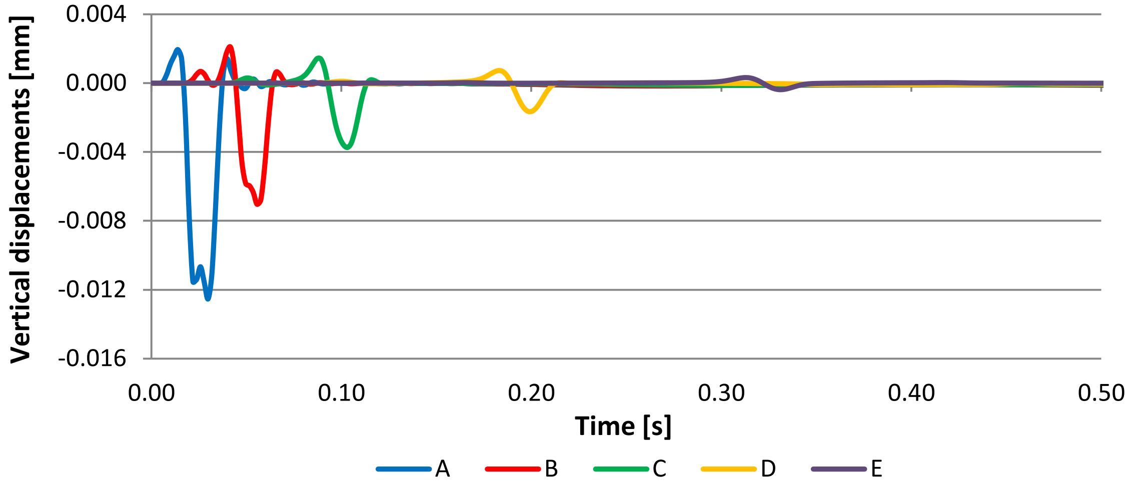

Figure 6.23. – Displacements recorded on the five monitored points along time: Rayleigh damping

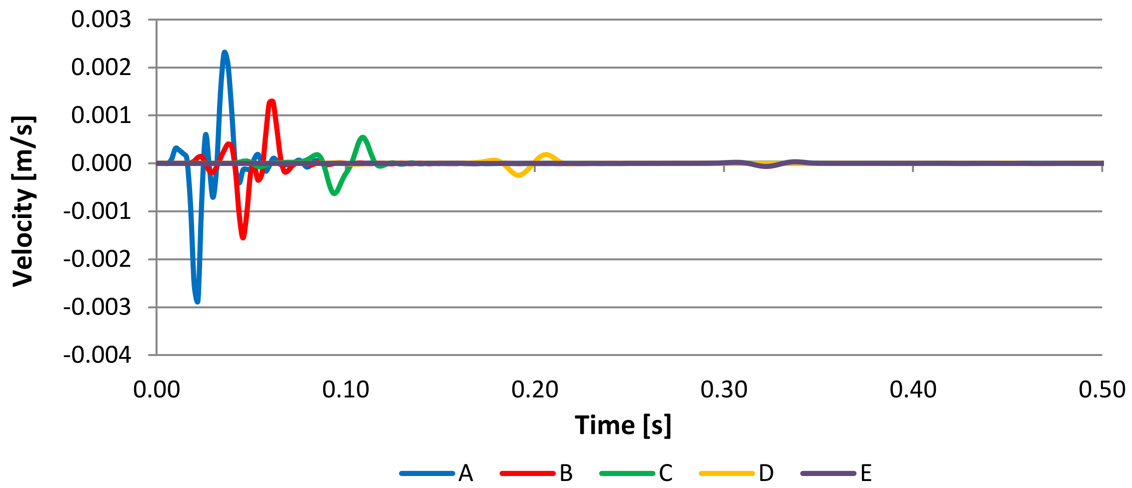

Figure 6.24. – Velocity recorded on the five monitored points along time: Rayleigh damping

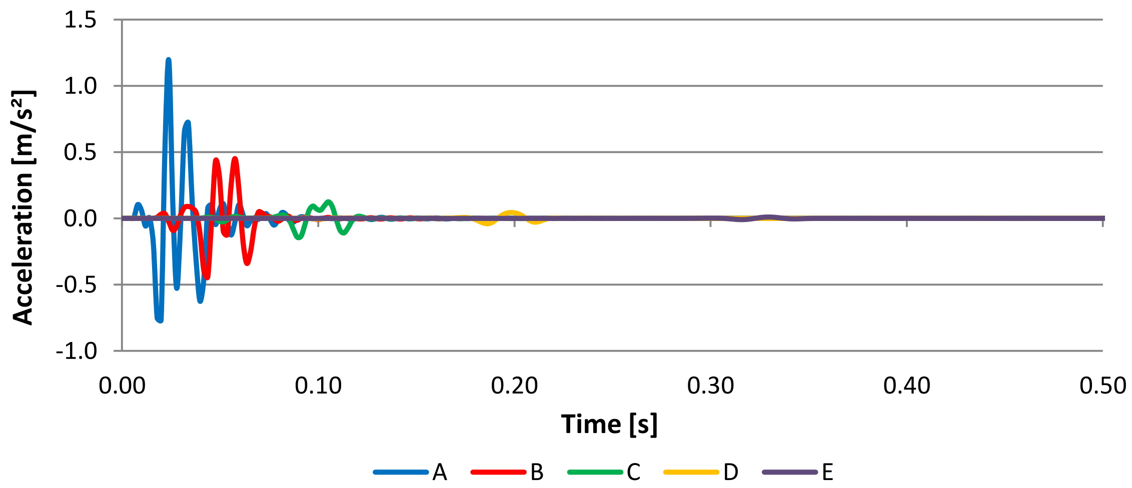

Figure 6.25. – Accelerations recorded on the five monitored points along time: Rayleigh damping

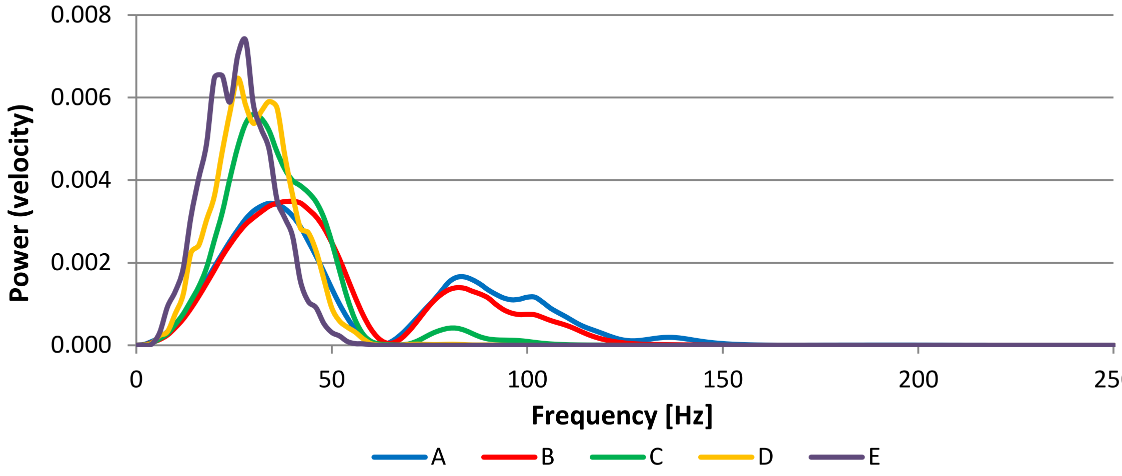

Figure 6.26. – Power spectrum of the five monitored points: Rayleigh damping

6.3.3. Free oscillation vs Forced Oscillation

The vibration frequency of a structure primarily depends on the mode it oscillates. When a signal is applied to a structure during a long period of time, it starts to accompany the frequency of the imposed load. Thus, this motion is usually called as forced oscillation. At the moment that the force is released, the structure starts to oscillate freely. At this phase the structure vibrates at its natural frequencies which depend on the mass and the stiffness matrices of the structure.

As the signal duration tends to zero, the structure is only induced to some initial conditions set for the velocity and displacement. Therefore, it starts immediately in a free oscillation motion. In this case, the frequency content of the structure only depends on its mass and stiffness matrices.

In order to confirm the previous considerations, the same model was tested with the same harmonic load frequency and amplitude but for two different durations, as shown in Figure 6.27. Load case 1 replicates a load with a short signal duration. On the other hand, the application of the second load case aims at inducing the structure to a forced oscillation mode.

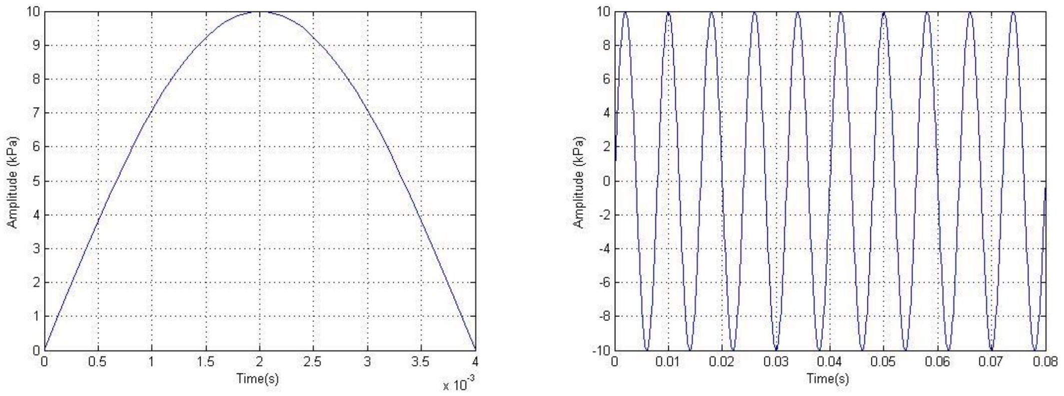

Figure 6.27. – Load case 1 (left); Load case 2 (right)

The frequency spectrum of the first studied case (Load case 1) for the five monitored points is illustrated in Figure 6.28. Analysing the first situation, it is clearly that the soil is responding with its natural frequencies. This corresponds to a free oscillation mode in which the natural frequencies of the soil are established by the soil stiffness and the mass. In fact, this figure is equal to Figure6.26 because the calculated model is the same. The response to Load case 2 is illustrated in Figure 6.29. It can be observed a frequency peak of about 125 Hz in points A and B, equal to the load frequency. The soil is therefore in a forced oscillation motion. However, due to material damping, as the distance to the load increases the soil appears to be responding in a freely oscillation mode.

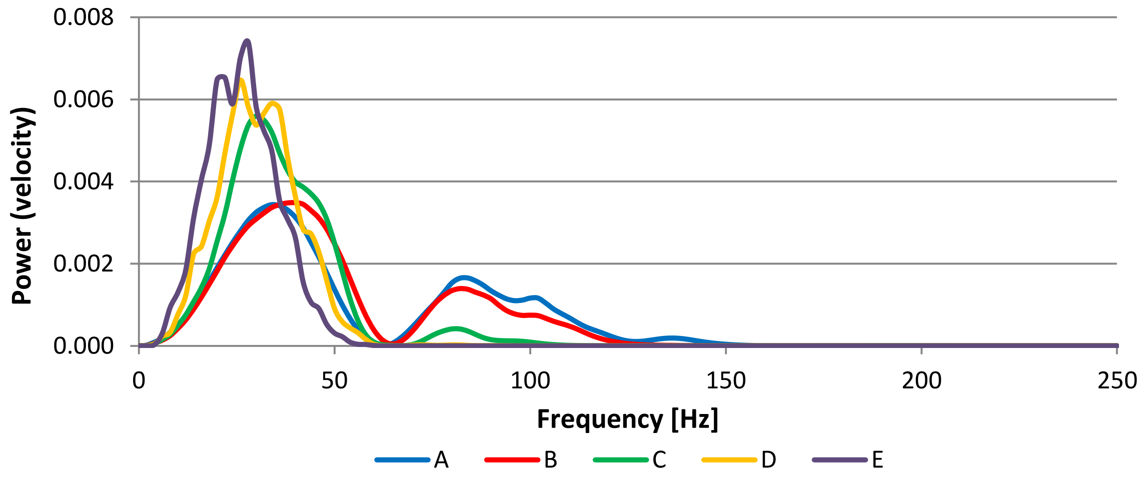

Figure 6.28. – Power spectrum of the five monitored points: Load case 1

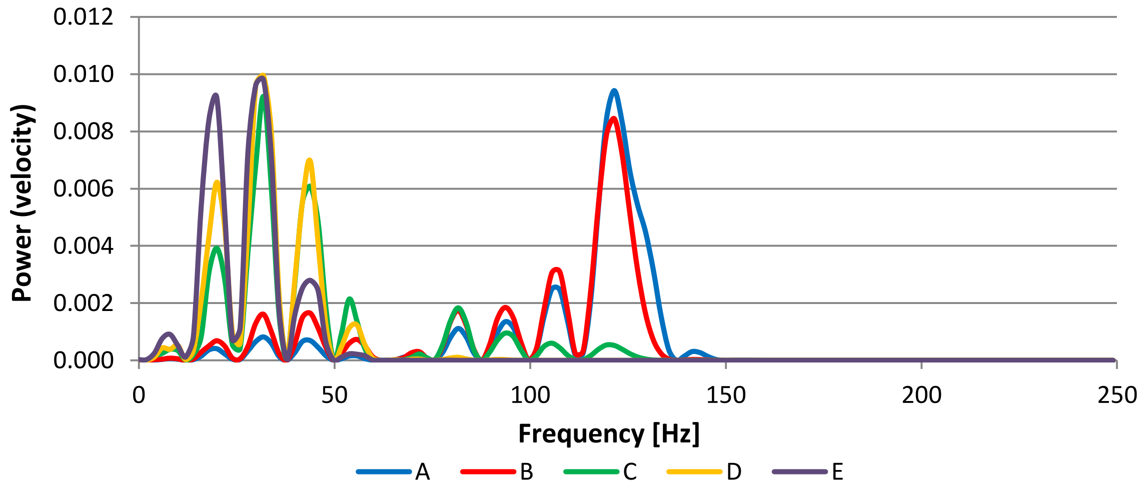

Figure 6.29. – Power spectrum of the five monitored points: Load case 2

6.4. Wave Equation Model

This intermediate step aims at comparing the results acquired from PLAXIS with the fundaments of wave equation analysis presented in Section 4.4.3. It was therefore analysed a model with only one pile and the soil layers were deactivated. Thus, no soil resistance is considered. The pile is also fixed at the bottom and free at the pile head. An illustration of this model is shown in Figure 6.30. Considering the previous simplifications, the principles of the wave equation analysis are clearly observed.

A 2.5 m diameter pile with a wall of 5 cm thickness was emulated and a length equals to 34.4 m. A linear-elastic model was considered to emulate the pile behaviour. The parameters of the pile were updated regarding the ones used in the static model. The pile unit weight and the Young's Modulus were established in accordance with the ones used in the CAPWAP back-analysis performed in the Cathie Associates project analysis. It was also not considered any type of damping. The parameters of the pile are presented in Table 6.3.

A force signal was applied on the pile head. The imposed signal is similar to the one used on the mesh refinement and damping analysis showed on the left side of Figure 6.27. Therefore, a harmonic signal with a frequency of 125Hz was applied for 4 ms. In order to get a better matching between the signal applied in PLAXIS and the measured signal in the real dynamic pile test, the amplitude of the signal was corrected to 64 MN. Just as in a dynamic pile test, the force and the velocity of the pile were monitored. Three pile sections (A-A', B-B' and C-C') were checked along the time.

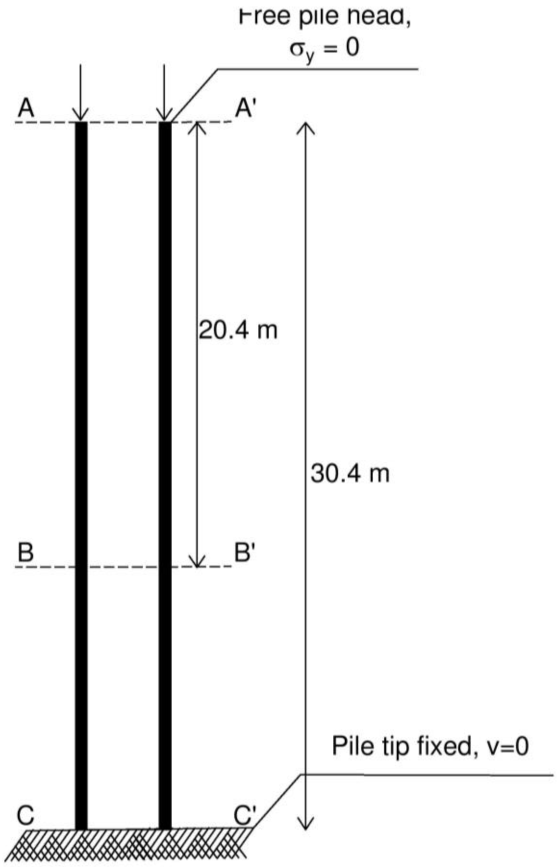

Figure 6.30. – Pile model and sections monitored

Table 6.3. – Pile features

Properties	Units	Steel Pile
Unit weight, γ	kN/m^3	77.3
Young's Modulus, *E'*	GPa	217
Poisson's ratio, ν'	-	0.3

The results are in accordance with the formulations of the wave equation analysis that were detailed in Section 4.4.3. Figure 6.31 and Figure 6.32 present the force and velocity calculated in the three monitored points over the time. As a single wave on the pile is considered, the proportionality between the force and the velocity mentioned in Section 4.4.3.1 is valid.

A compression wave starts therefore to propagate downward from the pile top. The applied signal is seen in the force and velocity results of section A-A'. Then, the wave continues going downwards the pile. As the pile tip is fixed, the compression wave is also reflected in a compression wave. Hence, the force will double when it arrives to section C-C'. Regarding the velocity, it is zero in section C-C' due to the bottom boundary condition (vertical displacement equals zero). In order to reach equilibrium between the downward and the upward velocity, the reflected wave will present a velocity value with the reversed sign.

When the reflected wave arrives to the pile top, the measured force in section A-A' will be governed by the boundary condition that imposes a vertical stress equal to zero. Thus, the measured force equals zero and the compression wave will be reflected as a tension wave. The velocity at this point will be the double and the wave is reflected with the same velocity signal. From this step on, there are multiple reflections and the cycle detailed above is repeated.

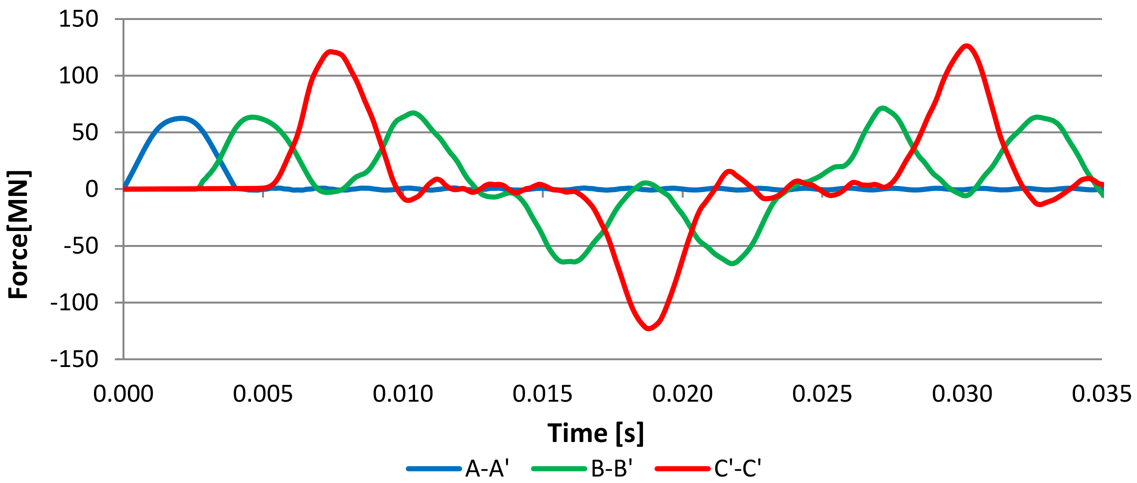

Figure 6.31. – Wave Equation Analysis: force signal calculated in three different sections

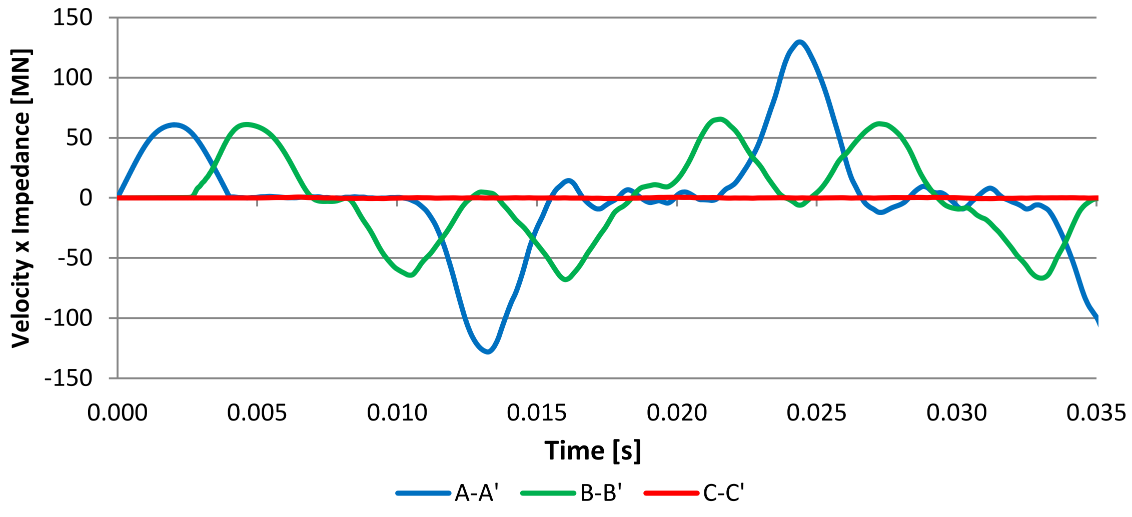

Figure 6.32. - Wave Equation Analysis: velocity signal calculated in three different sections

7

DYNAMIC MODEL FOR SOIL RESISTANCE DURING DRIVING ANALYSIS

7.1. OVERVIEW

In this chapter it is proposed an axisymmetric model in order to assess pile driveability in offshore tubular piles. This model is based on the 2D static model detailed in Chapter 5. Thus, once having built a good static model and having studied in detail dynamic numerical modelling, an axisymmetric model was developed taking advantage of the software package PLAXIS 2D Dynamics. Due to the dynamic calculations, the calculation times increase which makes these types of models to be hardly used in on going projects. Using a workstation equipped with an Intel ® Xeon (R) CPU X5650, 24.0 Gb of RAM memory at 2.67 GHz, each dynamic simulation took from 90 to 120 min.

In comparison with the static model, in a dynamic analysis it is necessary to take into account a larger number of aspects such as the damping (radiation or geometrical, material and numerical), reflections from the far field, frequency content of the soil and drained/undrained soil behaviour. Some updates to the soil and pile parameters used were adopted in order to create a robust model. A signal matching analysis was completed to adjust the soil parameters to the conditions of the tests in the field. The studies executed in Chapter 6 were also useful to create a reliable dynamical mode.

After creating the model, the results are discussed. At this point, the obtained results calculated from the numerical analysis are compared with the CAPWAP back-analysis calculations. Conclusions are taken regarding the reliability of the CAPWAP one-dimensional model.

7.2. AXISYMMETRIC DYNAMIC MODEL

After getting a better knowledge about PLAXIS and dynamic numerical modelling, the full axisymmetric model was created. The calculation was done using a staged construction structured in four phases defined as follows:

- Generation of the initial stresses;
- Pile installation;
- Residual stresses estimation;
- Pile axial capacity calculation.

In the first stage, the soil layers are allowed to reach equilibrium under self-weigh stresses. Afterwards, the resulted deformation is set to zero. In the second step, the pile is created and it is allowed to achieve equilibrium with the soil layers. The final deformations of this phase are also set to zero. In the third phase, the recorded velocity-time that resulted from the dynamic pile testing is input on the modelled pile. The calculated and measured velocity plots are exposed in Figure 7.1. Then, the force signal is calculated and compared with the one measured in the field. In this last phase the residual stresses installing in the pile due to pile driving are estimated. At the final of the third phase, the displacements are set to zero. In the final calculation, the pile is submitted to the same signal of the previous phase. At this phase it is used as input the residual stresses estimated from the previous calculation. Thus, in this last calculation it is emulated a dynamic pile testing taking into account the residual stresses observed in the pile due to pile driving. Further considerations about residual stresses will be given in this section

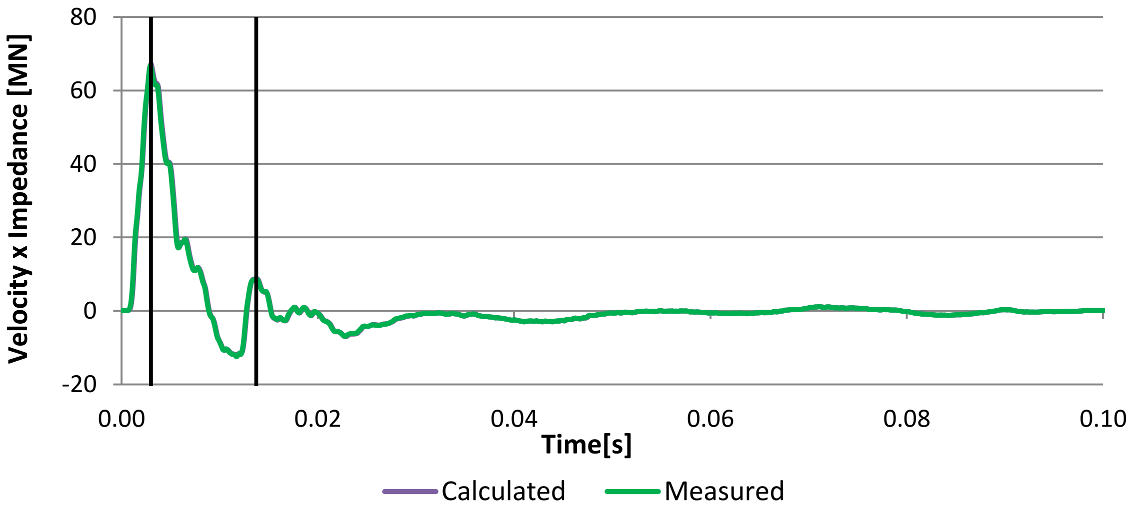

Figure 7.1. – Velocity times impedance signals: calculated and measured

7.2.1. MESH

As in the static model, 15-noded triangular elements were used. The mesh used is represented in Figure 7.2. A mesh with an ‘Average Element Size’, I_e, of 0.14 m showed to be adequate in order to get accurate results. A more refined mesh is considered close to the pile shaft as the frequency values are higher in this region and, so, lower wave length values occur close to the pile shaft. Thus, a more refined mesh is necessary in that region in order to obtain accurate results.

Because the mesh box used in the static model would not be feasible to run due to high calculation times and high memory requirements, and after having analysed the mesh used in Section 6.2, the mesh box dimensions were significantly reduced. Yang (2006) suggested an analytical estimation of the influence zone surrounding the pile tip of an axially loaded pile in sand. For piles in clean sand, the influence zone bellow the pile tip is between 3.5 to 5.5 times the pile diameter. For piles in more compressibility silty sand, the influence zone extends from 1.5 to 3.0 times the diameter bellow the pile tip. Figure 7.3 represents the influence zone surrounding the pile tip for these two soil cases.

Based on Yang's investigation, it was adopted a distance between the pile tip and the bottom boundary of 10 m. This value is within the limits suggested by Yang. A distance of 2D from the pile wall was found to be enough to capture the lateral response of the soil. The lateral mesh boundary was therefore placed 6.25 m from the pile wall.

In accordance with the analysis reported in Section 6.3.2.2, numerical damping was introduced in the model. Therefore the Newmark parameters, β and α, were set at 0.6 and 0.3025 respectively.

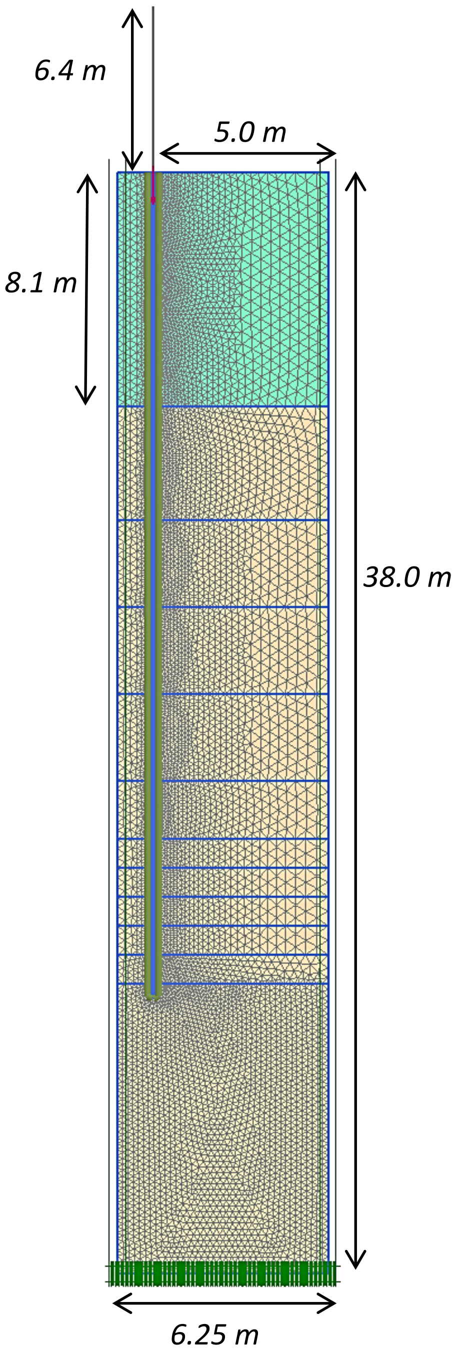

Figure 7.2. – Mesh used in the Axisymmetric Dynamic model

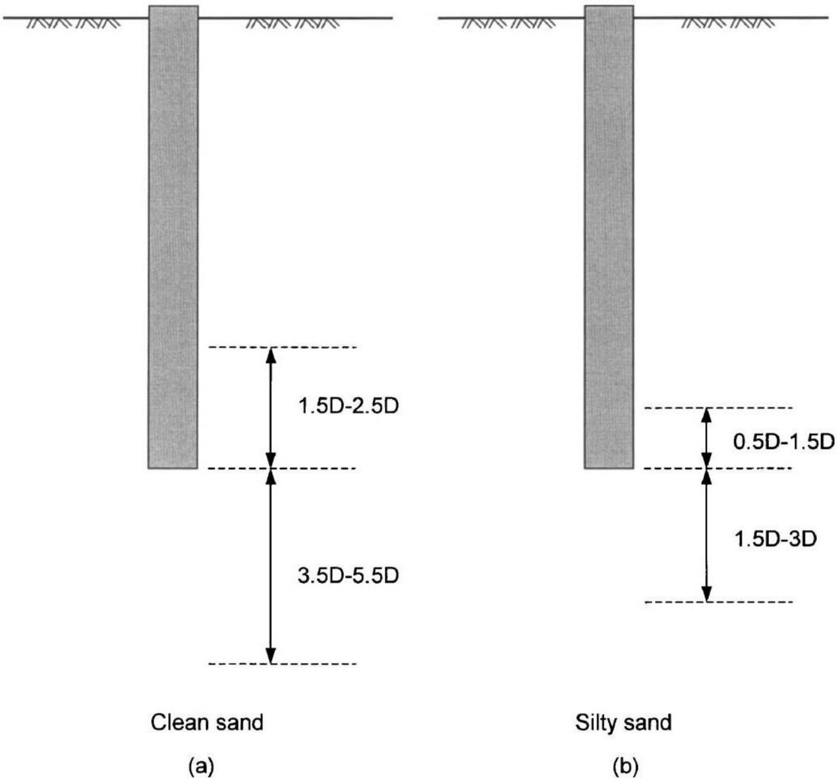

Figure 7.3. – Mean range of influence zone for piles in: a) clean sand; b) silty sand, Yang (2006)

7.2.2. Pile

The pile in study is the same pile investigated by Cathie Associates (Seçction 4.5.3). It is also the same pile examined in the static numerical model. Therefore, the steel tubular pile has a depth penetration of 28.0 m and a stick-up of 6.4 m. The cross-section is defined with an outer-diameter of 2.5 m and a thickness of 5 cm.

As in the static model, detailed in Chapter 5, the tubular pile was modelled using a single column of continuum elements. As the pile is much stiffer than the soil, it was defined a linear-elastic and non-porous material model to represent its behaviour. Other pile characteristics are detailed in Table 7.1.

The velocity signal recorded by the accelerometers, was input on the pile. A linear-elastic model was established in order to represent the pile behaviour. The parameters used in Section 6.4 were also defined for the final model. This is in accordance with the pile parameters defined in CAPWAP back-analysis performed by G-Octupus. In addition, Rayleigh damping was established in the pile.

Chopra (1995) presents damping ratio values for different types of structure and stress level. Table 7.2 provides the recommended damping values for different conditions of the structure and for two levels of motion: working stress levels or stress levels no more than one-half the yield point, and stresses at or just below the yield point. Hence, in a welded stress structure working no more than one-half the yield point, the damping ratio is between 2% to 3%.

Table 7.1. – Pile features, dynamic model

Properties	Units	Steel Pile
Unit weight, γ	kN/m^3	77.3
Young's Modulus, *E'*	GPa	217
Poisson's ratio, ν	-	0.3
Rayleigh damping, α	-	3.59
Rayleigh damping, β	-	4.55E-5

Table 7.2. – Recommended damping values, adapted from Chopra (1995)

Stress level	Type and condition of structure	Damping ratio
Working stress, no more than about ½ yield point	Welded steel Pre-stressed concrete Well-reinforced concrete	2 to 3
	Reinforced concrete with considerable cracking	3 to 5
	Bolted and/or riveted steel Wood structures with nailed or bolted joints	5 to 7
At or just below yield point	Welded steel Pre-stressed concrete (without complete loss in pre-stress)	5 to 7
	Pre-stressed concrete with no pre-stress left	7 to 10
	Reinforced concrete	7 to 10
	Bolted and/or riveted steel Wood structures with bolted joints	10 to 15
	Wood structures with nailed joints	15 to 20

Figure 7.4 shows the frequency spectrum calculated in the control section of the pile. It is observed that the pile responds in a range of frequencies until 200 to 250 Hz. The Rayleigh damping was established for target frequencies f_1 and f_2 of 10 and 200 HZ, respectively. The damping ratios defined for both of the frequencies was of 3%. These values lead to the Rayleigh parameters of α = 3.59 and β = 4.55E-5. Figure 7.5 shows the relationship between the frequency and the damping ratio for these values of Rayleigh damping parameters.

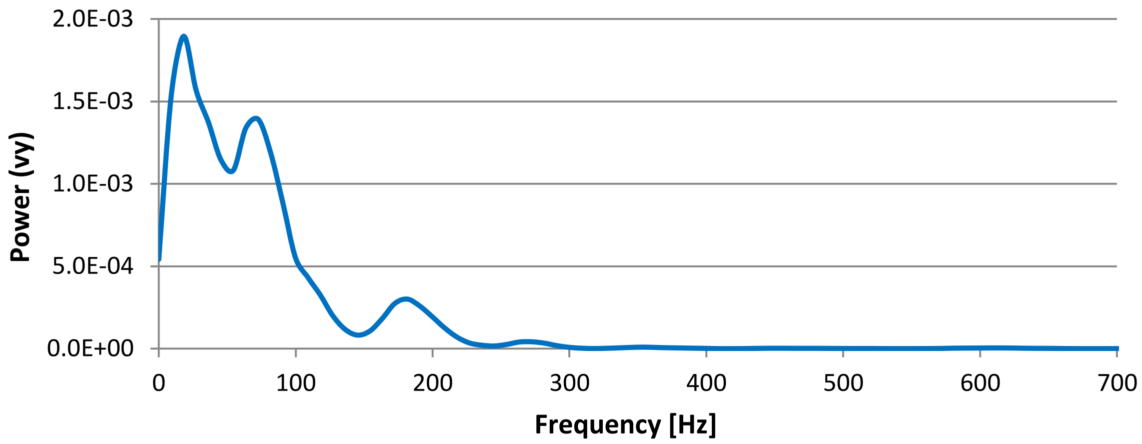

Figure 7.4. – Pile power spectrum

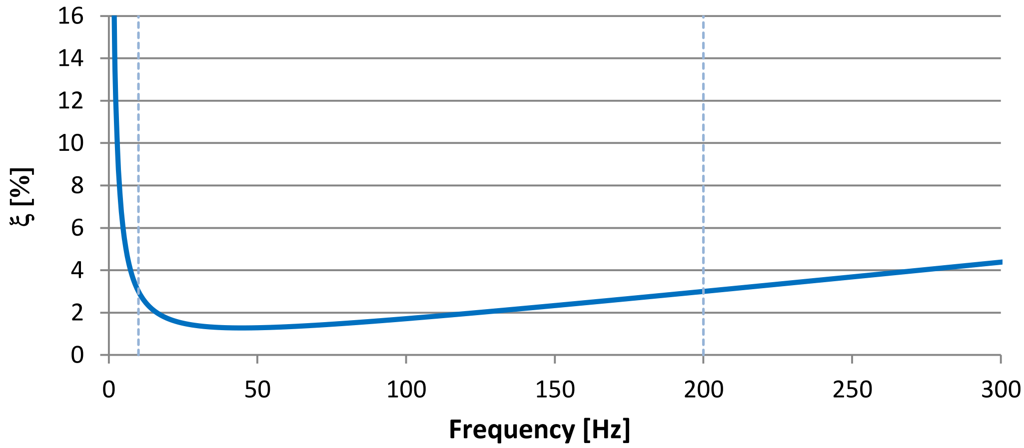

Figure 7.5. – Rayleigh damping

7.2.4. Signal Matching Analysis

A signal matching analysis was performed in order to correctly define the soil parameters for the dynamic model. As in a CAPWAP analysis, one of the measured signals (force or velocity) should be treated as an input signal in PLAXIS. Then, changing the resistance and the stiffness soil parameters, it was tried to obtain a reasonably match between the measured and the calculated force signal by a trial and error process.

In this model the velocity-time recorded was established as an input in the pile. Hence, the velocity signal was imposed in the same section where the transducers were located in the real driven pile (6.25 m bellow the pile head). With this approach and if the wave velocity is defined properly, the wave takes the same time in the real dynamic pile test and in PLAXIS to travel downward the pile and to arrive again to the control section. Thus, the measured and calculated signals are synchronised.

In order to assess the matching between the measured and the calculated signals, the measured and the calculated wave-up signals were compared. As the wave-up is related to the soil resistance and the measured velocity is directly applied in the PLAXIS model, a match between the wave-up signals will also be observed in the force signals comparison.

Before adjusting the soil parameters, the model was run with the soil parameters used in the static calculation. A comparison between the force and the wave-up measured in the field and the calculated by the model are shown in Figure 7.6 and Figure 7.7, respectively. In these plots the first wave peak and instant 2L/c is also indicated. Analysing Figure 7.6, it is observed that the compression wave imposed on the pile is reflected in a tension wave from the pile tip. Thus, the soil in this region appears to offer not sufficient resistance or to present low stiffness.

Several tests were conducted in order to clarify the doubts that came up due to the results obtained for the soil bellow the tip. It was concluded that the adjustment of the shaft parameters have larger influence for the signal matching than the change of the soil parameters bellow the tip. This can be explained because in dynamic conditions the pile is coring and the tip resistance has a small contribution to the total pile axial capacity. It was also realized that the most influencing time domain for the shaft resistance adjustments is between the peak velocity, or force, to 2L/c.

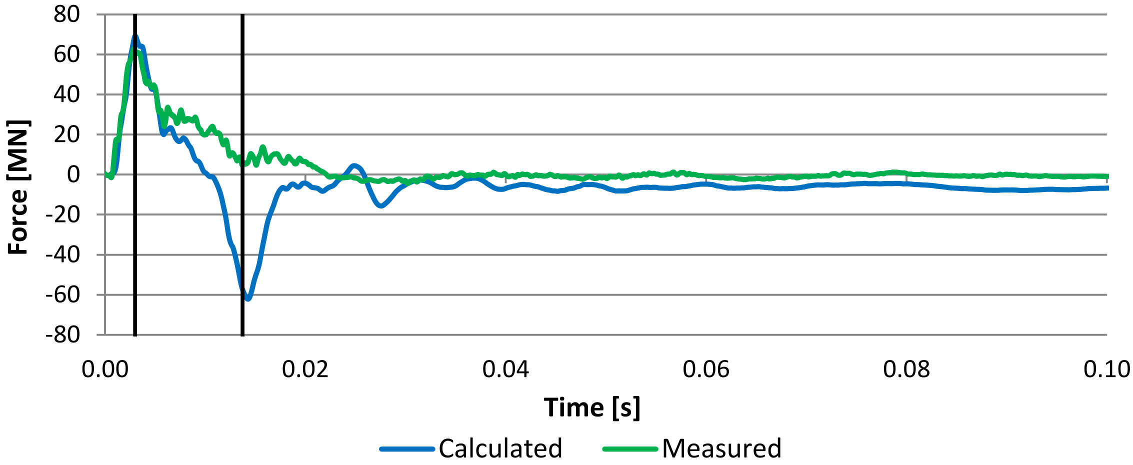

Figure 7.6. – Calculated and measured Force signals

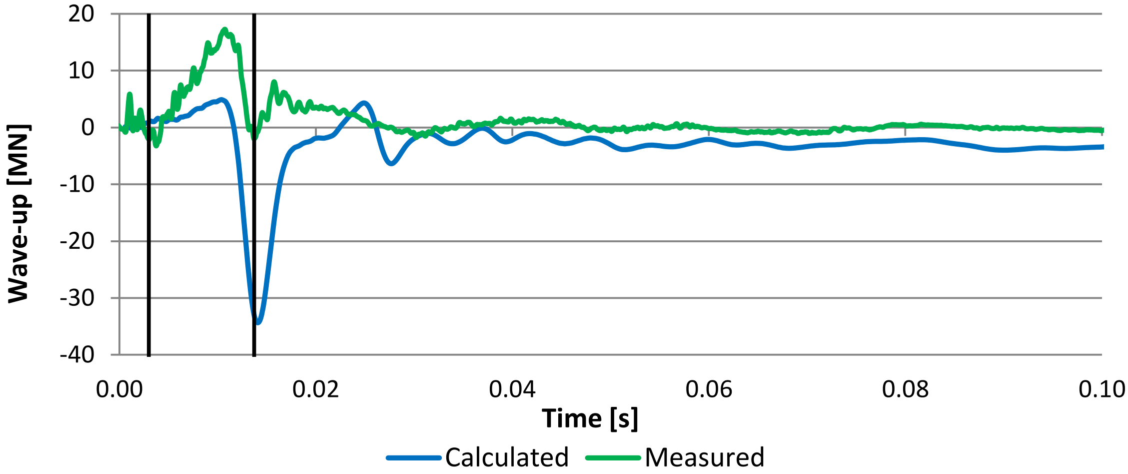

Figure 7.7. – Calculated and measured Wave-up signals

A signal matching analysis was thus conducted to match the measured and conducted force signals for this time (between the peak force and 2L/c). The match between the two signals was performed by adjusting the pile-soil interface strength and stiffness parameters and the soil bellow the tip resistance and the stiffness.

Thus, the final signal matching results are now present. Figure 7.8 shows a comparison between the measured and the calculated force signal. As it is observed, it was achieved a good match between both of the signals.

Figure 7.9 allows the assessment of the match of the wave-up obtained in the real pile dynamic test and the obtained by PLAXIS. It is therefore observed that the resistance considered for the soil is a good approximation with what was measured by the strain gauges and accelerometers.

Finally, it is evaluated if the signal that the hammer is sending to the pile is correctly input in the pile. This analysis is performed comparing the calculated and the measured wave-down curves, exposed in Figure 7.10. Although both the signals match it is also important to confirm that the energy submitted to the pile in PLAXIS is similar to the energy transferred by the hammer to the pile in the field. Figure 7.11 displays the measured and calculated energy along the time. The Enthru energy recorded by the PDA software was 698 kJ. On the other hand, the maximum energy imposing to the pile in PLAXIS is 715 kJ.

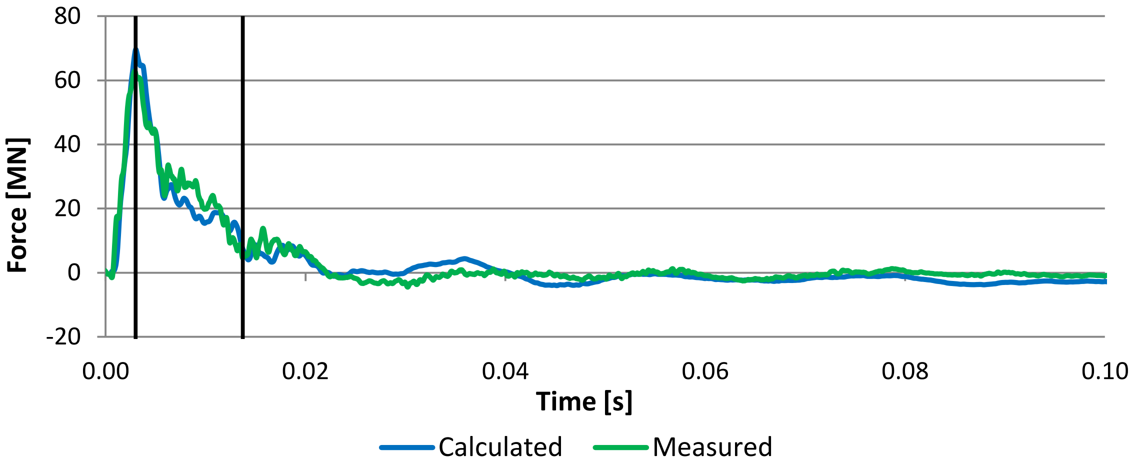

Figure 7.8. – Calculated and measured Force signals: signal matching

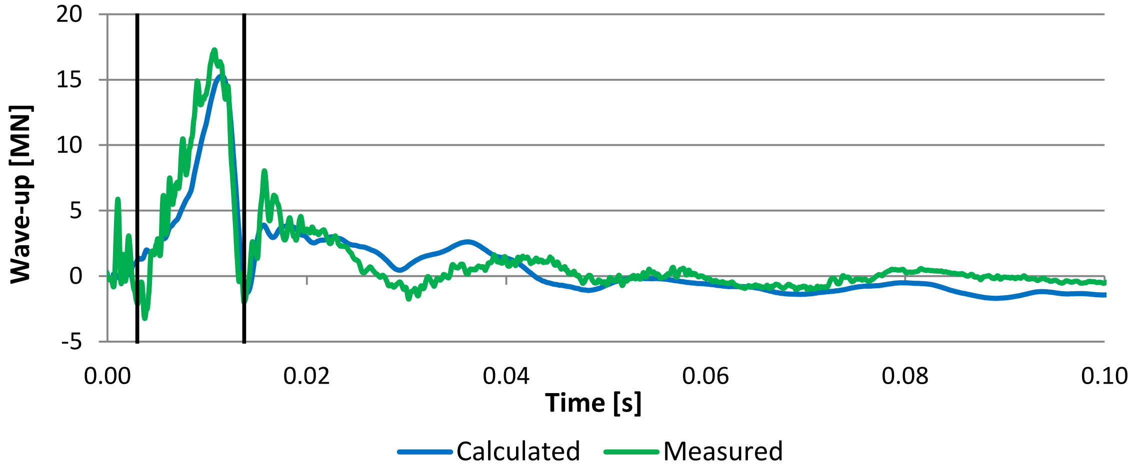

Figure 7.9. – Calculated and measured Wave-up signals: signal matching

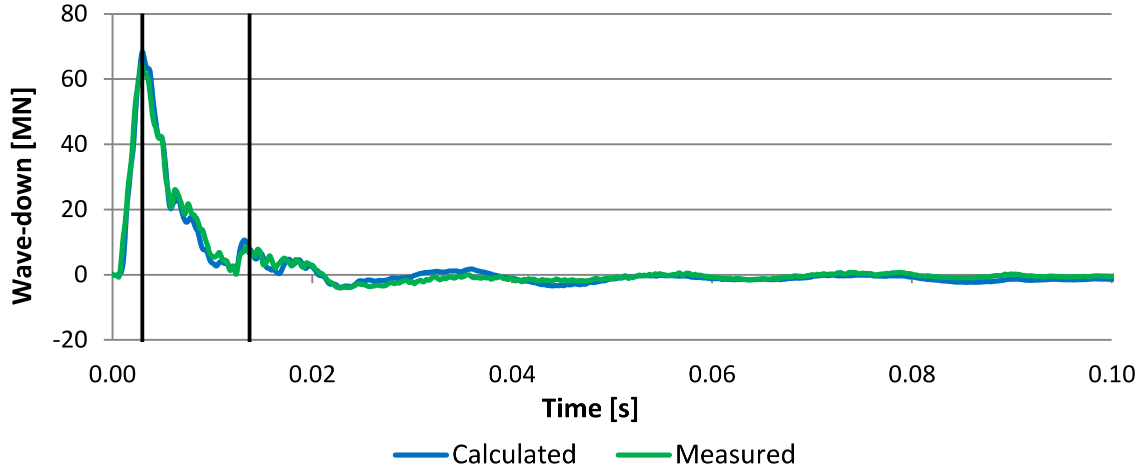

Figure 7.10. – Calculated and measured Wave-down signals: signal matching

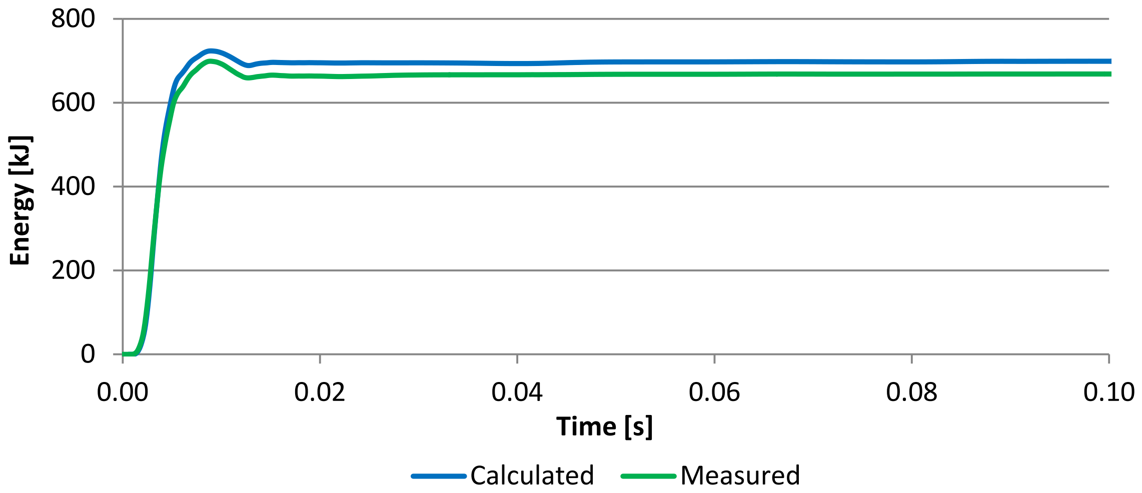

Figure 7.11. - Calculated and measured Energy: signal matching

7.2.5. SOIL

The soil was modelled based on the same CPT borehole log used for the static numerical model, illustrated in Figure 5.2. It was taken from the same Cathie Associates project in the North Sea. A simple drained Mohr-Coulomb model was defined to emulate the soil behavior. Table 7.3 details the soil properties defined in the final signal matching model. The coloured rows show the soil parameters that were modified from the static to the final dynamic model. The phreatic level is defined 32.2 m above the seabed. The next sections detail the values used for these parameters.

Table 7.3. – Soil parameters, dynamic model

Properties	Units	Medium Sand	Very Dense Sand Shaft	Very Dense Sand Soil bellow the tip
Effective Unit Weight, γ'	kN/m^3	9.5	10	10
Young's Modulus, *E'*	MPa	Linear increasing 23.3 to 350	350	350
Poisson's ratio, ν	-	0.3	0.3	0.3
Effective Cohesion intercept, *c'*	kPa	1.0	1.0	1.0
Angle of shearing resistance, ϕ_s	º	35	42.5	42.5
Interface friction angle, δ_f	-	21	34.5	34.5
Angle of Dilatancy, ψ	º	0	0	0
Lateral Earth Pressure, *K*	-	0.46	0.75 to 2.5	2.5
Rayleigh damping, α	-	5.98	5.98	5.98
Rayleigh damping, β	-	7.68E-5	7.68E-5	7.68E-5

7.2.5.1. Drained or Undrained Soil Model

A main question prior to any geotechnical investigation is to understand if the soil response is drained or undrained. Due to the rapid pile load test, excess pore pressure can be generated in the soil close to the pile, even in sand.

Holscher *et al.* (2009) concluded that during a rapid load test on a displacement pile in sand, excess pore pressure is generated in the soil around the pile base. In that work, they also concluded that if the dynamic test is performed in coarse sand, the resistance at the pile toe is not affected by the generation of pore water pressures. On the other hand, in medium and fine sand, the excess pore pressure results in an increase of the resistance. It would correspond to an undrained or partially drained soil model.

However, even though dynamic analyses may be partially drained, it is extremely difficult to provide reliable parameter values for undrained loading in sands. Partially drained analyses are numerically complex to implement. Thus, in the current model, the soil was established as drained and, therefore, no excess pore pressures are generated. Further investigations should be performed in order to assess the influence in the results if a partially drained or an undrained soil model was defined in the calculation.

7.2.5.2. Young's Modulus

In Section 6.2.6 it was mentioned that in a dynamic problem it is generally verified a small level of strains, usually lower than 10^{-3}. This assumption was confirmed verifying the strains along the time for three points, one 5 cm bellow the pile tip and the other two located close to the inner and outer pile-soil interface. The results are shown in Figure 7.12. However, in the pile-soil interface higher strains can occur. The monitored points in the shaft region are placed 0.5 m above the pile tip. It is also important to mention that all the results display the deviatoric strains of each point instead of the strains. Despite that, it is well known that the difference between these two parameters is not significant.

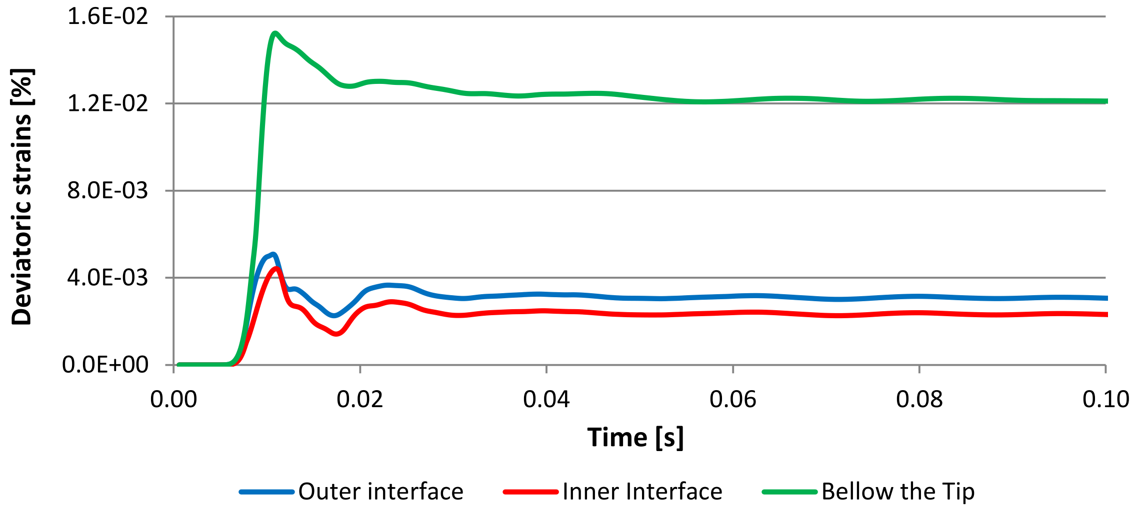

Figure 7.12. – Deviatoric strains of three monitored points

Adequate values of stiffness were established based on the results presented above. Regarding the soil stiffness, considering that a dense wave can offer shear wave velocities about 250 m/s to 300 m/s and densities of 20 kN/m^3, by Equation 6.12 it is concluded that values of, G_0, of 130 to 200 MPa for the Maximum Shear Modulus can be obtained. For these values and a *Poison* ratio of 0.3 we verify that values of the Young's Modulus between 350 and 500 MPa can be adopted in dynamic conditions. Thus, even if $G = 0.8.G_0$ is considered, values in that range can be easily obtained.

7.2.5.3. Interface Friction Angle

It is well-known that a dynamic excitation of the soil can promote instantaneous excess pore pressures and an increase of the dilatancy. Both of these effects cannot be naturally considered by the Mohr-Coulomb model. Thus, in order to emulate this increase of the soil resistance it may be necessary to increase the interface friction angle. Values of 35° were established for the dense sand in order to obtain a good match between the measured and calculated signals.

7.2.5.4. Lateral Earth Pressure

Alm and Hamre (2002) proposal to estimate the SRD and Jardine and Chow (2005) regarding the ICP method offer some formulations to estimate the radial effective stresses and so the lateral earth pressure at the end of driving.

Hence, applying Alm and Hamre proposal, using Equation 4.12, and assuming an overburden pressure of 300 kPa and a cone resistance of 50 MPa, a lateral earth coefficient, K, equal to 2.54 is obtained. Although this can look a quite high value, its magnitude can be explained due to the pile installation effects. While a pile is driving, high radial displacements close to the pile tip are generated which can origin high horizontal stresses. Thus, high lateral earth pressure coefficients are obtained in this region. It is important to remember that the lateral earth pressure formulation of Alm and Hamre is based on Jardine and Chow (1996) investigation.

Jardine and Chow (2005) proposed an estimation of the radial effective stress. The effect of the pile tip is accounted by a power function. The radial effective stress can be calculated by Equation 4.19. Taking the same values used in the prior calculation, the radial effective stress is 760 kPa. Thus, the lateral earth pressure close to the pile tip is 760/300 = 2.53. As it was expected the values from Alm and Hamre and ICP are similar because both these formulations for the lateral earth pressure were deducted by the authors Jardine and Chow.

The values calculated by both of the proposed methods are in accordance with the established lateral earth pressure coefficients established in the axisymmetric model (Table 7.3).

7.2.5.5. Rayleigh Damping

The collected literature in Section 6.2.6.2 was the basis for adequately establishing the soil damping values. As it was presented above, it is observed small level of strains in the soil. Thus, according with the researches completed, the damping ratios in the far field can be about 3%. Nevertheless, as pile driving promotes intense shear strains in the pile-soil interface, damping can possibly achieve values of 10% to 15% in this area.

It is extremely difficult to define correct values for the Rayleigh damping because it is not known the exact damping that is introduced in the model by numerical damping and irreversible soil deformations. Nevertheless, the same Rayleigh damping parameters were defined and numerical damping was also introduced in the model. Thus, Rayleigh damping values, ξ_1 and ξ_2, were set at 5% for target frequencies of f_1 = 10 Hz and f_2 = 200 Hz. These values lead to the Rayleigh parameters of α = 5.98 and β = 7.68E-5. Figure 7.13 shows the relationship between the damping and the frequency for these Rayleigh damping parameters.

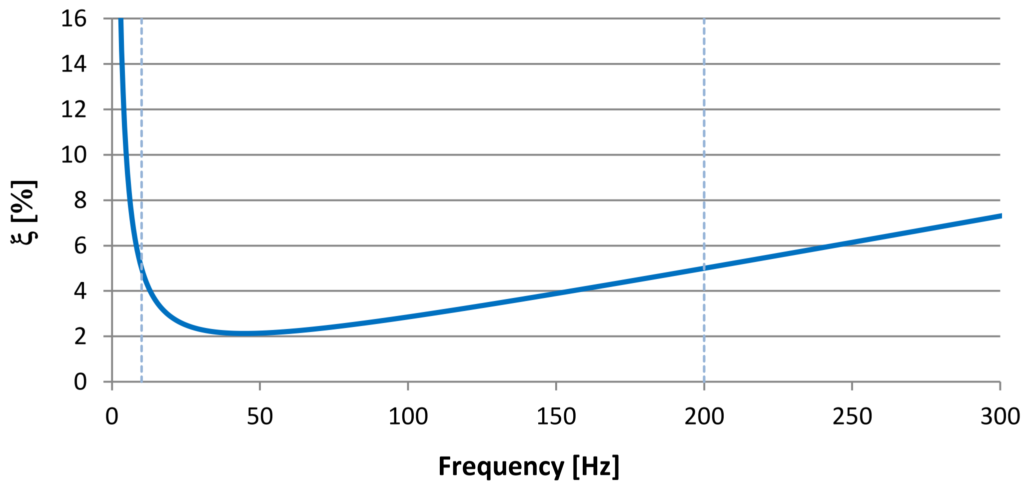

Figure 7.13. – Soil Rayleigh damping

7.2.6 Discussion of the Results – Calculation Phase 3

Due the continuous changing of the soil and pile response in a dynamic model, it is a challenge to capture, analyse and expose the results. Thus, in order to have a clear explanation of the results, three specific moments of the third calculation phase will be studied in this section. These three instants are indicated in the submitted signal to the pile present in Figure 7.14:

- t_1 = L/c = 5.6 ms – it corresponds to the instant at which the wave arrives to the pile tip;
- t_2 = 2L/c = 10.7 ms – it corresponds to the instant at which the wave arrives to the section control after being reflected in the pile tip;
- t_3 = 100 ms – it corresponds to the end of the analysis.

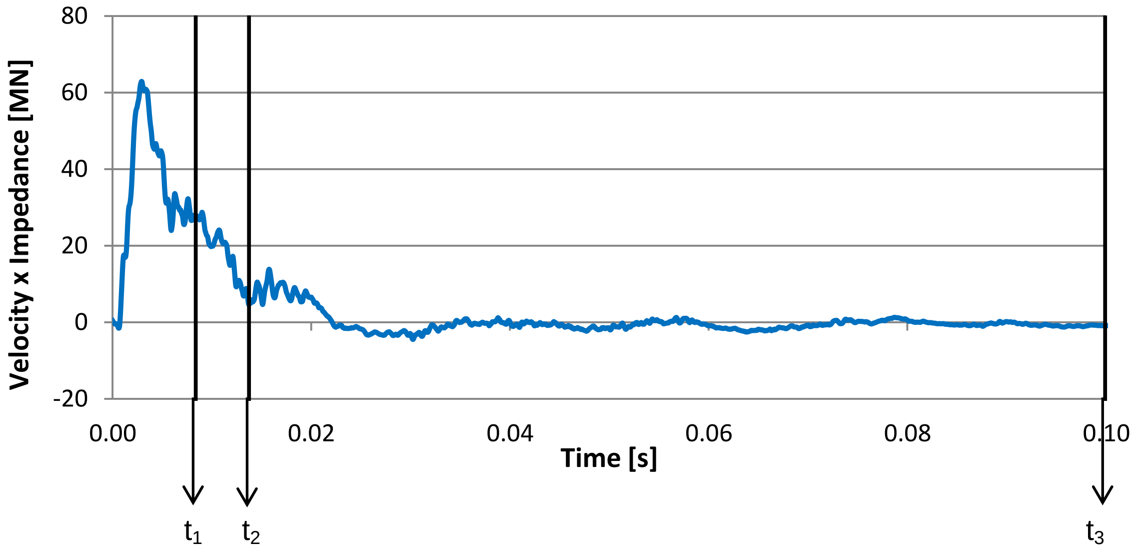

Figure 7.14. – Velocity x Impedance imposed signal and analysed isntants: t_1, t_2 and t_3

7.2.6.1. Plugged vs Unplugged Behaviour

As in the static axisymmetric model, it is also in this case analysed the degree of plugging of the pile. As mentioned in Section 4.2.3, according with Henke and Grabe (2009), when a pile is submitted to a dynamic load, the soil exhibits high soil compaction inside the pile due to the continuous cyclic shearing. This process leads to a reduction of the horizontal stresses. Hence, plug is unlikely to occur when the pile is installed by dynamic methods.

The most significant effective stresses were therefore investigated for the three instants mentioned above. The results that were obtained are presented in Figure 7.15. The same convention used in Chapter 5 for compression and tensile stresses is adopted in this representation. Unlike what happens in static conditions, the most important effective stresses do not involve the overall pile base. In the studied case, when a dynamic load is imposed to the pile, the largest effective stresses only involve the pile tip. This study aims at concluding that the pile is coring and, therefore, the pile does not penetrate in plug which is in accordance with several researches that have been conducted about this subject.

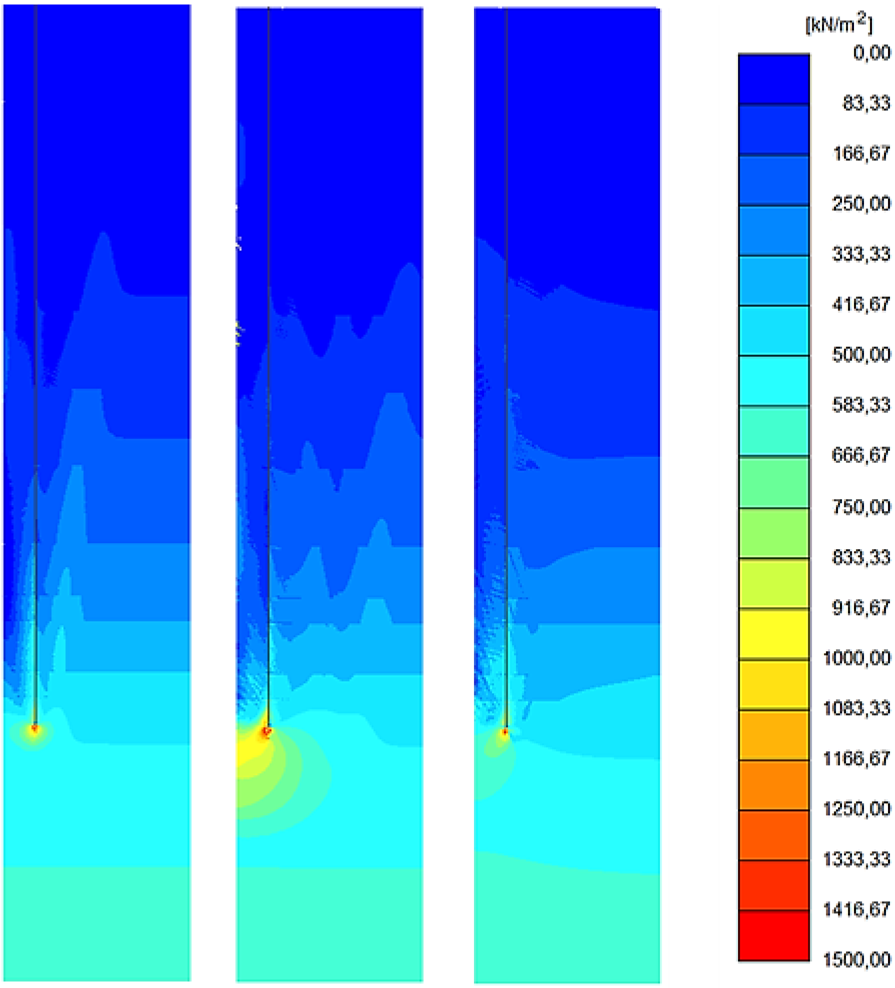

Figure 7.15. – Principal effective stresses in the studied instants: : t_1 (left), t_2 (middle) and t_3 (right)

7.2.6.2. Analysis at instant t_1 = L/c

As the plug topic is a controversial theme in pile driving researches, deeper investigations were performed regarding this issue. The three mentioned instants will thus be analysed in detail in order to get further insights on the soil behaviour along the time. It will be given special focus to the examination of the shaft friction and the incremental displacements for these instants. The shaft friction allows understanding the mobilized interface shear stress for each studied instant. On the other hand, the contour plots of the incremental displacements allow investigating the effects that are created in the soil in each moment. Both the shaft friction and the incremental displacements should be analysed simultaneously.

As mentioned previously, the instant L/c corresponds to the moment when the imposed wave arrives at the pile tip. In the shaft friction representation, displayed in Figure 7.16, with the same convention described in Chapter 5, it is observed that the higher stresses are mobilized in the region close to the tip which is in accordance with the studied instant. In the skin friction representation, it is admitted that positive inside skin friction corresponds to the upward direction while a negative friction indicates the downward direction. On the other hand, negative outside skin friction corresponds to the upward direction and the positive skin friction indicates the downward direction. A scheme of the pile with the direction of the skin friction is provided in Figure 7.17.

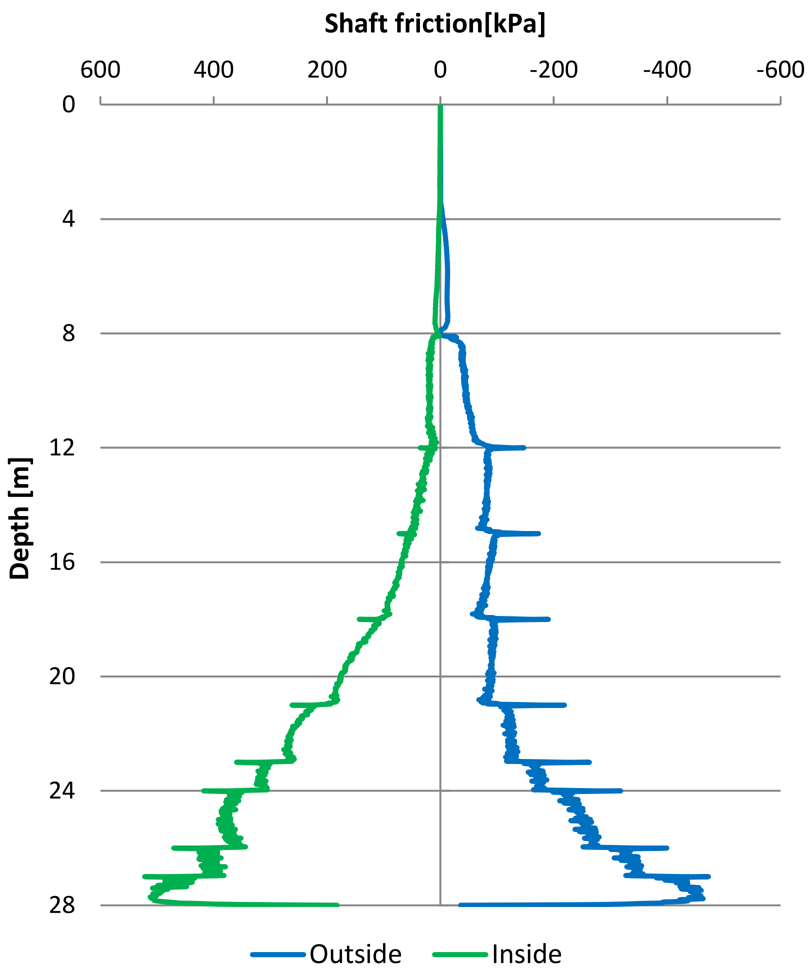

Figure 7.16. – Outside and inside Shaft Friction profile: instant t_1

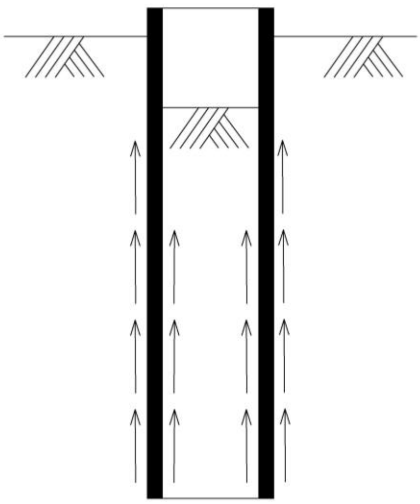

Figure 7.17. – Shear stress direction: instant t_1

Figure 7.18 shows the vertical incremental displacements that occurred at the L/c instant. It is observed that the pile tip displaced downward. The soil surrounding the pile (outside) also displaced downward but not so significantly. This can be examined as the pile and the soil correspond to a force-reaction system. Thus, the soil is resisting the pile with an upward shear stress which is in accordance with what was explained in the above paragraphs.

The analysis of Figure 7.18 also indicates that the surrounding soil (outside the pile) and the soil inside the column were not yet affected by these effects, although the pile displaced downward. It can be therefore concluded that the pile and the soil plug are not responding in phase. Thus, the pile and the soil plug should be treated as two different objects. This aspect will be confirmed in the next steps.

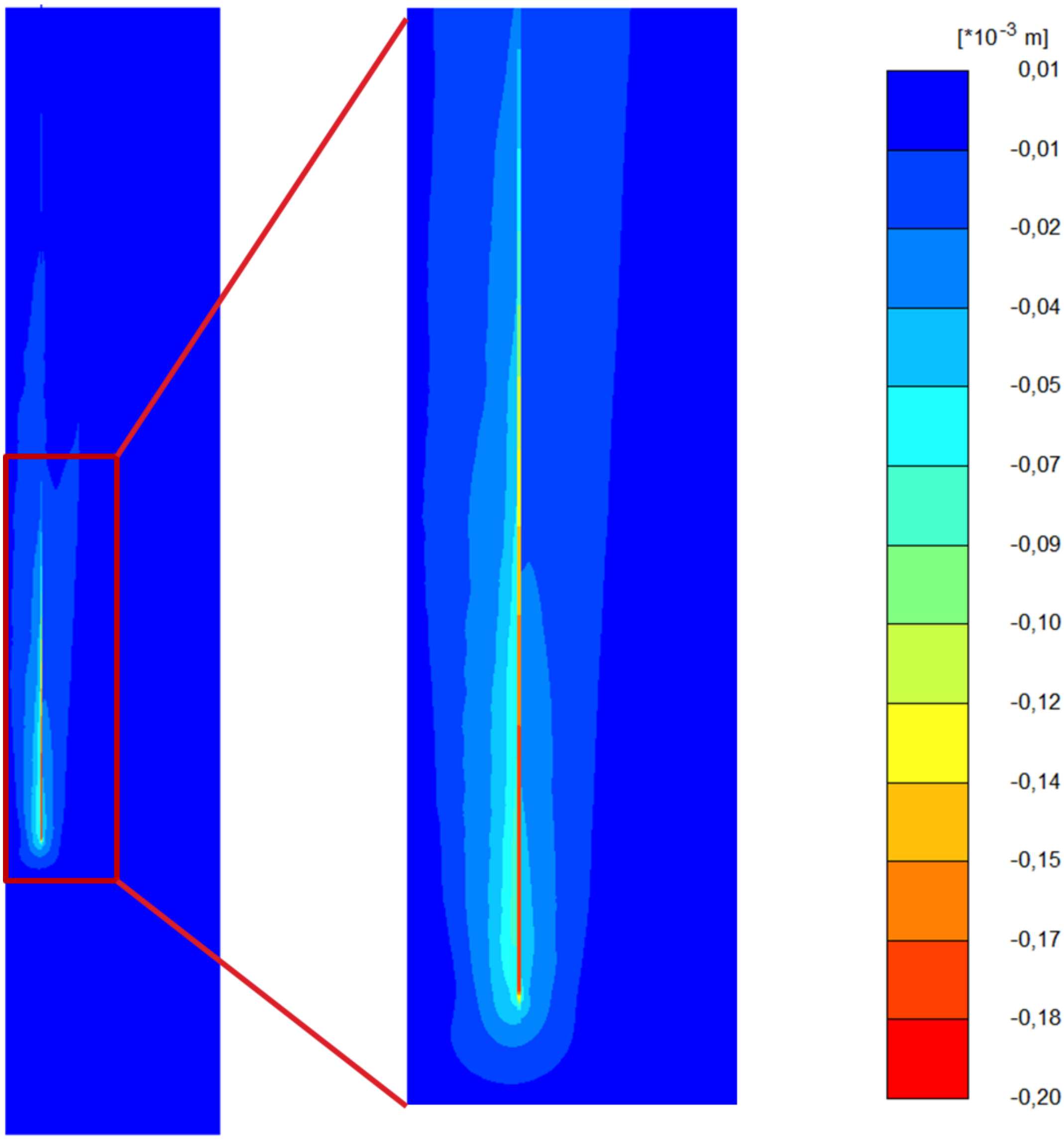

Figure 7.18. – Incremental vertical displacements: instant t_1

7.2.6.3. Analysis at instant $t_2 = 2L/c$

A similar analysis to the one exposed for the instant L/c is now performed for the next moment, 2L/c. At this step, the wave in the pile is on the section control after being reflected in the pile tip. Figure 7.19 presents the outside and the inside interface stresses. An illustration of the directions of the shear stresses is displayed in Figure 7.20. Then, Figure 7.21 presents the incremental vertical displacements for the current instant.

The results should now be analysed simultaneously. It is now realized that the inside shear stresses have a downward direction. This can be explained because the soil within the pile is only now affected by the phenomenon that occurred in the pile in the previous instant. Hence, the soil inside the pile is now going downward more significantly than the pile which promotes negative inside shear stresses. This phenomenon only occurs in the inside interface. In the surrounding soil, due to radiation damping, the wave is dissipated towards the far field and no singular changes occur in this region.

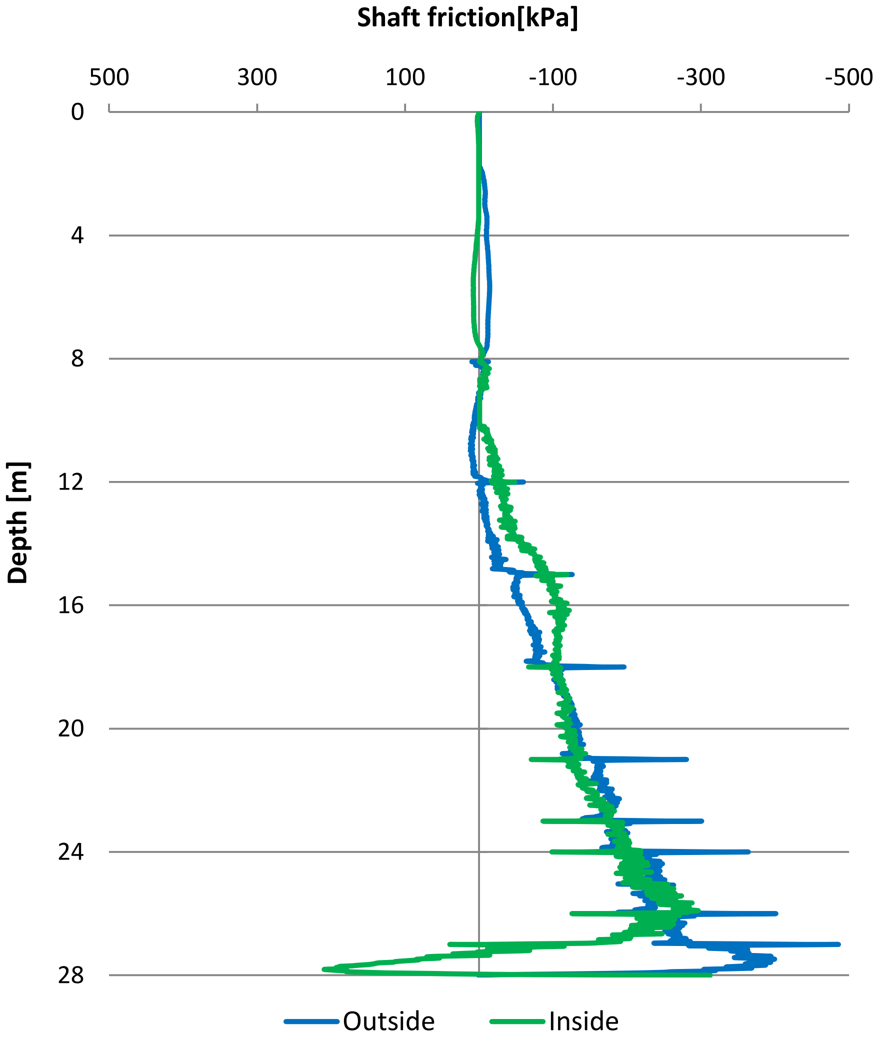

Figure 7.19. – Outside and inside Shaft Friction profile: instant t_2

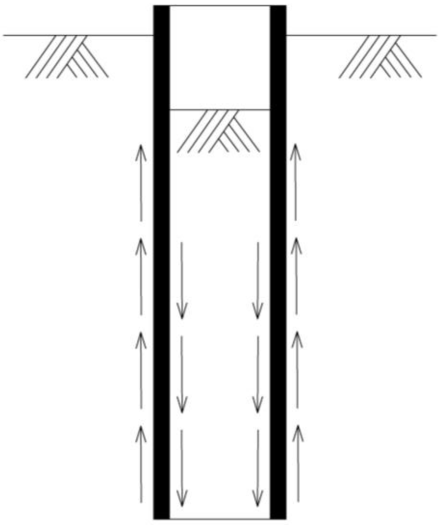

Figure 7.20. – Shear stress direction: instant t_2

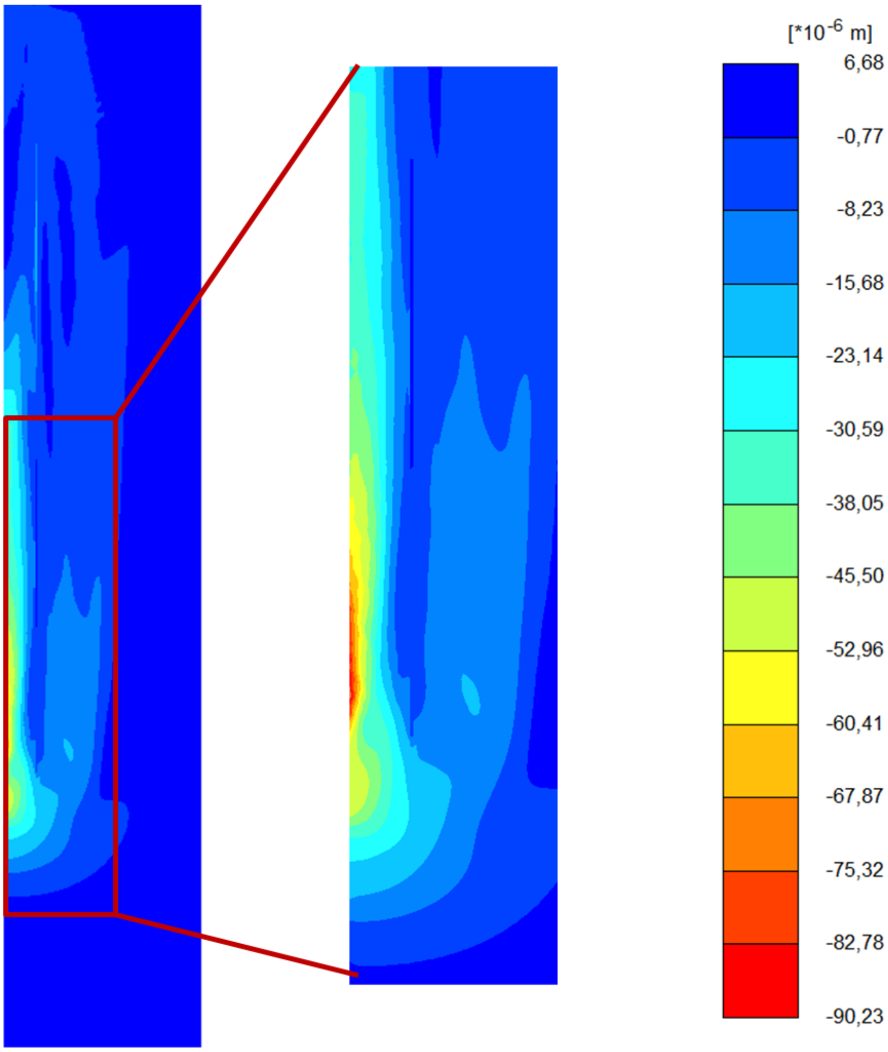

Figure 7.21. – Incremental vertical displacements: instant t_2

7.2.6.4. Analysis at instant t_3 - End of Analysis

For instant t_3 corresponding to the end of analysis, the pile shaft friction is presented in Figure 7.22. A representation of the shear stresses direction is displayed in Figure 7.23. In Figure 7.24 it is displayed the incremental vertical displacements at the end of the analysis.

The analysis of these results indicates that some residual stresses with downward direction are generated in the outside pile interface. This topic was already studied in Chapter 4. Further analyses are present in Section 7.2.6.5.

Figure 7.24 only represents the outside region of the pile. The inside region of the pile is not represented because that would turn it difficult to understand how the incremental displacements vary in this region. On the other hand, the results exposed in Figure 7.22 indicate that shear stresses inside the pile are close to zero. Therefore, the analysis of the outside shaft region is more relevant. Despite that, it is observed the wave being dissipated towards the far field.

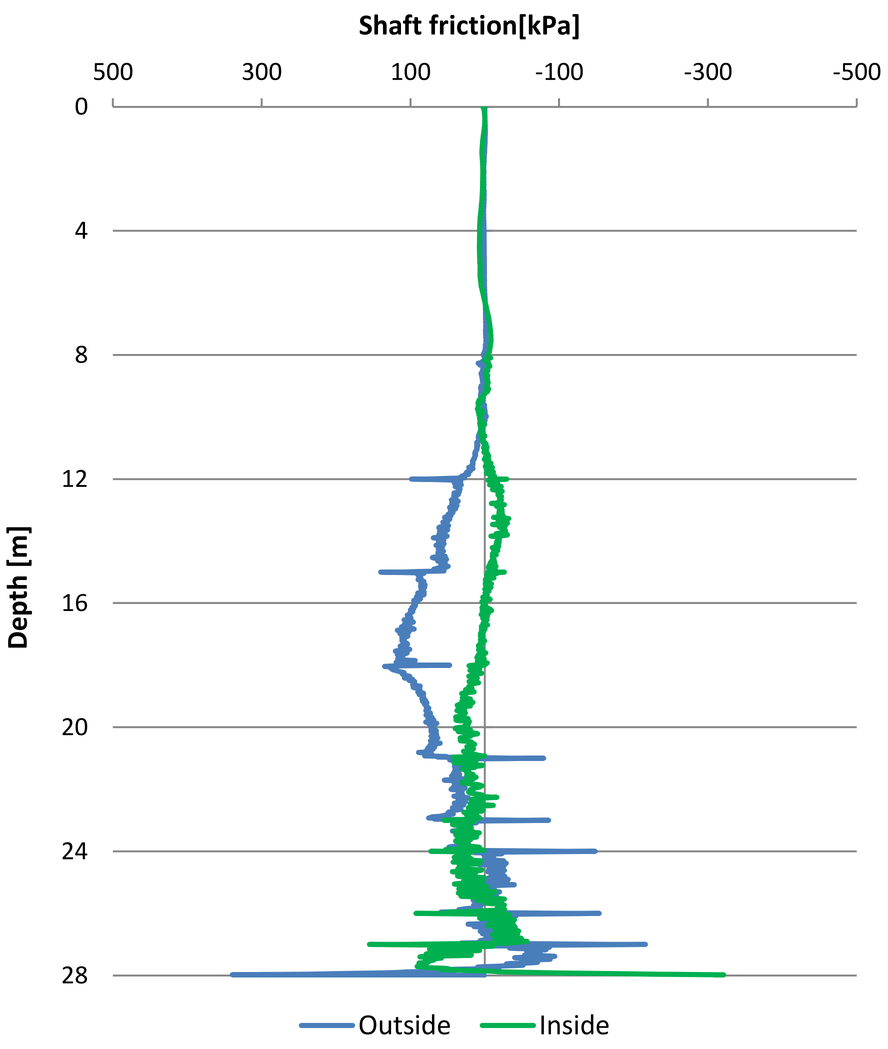

Figure 7.22. – Outside and inside Shaft Friction profile: instant t_3

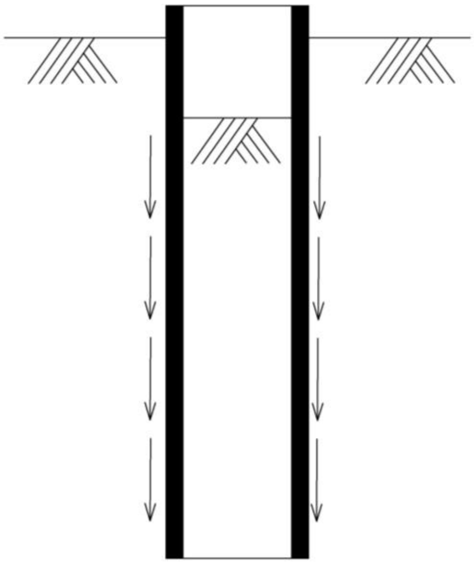

Figure 7.23. – Shear stress direction: instant t_3

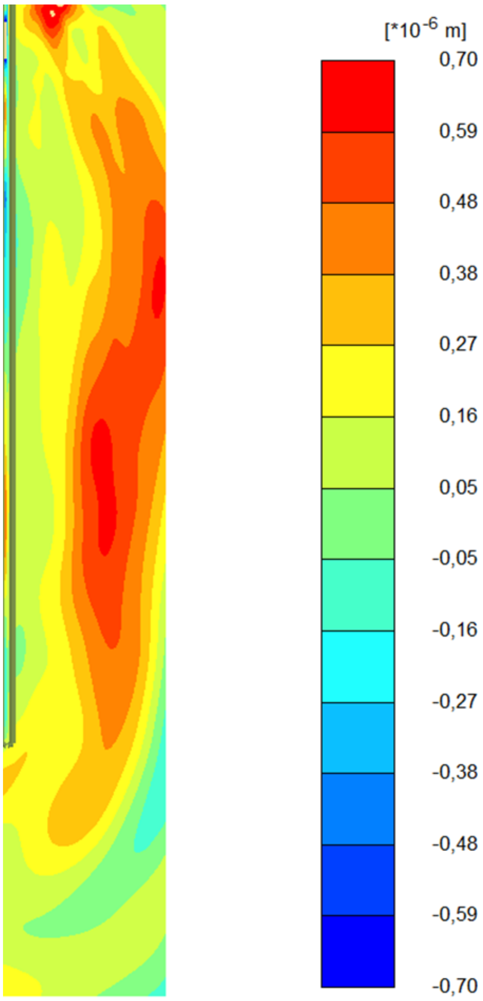

Figure 7.24. – Incremental vertical displacements: instant t_3

7.2.6.5. Residual Stresses

As mentioned in Section 4.2.3.3, according to Fellenius *et al.* (2007) and Viana da Fonseca *et al.* (2008), residual loads are present in almost all type of piles, being mostly significant in driven piles. Residual stresses in dynamically driven piles are caused as follows. During the last hammer blow, the pile goes down and mobilizes the upward resistance of the soil in both friction ($\tau_{shaft,\ 1}$) and tip resistance ($\tau_{tip,\ 1}$). Then, the pile rebounds and, as the skin friction is mobilized for very little displacements (u_1), the friction stresses change to the downward direction ($\tau_{shaft,\ 2}$). However, because it is necessary much larger displacements to totally decompress the pile tip, the soil still pushes the pile upwards ($\tau_{tip,\ 2}$). According to Viana da Fonseca *et al.* (2007), when no residual loads are considered at the calculation, the data may overestimate the shaft resistance and underestimate the toe resistance.

Figure 7.25 shows a simple scheme of the process detailed above. In green it is shown the shaft friction shear-stress behaviour and in red the pile tip response. In order to keep the scheme simple, the same stiffness was considered for the pile-soil interface and for the soil bellow the tip.

Typical curves of the distribution of residual stresses are presented in Figure 7.26 a). These curves were proposed by Holloway *et al.* (1978) and they are based in static load tests considering a linear initial distribution of the skin friction (curve 'R'). Curve 'O' represents the friction distribution at end of driving without considering the residual stresses. On the other hand, curve 'M' represents the friction distribution along the pile depth taking into account the residual stresses at the beginning. It is observed that the shape of the curves proposed by Holloway are similar to the ones obtained in the present work which gives a larger confidence in the model.

Wang and Zhang (2008) also investigated residual stresses generated due to impact driving. In the work by Wang and Zhang, eleven instrumented long steel H-piles with lengths between 34-60 meters were driven and the residual forces were monitored. Based on field measured results, it was suggested a method to estimate residual forces in long driven soils. Although the pile section and its depth studied in the present work are not equal to the ones investigated by Wang and Zhang, it is interesting to examine the shape of the obtained residual stress curves, present in Figure 7.26 b). It is observed that the shape of the curve is similar to the one obtained in the present study using PLAXIS (Figure 7.22). This is an important validation point in order to ensure that a robust model is obtained.

In order to take into account the residual stresses in a numerical model, the literature proposes some approaches to emulate these effects. It is therefore proposed to simulate a fictitious blow on the pile just to estimate the residual stresses that occur during pile driving. Thus, it is applied a second blow. This step uses as input the residual stresses from the output of the mentioned fictitious simulation. When going from the fictitious simulation to the second one the deformations are set to zero. Therefore, the current analysed step (3rd calculation phase) aims at estimating the residual stresses. This step corresponds to the fictitious blow on the pile. In the next section (Section 7.2.7), the second blow simulation will be studied.

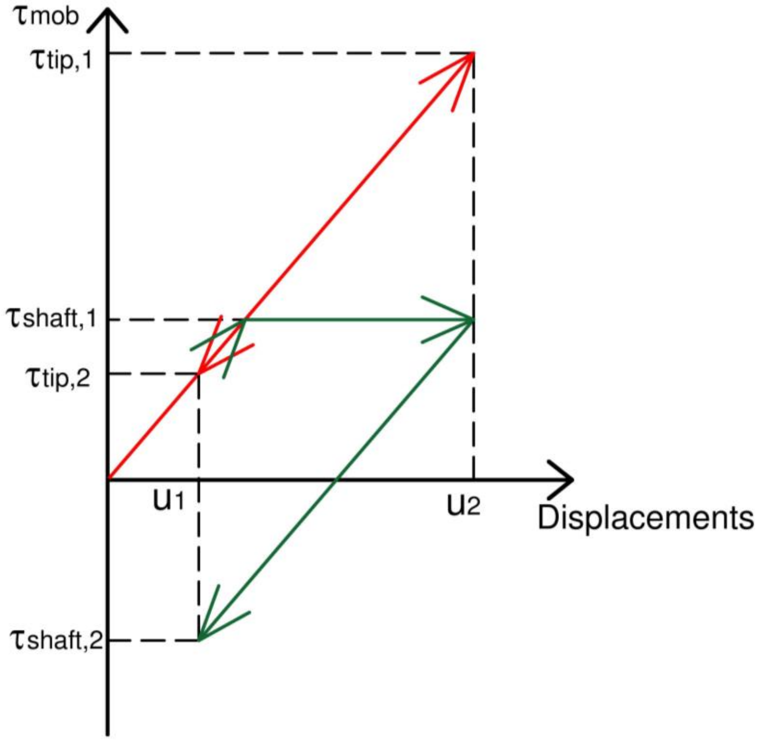

Figure 7.25. – Residual stresses

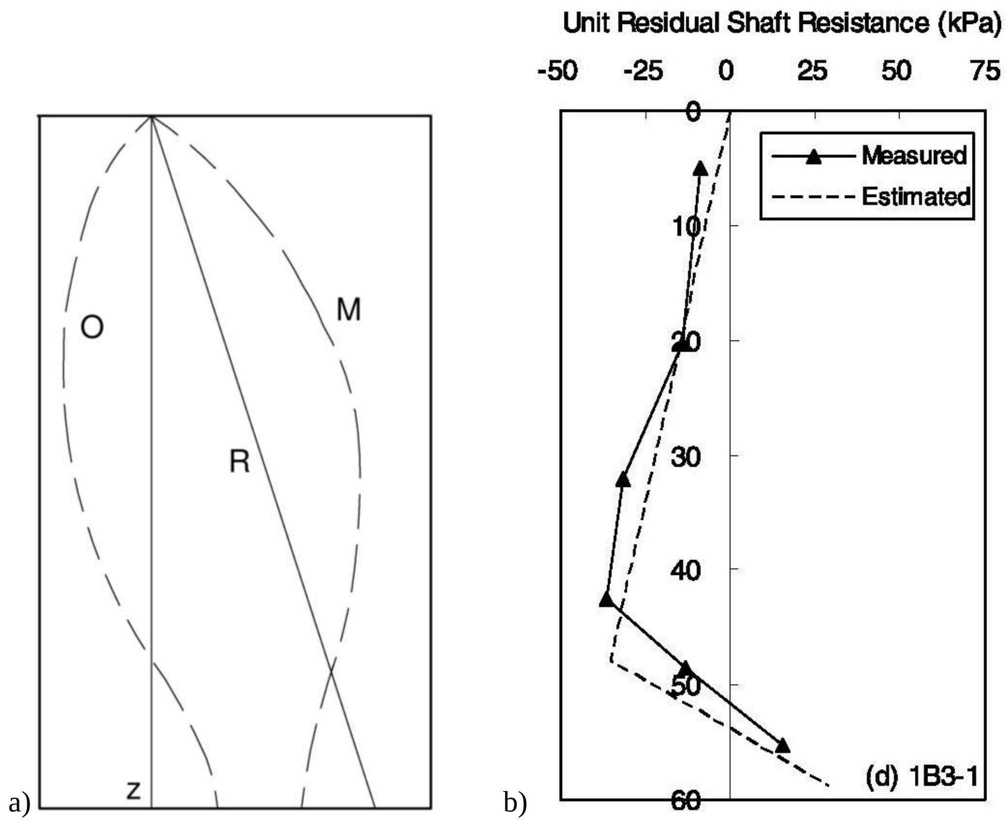

Figure 7.26. – Residual stresses curve shape: a) adapted from Holloway *et al.* (1978); b) adapted from Wang and Zhang (2008)

7.2.6.6. Soil Resistance

In order to determine the SRD, the end-bearing, Q_{bf}, and the shaft capacity, Q_{sf}, were calculated along the simulation. Regarding the pile end-bearing, it was monitored the pile vertical effective stresses, q_{bf}, of 4 points located along the pile cross section close to the tip. This analysis was important in order to verify if the stresses were similar along the pile cross section. The results are exposed in Figure 7.27. It is observed that the pile tip stresses can achieve variations of 4 MPa along the 5 cm of the pile wall thickness. It is therefore concluded that it is not a reasonable approximation to consider that the pile tip stresses are constant along the pile section.

Thus, in order to determine the end-bearing unit capacity of the pile it was calculated the average of the pile tip stresses obtained for the four monitored points. The calculation was performed using Equation 7.1. The end-bearing capacity is then the average of the pile tip stresses multiplied by the annulus area. These results are presented in Figure 7.28.

$$q_{bf} = \frac{q_{bf,1}+q_{bf,2}+q_{bf,3}+q_{bf,4}}{4} \quad (7.1.)$$

The maximum end-bearing capacity obtained by PLAXIS calculations is 5.3 MN. On the other hand, the end-bearing capacity determined using the Alm and Hamre proposal is 7.6 MN. The pile tip resistance obtained in the CAPWAP analysis performed by Cathie Associates project is 4.1 MN. Thus, the value calculated using the PLAXIS model is in the same range as the ones obtained by the proposed methods and by the post-calculations conducted in the Cathie Associates project. However, given that the residual stresses were not considered in the input calculations, it is important to recall that the end-bearing capacity is underestimated.

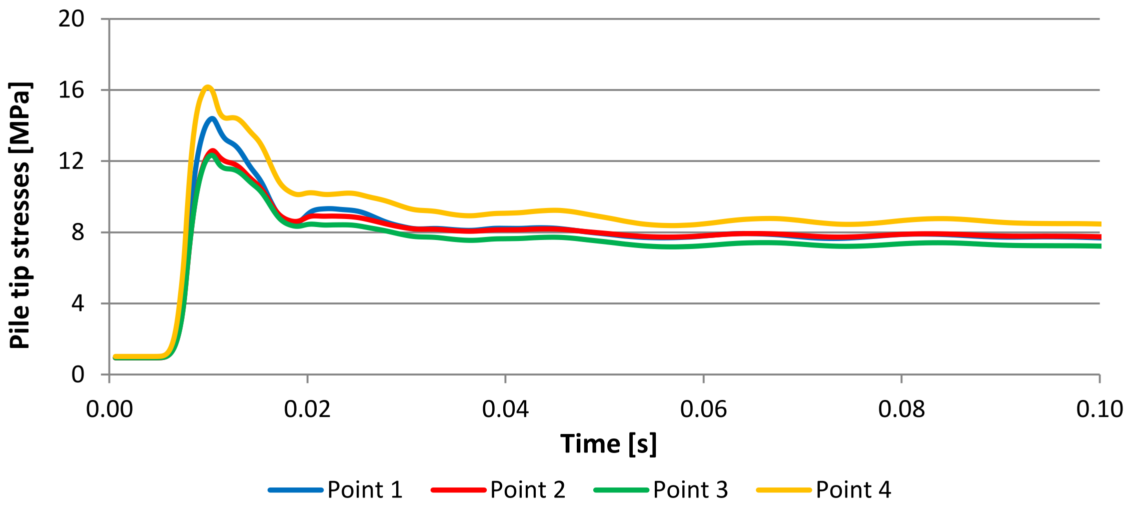

Figure 7.27. – Pile tip stresses in four points close to the pile tip: no residual stresses considered

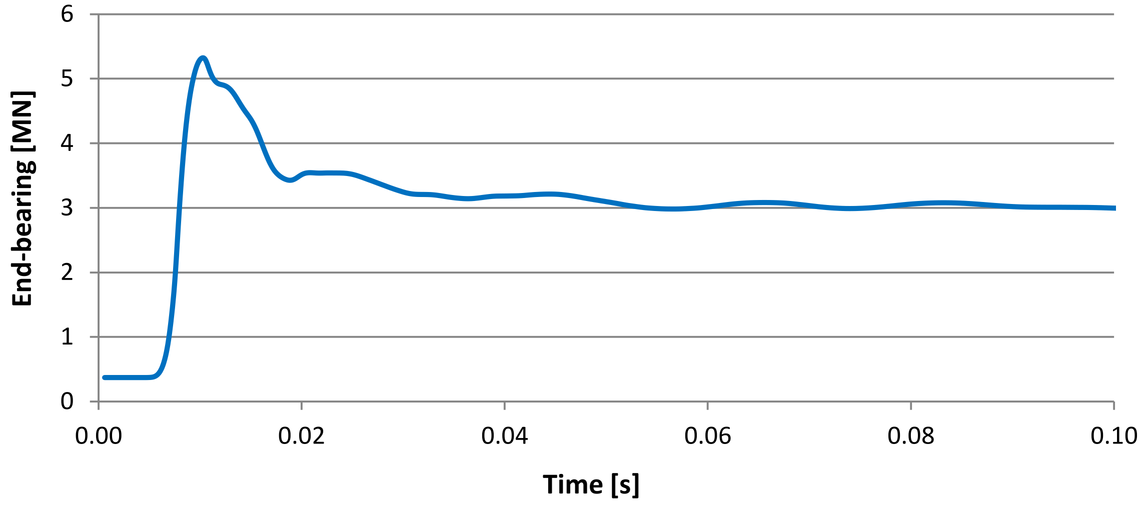

Figure 7.28. – End-bearing capacity: no residual stresses considered

Regarding the shaft capacity, the shaft friction profiles were integrated for several instants. It was therefore obtained a curve with the shaft capacity along the time. Figure 7.29 shows the outside and the inside shaft capacities along the time. The sum of the values in these two curves for each instant gives the total shaft capacity as presented in Figure 7.30.

The maximum shaft capacity equals 53 MN. This value is larger than the double of the value calculated by the executed CAWPAP back-analysis. This calculation leads to a shaft capacity of 26 MN. On the other hand, the shaft friction calculated by Alm and Hamre proposal equals 30 MN. Despite these differences, it is important to recall that the shaft capacity is being overestimated because no residual stresses were considered in the calculation.

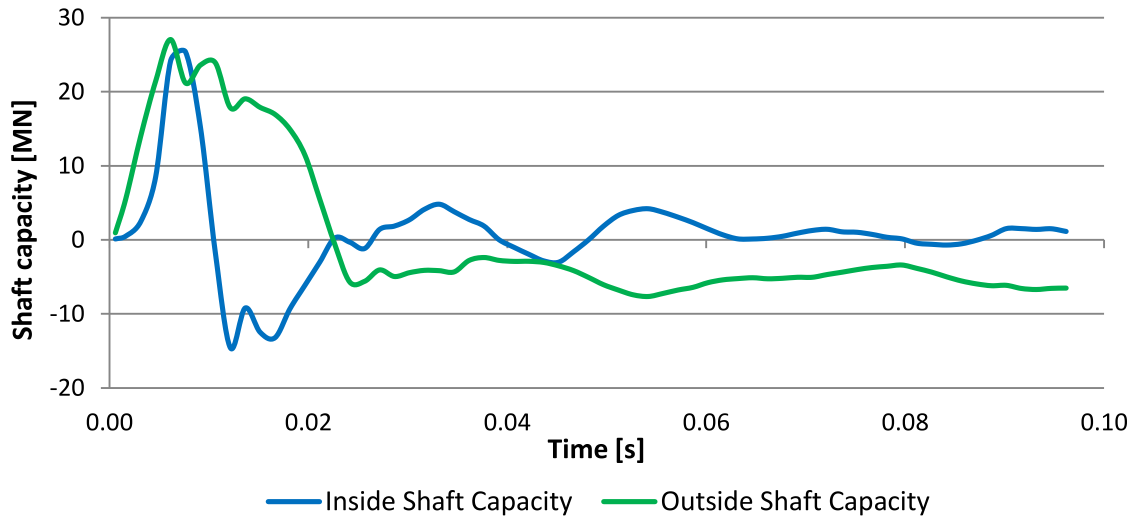

Figure 7.29. – Inside and Outside Shaft Capacities: no residual stresses considered

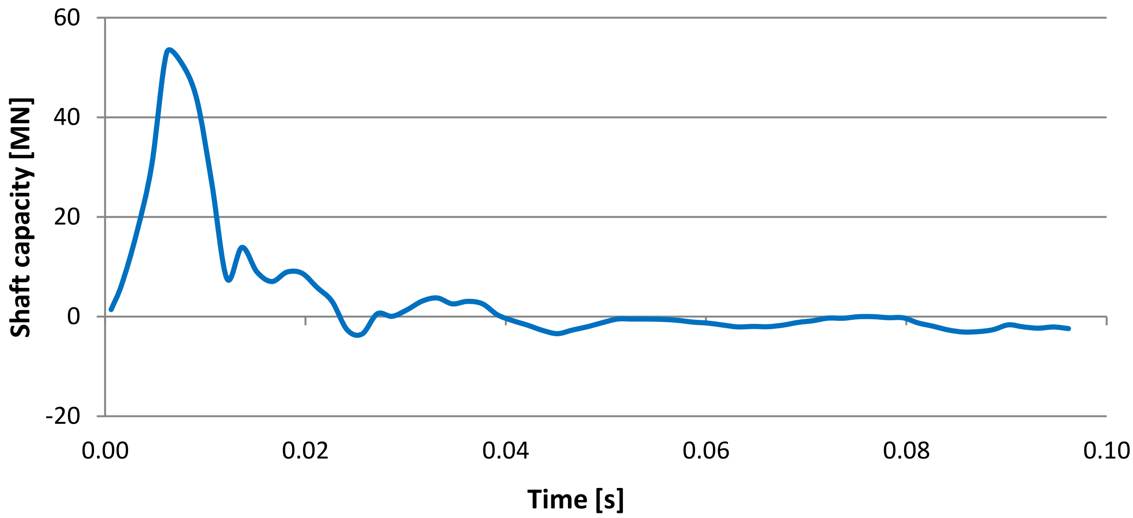

Figure 7.30. – Shaft Capacity: no residual stresses considered

Finally, it was calculated the total soil resistance by adding the end-bearing and the shaft pile capacities. Associating each time to a pile tip displacement it is obtained a load-displacement curve. Figure 7.32 shows the load-displacement curve that was built for the calculated model. The maximum load applied was 55 MN. As it was expected, this value is much larger than the estimated ones and the ones obtained using back analysis (Section 4.5.3).

The pile set due to the simulated blow is 9 mm. This pile permanent displacement is equal to the set read in the dynamic pile testing in the field. This information is important to validate the model because one of the most important elements to evaluate the quality of the signal matching analysis is that the pile set should be similar to the one that occurred in the field.

The presented results were all calculated using a dynamic model. It is important to recall that the SRD is defined as the static term of the soil resistance during driving. Thus, attention is needed when comparing the obtained results from the dynamic model with the SRD values estimated according to the Alm and Hamre proposal.

Despite that, it was determined a load-displacement curve of a static compression test performed with the dynamic soil parameters estimated from the signal matching analysis. This curve is also shown in Figure 7.31. However, this analysis can be misleading because in static conditions the soil parameters will be different regarding the ones proposed in the dynamic model. For example, given that in static conditions the soil will be submitted to larger strain levels, the stiffness of the soil should be modified.

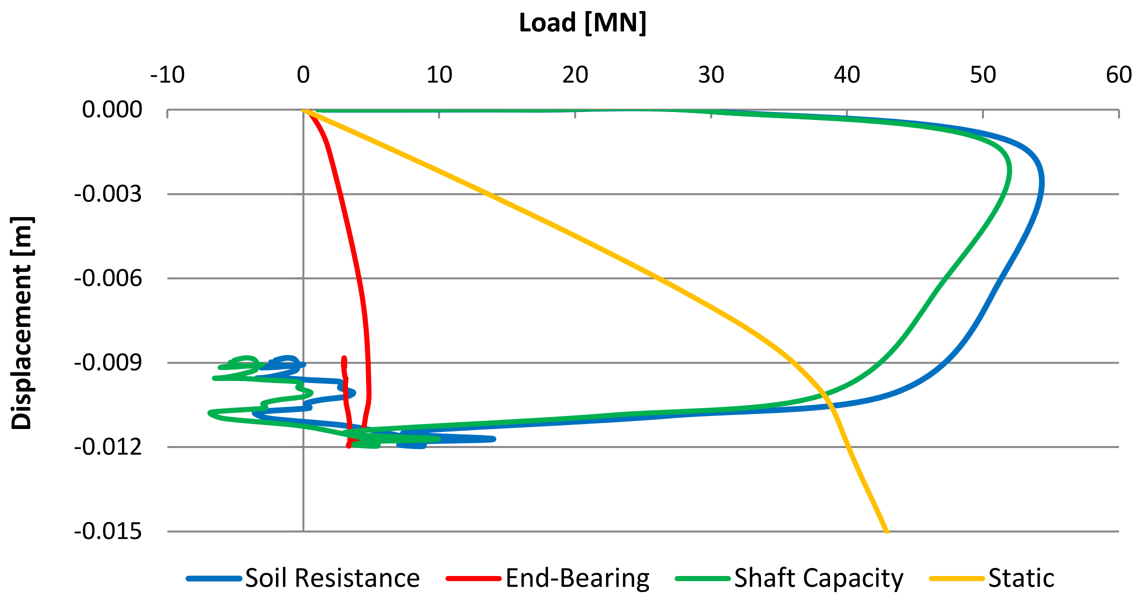

Figure 7.31. – Load-Displacement curve: no residual stresses considered

7.2.7. Discussion of the Results – Calculation Phase 4

A fourth and final calculation was performed in order to take into account the residual stresses that exist in the pile at the final of the last calculation. To achieve this objective, the pile was submitted to the same signal applied in the previous calculation phase. The same soil model and geotechnical parameters were used and the same pile model was also established.

In this section it will not be studied the behaviour of the soil plug as it was performed in the third calculation phase. The analysis of different moments that was conducted in the last section will also not be done in this case. These topics will not be analysed because the soil behaviour is generally similar in both calculations although the magnitude of the soil responses are different. This means that no different conclusions would be taken. Therefore, it was only analysed the pile axial capacity due to the second blow simulation.

Figure 7.32 displays the end-bearing capacity along time. It was calculated the average of four points of the pile tip cross section as presented in Section 7.2.6.6. The maximum end-bearing capacity equals 6.8 MN. This value is larger than the calculated in the previous section in which no residual stresses were taken into account. So, it is now confirmed that the end-bearing capacity was underestimated in about 2 MN when the residual stresses were not taken into account in the calculation. The determined end-bearing capacity is still in the range of the values estimated by the Alm and Hamre proposal and the ones obtained by the CAPWAP back-analysis performed by Cathie Associates. So, CAPWAP analysis appears to be capturing well the phenomenon that occurs in the pile tip.

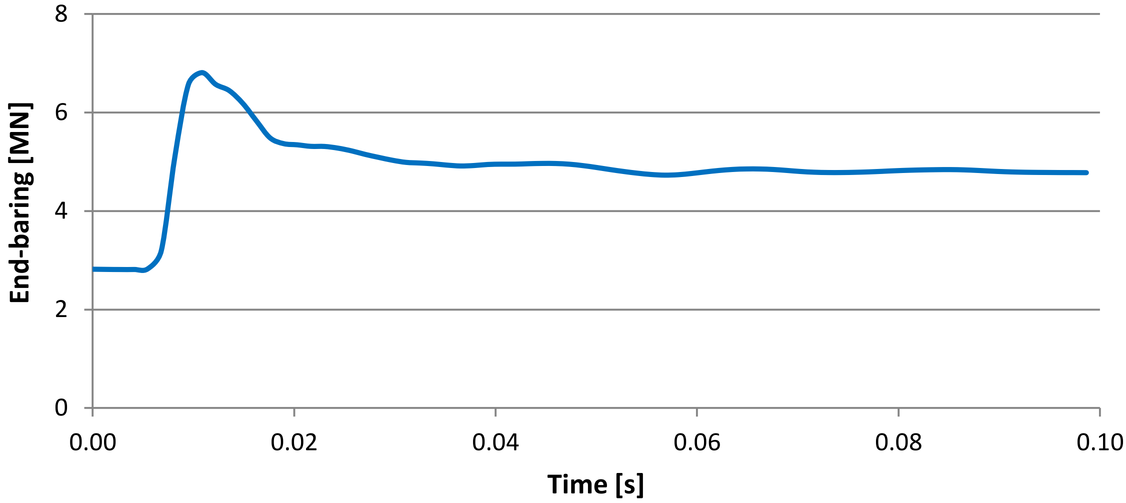

Figure 7.32 – End-bearing capacity: residual stresses considered

Regarding the shaft capacity, Figure 7.33 presents the inside and the outside shaft capacities along the time. Figure 7.34 shows the total shaft capacity over time. The maximum outside shaft capacity equals 25 MN and the maximum inside shaft capacity is of 21 MN. The total shaft capacity corresponds to 46 MN.

Thus, the outside shaft capacity equals 54% of the total shaft capacity. On the other hand, the inside shaft capacity equals 46% of the total shaft capacity. These values are not far from the 50% suggested by Alm and Hamre.

It is also confirmed that the shaft capacity was being overestimated in 7 MN when the residual stresses were not considered. However, the total shaft capacity continues to be much larger than the calculated by the Alm and Hamre proposal and by the CAPWAP back-analysis.

Thus, it can be concluded that the CAPWAP model is not capturing all the dynamic mechanisms that occur in a pile dynamic test. One possible reason for the observed difference of values is that CAPWAP is not considering the soil plug effects adequately. Another reason for this difference is due to not considering appropriately the radiation damping effects. It is important to recall that the CAPWAP analysis was executed with the limit values of radiation damping as established by the CAPWAP manual.

Finally, the load-displacement of the last calculation was determined and the results are presented in Figure 7.35. The total soil resistance obtained from the PLAXIS calculations was of 51 MN. This value is slightly lower than the one obtained when no residual stresses were considered. The pile permanent displacement is again of 9 mm, which is an important validation element to build a robust model. Again, attention is needed when comparing the dynamic results with SRD estimations (static soil resistance).

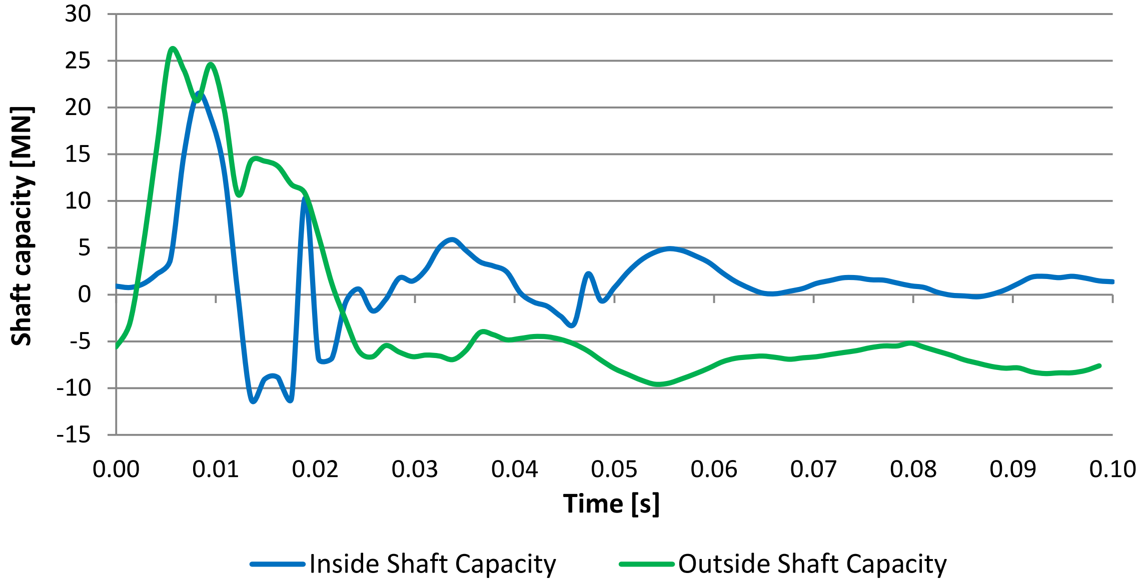

Figure 7.33. – Inside and Outise Shaft Capacities: residual stresses considered

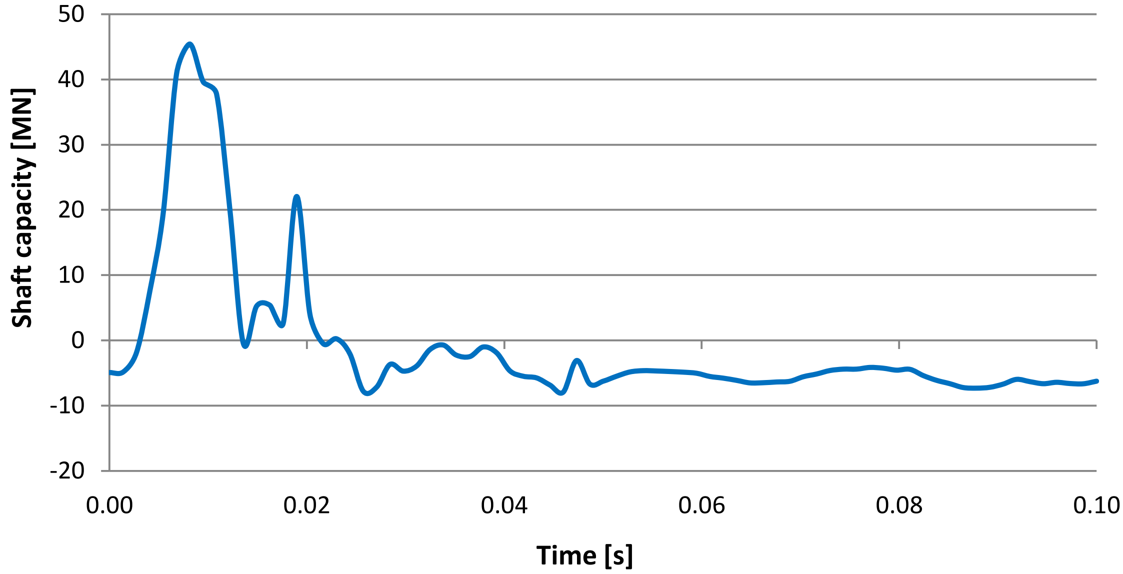

Figure 7.34. – Shaft Capacity: residual stresses considered

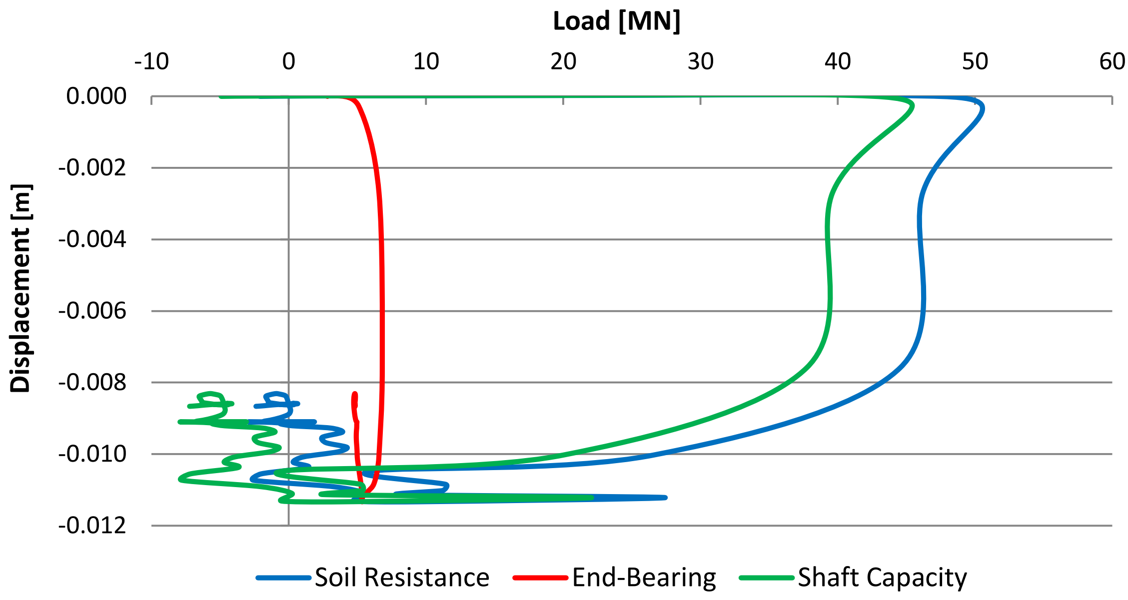

Figure 7.35. – Load-Displacement curve: residual stresses considered

8

CONCLUSIONS AND FUTURE DEVELOPMENTS

8.1. CONCLUSIONS

In this work a finite numerical model simulation was developed to simulate a pile static and dynamic testing in offshore conditions. The model tries to replicate a real driven pile designed by Cathie Associates. Large differences were observed between the SRD predicted by estimating methods and the back calculated SRD. Although a numerical model started to be developed, more improvements should be made in the future.

A Mohr-Coulomb model is used in both of the analysis to emulate the soil behaviour. The numerical analyses offered important conclusions about soil plug behaviour of a tubular pile with an outer diameter of 2.5 m into medium to very dense sand.

In Chapter 5, the static soil parameters were adjusted in order to get a reasonable approximation between the outside shaft profile and 50% of the shaft friction proposed by Alm and Hamre. The numerical simulations showed that in static conditions high horizontal stress peaks occur inside the pile. Thus, arching effect occurs in static loaded piles as concluded before by Kishida, Isemoto (1977). This behaviour is an indication of plug formation. Large effective stresses were shown in the inside pile wall 8.8 m above the pile tip. This value is in the range suggested by Leong, Randolph (1991) when they concluded that adequate end bearing can be mobilized by the soil plug, largely by high effective stresses in the bottom 3-5 diameters (7.5 – 12.5 m) of the soil plug. Still, it was observed that unplug behaviour occurs for shallow penetrations which is in accordance with the investigation carried out by Randolph (1988).

Still regarding the static numerical model, it was analytically obtained that the ratio between tension and compression outside shaft capacities is of 0.74. The inside shaft capacity cannot be included in this study because the results are clearly influenced by soil plug. From the design methods it is derived a ratio between the tension and compression shaft capacities ranging from 0.7 to 0.77.

In Chapter 6, a general analysis about dynamic numerical modelling was performed. These calculations offered a better understanding about the basic principles of a dynamic calculation and they also allowed checking if dynamic elements, such as the viscous boundaries, were working well in PLAXIS calculations. Therefore the calculations reported in Chapter 6 offered some confidence to the next analysis.

From these analyses, it is concluded that the mesh refinement has a large influence in the accuracy of the results. Also, some numerical damping may be necessary to be introduced in the model in order to reduce the spurious reflections observed in the results.

It is also concluded that the duration of the signal applied in the soil can lead to a free or to a force oscillation. A free oscillation occurs for short durations of the signal. In this case, the soil responds with its natural frequencies. On the hand, a forced oscillation occurs for long durations of the applied signal. The frequency content of the soil is governed by the frequency of the load in the field close to the local where the load is applied. On the far field, the soil responds as a free oscillation motion due to the low stiffness of the soil.

In Chapter 7, a dynamic pile testing is emulated on a numerical model. The results from PLAXIS were compared with the back calculated results from a real driven pile. The velocity signal measured by the strain gauges placed in the real driven pile was input in the PLAXIS calculation. A signal matching analysis was performed in order to establish adequate soil parameters. First, one calculation was run without considered the residual stresses of the soil due to pile driving. Finally, in a second calculation, the residual stresses obtained from the previous calculation are input on the mode.

Regarding the dynamic model, radiation damping is naturally considered in the model by PLAXIS. Still, numerical damping allowed reducing numerical instabilities in the soil. Some Rayleigh damping is also established in order to represent adequately the behaviour of the soil in the elastic range. Stiffness and damping values were established for the small strain levels observed in dynamic conditions.

From the executed analyses it is concluded that, when the pile is submitted to a dynamic load, the soil within the pile does not plug. This phenomenon is in accordance with the investigations developed by Henke and Grabe (2009). It is observed high effective stresses involving the pile tip which is an indication that the pile is coring.

However, the behaviour of the soil inside the pile requires further studies. Therefore, three different instants were analysed to understand the soil behaviour along the time. It is concluded that the wave that travels along the pile takes a while to produce effects in the surrounding soil and in the soil within the pile. Thus, the pile and the soil plug do not move in phase which is one possible reason for the wrong calculations executed with the CAPWAP model.

At the end of the third calculation phase, some residual stresses are observed on the outside pile wall. It is concluded that when no residual stresses are included in the analyses, the numerical model:

- Overestimates the shaft capacity;
- Underestimates the end-bearing capacity.

The end-bearing capacity calculated by the numerical model simulations is similar to the one estimated by Alm and Hamre proposal and back-calculated by CAPWAP. Despite that, the shaft capacity revealed to be much larger. Although the shaft capacity is being overestimated in the numerical model, CAPWAP does not appear to be correctly capturing some dynamic effects.

In the CAPWAP analyses, limited values of radiation damping were established which is a possible reason for the difference of axial pile capacities calculated between CAPWAP and the numerical model that was developed in the present work. The one-dimensional model may also be capable of capturing well soil plug mechanisms. In addition, it also does not consider residual stresses in the calculation which, as observed in the present work, can originate errors in pile capacity estimations. Finally, in the proposed model the soil was defined with a drained behaviour. Although this point is a limitation of the numerical model, its influence in the final results is not known.

8.2. FUTURE DEVELOPMENTS

The results that were obtained suggest that the developed numerical model is a promising tool to conduct more elaborate analyses of the SRD. Despite that, some improvements should be incorporated in order to create an even more robust model. Also, some validations and tests should be performed in the model. Future studies are now suggested:

- In fact, due to the confining pressure within the pile, the dilation of the soil can promote significant changes in the stresses within the open-ended pile. In the numerical model, this phenomenon can be captured by defining an improved soil model, such as a hardening soil model.
- When the soil is submitted to rapid motions, some excess pore pressures can be generated in the soil. However, this behaviour is extremely difficult to model. It is therefore proposed to perform further investigations in order to assess the influence of drained/undrained behaviour of the soil;
- Use other soil parameters in the signal matching analysis;
- Test the model in other locations and for other types of soil.

If with the suggested tests, the conclusions taken in the present work are confirmed, one challenging research would be to modify the CAPWAP one-dimensional model. This would be a huge development for the geotechnical community because, although finite element models are encouraged to be used in large projects, they can be time consuming in minor projects.

At the end, the author of this work thanks Cathie Associates for having proposed this research work and hopes that the developed model and the obtained conclusions can be helpful for the activities of this company.

REFERENCES

Alm, T., Hamre, L. (1998). *Soil Model for driveability predictions*. Offshore Technology Conference, 4-7 May, Houston, paper no. OTC 8835.

Alm. T, Hamre, L. (2002). *Soil Model for pile driveability predictions based on CPT interpretations*. Proceedings of the 15th International Conference on Soil Mechanics and Geotechnical Engineering, 27- 31 August, Istambul, vol.3, pp. 1297-1302, Taylor and Francis.

American Petroleum Institute (2010). *RP 2GEO: The new API Recommended Practice for Geotechnical Engineering.* American Petroleum Institute, Washington.

Amoroso, S. (2011). *G-γ decay curves by seismic dilatometer (SDMT)*. Ph.D. Thesis, University of L'Aquila.

Benz, T. (2007). *Small-strain Stiffness of Soils and its Numerical Consequences*. Ph.D. Thesis, Universität Stuttgart.

Bolton, M. (1986). *The strength and dilatancy of sands*. Géotechnique, March, vol. 126, no. 1, pp. 65-78, Institute of Civil Engineers.

Briaud, J.L. (2013). *Geotechnical Engineering: Unsaturated and Saturated Soils.* John Wiley & Sons, New Jersey.

Chopra, A.K. (1995). *Dynamics of structures.* Prentice Hall New Jersey, New Jersey.

Chow, Y.K. (1981). *Dynamic behaviour of piles*. Ph.D. Tesis, University of Manchester.

Elgamal, A., Yang, Z., Lai, T., Kutter, B., Wilson, D. (2005). *Dynamic response of saturated dense sand in laminated centrifuge container*. Journal of Geotechnical and Geoenvironmental Engineering, 1 May, vol. 131, no. 5, pp. 598-609, American Society of Civil Engineers.

Faria, R., (1994). *Avaliação do comportamento sísmico de barragens de betão através de um modelo de dano contínuo*. Ph.D. Thesis, Faculdade de Engenharia da Universidade do Porto.

Fellenius, B.H., Santos, J.A., Viana da Fonseca, A. (2007). *Analysis of piles in a residual soil – The ISC'2 prediction*. Canadian Geotechnical Journal, vol. 30, no. 2, pp. 201-220, NCR Research Press, Canada.

Fox, E. (1932). *Stress phenomena occurring in pile driving*. Engineering Journal, September, vol. 134, pp. 263-265, London.

Goble, G. G., Rausche, F. (1979). *Pile driveability predictions by CAPWAP*. Proceedings Conference on Numerical Methods in Offshore Piling, June 1979, Institute of Civil Engineers, London.

Goble, G.G., Rausche, F., Likins, G. (1999). *GRLWEAP Wave Equation Manual*. Cleveland.

Henke, S., Grabe, J. (2008). *Numerical investigation of soil plugging inside open-ended piles with respect to the installation method.* Acta Geotechnica, September, vol. 3, no. 3, pp. 215-223, Springer.

Henke, S., Grabe, J. (2009). *Numerical Simulations Concerning the Tendency of Soil Plugging in Open-Ended Steel-Piles*. Proceedings of the 28th International Conference on Ocean, Offshore and Arctic Engineering, 31 May– 5 June, Honolulu.

Holloway, D.M., Clough, G.W., Vesic, A.S. (1978). *The Effects Of Residual Driving Stresses On Pile Performance Under Axial Loads.* Proceedings of the Offshore Technology Conference, 8-11 May, Houston, no. OTC 3306, pp. 2225-2236.

Holscher, P., van Tol, A.F., Huy, N.Q. (2009). *Influence of Rate Effect and Pore Water Pressure during Rapid Load Test of Piles in Sand.* 9th International Conference on Testing and Design Methods for Deep Foundations, December, vol. 52, no. 6, pp. 1102-1117, CRC Press.

Issacs, D.V. (1931). *Reinforced concrete pile* formulas. Transactions of the Journal of the Institution of Engineers Australia, September, vol. 3, no. 9, pp. 305-324, Gloucester and Essex Streets, Sidney.

Jaky, J. (1944). *The coeficiente of earth pressure at rest*. Journal of Hungarian Architects and Engineers, October, vol. 1, pp. 355-358.

Jamiolkowski, M., LoPresti, D.C.F., Manassero, M. (2001). *Evaluation of relative density and shear strength of sands from CPT and DMT.* Soil Behaviour and Soft Ground Construction, pp. 201-238, American Society of Civil Engineers.

Jardine, R.J., Chow, F. (1996). *New Design Methods for Offshore Piles*. Marine Technology Directorate, London.

Jardine, R.J., Lehane, B.M., Everton, S.J. (1992). *Friction coefficients for piles in sands and silts*. Proceedings of the International Conference on Offshore Site Investigation and Foundation Behaviour, 22-24 September, London, vol. 28, no. 7, pp. 661-677, Springer.

Jardine, R.J., Chow, F., Overy, R., Standing, J. (2005). *ICP design methods for driven piles in sands and clays*. Thomas Telford, London.

Kim, D., Lee, J. (2000). *Propagation and attenuation characteristics of various ground vibrations*. Soil Dynamics and Earthquake Engineering, February, vol. 19, no. 2, pp. 115 – 126, Elsevier Science Lda.

Kishida, H., Isemoto, N. (1977). *Behaviour of sand plugs in open-ended steel pipe piles*. Proceedings of the 9th International Conference on Soil Mechanics, 10-15 July, Tokyo, vol. 1, pp. 601-604.

Kramer, S. (1996). *Geotechnical earthquake engineering.* Prentice-Hall, London.

Kleven, A., Lacasse, S., Andersen, K.H. (1986). *Soil parameters for offshore foundation design*. N61 Report, no. 40013-34, 9 April.

Lacasse, S., Nadim, F., Langford, T., Knudsen, S., Norwegian Geotechnical Institute (NGI), Yetginer, G., Guttormsen, T.R., Eide, A. (2013). *Model Uncertainty in Axial Pile Capacity Design Methods*. Offshore Technology Conference, Houston, 6-9 May, no. OTC 24066.

Leong, E., Randolph, M. (1991). *Finite element analyses of soil plug response*. International Journal for Numerical and Analytical Methods in Geomechanics, February, vol. 16, no. 2, pp. 121-141, John Wiley and Sons, Lda.

Lesny, K. (2010). *Foundations for Offshore Wind Turbines – Tools for Planning and Design*. VGE Verlag GmbdH, Essen.

Liyanapathirana, D.S., Deeks, A.J., Randolph, M.F. (1998). *Numerical Analysis of soil plug behaviour inside open-endend piles during driving*. International Journal for Numerical and Analytical Methods in Geomechanics, April, vol. 22, no.4, pp. 303-322, John Wiley and Sons, Lda.

Liyanapathirana, D.S., Deeks, A.J., Randolph, M.F. (2001). *Numerical modelling of the driving response of thin-walled open-ended piles*. International Journal for Numerical and Analytical Methods in Geomechanics, August, vol. 25, no. 9, pp. 933-952, John Wiley and Sons, Lda.

Lopes, P., Costa, P.A., Calçada, R., Cardoso, A.S. (2013). Numerical modeling of vibrations induced in tunnels: A 2.5D FEM-PML approach. In *Traffic induced Environmental Vibrations and Controls: Theory and Application*, pp. 113-166, Nova Science Publishers, Inc.

Lunne, T. (2010). *The CPT in offshore soil investigations-a historic perspective.* Proceedings of the 2nd International symposium on cone penetration testing (CPT' 10). 9-11 May, Huntington Beach, California.

Lunne, T., Christoffersen, H.P. (1983). *Interpretation of cone penetration testing for offshore sands*. Proceedings of the Offshore Technology Conference, Houston, no. OTC 4464, pp. 181-192.

Lunne, T., Robertson, P.K., Powell, J.J.M. (1997). *Cone Penetration Testing- Geotechnical Practice.*E and FN Spon.

Masoumi, H., François, S, Degrande, G. (2009). *A non-linear coupled finite element–boundary element model for the prediction of vibrations due to vibratory and impact pile driving*. International Journal for Numerical and Analytical Methods in Geomechanics, 10 February, vol. 33, no. 2, pp. 245-274, John Wiley & Sons, Ltd.

Masoumi, H., Degrande, G. (2008). *Numerical modeling of free field vibrations due to pile driving using a dynamic soil-structure interaction formulation.* Journal of Computational and Applied Mathematics, June, vol. 215, no. 2, pp. 503-511, Elsevier Science Lda.

Masouleh, S.F., Fakharian, K. (2008). *Verification of Signal Matching Analysis of Pile Driving Using Finite Differente Based Continuum Numerical Method.* International Journal of Civil Engineering, September, vol. 6, no. 3, pp. 174-182.

Meynard, A., Corte, J. (1984). *Experimental study of lateral resistance during driving*. Proceedings of the 2nd International Conference on the Application of Stress-Wave Theory of Piles, Stockholm.

Mouta da Costa, L. (1994). *Previsão do Comportamento das Estacas Considerando As Tensões Residuais de Cravação.* Ph.D. Thesis, Universidade Federal do Rio de Janeiro.

Overy, R. (2007). *The use of ICP design method for the foundations of nine platforms installed in the UK North Sea.* Offshore Site Investigation and Geotechnics, Confronting New Challenges and Sharing Knowledge, 11-13 September, London.

Overy, R., Sayer, P. (2007). *The use of ICP design methods as a predictor of conductor drill-drive installation.* Offshore Site Investigation and Geotechnics, Confronting New Challenges and Sharing Knowledge, 11-13 September, London.

Pinto, P.L., Grazina, J.C., Lourenço, J.C. (2008). *Evaluation of 1D and 2D numerical modelling techniques of dynamic pile testing.* Proceedings of the 8th International Conference on the Application of Stress-Wave Theory to Piles (Santos, J.A., ed.), 8-10 September, Lisbon, pp. 353-357, IOS Press.

PLAXIS (2014a). *PLAXIS 2D Material Models Manual – Anniversary Edition*. February.

PLAXIS (2014c). *PLAXIS 2D Scientific Manual – Anniversary Edition*. February.

Randolph, M.F. (1988). *The axial capacity of deep foundations in calcareous soil (state-of the art report).* Proceedings of the International Conference on Calcareous Sediments, Perth, vol.2, pp. 837 – 857.

Randolph, M., Gouvernec, S. (2011). *Offshore for geotechnical engineering*. Spon Press, Abingdon.

Randolph, M., Leong, E., Houlsby, G. (1991). *One-dimensional analysis of soil plugs in pipe piles*. Géotechnique, December, vol. 41, no. 4, pp. 587-598.

Rausche, F. (2000). *Pile Driving Equipment - Capabilities and Properties*. Proceedings of the 6th International Conference on the Application of Stress-Wave Theory to Piles 2000, 11-13 September (Niyama, Beim), São Paulo, pp. 75-89, Balkema.

Robertson, P. K., Cabal, K. L. (2010). *Guide to Cone Penetration Testing for Geotechnical Engineering.* Gregg Drilling and Testing Inc., California.

Schneider, J., Xu, X., Lehane, B. (2008). *Database Assessment of CPT-Based Design Methods for Axial Capacity of Driven Piles in Siliceous Sands*. Journal of Geotechnical and Geoenvironmental Engineering, 1 September, vol. 134, no. 9, pp. 1227-1244, American Society of Civil Engineers.

Seed, H.B., Idriss, I.M. (1970). Soil moduli and damping factors for dynamic response analysis. Report 70-10 EERC, Berkeley.

Seed, H.B., Wong, R.T., Idriss, I.M., Tokimatsy, K. (1986). *Moduli and damping factors for dynamic analyses of cohesionless soils.* Journal of Geotechnical Engineering, November, vol. 112, no. 11, pp. 1016-1032, American Society of Civil Engineers.

Simons, H.A., Randolph, M.F. (1985). *A new approach to one dimensional pile driving analysis*. Proceedings of the 5th International Conference on Numerical Methods in Geomechanics (Kawamoto, T, Ichikawa, Y.), 1-5 April, Nagoya, pp. 1457-1464, Balkema.

Smith, E.A.L. (1960). *Pile-driving analysis by the wave equation*. Journal of the Soil Mechanics and Foundations Division, August, vol. 86, no. 4, pp. 35-61, American Society of Civil Engineers.

Viana da Fonseca, A., Santos, J.A., Costa Esteves, E.F.M., Massad, F. (2007). *Analysis of Piles in Residual Soil from Granite Considering Residual Loads*. Soils and Rocks International Journal, vol. 30, no. 1, pp.63-80. ABMS.

Viana da Fonseca, A., Santos, J.A. (2008). *Behaviour of CFA, Driven and Bored Piles in Residual Soil. International Prediction Event – Experimental Site – ISC'2*. Published by FEUP/IST.

Wang, H.., Zhang, L.M. (2008). *Estimating residual stresses in long* driven piles in weathered soils. Proceedings of the 8th International Conference on the Application of Stress-Wave Theory to Piles (Santos, J.A., ed.), 8-10 September, Lisbon, pp. 353-357, IOS Press.

Yang, J. (2006). *Influence Zone for End Bearing of Piles in Sand*. Journal of Geotechnical and Geoenvironmental Engineering, September, vol. 132, no. 9, pp. 1229-1237, American Society of Civil Engineers.

REVIEWED BIBLIOGRAPHY

Achmus, M., Muller, M. (2011). *Evaluation of pile capacity approaches with respect to piles for wind energy foundations in the North Sea.* Proceedings of the 2nd International Frontiers in Offshore Geotechnics (Gouvernec, S., White, D.), 8-10 November, Perth, pp. 563-568, Taylor and Francis.

Alvarez, C., Zuckerman, B., Lemke, J. (2006). *Dynamic Pile Analysis Using CAPWAP and Multiple Sensors*. Proceedings of the GeoCongress 2006: Geotechnical Engineering in the Information Technology Age (DeGroot, D., DeJong, J., Frost,D., Baise, L.), 26 February – 1 March, Atlanta, pp. 1-5, American Society of Civil Engineers.

Alves, A.M.L., Lopes, F.R., Danziger, B.R. (2008). *Dimensional analysis of the wave equation applied to pile driving.* Proceedings of the 8th International Conference on the Application of Stress-Wave Theory to Piles (Santos, J.A., ed.), 8-10 September, Lisbon, pp. 353-357, IOS Press.

Alves da Costa, P. (2011). *Vibrações do sistema via-maciço induzidas por tráfego ferroviário : modelação numérica e validação experimental*. Ph.D. Tesis, Faculdade de Engenharia da Universidade do Porto.

Alves da Costa, P., Calçada, R., Couto Marques, J., Cardoso, A. (2010). *2.5 D finite element model for simulation of unbounded domains under dynamic loading.* Proceedings of the 7th European Conference on Numerical Methods in Geotechnical Engineering (Benz, T., Nordal, S.), 2-4 June, Trondheim, CRC Press.

Atkinson, J. (2007). *The Mechanics of Soils and Foundations (2nd Edition)*. Taylor and Francis, Abingdon.

Belloti, R., Crippa, V., Pedromi, S., Ghionna, V.N. (1988). *Saturation of sand specimen for calibration chamber tests.* Proceedings of the International Symposium on Penetration Testing, Orlando, Balkema.

Brennan, A., Thusyanthan, N., Madabhushi, S. (2005). *Evaluation of shear modulus and damping in dynamic centrifuge tests.* Journal of Geotechnical and Geoenvironmental Engineering, 1 December, vol. 131, no. 12, pp. 1488-1497, American Society of Civil Engineers.

Byrne, T., Doherty, P., Gavin, K., Overy, R.(2012). *Comparison of Pile Driveability Methods In North Sea Sand.* Offshore Site Investigation and Geotechnics: Integrated Technologies-Present and Future, 12-14 September, London.

Chai, H.Y., Wei, C.F. (2008). *Analysis of wave propagation in piles*. Proceedings of the 8th International Conference on the Application of Stress-Wave Theory to Piles (Santos, J.A., ed.), 8-10 September, Lisbon, pp. 87-92, IOS Press.

Clough, R.W., Penzien, J. (1975). *Dynamics of structures.* McGraw-Hill, Incorporated, New York.

Dean, E.T.R. (2010). *Offshore geotechnical engineering – Principles and practice*. Thomas Teldford Limited, London.

Deeks, A. (1992). *Numerical Analysis of Pile Driving Dynamics*. Ph.D. Thesis, University of Western Australia.

Eidsvig, U., Nadim, F., Yetginer, G., Guttormsen, T., Lacasse, S., Andersen, K., Eide, A., Knudsen, S. (2013). Offshore Technology Conference, 6-9 May, Houston, Texas.

Fellenius, B. (1999). *Basics of Foundation Design – Electronic Edition*. BiTech Publications, British Columbia.

Gerwick, Jr. (2007). *Construction of Marine and Offshore Structures.* CRC Press, San Francisco.

Jackson, A. M. (2007). *Pile jacking in sand and silt.* Winner of the ICE's national Graduates and Students Papers Competition 2008, February.

Linkins, G., Piscsalko, G., Roppel, S., Rausche, F. (2008). *PDA Testing: 2008 State of the art.* kProceedings of the 8th International Conference on the Application of Stress-Wave Theory to Piles (Santos, J.A., ed.), 8-10 September, Lisbon, pp. 353-357, IOS Press.

Linkins, G., S., Rausche, F. (2004). *Correlation of CAPWAP with static load tests*. Proceedings of the 7th International Conference on the Application of Stress-Wave Theory to Piles, August, Petaling Jaya, pp. 153-165.

Liyanapathirana, D.S., Deeks, A.J., Randolph, M.F. (2001). *Behaviour of Thin-Walled Open-Ended Piles During Driving*. Computational Mechanics-New Frontiers for the New Millennium (Valliappan, S., Khalili, N.), vol. 2, pp. 393-398, Elsevier Science Lda.

Mabsout, M., Reese, L., Tassoulas, J. (1995). *Study of pile driving by finite-element method.* Journal of GeotechnicKal Engineering, July, vol. 121, no. 7, pp. 535-543, American Society of Civil Engineers.

Matos Fernandes, M. (2006). *Mecânica dos Solos – Conceitos e Princípios Fundamentais*. FEUP Edições, Porto.

Matos Fernandes, M. (2011). *Mecânica dos Solos – Introdução à Engenharia Geotécnica*. FEUP Edições, Porto.

Novak, M. (1977). *Vertical vibration of floating piles*. Journal of the Engineering Mechanics Division, January and February, vol. 103, no. 1, pp. 153-168, American Society of Civil Engineers.

Novak, M., Nogami, T., Aboul-Ella, F. (1978). *Dynamic soil reactions for plane strain.* Journal of the Engineering Mechanics Division, July and August, vol. 104, no. 4, pp. 953-959, American Society of Civil Engineers.

PLAXIS (2014b). *PLAXIS 2D Reference Manual – Anniversary Edition*. February.

PLAXIS (2014d). *PLAXIS 2D Tutorial Manual – Anniversary Edition*. February.

Powrie, W. (1997). *Soils Mechanics Concepts and Applications*. Spon Press, Abingdon.

Puech, A., Foray, P. (2002). *Refined model for interpreting shallow penetration CPTs in sands.* Proceedings of the Offshore Technology Conference, 6-9 May, Houston.

Randolph, M. (2003). *Science and empiricism in pile foundation design*. Géotechnique, December, vol. 53, no. 10, pp. 847-875, Institute of Civil Engineers.

Randolph, M., May, M., Leong, E., Hyden, A., Murff, J. (1992). *Soil plug response in open-ended pipe piles.* Journal of Geotechnical Engineering, 1 May, vol. 118, no. 5, American Society of Civil Engineers.

Rausche, F., Goble, G. G. (1972). *Performance of Pile Driving Hammers.* Journal of the Construction Division, September, vol. 98, no. co2, pp. 201-218, American Society of Civil Engineers.

Rausche, F., Nagy, M., Webster, S., Liang, L. (2009). *CAPWAP and Refined Wave Equation Analyses for Driveability Predictions and Capacity Assessment of Offshore Pile Installations*. Proceedings of the 28th International Conference on Ocean, Offshore and Arctic Engineering, Honululu, 31 May – 5 June, vol. 7, no. OMAE2009-80163, pp. 375-383, American Society of Mechanical Engineers.

Rausche, F., Robinson, B., Liang, L. (2000). *Automatic signal matching with CAPWAP*. Proceedings of the 6th International Conference on the Application of Stress-Wave Theory to Piles (Niyama, Beim), 11-13 September, São Paulo, pp. 53-58, Balkema.

Rausche, F., Robinson, B., Seidel, J. (2000). *Combining static pile design and dynamic installation analysis in GRLWEAP*. Proceedings of the 6th International Conference on the Application of Stress-Wave Theory to Piles (Niyama, Beim), 11-13 September, São Paulo, pp. 59-64, Balkema.

Rausche, F., Webster, S. (2007). *Behavior of cylinder piles during pile installation*. Contemporary Issues in Deep Foundations: Proceedings of Sessions of Geo-Denver 2007 (Camp, W., Castelli, R., Laefer, D.F., Paikowsky, S.), 28-21 February, Denver, pp.1-13, American Society of Civil Engineers.

Rollins, K., Evans, M., Diehl, N., Daily III, W. (1998). *Shear modulus and damping relationships for gravels*. Journal of Geotechnical and Geoenvironmental Engineering, 1 May, vol. 124, no. 5, American Society of Civil Engineers.

Schofield, A., Wroth, C.P. (1968). *Critical state soil mechanics.* McGraw-Hill, London

Smith, I.M., Chow, Y.K. (1982). *Three-Dimensional Analysis of Pile Drivability.* Proceedings of the 2nd International Conference on Numerical Methods in Offshore Pilling, 29-30 April, Austin, University of Texas, Austin.

To, P., Smith, I.M. (1988). *A note on finite element simulations of pile driving*. International Journal for Numerical and Analytical Methods in Geomechanics, March-April, vol. 12, no. 2, pp. 213-219, John Wiley & Sons, Ltd.

Tomlinson, M.J. (2005). *Pile Design and Construction Practice.* Taylor and Francis, Abingdon.

Verruijt, A. (2010). *An introduction to soil dynamics.* Springer, Delft.

Yang, J., Kuo, S., Hung, H. (1996), *Frequency-Independent Infinite Elements for Analysing Semi-Infinite Problems.* International Journal for Numerical Methods in Engineering, 30 October, vol. 39, no. 20, pp. 3553-3569, John Wiley and Sons, Lda.

Yu, F., Yang, J. (2011). *Base capacity of open-ended steel pipe piles in sand*. Journal of Geotechnical and Geoenvironmental Engineering, September, vol. 138, no. 9, pp. 1116-1128, American Society of Civil Engineers.

WEBSITE REFERENCES

[1] http://www.rechargenews.com/news/, March 14, 2014

[2] http://www.upstreamonline.com/, March 14, 2014

[3] http://www.dongenergy.com/, March 16, 2014

[4] http://ngi.no/, March 14, 2014

[5] http://www.maritime-executive.com, March 15, 2014

[6] http://www.ptc.fayat.com, March 16, 2014

[7] http://www.vulcanhammer.info/, March 14, 2014

[8] http://www.mywindpowersystem.com, March 15, 2014

[9] http://www.apevibro.com, March 15, 2014